Zinc oxide growth and its interfaces with metals observed by photoemission

Ekaterina Chernysheva

Université Pierre et Marie Curie

Ecole Doctorale 397 « Physique et Chimie des Matériaux »

Institut des NanoScience de Paris, Equipe « Oxydes en Basses Dimensions »

Unité Mixte CNRS/Saint-Gobain Recherche « Surface du Verre et Interfaces »

Zinc oxide growth and its interfaces with metals observed by photoemission

Par Ekaterina CHERNYSHEVA

Thèse de doctorat de Physique

Dirigée par Rémi LAZZARI et Sergey GRACHEV

Présentée et soutenue publiquement le 24 Mars 2017

Devant un jury composé de :

M. Bruno Domenichini	Professeur (ICB)	Rapporteur
M. Gunnar Niklasson	Professeur (Uppsala)	Rapporteur
M. Olof Karis	Professeur (Uppsala)	Examinateur
M. Fabrice Bournel	Maître de conférences (LCPMR)	Examinateur
M. Sergey Grachev	Ingénieur (Saint-Gobain Recherche)	Examinateur
M. Rémi Lazzari	Chargé de Recherche (INSP)	Examinateur

Contents

Acknowledgements

I would like to express sincere appreciation and gratitude to my supervisors at Saint-Gobain Recherche, where I spent most of my time during last three years: Sergey Grachev, my official and dear supervisor at SGR and Hervé Montigaud, who was supposed to follow the PhD from the engineering side, but who did much more than that... Thank you Sergey and Hervé for the possibility to learn so much while working and discussing with you, and thanks to the collaborations that you initiated with our industrial R&D colleagues. Thank you for your trust and patience, for your support... and for great examples you were for me through these three years. I value all this a lot. Thanks for your guidance, advice, kindness, pedagogical approach, help, understanding... Thanks for leaving a lot of space for initiative and autonomy, for being receptive and accessible, for sharing your knowledge and experience... And for the great moments we spent together at SGR or during our beamtimes at BESSY. I particularly appreciated your help and encouragements during writing the PhD thesis. It is more than precious, because no one else understood and cheered me up better than you did.

I would also like to thank Elin Søndergård who initiated my PhD together with Sergey Grachev and Rémi Lazzari – she was there during the launch of the PhD as the SVI laboratory director at the time and witnessed our first results. Another big thank you is for Emmanuelle Gouillart who is the actual director of SVI. Thanks for being such keen and attentive, encouraging and supportive – for my professional and extra-professional activities. That is really precious, and I wonder if I ever happen to have again a director like you. Thanks for everything! I am also grateful to my laboratory colleagues with whom we worked together – it was fantastic: Raphaël Danguillaume, Ekaterina Burov, Emmanuel Garre, and Iryna Gozhyk. Raphaël, you are a great colleague, thanks for keeping MISSTIC working, for your help and collaboration on thermocouple studies, as well as for one of the beamtimes in Berlin, when we worked together. Katia, I remember the day when you came to one of my last *points de thèse* and said that what was missing in the beautiful picture of the Ti-ZnO reaction was thermodynamics. Thank you and Hervé for your help with that part of the study, which made it complete. Thanks to my dear colleagues, and especially PhD students (past and present) – no one can understand you better than your mate who is/was living the same situation. Thanks for the *culbitures*, skiing, and not only! Thanks for the magic young atmosphere you created – please go on! And a special word for the inhabitants of the *bureau* 536. I love you, guys. Thanks for the mood, for the music, for every single moment we shared.

I am also grateful to people from SGR who followed my PhD and participated in discussions, or with whom we worked on related topics interesting for the industrial side. Thank you Mathieu Joanicot, François Creuzet, David Nicolas, Benoit Georges, Denis Guimard, Florent Martin, Johann Skolski, Silvia Mariani... This list can be continued, and if you do not find yourself in it, please do know that I really appreciated working with you and learning from you. Also, a special thanks to the engineers of the microanalysis department for the EPMA, XRD, and SIMS measurements.

I would like to thank my *directeur de thèse* Rémi Lazzari who did not let it go till the last moment, and encouraged me in some difficult times. I learnt a lot from you as my scientific advisor, and I thank you for that. But also, I will remember the conference in Dubrovnik, where we went together – I had a chance to discover your personality that I truly appreciated. I am really thankful to Jacques Jupille and Greg Cabailh who followed my work from the INSP side. Our fruitful discussions and your kindness are a big part of what made it all possible. Thanks to the colleagues at INSP I became attached to: Francia Haque, Stéphane Chenot, Younes Mouchaal, Patricia Borghetti, Maya Messaykeh, Rémi Cavallotti, Claudine Noguera, Jacek Goniakowski... The list is not exhaustive – thank you all! And a huge thanks to Sarah Hidki for the XRD measurements at INSP.

My deep appreciation goes to Nicola Bartolomei and Sebastian Castilla who contributed to this work

through their internships at SGR and INSP. I am happy to know you – you are simply the best.

This PhD would not be possible without our collaborators on synchrotron experiments from Uppsala University and Helmholtz Zentrum Berlin: Rebecka Lindblad, Bertrand Philippe, and Mihaela Gorgoi. Thank you for making it happen being there day and night. And I sincerely thank Olof Karis and Håkan Rensmo for your guidance and expertise in terms of our collaboration.

We also had a chance to exchange and collaborate on ZnO thin films with our colleagues from NIMS, Japan: Naoki Ohashi and Benjamin Dierre. Thank you Ohashi-san and Benjamin for the discussions going beyond the collaboration, and for your help with PL measurements.

I would also like to express my gratitude to the reviewers and jury members who kindly accepted to evaluate my thesis: Prof. Bruno Domenichini, Prof. Gunnar Niklasson, Prof. Olof Karis, and Dr. Fabrice Bournel.

Last but not least, I would like to thank my Family and Friends for their love, patience, continuous support and trust in me. Thank you Dima-my-love, Mom, Granny, Asiya, Francia, Ferdinand, Dima I., Artur, William, Avishek, Tanya, Lera, Daouda, Dima E., Leonid, Daria, Sergey, Benjamin, Nicola, J-Paul, Jean-Claude, JB, Jean-Yvon, Aymeric, Damien, Maxime, Corinne, Natasha, Tima, Indira, Vanya,.. and all the dearest people around me.

Thank you.

Résumé en français

Les films minces sont couramment employés pour apporter de nouvelles fonctionnalités au verre plat. Dans une grande gamme de produits industriels pour le bâtiment et l'automobile, l'isolation thermique est améliorée par le dépôt de films nanométriques d'argent qui sont suffisamment minces pour la transparence optique mais suffisamment épais pour refléter l'infrarouge. Ces revêtements bas-emissifs sont des empilements complexes de films minces qui sont déposés à l'échelle industrielle par pulvérisation cathodique sur les panneaux de verre. Le démouillage ou la délamination peuvent réduire la performance optique et la durabilité du produit en raison de l'adhésion médiocre entre l'Ag et les couches adjacentes. Le film d'Ag est par conséquent pris en sandwich entre des couches texturées {0001} de ZnO qui se trouve être le meilleur candidat pour améliorer la cristallisation et l'adhésion. Des couches dites bloqueurs de métaux de transition tels que le Ti sont également ajoutées à l'interface. Dans ce cadre industriel, cette thèse s'est penchée sur divers aspects fondamentaux des interfaces métaux/ZnO en combinant des approches de science des surfaces sur des monocristaux et des films pulvérisés. Plusieurs stratégies de mesure et systèmes modèles ont été employés pour aborder les question du contact électrique à l'interface Ag/ZnO, du contrôle de la polarité dans les films pulvérisés de ZnO et de l'évolution de la chimie à une interface enterrée Ti/ZnO lors d'un traitement thermique.

Des films d'Ag, de la sous-monocouche jusqu'à la percolation, ont été élaborés par évaporation thermique sur des surfaces (1×1) de ZnO(0001) terminées O ou Zn et préparées par bombardement/recuit sous vide. La diffraction, la microscopie et la plasmonqiue ont démontré une croissance épitaxiale (111) hexagone/hexagone sous la forme de particules à toits plats. L'épitaxie est expliquée par une nucléation/croissance préférentielle suivant les bords de marches polaires. Le lien entre morphologie, polarité et adsorption d'hydrogène sur l'alignement de bandes à l'interface Ag/ZnO a été exploré en combinant la photoémission UV ou sous rayons X durs. Les surfaces natives présentent une forte courbure de bande vers le haut et la préparation de surface conduit à un semi-conducteur dégénéré ayant un niveau de Fermi au-dessus de la bande de valence. L'exposition à l'hydrogène atomique courbe les bandes vers le bas, et H réagit chimiquement avec les deux faces. Aux premiers stades de la croissance qui correspondent à la formation de particules 2D, un transfert de charge a lieu à l'interface conduisant à un dipôle. Ensuite, l'adsorption d'Ag devient rapidement métallique. Pour des films épais, le contact électrique Ag/ZnO est de type Schottky avec une hauteur de barrière de 0.5-0.7 eV, indépendamment de la terminaison ou de l'hydrogénation.

Le contrôle de la terminaison et de la cristallinité de films de ZnO déposés par pulvérisation cathodique sur de Si a été systématiquement exploré en fonction de la température du substrat et de sa polarisation électrique. La vitesse de croissance peut être fortement influencée par un effet combiné de re-pulvérisation et de température. Sur un substrat chaud, la formation de SiO_x et/ou l'interdiffusion sont favorisées ralentissant grandement la vitesse de croissance. Tous les échantillons sont polycristallins, texturés {0002}. En utilisant une empreinte spécifique à la polarité dans le spectre X de la bande de valence de ZnO, un diagramme expérimental température/polarisation a été obtenu démontrant les conditions pour lesquelles la polarité peut être contrôlée.

La réaction interfaciale entre ces films de ZnO et le Ti a été étudiée dans des empilements modèle Si / ZnO / Ti / Mo lors de traitements thermiques. En croisant photoémission haute énergie et la désorption thermique, il a été démontré que la réaction rédox Ti-ZnO donne lieu à la formation d'un ensemble de sous-oxydes de Ti et de Zn métallique qui désorbe de l'échantillon. Après un recuit à 550 ° C, Ti^{4+} devient dominant et un composé mixte $ZnTiO_x$ se forme à l'interface. L'influence de la quantité de ZnO et de sa cristallinité a également été abordée. Ces constatations ont été corrélées avec des simulations thermodynamiques du diagramme de phase Ti-ZnO.

Summary

Thin films are a common way to add functionality to flat glass. In a wide range of commercial products for building materials and automotive industry, thermal insulation is improved by the deposition of a continuous nanometric film of silver which is thin enough to ensure optical transparency but thick enough to reflect infra-red light. The low-emissive coatings consist of complex stacks of thin films deposited at the industrial scale by magnetron sputtering on window-sized glass plates. Dewetting or delamination may impact the performance and lifetime of the product due to a poor adhesion of silver. Therefore, silver is sandwiched in between ZnO{0001}-textured films which turned out to be the best candidate to improve silver crystallization and adhesion. Blocker layers of transition metals, such as titanium, are also added at the interface. In this industrial context, the present thesis focused on several fundamental aspects of metal/ZnO interfaces by combining surface science approaches on single crystals and model sputtered films. Several original measurement strategies and model systems have been employed to tackle the questions of: (i) the Ag/ZnO electrical contact, (ii) the control of the polarity of sputtered ZnO films on amorphous substrates, and (iii) the evolution of the chemistry of buried Ti/ZnO interface during thermal treatment.

Silver films from submonolayer to percolated thick films were grown by thermal evaporation on (1×1) O- and Zn-terminated ZnO(0001) surfaces prepared by sputtering-annealing cycles in vacuum. Diffraction, microscopy and plasmonics showed that Ag grows epitaxialy with (111) hexagon-on-hexagon orientation in the form of flat top clusters. The epitaxy is explained by a preferential nucleation and growth at polar step edges. The interplay between morphology, polarity and hydrogen adsorption on the band alignment between silver and ZnO(0001) faces was explored by combining ultra-violet and hard X-ray photoemission. Pristine surfaces present a strong upward band bending and the surface preparation leads to a degenerated semiconductor with a Fermi level above the conduction band. Exposure to atomic hydrogen bends the band downwards, and H chemically reacts with the two ZnO surfaces. At the early stages of Ag growth, when 2D particles are formed, charge transfer occurs at the Ag/ZnO interface. Then, the adsorption of silver rapidly becomes neutral. For thick films, the electrical contact at the interface is of Schottky type with a barrier height around 0.5-0.7 eV, independently of the surface termination or hydrogenation state.

The control of surface termination and crystallinity of ZnO thin films deposited by magnetron sputtering on Si wafer was systematically explored as a function of substrate temperature and bias voltage. It was discovered that the growth rate can be highly influenced by a combined effect of re-sputtering and temperature. On a hot susbtrate, SiO_x formation and/or intermixing are favoured, significantly slowing down ZnO growth. All ZnO samples were polycrystalline {0002}-textured. Using an orientation-dependent fingerprint in the X-ray valence band spectrum of ZnO, an experimental temperature/bias diagram was derived showing the conditions in which the film polarity can be controlled.

The interfacial reaction between those ZnO films and Ti was investigated in model Si / ZnO / Ti / Mo (cap) stacks upon thermal treatment. Using a combination of high energy photoemission at the synchrotron and desorption spectroscopy, it was found that the redox reaction between ZnO and Ti gives rise to the formation of a set of Ti sub-oxides (Ti(II), Ti(III), Ti(IV)) and metallic Zn that is highly mobile and escapes the sample. After annealing at 550 °C, Ti^{4+} becomes the dominant oxidation state and a mixed $ZnTiO_x$ compound is formed at the Ti-ZnO interface. The influence of the initial ZnO quantity and crystallinity on the reaction was also studied. Those findings were correlated with thermodynamic simulations of the phase diagram of the Ti-ZnO system.

Introduction

Industrial context

Glass products offer a unique opportunity to reduce greenhouse gas emissions and mitigate the effects of climate change. Since over 40% of all energy in the European Union is used in buildings (Fig. 1a), making new and existing ones as energy efficient as possible will thus enable significant strides towards the ambitious and mandatory CO_2 reduction goals. Low-emissivity (Low-E) insulating glazing windows (Fig. 1b,c) are specially coated with transparent silver-based thin films (around 10 nm) that reflect heat, *i.e.* infrared radiation (IR), back into the building, thereby reducing the heat loss through the window [1, 2]. The IR reflectivity is directly correlated to the metal emissivity and therefore the metal conductivity; the higher the conductivity, the higher the IR reflectivity, and in turn the better the insulating properties of the glazing. In addition, the coating should allow for large amounts of free solar energy to enter the building, thereby heating it passively, as well as maximum levels of visible light transmission for increased comfort (Fig. 1b). The energetic performance of a window is assessed by the heat loss coefficient U_g and solar factor g, that measures the percentage of solar heat that penetrates through the glass. The lower U_g and/or the higher g, the more energy efficient is the window. Silver is conventionally used as it is among the metals with the lowest bulk resistivity. This calls for metal films, which are as thin as possible to maximize solar gain and visible light, yet also as conductive as conceivable (low heat loss). Introduction of double glazing ($U_g \sim 2.5$ W$\cdot$m$^{-2}\cdot$K^{-1}) in the 70's allowed dividing by a factor of two the heat losses through windows compared to single glazing ($U_g \sim 6$ W$\cdot$m$^{-2}\cdot$K^{-1}), and the introduction of low-E glass further divided heat losses by the same factor ($U_g \sim 1.2$ W$\cdot$m$^{-2}\cdot$K^{-1}) (Fig. 1d). Today, less than 15% of Europe buildings contain energy-saving glass. The use of low-E glass in all new and existing buildings in Europe would lead to a potential energy saving per year of 900000 terajoules (TJ), leading to a reduction in CO_2 emissions of up to 90 million tons annually, *i.e.* 30% of the annual target of the European Union. Given increasingly energy-saving regulation rules, there is thus a strong urge to further improve the energy saving properties of coated glass products. For instance, for a given emissivity value, a 20% decrease in silver resistivity would yield an increase of g value of 5%, corresponding to a potential energy saving per year of around 100000 TJ, a sizeable figure in the worldwide problem of global warning. There is therefore a fierce world-wide competition among glass manufacturers to improve this figure. Not only the housing market is concerned but also the automotive one with the spread of car air-conditioning [1].

In industrial glazings, Ag layers are conventionally deposited by magnetron-sputtering in dedicated factories on windows panes of 3×6 m^2; in the vast majority of products, a thin ZnO layer (around 10 nm) is used as a crystallization or seed layer (Fig. 1c). Aside from the fact that it is a cheap and well-mastered material at the industrial level, ZnO allows Ag layers to be out-of-plane (111) textured (but random in plane); it is today the material that yields the lowest Ag resistivity. Its introduction in the middle 90's allowed a significant decrease of silver resistivity (Fig. 1d). Since then, performance improvement via optimization of the Ag/ZnO system and surrounding dielectric materials has only been incremental though, and has reached a limit today (Fig. 1d). At present, the resistivity of polycrystalline Ag thin films employed is of around 3.5 $\mu\Omega$·cm for 10 nm thick Ag films, *i.e.* significantly higher than the bulk value of 1.6 $\mu\Omega$·cm. Any improvement of this figure of merit should go through a deeper understanding of the core Ag/ZnO interface to pinpoint the key levers. In this quest, low-E coatings became a so finely tuned systems in terms of materials and deposition conditions that each layer (up to 20) play a key role which sometimes remains blurred. Being a noble metal, silver presents a very poor chemical affinity with the underlying oxide; the film morphology used to reflect IR light is therefore thermodynamically out-of-equilibrium since interface

[1] It must be noted that the working pricniple of low-E coatings can be also used in warm climate, to prevent heat transfer from the outside. In this case, one needs several Ag layers that shift the working wavelenth of the coating to the near infrared range.

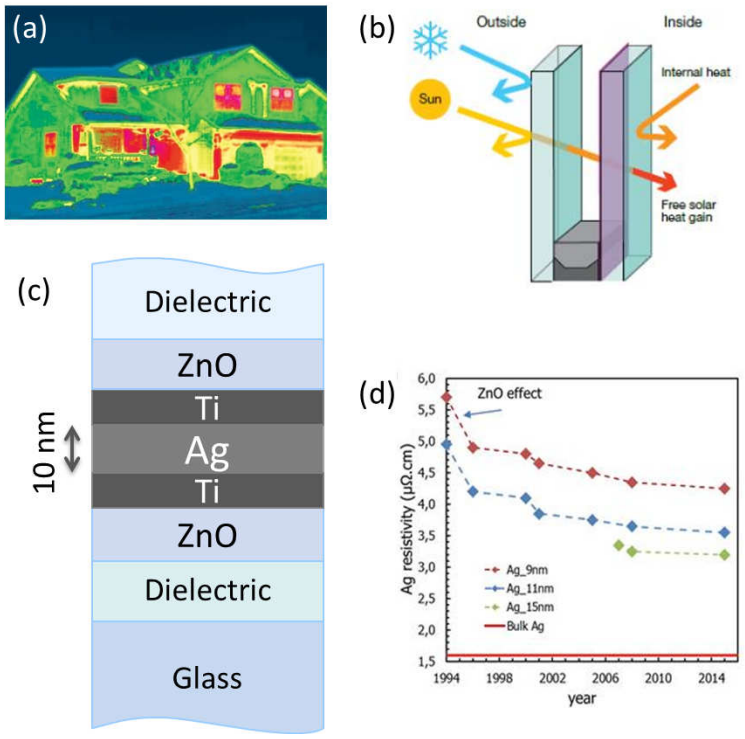

Figure 1: (a) Thermal losses of a house measured with an infrared-camera. Main leaks come from windows. (b) Principle of operation of double glazing with internal low-emissive coating. (c) Typical dielectric stack based on low-emissive coating. A thin but transparent silver film is sandwiched in between ZnO layers; blocker or buffer layers of transition metal are often used to improve silver adhesion and prevent diffusion of oxygen when heating. (d) Evolution of the in-plane resistivity of low-emissive coating developed by the glass industry over the years.

energies clearly favour discontinuous layers. Dewetting or delamination may occur, and therefore reduce the lifetime of the product and its transparency [2], either during handling or when thermal treatment is applied to the windows in order to temper or shape it. This post-deposition [3] processing is required, among other, for windshields in the automotive industry. To overcome this issue, the so-called blocker or buffer layers of transition metals are often introduced at the weak interface between Ag and ZnO to improve adhesion and to prevent diffusion of oxygen that is known to promote solid-state dewetting of silver. But heating is a complex process during which many phenomena occur among which solid-state reactions, diffusion of species, release of stress accumulated during deposition, dewetting etc. Their interplay is often subtle and remains unknown to some extent.

This thesis

In this industrial context, this thesis proposes to explore, on a fundamental point of view, specific aspects of these complex stacks which could have potential impacts on one of the above developed key problem. The work combined surface science approaches on single crystals and studies on more realistic but still model sputtered layers. While being complementary to trial-and-error screening, this strategy allows to dissect given phenomena. The manuscript is divided in four chapters preceded by a more detailed state-of-the-art of the question at hand.

The experimental set-ups and techniques employed during this work are introduced in Chapter 1. In particular, the sputtering deposition chamber used at Laboratoire Mixte CNRS/Saint-Gobain and the multi-technique surface science tool at Institut des NanoSciences de Paris are described. The emphasis is put on photoemission spectroscopy which was a guideline in this study and more specifically, on HArd X-ray Photoemission Spectroscopy (HAXPES) as performed on the KMC-1 beamline of BESSY synchrotron.

Resistivity in thin films is governed by scattering of electrons at interfaces and at grain boundaries. The latter are driven by the in-plane texture and the epitaxy at the interface while, beside roughness, the nature of the electronic barrier at the Ag/ZnO interface govern to a larger extent the reflection coefficient of electrons. Beyond the interest in the low-E field, mastering this electrical contact would open interesting perspective in

[2] After dewetting, pink blurring is due to plasmon resonances in Ag nanoparticles.
[3] Layers can only be deposited on flat glass.

the use such metallic film as transparent electrodes, in particular in the context of Organic Light Emitting Devices. Chapter 2 presents our results on the interplay between film morphology and Schottky barrier at the interface between silver and the polar faces of zinc oxide. This orientation was selected because of the preferential columnar growth along the c-axis of sputtered thin films (see Chapter 3). This surface science study on single crystal surfaces combined electron diffraction, near-field microscopy, optical spectroscopy and photoemission. The goal was to analyse the role of polarity and the interaction of hydrogen with ZnO on band bending and Schottky barrier with Ag. In an original way, surface sensitivity of ultra-violet laboratory photoemission and bulk sensitivity of HAXPES were associated to draw a complete band alignment at Ag/ZnO interface.

The potential transfer of the observation made on single crystals is based on the ability to control the crystallographic orientation (*i.e.* ZnO-O or ZnO-Zn termination) of sputtered ZnO films. As previously shown, orientation was controlled by applying a polarization to the sample during growth and detected through a specific fingerprint in the X-ray photoemission valence band that is related to the orientation of the c-axis of the wurtzite structure. A complete temperature-bias phase diagram was established showing the suitable conditions to avoid re-sputtering of the layer and to achieve a given orientation. Stoichiometry, grain size and crystallinity as seen from diffraction, atomic force microscopy and photoluminescence were correlated with the growth conditions.

Those layers were used as shown in the last chapter (Chapter 4) to tackle the question of the chemical reaction at Ti/ZnO interface. The use of high kinetic energy photoelectrons of HAXPES and the associated increase of inelastic mean free paths allowed to probe *in situ* the temperature dependent chemistry at the buried interface. Mo-capped Ti/ZnO films were specially designed to follow the reaction as a function of annealing temperature, film thickness and crystallinity. The reduction of ZnO by Ti was quantified by a precise decomposition in terms of oxidation degree of the Ti and Zn core levels. The spectroscopic observation were also correlated with laboratory Thermal Desorption Spectroscopy and Electron Probe Micros Analysis showing the more or less impeded diffusion of free Zn across the stack. Finally, these experimental findings were rationalized through the simulation of the phase diagram of the ZnO-Ti system.

The final conclusion reviews the main results of this work and opens some perspectives on unresolved issues.

Chapter 1

Experimental techniques and setups

This work was performed at the Joint CNRS/Saint-Gobain Recherche Laboratory, Surface du Verre et Interfaces (SVI, Aubervilliers) and at Institut des NanoSciences de Paris (INSP, Paris), and was complemented by experiments at BESSY II synchrotron (Berlin). Surface science approaches on single crystals, studies of magnetron sputtered films, *ex situ* and *in situ* techniques were combined. This chapter provides a brief overview of all the employed experimental tools with an emphasis on laboratory and synchrotron photoemission which turned out to be central in this thesis.

1.1 Thin film growth techniques and setups

Two techniques of thin film growth were used in this work, namely the molecular beam epitaxy as performed in surface science analysis and the magnetron sputtering deposition, a common deposition technique in the glass industry.

1.1.1 Molecular Beam Epitaxy

The surface science setup of Oxydes en Basses Dimensions group at INSP (Fig. 1.1) is composed of two chambers (preparation and analysis, base pressures of 3×10^{-10} and 5×10^{-11} mbar), where a number of *in situ* techniques [3, 4] are gathered:

- Photoemission spectroscopy (Section 1.2.1) with an *Omicron EA125* hemispherical analyser (5 channeltrons), a non-monochromatic Al Kα (1486.6 eV) and Mg Kα (1253.6 eV) X-ray source (XPS), a differentially pumped discharge lamp for ultra-violet excitation (UPS, He I 21.2 eV); the analysis chamber made of µ-metal is efficiently shielded against external magnetic field;
- Near-field microscopy, herein Scanning Tunnelling Microscopy (STM) with an *Omicron* VT-AFM head (Section 1.2.2);
- Electron diffraction: Low Energy Electron Diffraction (LEED, *ErLEED 150* from *SPECS*) and Reflection High Energy Electron Diffraction (RHEED, *Staib Instruments*) at grazing incidence for growth monitoring (Section 1.2.3.3);
- Thermal Desorption Spectroscopy (TDS) with a differentially pumped quadrupole mass spectrometer (*Pfeiffer*, 1-200 amu) (Section 1.2.5);
- Surface Differential Reflectivity Spectroscopy (SDRS), a UV-visible reflectometry technique performed during growth (Section 1.2.8).

Samples are transferred between the different parts of the experimental setup using magnetic rods compatible with *Omicron* sample holders. Vacuum is maintained by ionic pumps (*Varian StarCell* – analysis 500 l/s, preparation 300 l/s) associated with Ti sublimators and turbomolecular pumps (*Pfeiffer*, 200 l/s). In the preparation chamber the sample can be cleaned by Ar^+ bombardment and annealed at up to 1400 °C on a home-made electron-bombardment furnace. The sample can then be transferred on a manipulator with 5-degrees of freedom where samples can be cooled down to liquid nitrogen temperature (down to −170 °C=100 K). It allows putting the sample in front of (i) a silver evaporation cell calibrated by a quartz microbalance or (ii) an Ir-based thermal gas cracker to produce atomic hydrogen. At the same position,

SDRS, RHEED and TDS measurements can be performed. Flows of ultra-pure gases that can be introduced into the chamber (H_2, O_2, Ar, He) are controlled through series of leak valves connected to a manifold ancillary gas pipe.

Silver deposition is performed by Molecular Beam Epitaxy (MBE). In MBE atomic species are supplied by evaporation or sublimation of ultra-pure materials from crucibles (see *e.g.* [5]). Contrary to magnetron sputtering, MBE process is slow (typical deposition rates are in the order of a monolayer per minute or lower), and the deposited atoms have thermal energies. Therefore, in order to avoid contamination, growth is performed under Ultra-High Vacuum (UHV) conditions. One of the most notable features of MBE is the availability of *in situ* and real-time characterization techniques in the same or in the neighbouring chamber connected under UHV, as described above.

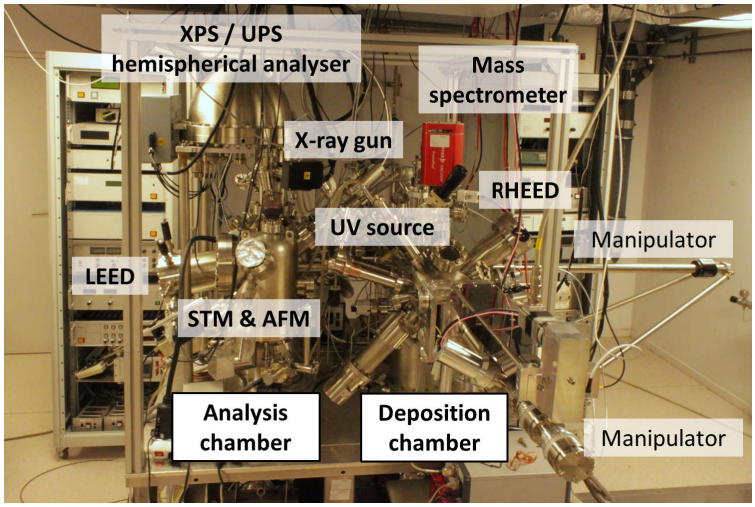

Figure 1.1: Ultra-high vacuum surface science setup at INSP where thin films can be grown and characterized by various *in situ* techniques.

1.1.2 Magnetron sputtering

As a very versatile coating technique, magnetron sputtering has been chosen by the glass industry to deposit a wide-range of materials (oxides, nitrides, metals) in the form of thin films with high purity, controlled microstructure and tunable properties (see *e.g.* [6]). The principle of direct current magnetron sputtering operation is illustrated in Fig. 1.2. The sputtering system is composed of two electrodes: a target of material to be deposited (cathode) is surrounded by a grounded anode. The cathode is set in front of a substrate in a vacuum chamber filled with a controlled flow of an inert gas, typically Ar. Negative voltage of a few hundred volts is applied to the target creating a glow discharge. Generated Ar^+ ions are accelerated towards the cathode by the electric field, bombard the target and knock out the atoms. At the same time, electrons (and therefore, plasma) are trapped near the target by a magnetic field generated by a system of permanent magnets. Electrons travelling along spiral trajectories in the magnetic field increase the ionisation of the gas. Sputtered target atoms condense onto a (heated) substrate yielding to the film growth. The resulting film is typically polycrystalline. The technique allows maintaining stoichiometry and film thickness uniformity, and has the flexibility to deposit a wide range of crystalline and amorphous materials.

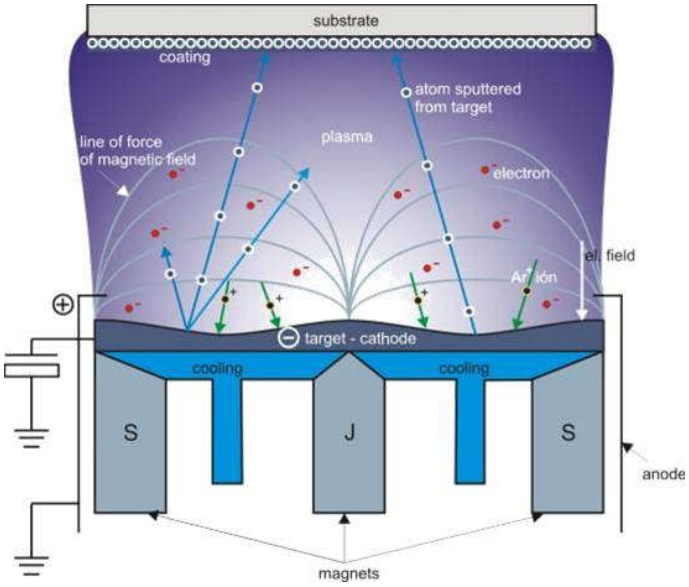

Figure 1.2: Scheme of the sputtering process. A magnetic field confines the plasma close to the cathode. Ar^+ ions sputter the polarized target, and the material condenses on the substrate surface. [7].

In this work, the MISSTIC (Multilayers and Interfaces on Structured Substrates and *In situ* Characterizations) deposition and characterization setup, designed by the Joint CNRS/Saint-Gobain Recherche Laboratory and produced by MECA2000, was used for magnetron sputtering depositions (see Fig. 1.3). It consists of a deposition chamber (base pressure 5×10^{-7} mbar) and an analysis chamber (base pressure 5×10^{-9} mbar) connected under vacuum through a load-lock. The analysis chamber houses a photoemission analyser (*Phoibos 100* from *SPECS*, 5 channeltrons) and the deposition chamber is equipped with three magnetron heads which allow for deposition of multilayers without breaking the vacuum. The cathodes can be powered either by direct current, radio-frequency, or high-power impulse generators. The setup allows varying deposition parameters, such as sample-target distance, Ar pressure, partial reactive gas (O_2 or N_2) pressure, cathode electric power and substrate potential.

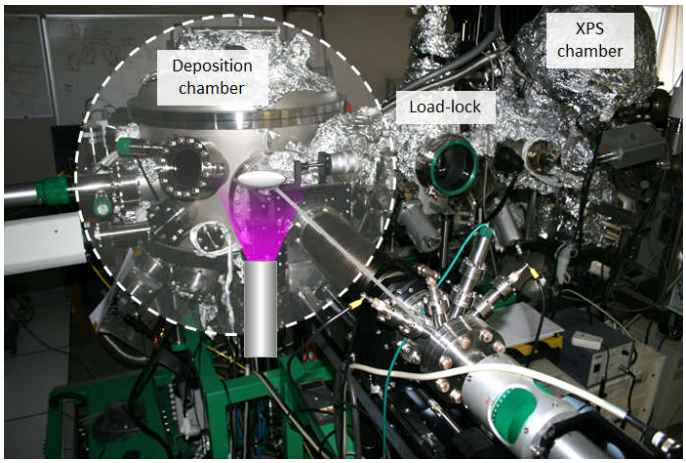

Figure 1.3: MISSTIC setup at SVI consisting of a load-lock, a deposition and an XPS chamber. A magnetron plasma discharge and a sample are schematically depicted in the deposition chamber.

The manipulator which holds the substrate is equipped with a heating stage. This latter is controlled by a thermocouple (TC1) placed behind the sample holder as shown in Fig. 1.4.

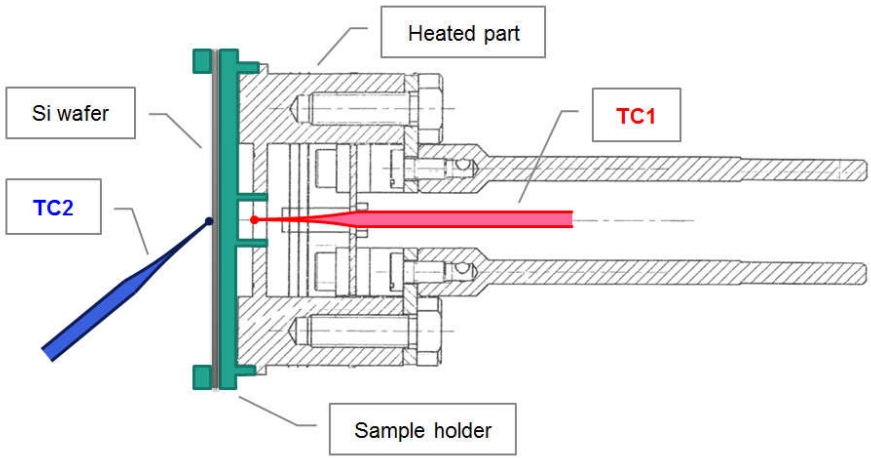

Figure 1.4: Scheme of the sample manipulator showing the two thermocouples. TC1 is installed behind the sample holder and TC2 is set in contact with the Si wafer.

For calibration purposes, the exact temperature of the surface of a 2 inches two-side polished Si wafers (used in experiments) was measured as function of the set-point temperature by an additional thermocouple (TC2) directly glued onto the wafer with Ag paste. The temperature difference with respect to the set-point varied from 150 to 420 °C (Fig. 1.5a) manifesting a poor thermal contact with the holder.

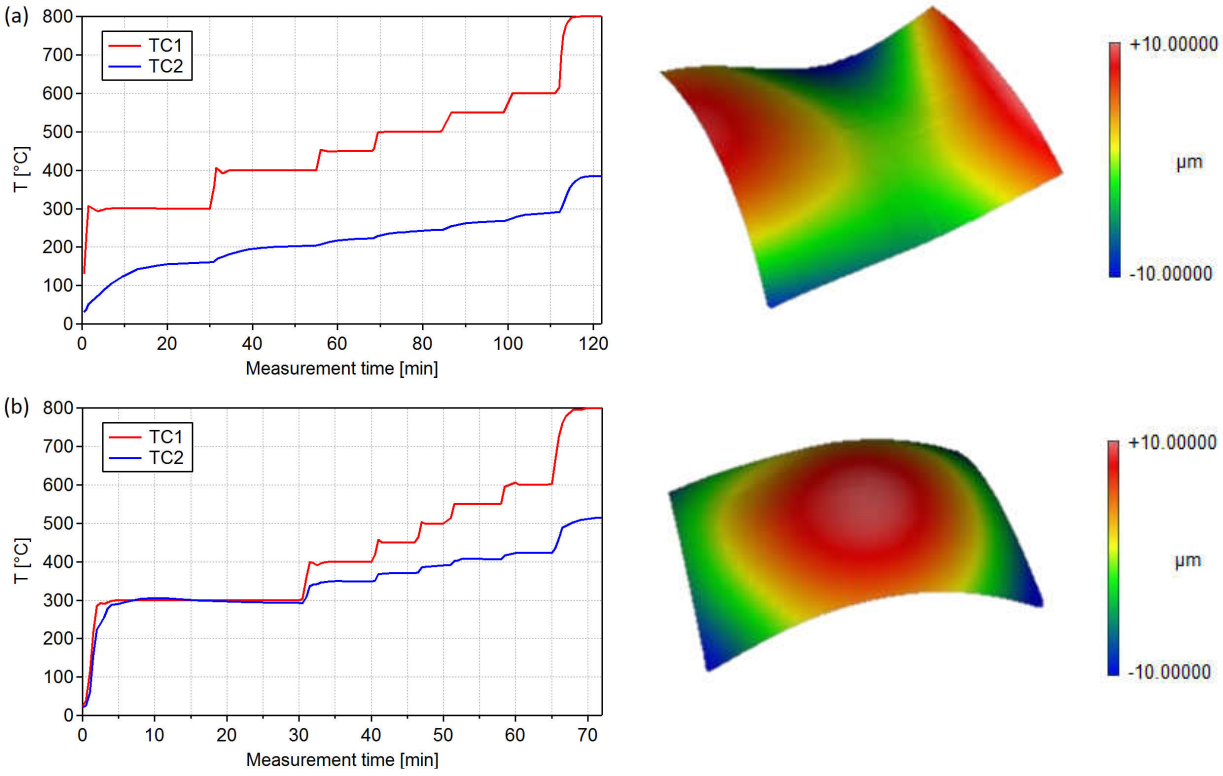

Figure 1.5: Temperatures read by the thermocouples TC1 and TC2: (a) on an arbitrary substrate and (b) after clamping of a spherically curved one on its out-bowed side. On the right side are the wafer profiles measured by an optical profilometer *NewView 2000*: (a) a wafer with an arbitrary shape, (b) a wafer with a spherical curvature. The scan size is 20×20 mm^2.

Wafer shapes, as measured by an optical profilometer (*NewView 2000*), showed saddle-like arbitrary shapes (Fig. 1.5a) or more spherical ones (Fig. 1.5b). Therefore, in order to achieve a good thermal contact,

wafers with spherical curvature were systematically chosen and firmly clamped with their out-bowed side facing the sample holder. By doing so, the difference of temperature (from 0 to 280 °C) was drastically reduced (Fig. 1.5b).

1.2 *In situ* and *ex situ* characterization techniques

1.2.1 Photoelectron spectroscopy

1.2.1.1 X-ray Photoelectron Spectroscopy

X-ray Photoemission Spectroscopy (XPS), also known as Electron Spectroscopy for Chemical Analysis (ESCA), is a surface analysis technique consisting in the irradiation of a sample by soft X-rays and subsequent energy analysis of emitted electrons [3, 4, 8, 9]. X-rays focused on the sample surface eject electrons from core level states with different binding energies E_B. The kinetic energy E_K of the photoelectrons is given by the energy conservation law (Einstein's photoelectric equation):

$$E_K = h\nu - E_B - \Phi, \tag{1.1}$$

where $h\nu$ is the incident photon energy and Φ is the work function of the sample. Electrons in a solid have characteristic binding energies giving rise to corresponding XPS peaks, as shown in Fig. 1.6a. Thus, the analysis of the resulting XPS spectra provides quantitative information about the sample composition and the environment/charge state of the atoms. Energy distribution of photoelectrons has the following features:

- a large decay at a low kinetic energy due to secondary electrons (SE) produced in inelastic processes and discrete peaks throughout the spectrum corresponding to the states (core levels) from which electrons are ejected;
- two cut-off energies: $E_K = h\nu - \Phi$ corresponding to $E_B = 0$ (electrons extracted from the Fermi level of the sample), and $E_K = -\Phi$ (the SE cut-off, *i.e.* the minimum kinetic energy required to exit the sample).

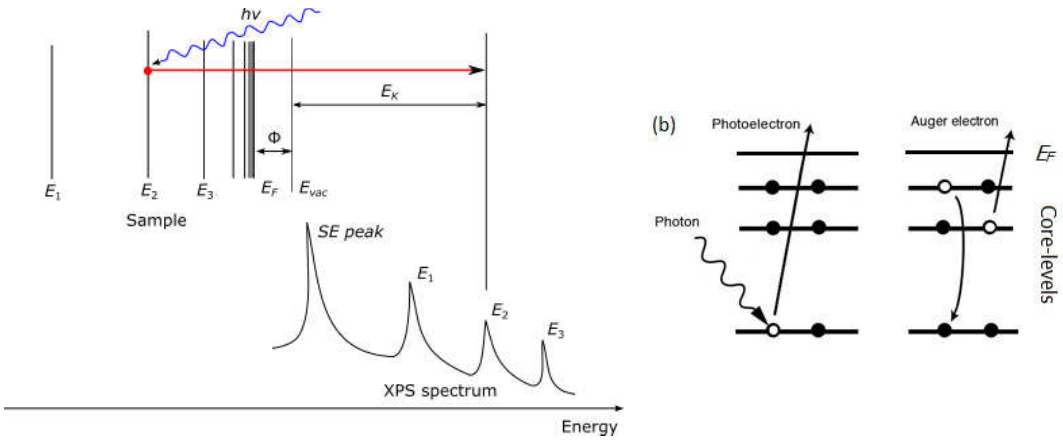

Figure 1.6: (a) Correlation between a photoemission spectrum and the sample energy levels. An X-ray photon with an energy $h\nu$ excites an electron of a given core level thus contributing to a line in the measured spectrum. (b) Illustration of an Auger process [10]: an electron falls into the vacancy created by photoemission and its excess energy is transferred to another electron on an upper orbital, leading to its emission.

For a photoexcited atom, there are two possible processes to retrieve the initial ground state: emission of a photon or of an electron through the Auger process [11]. In the latter case, when a photoelectron is emitted from an inner orbital, an outer electron can fall into the created vacancy, and its excess kinetic energy can be transmitted to another electron on an upper orbital leading to its emission to the vacuum level. Such electrons are called Auger electrons, and their kinetic energies are specific to energy differences between the

energy levels involved in the process (Fig. 1.6b). These Auger electrons are also detected during photoemission measurements. They are labelled by the involved energy levels (*e.g.* KLL).

The Inelastic Mean Free Path (IMFP) of photoelectrons in a solid is of the order of a few nanometres, which makes the XPS technique very surface sensitive. The IMFP follows a "universal" V-shaped curve as function of the kinetic energy (see Fig. 1.7). The surface sensitivity maybe reduced even further by analysing the photoelectrons escaping under a grazing angle.

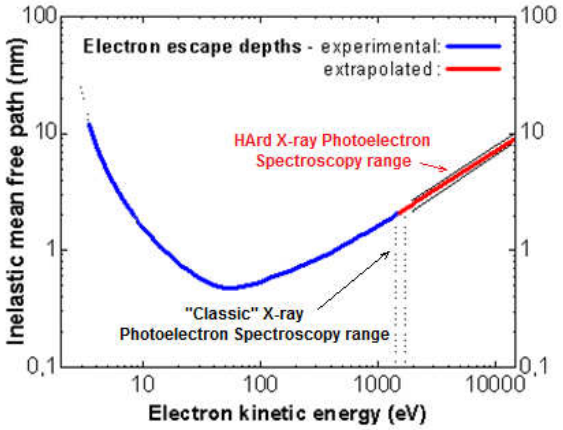

Figure 1.7: Electron inelastic mean free path universal curve for different elements and compounds adapted from Ref. [12]. Typical ranges of excitations for classical and high energy photoemission are highlighted [13].

Electrons leaving the sample are analysed according to their kinetic energy by an electrostatic analyser, the most-common one being the hemispherical one. The *EA 125* from *Omicron* (INSP) and *Phoibos 100* from *SPECS* (SGR) (shown schematically in Fig. 1.8a) have been used in the present work. Electrons are decelerated / accelerated by dedicated electrostatic lenses up to a given kinetic energy, the so-called pass energy E_{pass}, before entering the analyser. The hemisphere acts as a narrow band kinetic energy filter around E_{pass}. The resolving power of the analyser ΔE depends on the chosen pass energy E_{pass} as:

$$\frac{\Delta E}{E_{pass}} \cong \frac{s}{2R_0}, \tag{1.2}$$

where s is the width of the entrance slit and R_0 is the radius of the analyser. At the output of the analyser, electrons are detected as discrete events through electron amplifiers (channeltrons), and their number for a given detection time is recorded.

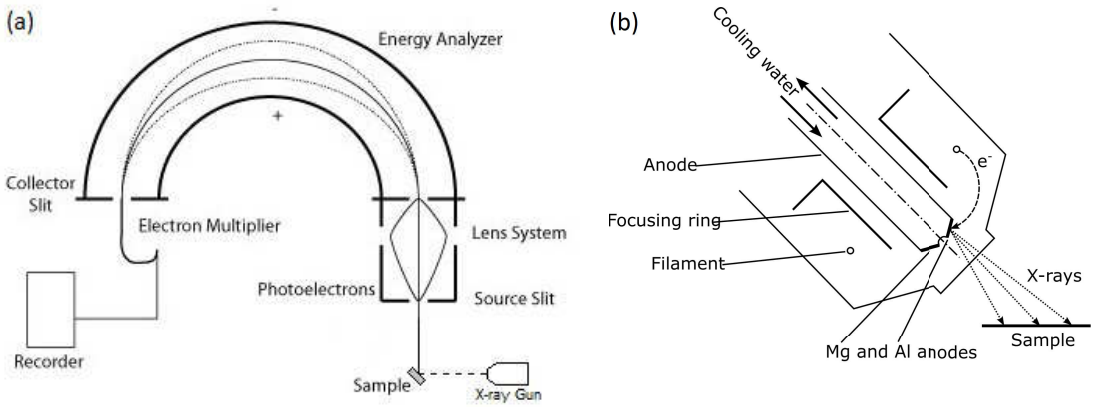

Figure 1.8: (a) Illustration of the hemispherical electron energy analyser. Energy of photoemitted electrons is adjusted to the pass energy by a system of input electrostatic lenses; dispersed inside the hemispherical analyser with respect to their energy, electrons are collected at the exit plane [14]. (b) Scheme of the X-ray gun: electrons bombard a selected anode, ejecting electrons from deep levels which are refilled, thus producing X-ray radiation.

Non-monochromatic X-ray sources *DAR X 400* from *Omicron* (INSP) and *XR50* from *SPECS* (SGR) having twin anodes emitting either Mg α or Al Kα photons with energies of 1253.6 or 1486.6 eV, respectively, were used. For these sources, resolution is limited by the life time of the Kα emission, the presence of satellites, and continuous Bremsstrahlung emission. As shown schematically in Fig. 1.8b, electrons extracted from a heated filament bombard a selected anode that is kept at a high positive potential (10-15 kV). To prevent Al or Mg evaporation, the anode is water-cooled. A better resolution and higher intensity can be achieved by using specific emission from a discharge in a neutral gas, as in the case of Ultra-violet Photoemission Spectroscopy (UPS). UPS is well-suited for the analysis of the valence band of materials, as the excitation energy is lower than in XPS. The unpolarised He I line at 21.2 eV produced by a differentially pumped source (*Omicron HIS 13*) was used in the present study.

1.2.1.2 HArd X-ray Photoelectron Spectroscopy

HArd X-ray PhotoElectron Spectroscopy (HAXPES) is based on the same principle as laboratory XPS, except for higher excitation energies. Photon energies can exceed 10 keV, while in case of XPS they are usually in the range of 1.3-1.5 keV. At such high excitation energies, the electron IMFP can be increased to ~10 nm compared to ~2-3 nm in case of XPS (Fig. 1.7). This characteristic makes HAXPES "bulk" sensitive, but one has to use (i) a brighter, synchrotron source (due to the decay of photoionization cross sections with photon energy) and (ii) a larger analyser with specially designed high voltage power supplies. Another feature of this technique is the capability of depth profiling through varying the photon energy. For this purpose, photon energies from 2 to 8 keV were used in the present study.

HAXPES experiments were conducted at the HIgh Kinetic Energy (HIKE) end-station of the KMC-1 beamline of BESSY II synchrotron, Helmholtz Zentrum Berlin. A full description of this setup can be found in Ref. [13, 15, 16]. Synchrotron light is produced by the acceleration experienced by electrons on curved trajectories. In this process, electrons with a speed close to the speed of light tangentially emit photons. KMC-1 beamline uses a bending magnet for electron deflection and photons are focused on the monochromator by a toroidal mirror which rejects high energy photons (Fig. 1.9). Bragg diffraction on the Si double-crystal water-cooled monochromators is used to select beam energy with the resolution down to 20 meV. The combination of three crystals Si(111), Si(311) and Si(422) allows to cover photon energies from 2 to 12 keV.

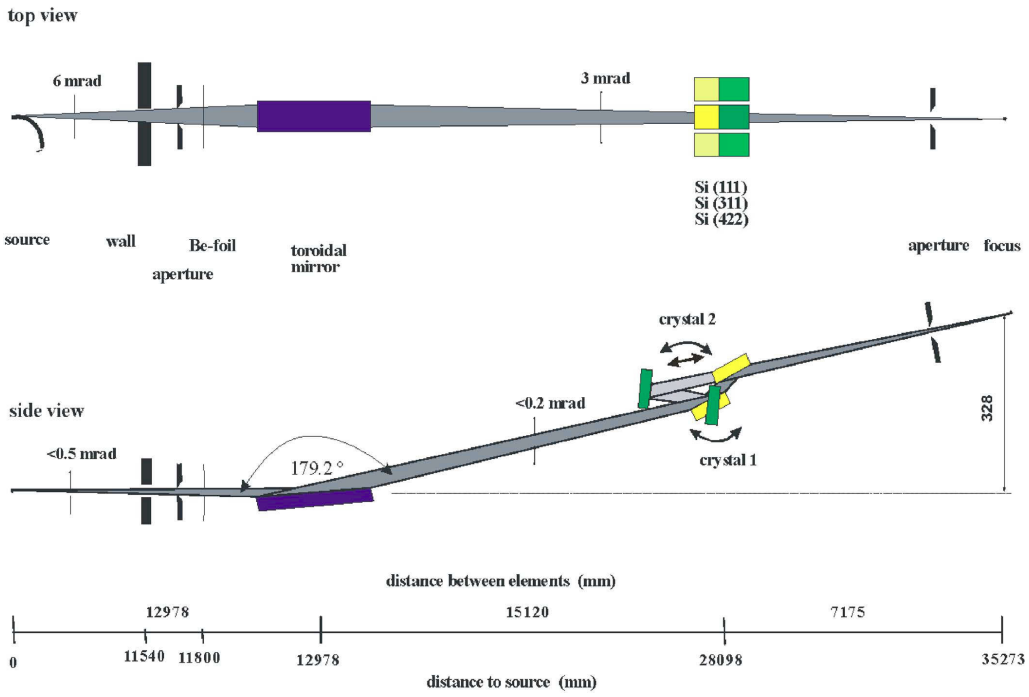

Figure 1.9: Sketch of the optics of the KMC-1 beamline [15, 16].

The beam then passes through an ionization chamber which is used for flux monitoring, and enters the experimental end station through a focusing capillary (Fig. 1.10). The vessel holds a six-axis manipulator (translation and tilt with respect to detector) for sample adjustment and a *SCIENTA R4000* hemispherical electron analyser optimized for electron kinetic energies up to 10 keV. A fluorescence detector is also located in the analysis chamber and complements the photoelectron analyser. The manipulator is equipped with a resistive heating stage (up to 800 °C). The analysis chamber is connected to the preparation chamber, where the sample can be etched by Ar^+ ions to clean or sputter a part of the sample, if needed. The base pressure of the system is $\sim 10^{-9}$ mbar.

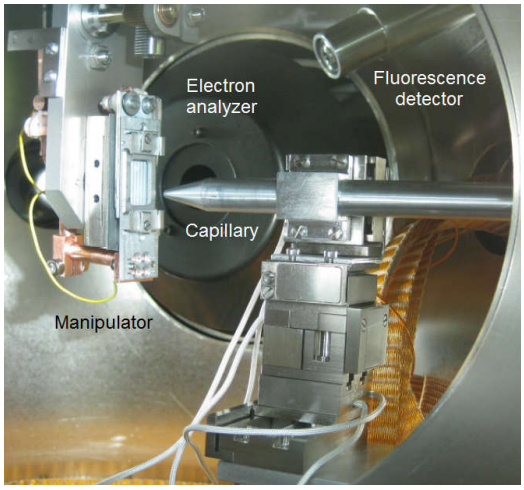

Figure 1.10: Picture of the inside of the HIKE chamber at KMC-1 beamline: the manipulator, X-ray capillary, electron analyser, and fluorescence detector (adapted from Ref. [13]).

1.2.1.3 Core level spectroscopy and lineshape analysis

XPS or HAXPES spectral lines are either singlets or doublets (in case of spin-orbit splitting). But simple Gaussian and Lorentzian functions are inadequate to simulate their shape due to several physical and in-

strumental effects [8, 17], such as:

- the profile of the X-ray line;
- broadening of the core level state due to its finite lifetime;
- thermal (phonon) broadening;
- differential surface charging of the sample or band bending;
- response function of the electron energy analyser.

The shape of the source X-ray line is Lorentzian in case of the laboratory XPS and Gaussian in case of HAXPES. The peak shape of a photon excited core level is inherently Lorentzian, and its width is the inverse of the core hole lifetime. Phonon and instrumental effects are often described through Gaussian broadening. Therefore, measured peak shapes are generally well reproduced by a convolution of a Lorentzian $L(x)$ and a Gaussian $G(x)$ profiles, called the Voigt function $V(E)$:

$$V(E) = \int_{-\infty}^{+\infty} L(x) \cdot G(E-x)\mathrm{d}x, \tag{1.3}$$

where

$$L(x) = \frac{1}{1 + \left(\frac{x-x_0}{0.5 f_L}\right)^2} \tag{1.4}$$

and

$$G(x) = \mathrm{e}^{-\ln 2\left(\frac{x-x_0}{0.5 f_G}\right)^2}, \tag{1.5}$$

where f_i is the Full Width at Half-Maximum (FWHM) of the corresponding i profile, and x_0 is the peak position. The total width of the Voigt profile can be estimated as a function of f_L and f_G as follows [18]:

$$f_V \simeq 0.5346 f_L + \sqrt{0.2166 {f_L}^2 + {\mathrm{f}_G}^2}. \tag{1.6}$$

However, the actual profile may be greatly influenced by what is known as many-body phenomena, such as electron-hole pair excitations near the Fermi level and plasmon excitations of the valence sea of electrons. For solids with a large density of states at or near the Fermi energy, such as metals, the former process leads to peak shapes skewed towards higher binding energies. For energies of only a few eV from the peak energy, where the valence band density of states may be considered roughly constant, the combined effect of these electron-hole pair excitations and the lifetime broadening is described by a formula derived by Doniach and Sunjic [19]:

$$DS\left(x, \alpha\right) = f_{DS} \frac{\cos\left\{\pi\frac{\alpha}{2} + (1-\alpha)\arctan\left[\frac{x-x_0}{f_{DS}}\right]\right\}}{\left[\left(x-x_0\right)^2 + {f_{DS}}^2\right]^{\frac{1-\alpha}{f_{DS}}}}, \tag{1.7}$$

where α is the asymmetry parameter. Another way to describe the peak asymmetry was proposed by Van der Straten. [20] and formalized in the so-called Post-Collision Interaction (PCI) shape:

$$PCI = \frac{\exp\left(2\alpha \arctan\left[2\frac{(x+\Delta x)-x_0}{f_{PCI}}\right]\right)}{1 + 4\frac{((x+\Delta x)-x_0)^2}{{f_{PCI}}^2}}, \tag{1.8}$$

with

$$\Delta x = \frac{\alpha f_{PCI}}{2}. \tag{1.9}$$

Both Doniac-Sunjic and PCI shapes converge into a Lorentzian for $\alpha = 0$. In practice, in order to account for the asymmetric peak shapes (*e.g.* for metals), the Lorentzian contribution should be replaced by an asymmetric line shape, Doniach-Sunjic or PCI functions.

Another important feature of the spectra is the background due to secondary electrons; its subtraction is crucial for data interpretation. The often used Shirley background assumes a background proportional to

the integral up to a given kinetic energy of the actual signal; it naturally accounts for an increase in the overall measured background for each subsequent core level [21].

In this thesis, photoemission spectra were fitted using the *SPANCF* (Spectrum Analysis by Curve Fitting) macros package for *Igor Pro* created by E. Kukk [22]. The background was described as a combination of linear and Shirley shapes. Peaks were fitted with Voigt profiles, and asymmetry of metallic core levels was taken into account using the PCI-shape.

1.2.1.4 Quantification

Through data fitting, photoemission can provide a quantification of coverage, atomic density or film thickness [9]. For a thin layer of thickness dz buried at a depth z in a substrate [23], the photoelectron intensity at kinetic energy E_K is given by:

$$I \propto F_x \sigma\left(h\nu\right) \exp\left(-\frac{z}{\lambda\left(E_K\right)\cos\theta}\right) \rho A_0 T\left(E_K\right) D\Omega \mathrm{d}z, \tag{1.10}$$

where:

- F_x is the average flux of X-rays on the sample,
- σ is the photoionization cross-section of the corresponding core level at an excitation energy $h\nu$,
- $\lambda\left(E_K\right)\cos\theta$ is the electron escape depth which depends on the collection angle θ and the IMFP $\lambda\left(E_K\right)$ of photoelectrons in the sample; it comes into play through an exponential damping of Beer-Lambert type,
- ρ is the atomic density of the probed element,
- A_0 is the sample area illuminated by X-rays viewed by the analyser,
- $T\left(E_K\right)$ is the analyser transmission function which is close to the inverse of the kinetic energy $1/E_K$ for a perfect hemispherical analyser,
- D is the detector efficiency,
- Ω is the acceptance solid angle of the detector.

While absolute intensity determination through reference samples is difficult [11, 23], quantification can still be achieved by simply looking at the ratio of peak areas acquired during a given run since the ionization cross section, IMFP and transmission function are known quantities and the remaining ones can be assumed to be constant. The strategy depends on the sample geometry and the question at hand.

If a material A is homogeneously mixed with a material B (*e.g.* in a solid solution AB), the volumic ratio between the materials in the mixture can be determined from the photoemission data based on the measured intensities I_A and I_B of some core levels of the elements A and B (see Section 1.2.1.1 and Eq. 1.10):

$$\frac{n_A}{n_B} = \frac{I_A}{I_B} \times \frac{T_B \sigma_B \lambda_B^{AB}}{T_A \sigma_A \lambda_A^{AB}}, \tag{1.11}$$

with T_i the analyser transmission function for the electron kinetic energy corresponding to the peak, σ_i the cross-section of the core level under consideration, λ_i^{AB} the IMFP of the electrons coming from the atom i for the material AB.

For a thin film of thickness d on top of a semi-infinite substrate, in case of normal emission, the signals of the adsorbate and the substrate can be derived by integrating the Eq. 1.10:

$$I_a \propto T_a \cdot \sigma_a \cdot \rho_a \cdot \int_{-d}^{0} \exp\left(z/\lambda_{aa}\right) \mathrm{d}z = T_a \cdot \sigma_a \cdot \rho_a \cdot \lambda_{aa} \cdot \left(1 - \exp\left(-d/\lambda_{aa}\right)\right), \tag{1.12}$$

$$I_s \propto T_s \cdot \sigma_s \cdot \rho_s \cdot \int_{-\infty}^{0} \exp\left(z/\lambda_{ss}\right) \mathrm{d}z = T_s \cdot \sigma_s \cdot \rho_s \cdot \lambda_{ss}, \tag{1.13}$$

where λ_{ss} and λ_{aa} are the IMFP of the substrate (adsorbate) photoelectron line in the substrate (adsorbate). The further attenuation of the electrons coming from the substrate can be taken into account by adding another exponential factor:

$$I_s \propto T_s \cdot \sigma_s \cdot \rho_s \cdot \lambda_{ss} \cdot \exp\left(-d/\lambda_{sa}\right), \tag{1.14}$$

where λ_{sa} is the IMFP of substrate electrons in the adsorbate. Once measured, the ratio I_a/I_s gives an indirect access to the film thickness, if the atomic densities are known. Beyond the uncertainty of the morphology, the accuracy is often limited by that of inelastic mean free path.

1.2.2 Near-field Microscopy

1.2.2.1 Scanning Tunnelling Microscopy

When a polarized metallic tip is positioned in the vicinity of a conductive sample ($\sim$1 nm), quantum tunnelling can occur between the tip and the sample surface, and the current flow depends on the bias voltage V_g according to:

$$I_t \propto V_g \cdot \rho_{sample} \cdot \rho_{tip} \cdot \mathrm{e}^{-K\sqrt{\Phi}d}, \tag{1.15}$$

with ρ_{sample} and ρ_{tip} the electron density of states of the sample and of the tip, respectively, Φ the work function of the sample, d the distance between the tip and the sample surface, and K a coefficient that depends on the shape of the tunnel barrier and on the kinetic energy of electrons. The exponential dependence on the tip-sample distance is the key feature of the Scanning Tunnelling Microscopy (STM) technique [3] which allows resolving the sample surface morphology down to individual atoms. Experimentally, the tip can be moved along the three directions of space with subatomic resolution using piezoelectric ceramics. The most-common operating mode is the so-called constant current mode for which an electronic feedback loop keeps the current constant while scanning the surface. The variation of the voltage applied to the piezo crystal $\triangle V$ is recorded and then converted into the change of the tip-sample spacing (to a first approximation, $\triangle V \propto d$). The obtained image is therefore a convolution of topographic and electronic effects due to the local variation of the density of states.

The STM images presented in the current work were obtained *in situ* with Pt/Ir or chemically etched W tips using *Omicron* STM operated at room temperature in the constant current imaging mode with sample biases V_g from -1.5 to 2.7 V and tunnelling currents I_t of 0.05-2.5 nA.

1.2.2.2 Atomic Force Microscopy

The principle of Atomic Force Microscopy (AFM) is similar to STM but it is based on the force of interaction between a tip mounted on a cantilever and the sample surface. The main advantage of AFM over STM is that it allows studying insulating surfaces. There are two principle modes of AFM operation:

- In the contact mode the tip is in contact with the sample surface. Due to the Lennard-Jones interaction potential, the force between the tip and the sample surface bends the cantilever from its equilibrium position. The bending is measured through the deflection of the laser beam reflected from the back of the cantilever. Thus, based on the knowledge of the spring constant k of the cantilever and its deflection Δz, the Hooke's law gives the force exerted on the tip:

  $$F_{tip-sample} = k\Delta z. \tag{1.16}$$

  While scanning, the feedback loop maintains this force constant with the help of piezoelectric ceramics.

- In the tapping mode the cantilever is forced to oscillate by a piezo-crystal at a frequency close to its resonance. The laser deflection signal is sent to the feedback loop that ensures that the oscillation amplitude remains constant, and therefore, a constant tip-sample interaction is maintained during scanning.

In this work, AFM images were obtained *ex situ* in air using a *Bruker Dimension Icon* microscope operating in tapping mode. AFM images were analysed in *Nanoscope Analysis* software in order to determine the average roughness, grain size and surface coverage.

1.2.3 Diffraction techniques

1.2.3.1 Low Energy Electron Diffraction

Low Energy Electron Diffraction (LEED) [3, 4] uses an electron beam with a kinetic energy of 20-200 eV which is sent on the sample at normal incidence. Diffracted electrons are collected in the backward direction on a fluorescent screen after being accelerated by a system of grids which also suppress inelastic electrons. According to the De Broglie's equation, the corresponding electron wavelength (in the range of the Angstrom) is suitable for the particle to be diffracted by the crystalline lattice of the sample. Since low kinetic energy electrons strongly interact with electronic clouds of the atoms, the penetration depth is restricted to the first atomic layers. Therefore, the probed reciprocal space consists of diffraction rods normal to the sample surface. Spot symmetry, broadening and intensity provide information on the surface reconstruction. The coherence length is mainly limited by the energy spread and beam divergence and is in the range of a few nanometres.

1.2.3.2 Reflection High Energy Electron Diffraction

Reflection High Energy Electron Diffraction (RHEED) [3, 4] is a technique often used in the field of thin film growth to monitor the evolution of roughness and strain. It involves electrons that impinge on the surface at grazing incidence (a few degrees) with a kinetic energy from 10 to 30 keV which corresponds to a wavelength much smaller than in LEED. The corresponding Ewald sphere is therefore so large that it can be assimilated to its tangent plane that can intersect or not with the rods characteristic of the surface. Due to higher kinetic energy, electron trajectories are less perturbed and sensitive to the environment. But small diffraction angles require large distance between the sample and the fluorescent screen. Depending on the roughness, the pattern can switch from spotty bulk like diffraction in transmission to rod-like on a very flat surface. RHEED and LEED device references are given in Section 1.1.1.

1.2.3.3 X-Ray Diffraction and Reflectivity

X-Ray Reflectivity (XRR) and X-Ray Diffraction (XRD) are non-destructive X-ray scattering techniques sensitive to the atomic structure down to the nm-scale [24, 25]. In case of XRD and XRR, X-rays are diffracted from the crystal planes, and from interfaces, respectively. Most of the X-ray laboratory sources, and as used herein, use the Cu Kα emission at a wavelength $\lambda = 0.154\,\mathrm{nm}$.

In this study XRR and XRD were performed in a $\theta - 2\theta$ Bragg-Brentano geometry for which both the incident angle of the incoming beam on the sample and the scattering one are scanned in parallel. Depending on the range of angles, the induced wave vector transfer perpendicular to the surface allows to probe:

- interlayer distances ($\theta = 0 - 10^{\circ}$), since at such angles, the scattering length depends only on the electronic density of the material;
- interatomic distances ($\theta = 20 - 80^{\circ}$) and more precisely atomic planes which are parallel to the surface. The observed diffraction peaks obey the well-known Bragg's law:

$$n\lambda = 2d_{hkl}\sin\theta_{hkl}, \tag{1.17}$$

  where n is an integer number corresponding to the diffraction order, λ is the X-ray wavelength, hkl are the Miller indices of the corresponding planes of the crystalline lattice, d_{hkl} is the distance between the planes of the (hkl) family, and θ_{hkl} is the half value of the scattering angle 2θ for the (hkl) plane.

From the broadening of diffraction peaks one can extract the information about the mean domain size L using the Scherrer equation [26]:

$$L = \frac{K\lambda}{\beta_L \cos\theta}, \tag{1.18}$$

where β_L is the FWHM of the peak and K is the dimentionless crystallite shape factor (typically ~ 0.9). When both crystallite size and microstrain are present, the total diffraction peak width β_{tot} is a summ of size broadening β_L and strain broadening $\beta_e = 4\varepsilon\tan\theta$, with ε the strain:

$$\beta_{tot} = \beta_L + \beta_e = \frac{K\lambda}{L\cos\theta} + 4\varepsilon\tan\theta = \frac{1}{\cos\theta}\left[\frac{K\lambda}{L} + 4\varepsilon\sin\theta\right]. \tag{1.19}$$

The quantity $\beta_{tot} \cos\theta$ can be then plotted as a linear function of $\sin\theta$. This method is called the Williamson-Hall Plot [27]. Its intersection with the y-axis ($\frac{K\lambda}{L}$) provides the information about the domain size, and the slope (4ε) – about the strain.

As XRR is mainly sensitive to electron density variations, film thicknesses, interfacial roughness and layer densities can be extracted respectively from the interference fringes, the decay of the intensity and the value of the critical angle (angle below which total external reflection occurs). XRD is widely used for determination of crystalline phases and strain in thin films. Crystallographic orientation distribution can be mapped by fixing the detector at a certain characteristic 2θ angle and tilting and rotating the sample (see *e.g.* [28]). The results are plotted in a 3D pole figure.

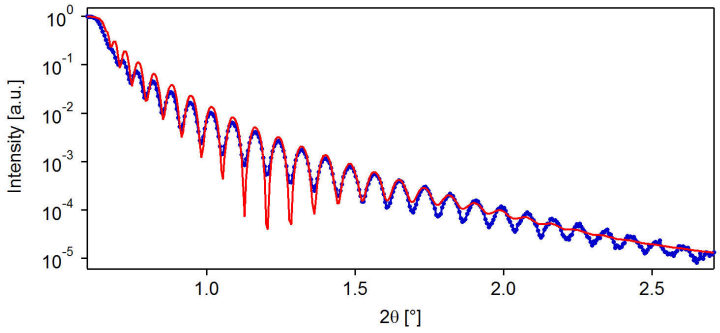

Figure 1.11: Reflectivity data from a ZnO sample deposited on a Si wafer fitted with a layered structure of Si / SiO_2 (5.6 nm) / ZnO (96 nm). After a plateau of total external reflection, the so-called Kiessig fringes of interference are observed due to the finite thickness of the ZnO film.

In this work, *Bruker D8* (SGR) and *Rigaku Smartlab* (INSP) diffractometers were used for XRD and XRR measurements. XRR data was fitted in *GenX* freeware [29], in order to determine film thickness and interfacial roughness values. Fig. 1.11 shows an example of the fit of XRR data for a 96 nm ZnO film.

1.2.4 Electron Probe MicroAnalysis

Electron Probe MicroAnalysis (EPMA) is a quantitative non-destructive method for elemental analysis of micron-sized volumes of material (see *e.g.* [30]). An electron beam (from 2 to 30 keV) focused on the sample surface generates different emissions due to elastic and inelastic interactions with the atoms in the sub-surface region, as shown in Fig. 1.12. Elastic interactions generate so-called back scattered electrons used in scanning electron microscopy for elemental cartography. The inelastic interactions induce: (i) inner shell ionization, (ii) electron emission (secondary electrons and Auger electrons), (iii) phonon excitations, and (iv) photon emission, such as emission of X-rays with well-defined wavelengths.

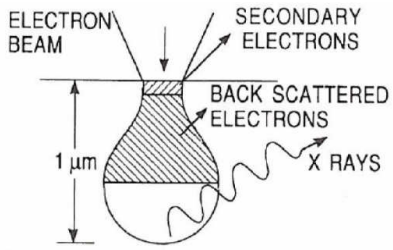

Figure 1.12: Electrons and photons emitted from the interaction volume during electron impingement on surface sample.

EPMA is a technique based on the collection of the X-rays emitted through the filling of an electron hole created by inelastic electron scattering. The emitted X-rays are analysed in terms of energy (to identify the elements) and intensity (to evaluate the composition of the probed volume). EPMA setup is composed of the following main parts:

- an electron gun equipped with a lens system for focusing the electron beam on the sample surface and surface scanning;
- Wavelength Dispersive Spectrometers composed of various moveable monochromators (crystals or pseudo-crystals – PET, LIF, TAP, etc.) used in order to optimize the EPMA sensitivity (at the level of ppm) and to guarantee a high spectral resolution by reducing interference of X-rays;
- X-ray detectors (usually gas proportional counters).

Quantification by EPMA is performed by comparing the intensity of a selected X-ray line of the sample with that of a reference standard. The measured ratio between the two intensities is thus related to the material concentration within the analysed sample. But this relation is not linear, because of the adsorption, fluorescence, detection efficiency function, etc. Therefore, calibration models were created to simulate the in-depth distribution of the ionization function (called $\varphi(roz)$). The most widely used ZAF model treats the relation between the element concentration and the X-ray characteristic by means of multiplicative factors related to the atomic number (Z), absorption (A), and fluorescence (F). The $\varphi(roz)$ model and its variants (PAP, XPP, XPHI, etc.) are based on data obtained with tracers. The XPP model specifically adapted for stratified samples [31] was used in the present work.

EPMA analyses for the thickness evaluation of ZnO, TiO_x, Mo and SiO_x layers have been performed on *CAMECA SXFive* apparatus. The electron energy was 15 keV and the current was 150 nA. The X-rays line selected were the following: Zn Lα, Ti Kα et Mo Lα. Since the surface of the samples was conductive enough, no carbon overlayer was deposited. The standards used for the quantifications were: ZnO grid 16c, Mo grid Cameca, TiO_2 grid 16c. The modelling was performed using *Stratagem* 4.8 software. The densities used for the thickness estimation were: 10.2, 5.6, 4.2, 4.5 g/cm^3 for for Mo, ZnO, TiO_2, and Ti, respectively. Typical EPMA error of thickness evaluation was of the order of 0.5 nm.

1.2.5 Thermal Desorption Spectroscopy (TDS)

Thermal Desorption Spectroscopy (TDS) also known as Temperature Programmed Desorption is one of the oldest characterization technique in surface science. The species desorbing from a sample are analysed by a mass spectrometer while ramping the sample temperature. TDS allows for the determination of the adsorption states of molecules / atoms and the activation energies of desorption which in the first approximation correspond to the energies of adsorption [3, 4]. (See Sect. 4.9 for more details.)

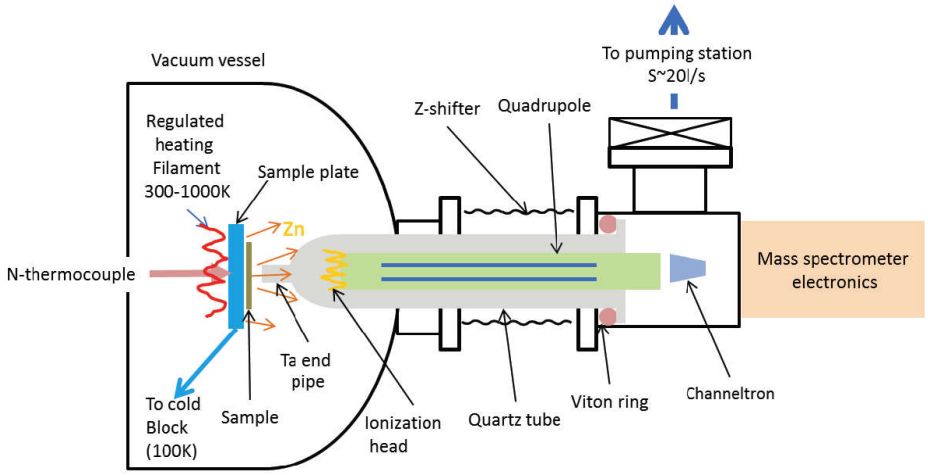

Figure 1.13: Scheme of the Thermal Desorption Spectroscopy setup. The spectrometer enclosed in a differentially pumped tube is approached to about a millimeter distance from the sample surface. The spectrometer allows measuring partial pressures with a high precision (up to 10^{-13} mbar).

In the TDS setup used in this work the sample is set in front of a quadrupole mass spectrometer (*QMG 220 Pfeiffer*, 1-200 amu), as shown in Fig. 1.13. This latter is enclosed in a differentially pumped tube, the small aperture of which is placed in front of the sample at a millimetric distance, in order to spatially select only the molecules coming for the studied sample and to avoid those from the sample holder and surroundings.

Sample temperature is measured by a calibrated N-type thermocouple clamped on the sample holder and ramped linearly (0.5 K/s) by a PID regulator that drives the resistive heater behind the sample. This linear ramp allows for the determination of the activation energies of desorption [32]. For a sufficient pumping speed, the desorption rate *i.e.* the time derivative of the amount of desorbing species is proportional to the measured signal (ionic current).

1.2.6 Secondary Ion Mass Spectrometry

Time of Flight Secondary Ion Mass Spectrometry (ToF-SIMS) is a surface analysis technique which allows measuring all elements from H to U, as well as isotopes and molecular species (see *e.g.* [33]) with sensitivity down to ppb range.

In a SIMS-ToF experiment primary ions such as Ga^+, or Bi^+ are accelerated at 15-25 kV and focused at the sample surface. The interaction of this incident ion beam with the target induces a sputtering phenomenon. A small proportion of the ejected material is composed of ions (positive and negative) which can be collected by applying a polarity (negative or positive) between an extractor and the sample surface. The produced ions have the same energy but different masses. Therefore, they travel with different velocities over the drift path to the detection system (which integrates the number of impacts as function of the time), lighter ions coming first. Primary ion beam is pulsed and the mass resolution directly depends on the pulse width. Due to the low flux of the incident primary beam, depth profiling requires surface abrasion by another ion beam of O_2^+, Cs^+, C_{60}^+, Ar^+ operating at a higher intensity, but lower ion energy (500 to 2 keV to reduce implantation). The "abrasion" beam sputters a crater, while the "analysis" beam progressively probes the centre of the bottom of the crater. The depth resolution depends directly on the abrasion beam settings, such as intensity, abrasion duration for each cycle, but also on induced phenomena such as ion implantation, intermixing, re-deposition, topography changes, etc. SIMS data are usually presented as the ionic current of detected species as a function of the etching time.

The secondary ion current I_s^x for species x can be expressed as:

$$I_s^x = I_p C_x S \gamma F, \tag{1.20}$$

where I_p is the current of the primary ion beam, C_x is the concentration of species x (more precisely, of the selected isotope), S is the sputter ion yield of x, γ is the ionisation efficiency, and F is the transmission function of the analyser. The key parameters influencing the intensity of the collected secondary ions are the sputtering yield and the ionisation efficiency, which depend on the nature of the primary ions beam and on the nature of the target material. The ionization is highly influenced by the chemical environment of the studied species ("matrix effect"). However this effect can be taken into account by using standards.

In this work, the depth profiles were obtained with a *ToF5* instrument provided by *IonTof*, equipped with a Bi *Nanoprobe* ion source dedicated for the analysis, a Cs/O_2 dual source column for the crater abrasion, a low energy electron flood gun for charge compensation on insulating surfaces, and a high mass resolution ToF spectrometer. The following operating conditions were selected: Bi^+, 30 keV, 0.23 pA, 50×50 µm^2; Cs^+, 2 keV, 85 nA, 300×300 µm^2.

1.2.7 PhotoLuminescence Spectroscopy

In a PhotoLuminescence (PL) experiment, the sample is excited by a monochromatic UV source, and the reemitted radiation is monitored as a function of the wavelength. PL is one of the most useful optical methods for semiconductor analysis, since it is sensitive to the impurities and defects content (see *e.g.* [34, 35]). PL spectrum shows characteristic features of the sample band structure. It is thus capable to determine the semiconductor band gap and identify different defect types by their spectral fingerprints. In some cases it is even possible to measure the corresponding defect concentrations.

PL experiments in this work were performed at National Institute of Material Science (Tsukuba, Japan). The spectra were measured at room temperature using a micro PL system (*HORIBA LabRam HR*) with a 325 nm He-Cd laser source and a Perce type CCD detector.

1.2.8 Surface Differential Reflectivity Spectroscopy

Surface Differential Reflectivity Spectroscopy (SDRS) is a linear UV-visible spectroscopy which consists in measuring the relative sample reflectivity $^{\Delta\mathcal{R}}/_{\mathcal{R}}$ while changing the dielectric properties of the surface, for instance, through the growth of a thin film. For metal growth on oxides, submonolayer sensitivity is easily achieved because of the strong dielectric contrast between materials. In the case of the growth of metallic

nanoparticles, the measurement is sensitive to plasmon excitations which appear as dips and enhancements of reflectivity. From this point of view, Ag films studied in this work are a test bed, because of the nearly free electron like behaviour of Ag. The measured signal depends on the film thickness and its dielectric properties.

To a first approximation, the low energy (high energy) resonances are excited by the parallel (perpendicular) components of the incident electric field of the p-polarized light, as the incident field polarizes the Ag electronic cloud [36]. The imaginary part of the metal dielectric constant that corresponds to absorption leads to the damping of the induced dipole. The resonance energy positions and their relative intensities are highly sensitive to: (i) the particle shape and the image field via the depolarization factor, (ii) the particle density via the particle-particle electromagnetic interaction, and (iii) the average size via the amount of polarizable medium [37, 38, 39]. In addition, the dominance of these parameters strongly depends on the growth conditions. For supported films formed by individual atoms deposition the optical response is dominated by the aspect ratio of the particles during the nucleation and growth, as well as at the beginning of coalescence before percolation. In contrast, deposition of three-dimensional clusters may result in their agglomeration for which the particle-particle interaction is the main parameter [40, 41].

It can be shown that in the long wavelength approximation and for a nonabsorbing substrate [36, 42, 43], the differential reflectivity term $\Delta\mathcal{R}/\mathcal{R}$ reads as

$$\frac{\Delta\mathcal{R}_s}{\mathcal{R}_s} = 4\frac{\omega}{c}\frac{\sqrt{\epsilon_1}\cos\theta_0}{\epsilon_2-\epsilon_1}\mathrm{Im}\left(\gamma\right), \tag{1.21}$$

$$\frac{\Delta\mathcal{R}_p}{\mathcal{R}_p} = 4\frac{\omega}{c}\frac{\sqrt{\epsilon_1}\cos\theta_0}{\left(\epsilon_2-\epsilon_1\right)\left(\epsilon_2\cos^2\theta_0-\epsilon_1\sin^2\theta_0\right)} \times \left[\left(\epsilon_2-\epsilon_1\sin^2\theta_0\right)\mathrm{Im}\left(\gamma\right)-\epsilon_2^2\epsilon_1\sin^2\theta_0\mathrm{Im}\left(\beta\right)\right], \tag{1.22}$$

where $\mathcal{R}_s$, $\mathcal{R}_p$ are the Fresnel reflection coefficients in s and p polarizations, $\omega/2\pi = c/\lambda$ the light frequency, c the speed of light, θ_0 the incident angle, ϵ_1, ϵ_2 the dielectric constants of the deposit and of the substrate, and γ and β are the interface susceptibilities. γ gives the integrated surface polarization parallel to the surface in terms of the electric field along the surface and β corresponds to the integrated surface polarization normal to the surface in terms of the electric displacement field normal to the surface.

The SDRS signal only depends on the imaginary part of the interface susceptibilities. For supported clusters (the case of a non-percolated thin film), $\gamma = \rho\left\langle\alpha_{\parallel}\right\rangle$ and $\beta = \rho\left\langle\alpha_{\perp}\right\rangle/\epsilon_1$, where ρ is the density of nanoparticles and $\left\langle\alpha_{\parallel}\right\rangle$, $\left\langle\alpha_{\perp}\right\rangle$ are the average island polarizabilities along the two main directions [44, 45]. For monodisperse particles, the polarizabilities $\alpha_{\parallel}$ and $\alpha_{\perp}$ are calculated in the quasistatic approximation by modelling clusters by truncated spheres [46, 47, 48, 49] of diameter D, height H, truncation $t_r = 2H/D - 1$ or contact angle $\theta_c = \arccos\left(-t_r\right)$ (see Fig. 1.14). For film thickness t below 6 nm, particle size below 10 nm and wavelength λ higher than 200 nm, the quasi-static condition is clearly fulfilled [36].

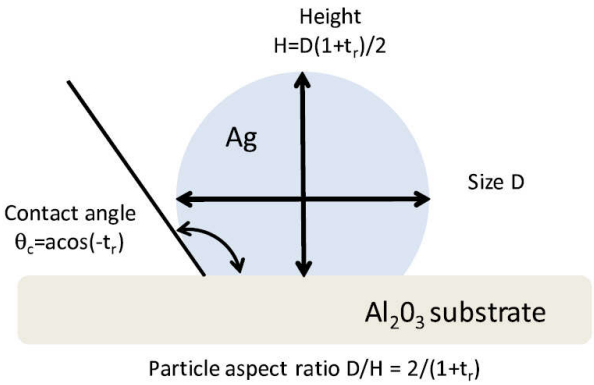

Figure 1.14: Schematic view of a truncated sphere thin film morphology used for optical response modelling showing the aspect ratio D/H, the truncation t_r and the contact angle θ_c.

The positions in energy and the intensities of the plasmon resonances can be thus modelled for a monodisperse morphology (D, t_r, ρ) and given values of the dielectric constants. But the complete modelling of

data requires one to take into account phenomena that contribute to the energy positions, shapes and widths of the absorption peaks. These include the temperatureinduced variations of the dielectric constants, the intrinsic finite-size contribution to the dielectric constant (interface damping, quantum surface effects and fluctuations of the relaxation time), the extrinsic component arising from the size and shape (aspect ratio) distributions and the broadening due to local fluctuations of the particle-particle electromagnetic coupling. These contributions are considered one after another, prior to being used together for critically analysing data [36].

Somehow, SDRS is related to the well-known ellipsometry technique. Basically, the light emitted by a deuterium-halogen lamp is focussed on the sample surface through an optical viewport mounted on the vacuum chamber. The reflected light is collected, split into s- and p-polarization states and the corresponding signals are recorded by grating spectrometers on Si detectors (1.5-5 eV / 250-800 nm), as shown in Fig. 1.15 A correction for the source drift can be applied, and all the unknown variables, such as transmission, detector response, lamp emission, etc. are eliminated by taking the ratio of signals before and after growth, provided that the optical bench is stable enough (in the range of 2×10^{-3}). The home-made setup (INSP) used in this study is mainly based on grating spectrometers from *Avantes* and a barium borate Wollaston prism polariser.

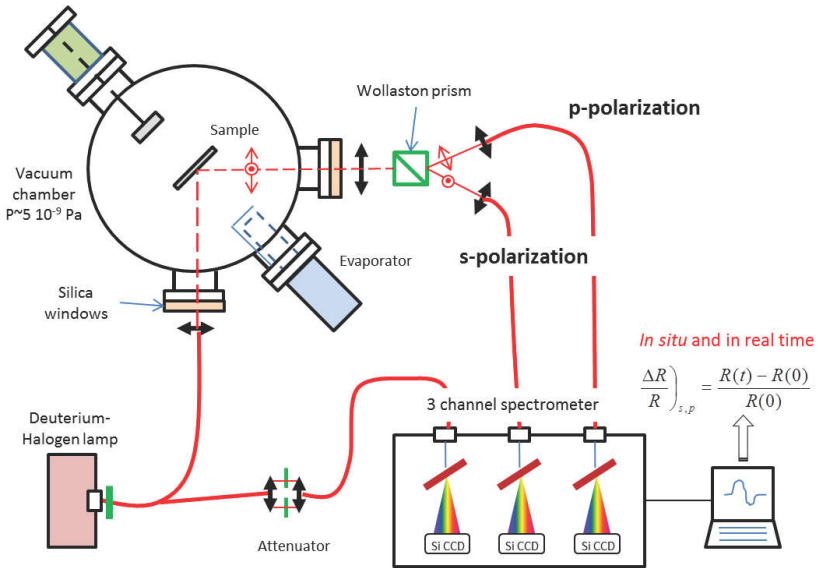

Figure 1.15: Scheme of the differential reflectivity setup used at INSP. The signal before growth is used to get rid of all the unknown variables: emission of the lamp, optics transmission, detector response, etc.

Chapter 2

Electronic properties of the Ag/polar-ZnO interface

Silver based low-emissive and anti-solar coatings developed by the glass industry utilize the in-plane transport properties of the metallic film to reflect infrared light. Beyond mechanical or chemical stability due to poor adhesion at the silver/oxide interface, sheet conductivity is the figure of merit of all research conducted on such products. As demonstrated in the seminal works of Fuchs-Sondheimer [50] and Mayadas-Schatzke [51] on thin metal film resistivity, scattering of electrons at film interfaces and at grain boundaries are the key factors that govern the increase of resistivity compared to bulk. The former is driven, not only by roughness, but also by the nature of the electrical barrier at the metal/semiconductor interface. The latter is related to the size of the metallic grains and to the in-plane texture. Beyond glazing applications, ZnO/Ag/ZnO stack is foreseen as a potential candidate for transparent electronics, in particular in the field of Organic Light Emitting Diodes (OLEDs). Associated with the conductivity of silver, ZnO is a cheap and transparent material that could compete with transparent conductive oxides, the commonly used archetype of which is Indium Tin Oxide (ITO) [1]. This kind of application requires tailoring the electronic transport along the perpendicular direction to inject carriers in the active organic film. But the problem raised by the Ag/ZnO interface lies in the inability to switch in a reliable way from a Schottky to an ohmic contact. Therefore, both the low-emissive coating and transparent electronics fields call for a better understanding of this specific interface from a transport point of view.

This chapter aims to explore the band alignment at Ag/ZnO interface from a fundamental point of view. As demonstrated in Chapter 3, the columnar growth of ZnO along the c-axis leads to polycrystalline ZnO layers exposing mainly (0001) polar orientation on which subsequent Ag layers are deposited in the industrial stacks. To understand the intrinsic structural and electronic properties of this interface, a surface science study of Ag on (0001)-oriented ZnO single crystals was undertaken by combining morphology (STM), structural (LEED/RHEED) and chemical (XPS) analysis. Band alignment at the interface, work function changes, band bending and space charge layer were determined by matching laboratory ultra-violet (UPS) and synchrotron high energy (HAXPES) photoemission techniques.

This chapter is structured as follows. It starts with a deep, but not exhaustive, overview of the understanding of ZnO surface and its contact with metals based on analysis made on single crystals with surface science approaches. The emphasis is put on the numerous open questions raised by the polar surfaces of ZnO and their interplay: (i) the polarity healing (Section 2.1.1), (ii) the role of hydrogen at surface and in the bulk on the electronic properties (Section 2.1.2), (iii) metal wetting and electrical contact (Section 2.1.4). The basics of metal/semiconductor contacts are also reminded.
After an introduction on sample preparation, morphology, epitaxy and plasmonics of Ag on ZnO(0001)-O and ZnO($000\bar{1}$)-Zn polar surfaces are explored in Section 2.2. Next, through laboratory photoemission, Section 2.3 tackles the question of the evolution of work function, band bending, ionization energy and Schottky barrier during silver growth in the regime of few monolayers. The results are put in parallel with the structural observations. As prepared and hydrogenated surfaces are explored as well as the chemistry evolution during hydrogen adsorption. In the last part (Section 2.4), high energy photoemission is employed to have access to the absolute band bending and to position the Fermi level. To do so, a dedicated modelling is developed. The chapter ends with a summary of the main results of this work and of the unsolved issues.

[1] The availability and scarcity of In causes geopolitical issues.

2.1 State of the art

2.1.1 ZnO polar orientations: polarity healing and environment

The aim of this section is to review all the efforts of the surface science community to understand the question of polarity healing of ZnO basal surfaces. The stabilization mechanism is strongly environment-, face- and temperature-dependent, and hydrogen and hydroxylation play a paramount role in it [52].

For instance, bulk ZnO wurtzite (space group $P6_3mc$, $a = 3.2495$ Å , $c = 5.2069$ Å , $u = 0.3825$) is built by stacking consecutive hexagonal layers of oxygen and zinc atoms with formal charges ± 2 along the [0001] direction with alternating distances $R_1 = 0.61$ Å and $R_2 = 1.99$ Å. When cleaving ZnO along this axis, two different surfaces are created, the Zn- and O-terminated ones, denoted by ZnO(0001)-Zn and ZnO$(000\bar{1})$-O (Figs. 2.1-2.2).

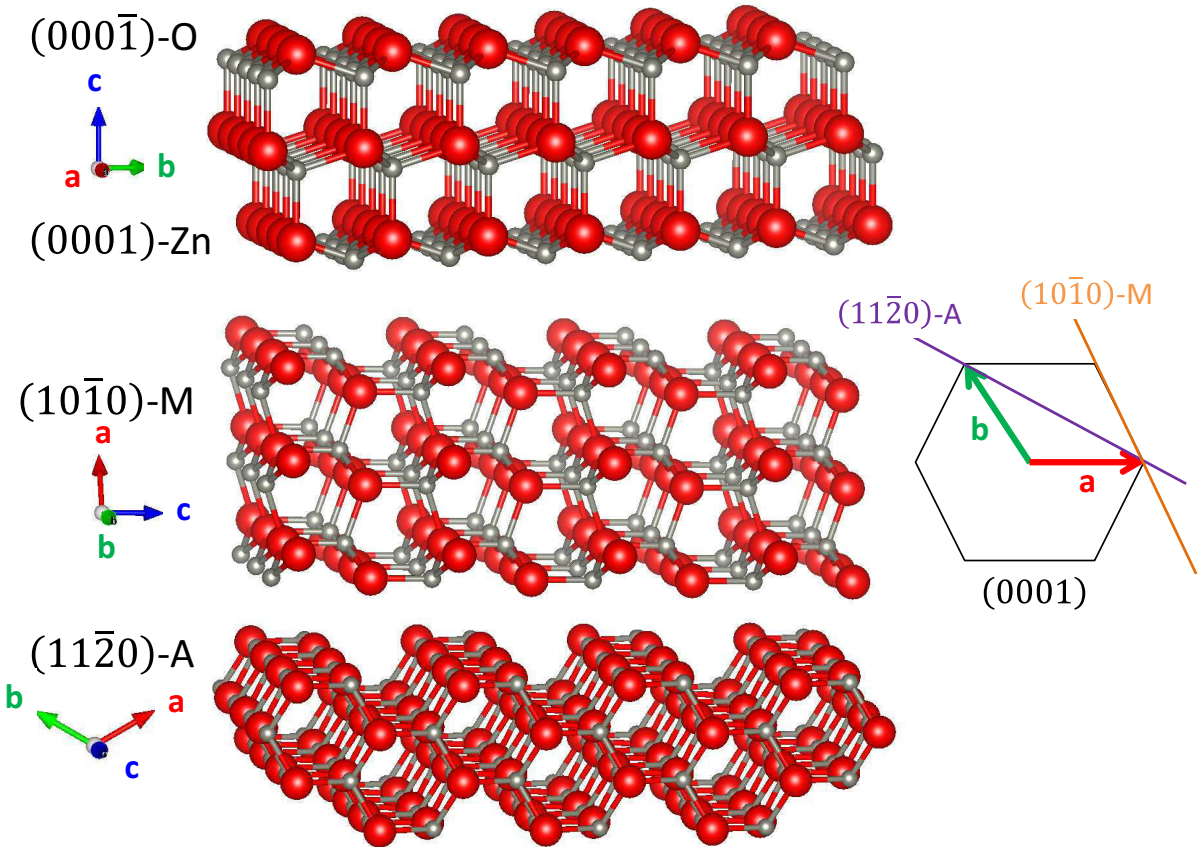

Figure 2.1: Balls and sticks model of most stable surfaces of ZnO wurtzite (bulk truncation): ZnO$(000\bar{1})$-O, ZnO(0001)-Zn, ZnO$(10\bar{1}0)$-M and ZnO$(11\bar{2}0)$-A. O atoms are shown in red and Zn in grey.

Polar surfaces are crystallographic orientations for which the projection of the dipole moment related to the repeating unit cell along the surface normal is non-zero (Fig. 2.3a,b). In contrast to the rhombohedral ZnO$(10\bar{1}0)$-M and ZnO$(11\bar{2}0)$-A faces (Fig. 2.1), ZnO(0001) surfaces are polar and belong to the "Tasker-type 3" [53, 54, 55]; the dipole moment that lies along the [0001]-axis gives rise to an electrostatic field that scales with the thickness of the crystal and to a diverging surface energy (Fig. 2.3c).

As a consequence, the (0001)-surfaces formed by truncation of the bulk structure are unstable [53, 54, 55]. For macroscopic samples, the so-called polar instability has to be compensated by changing the surface charges. In order to quench the macroscopic dipole, electrostatics requires a charge transfer across the sample. The sample can be represented by a set of capasitors connected in series. So, the charge transfer across the sample can be expressed as $R_1/(R_1 + R_2)\sigma$, where σ is the surface charge density of the ionic plane and $R_{1,2}$ is the distance involved in the stacking (see Fig. 2.3). It amounts to $(1 - 2u)\sigma = 0.235\sigma$ for

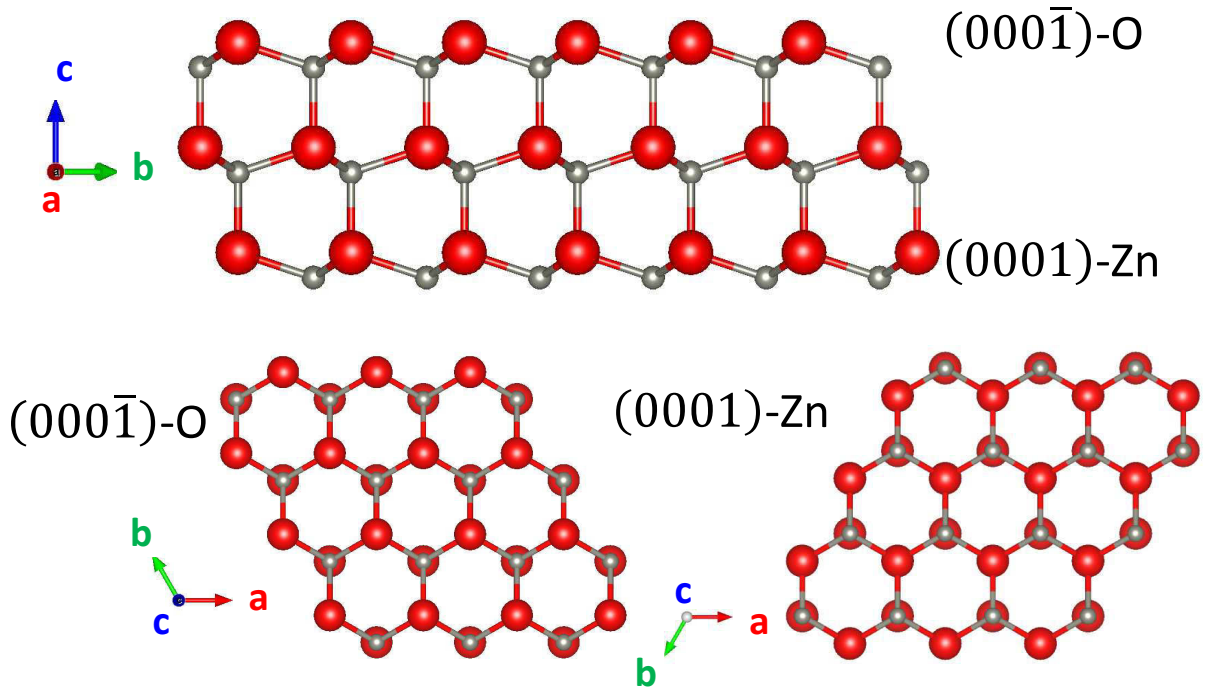

Figure 2.2: Balls and sticks model of polar ZnO(0001)-Zn and ZnO(000$\bar{1}$)-O faces viewed along the c-axis or in-plane (O atoms in red and Zn in grey).

ZnO where $u = 0.3825$ is the atomic position parameter of the P6$_3$mc structure of ZnO. Various mechanisms of polarity healing are possible:

- charge transfer between the two polar surfaces without significant spatial rearrangement of atoms; the macroscopic electric field induces the crossing in energy of the valence and conduction band across the sample and the surfaces become metallic-like;
- removal of atoms and formation of vacancies (with possible relaxations and reconstructions due to the lack of stoichiometry),
- adsorption of foreign elements that provide the required extra-charges, the most obvious ones being hydrogen through hydroxyl groups or even metallic films,
- surface nano-faceting along non-polar orientations,
- change of atomic structures (graphitic or p-BN like ZnO [56]) or uncompensated polarity, both mechanism being active only at the limit of ultra-thin oxide films [57].

The prevalence of one route over the others strongly depends on the temperature and the environment, in particular on the chemical potentials of oxygen and hydrogen. Most of those mechanisms of stabilization have been invoked to explain the polarity healing of ZnO which is, in addition, orientation dependent. Despite the use of reference surfaces prepared in ultra-high vacuum using sputtering/annealing cycles, existing microscopic models for the basal ZnO surfaces are rather contradictory and are still under discussion [55], probably because of the difficulties in achieving reproducible atomic scale imaging. While earlier studies in the 70s pointed out reconstructions due to segregation of bulk impurities, most of the recent experimental studies lead to surfaces that are free of impurities, except hydrogen [52], and that have an apparent (1×1) LEED pattern.

The metallization of the surface by charge transfer from one face to another was initially suggested based on crystal truncation rod analysis obtained through grazing incidence diffraction and *ab initio* calculations [58]. Polar surfaces were found bulk terminated with no significant relaxations. However, this interpretation was quickly questioned by DFT studies [59], by more recent works, and the lack of any traces

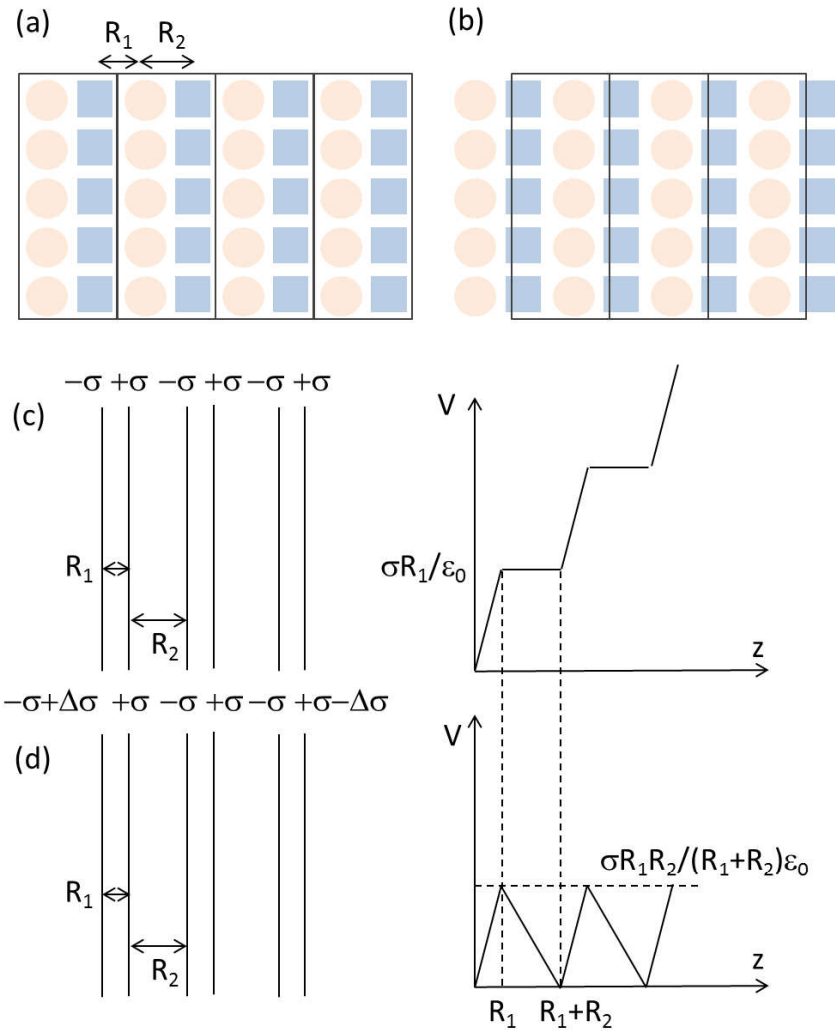

Figure 2.3: (a) Tasker's representation of a polar surface. Repeated units start from vacuum (on the left and right of the atomic layers) and carry a dipole moment. (b) Charge neutrality consideration for the same system: a neutral and dipole free unit cell is chosen leaving excess charges on the two faces. Capacitor description of the charged layer stacking without (c) and with (d) the compensating charges on the outer surfaces. The corresponding electrostatic potential accross the stack is depicted. (Adapted from Ref. [55].)

of evidences of partially filled surface states in photoemission [60, 61].

Change of stoichiometry may provide the required charge reduction. Although it is difficult to unravel with photo-diffraction [62] or ion scattering techniques [63, 64] due to the lack of long range order, there were substantial evidences that the polar faces of ZnO exhibit a high degree of disorder, since the introduction of 1/4 of vacancies on ZnO(0001)-Zn improves the fit of GIXD [65] and matches with TEM observations [66]. However, the O-terminated surface did not show such clear deficiency trend [65, 66]. Later on, based on STM imaging [68, 69, 70] (similar images where obtained also in Ref. [71]) confirmed by AFM observations [72], Diebold and co-workers proposed a surface stabilization mechanism of ZnO(0001)-Zn through the formation of nanoscopic triangular islands and pits of half-unit cell height that are successively rotated by 180° (Fig. 2.4a). Their step edges (aligned along the $[10\bar{1}0]$ direction) that are O-terminated and polar [73] lead to a change of surface stoichiometry. Atoms counting agrees with the required charge compensation through the 1/4 charge of surface zinc atoms [55], although the interpretation of the driving force is questioned based on the electron counting rule [74]. The triangular reconstructions were confirmed by *ab initio* calculations [75, 76] and Monte-Carlo simulations [77] to be an efficient mechanism of charge compensation with a great flexibility in terms of size of the features (Fig. 2.5a). Aside the triangular features, gentle ion bombardment generates hexagonal shaped cavities, the bottom of which is O-terminated [78]. For high temperature annealing under vacuum ($T > 1300$ K), the surface seems to be stabilized by a complex interplay between triangular structures and faceting leading to highly ordered step arrays with edges exhibiting $\{10\bar{1}0\}$ nanofacets [79]. Longer annealing leads to large area of $\{10\bar{4}0\}$ facets [80]; this specific orientation has a vanishing component of the dipole moment normal to it and satisfies the semiconductor electron counting rule in terms of anion/cation dangling bonds.

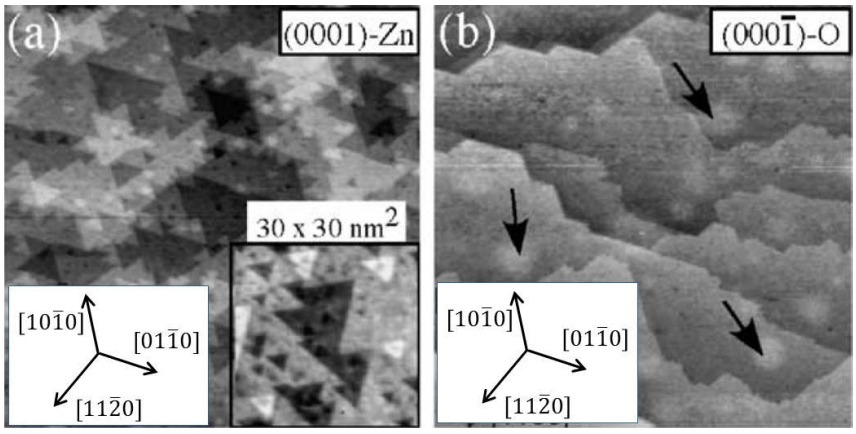

Figure 2.4: STM images of polar surfaces of ZnO (200×200 nm^2, $V_g = +2$ V and $I_t = 1.5$ nA showing: (a) one-step triangular terraces (islands and holes) for ZnO(0001)-Zn and (b) double-step structures rotated by 120° for ZnO(000$\bar{1}$)-O [68, 70]. Compared to the original figure, the actual crystallographic axes are corrected.

As the Zn-terminated surface, ZnO(000$\bar{1}$)-O displays a (1×1) LEED pattern. Such nanoscopic features as on the Zn-terminated face have never been observed on the O-terminated surface by STM [69, 70] (Fig. 2.4b). Instead, Wöll and co-workers [81] used the surface sensitivity of Helium Atom Scattering (HAS) combined with LEED to point at a possible (1×3) missing row reconstruction on the clean ZnO(000$\bar{1}$)-O that is easily lifted upon hydrogen adsorption leading to an OH-covered surface [82, 83] as seen by photoemission. However, this reconstruction does not fulfil the electrostatic healing rule [55] and requires an extra-source of charges (hydrogen atoms). This (1×3) reconstruction has been observed on Zn-terminated surfaces only at a very local scale with AFM [72], but was questioned by DFT calculations [84], since it overcompensates the polarity. According to theory, when hydrogen is present, the reconstruction is lifted, and hydroxyl groups stabilize the otherwise unreconstructed O-terminated surface [75, 85]. The presence of hydrogen was experimentally demonstrated using CO as a probe molecule of the surface termination [86]. An accurate LEED analysis [87] concluded at a fractional coverage of disordered H atoms (1/3 ML). The fully hydroxylated ZnO(000$\bar{1}$) surface proposed by Wöll [52, 83] does not fulfil the requirement of electrostatics which should be 1/2 ML of coverage and is found theoretically unstable [85, 88]. On the other hand, Lindsay

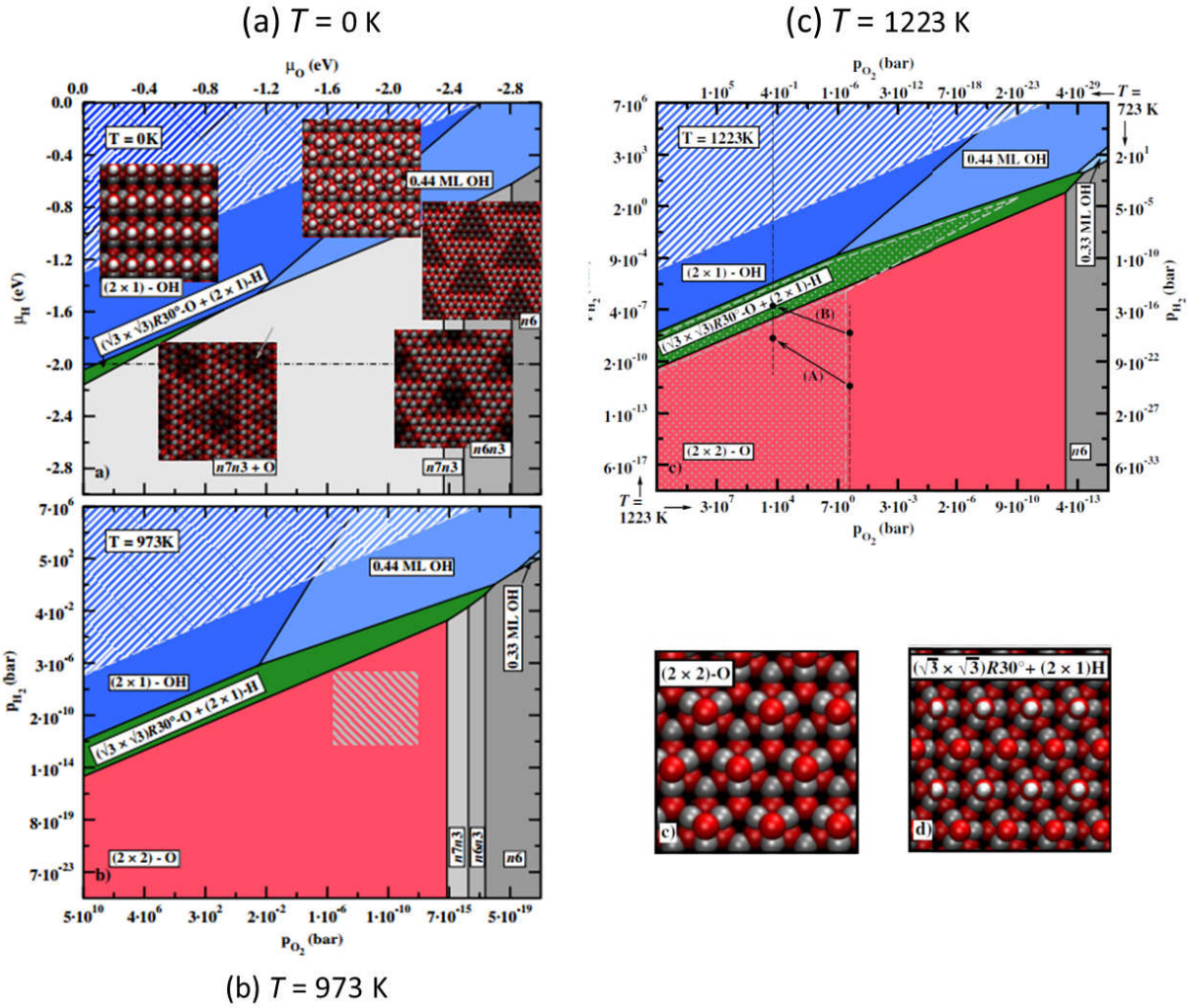

Figure 2.5: Calculated phase diagram of ZnO(0001)-Zn in contact with a humid atmosphere at different temperatures [75, 76]. The upper left corner corresponds to condensation of water. a) $T = 0$ K. The geometries of the stable structures, the H-covered surfaces as well as the triangular reconstructions are shown with ball models. b) $T = 973$ K c) $T = 1223$ K. The hashed square corresponds to typical UHV conditions. Notice the extension of the domain of existence of the (2×2) and $(\sqrt{3} \times \sqrt{3})R30°$ structures that are shown on the left.

and co-workers [89] claimed that an OH-free surface can be obtained under vacuum (as judged by O 1s line shape and lack of OH stretching frequency in the High Resolution Electron Energy Loss spectrum) without the (1×3) reconstruction but instead with a (1×1) LEED pattern. Though, their surface preparation recipe involved annealing at much higher temperatures than in other studies (1200-1370 K). In some conditions, ZnO(0001)-Zn can also be stabilised by OH groups. But this requires special wet chemical preparation methods with a hydroxide coverage that depends strongly on the chemical environment [90, 91]. OH-rich (2×2) and $(\sqrt{3}\times\sqrt{3})R30°$ reconstructions were observed on the ZnO(0001)-Zn terminated surface after thermal treatment in dry and humid oxygen atmosphere [76, 92]. AFM showed large scale terraces with the absence of triangular pit/islands [90, 91, 92]. These observations pushed to reconsider the phase diagram dominated by under-stoichiometric reconstructions [75] and to include vibrational entropy that renders its explicitly temperature dependent (Fig. 2.5). Until recently, no atomic resolution in near-field microscopy was obtained on the O-terminated surface. Only hexagonal terraces separated by double steps with step edges at 120° were observed [70, 93] (Fig. 2.4b). Lauritsen *et al.* obtained high resolution STM and non-contact AFM images (Fig. 2.6) on the O-terminated surface [93]. Depending on the imaging temperature, they found: (i) a (1×2) H covered surface at room temperature, in agreement with polarity healing rule, (ii) a (5×5) honeycomb structure in which the removal of 11 O atoms and 7 Zn atoms is further stabilized by 5 OH groups, and (iii) a (2×2) constructed theoretically on the same principle of atom removal. These observations were accompanied by an accurate phase diagram obtained by *ab initio* simulations by Kresse's group [88] (Fig. 2.7).

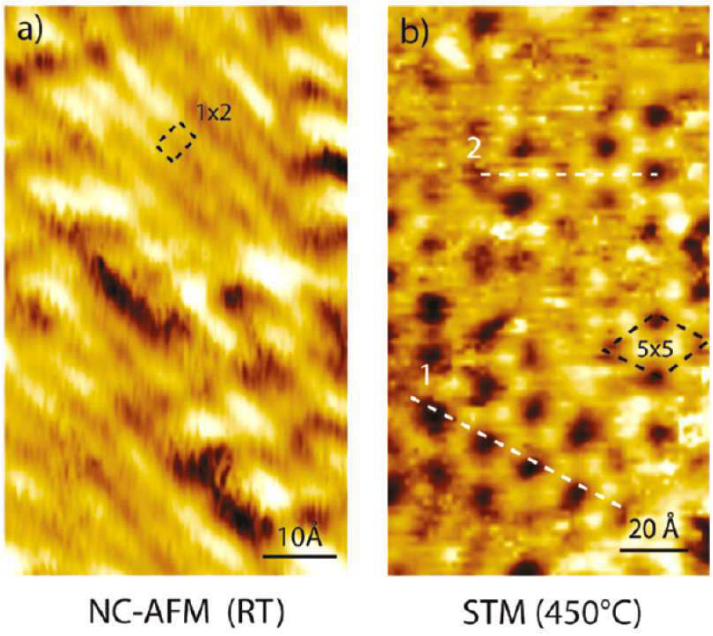

Figure 2.6: High resolution images of the ZnO$(000\bar{1})$-surface: (a) constant high NC-AFM image (8×8 nm^2) at room temperature showing the local (1×2) H reconstruction and (b) STM image at 450° C (11×18 nm^2) showing the (5×5) reconstruction. (Adapted from Ref. [93].)

To sum up, the mechanisms of polarity healing on ZnO(0001) surfaces are still debated. It is highly temperature- and environnement-dependent, and hydrogen plays an unmistakable role in it. It is worth noticing that the surface science literature forgets the potential role of sub-surface point defects (H, Zn interstitials and O vacancies) that are produced by sputtering-annealing cycles during surface preparation and that may spread the compensation charge over several layers and not on the top surface. Their role in the change of wetting of Cu particles upon annealing was recently highlighted [94].

2.1.2 ZnO and hydrogen

Hydrogen in ZnO impacts not only the stability of the polar surfaces through the presence of hydroxyl groups (as shown above), but also seems to drive the n-type conductivity of the material and the formation of an electron accumulation zone at its surface through band bending. The modulation of the conductive channels of the ZnO surface upon adsorption is used in the gas detector applications. For many decades, it has been known that H diffuses in ZnO, but there are still conflicting conclusions on its chemical state, amount, role (and similarly that of native point defects) in the transport properties of ZnO (see *e.g.* reviews [95, 96, 97, 98, 99, 100]). H in ZnO is of concern for several scientific communities [99] interested by the bulk [101] or

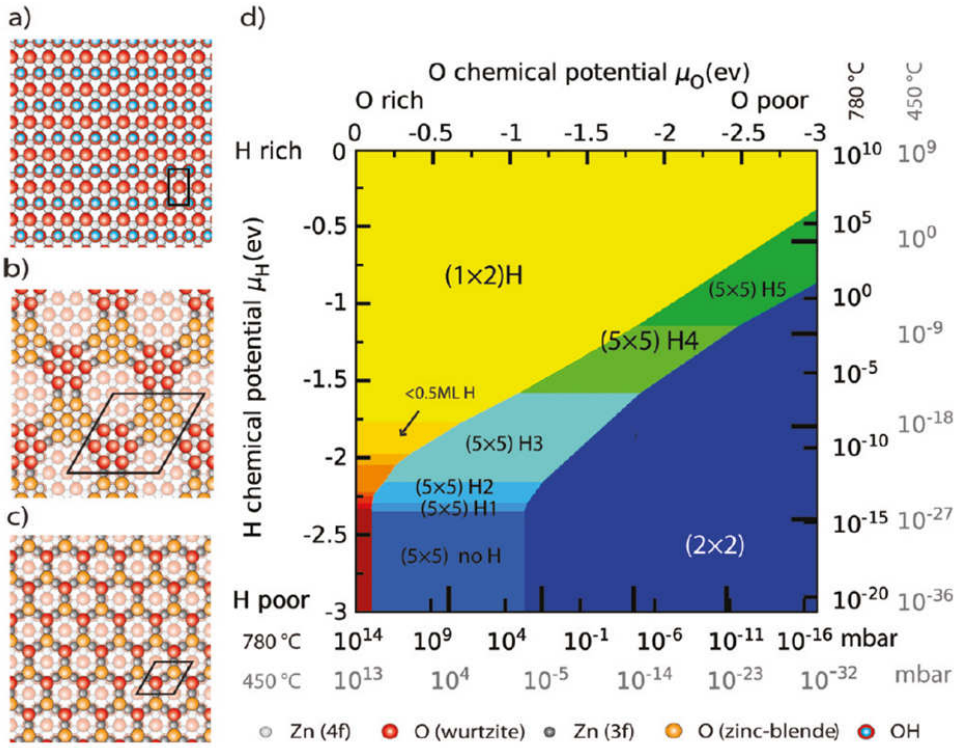

Figure 2.7: Calculated phase diagram and ball models for the reconstructions of the ZnO$(000\bar{1})$ surface. From Refs. [88, 93]. (a) (1×2) H covered with 0.5 ML, (b) (5×5), (c) (2×2). The (5×5) Hn refers to the number n of adsorbed H in the unit cell. Chemical potentials have been converted in partial pressures at the two indicative temperatures.

the extreme surface [52] of the material, by electronic properties of ZnO or of the produced devices [95], ZnO contacts with metals [100, 102] or its catalytic properties [52]. The aim of this section is to set up the landscape of the questions risen by H in ZnO without being exhaustive [103].

2.1.2.1 Hydrogen and defects in the bulk

The origin of the n-type conductivity of non-intentionally doped ZnO is one the controversial issues in the ZnO literature. Among several candidates, the seminal Density Functional Theory work of Van de Walle pointed at the role of atomic H in the formation of shallow donor states [98, 101, 104]. Because of its amphoteric character that depends on the host, H can act as a donor (H^+) or an acceptor (H^-) [105]; in ZnO it counteracts and passivates any intentional p-type doping, even in the best single crystal. Therefore, p-type doped ZnO is *per se* an active field of research and is still a Graal [100]. The donor character of H in ZnO has been recognized by the fact that H doping enhances bulk electrical conductivity [106]. Its ionization energy is found in the range of a few tens of meV [106, 107, 108, 109, 110, 111].

If not introduced intentionally through exposure to H_2 at high temperature, plasma or atomic hydrogen, H is always present, in particular during the course of the hydrothermal synthesis of single crystals. Beside the increase of conductivity, the presence of H in the bulk has been demonstrated through its several experimental signatures: infra-red or Raman H-related stretching frequency [108, 110, 112, 113, 114, 115, 116, 117], electron paramagnetic resonance [107], muon-implantation spectroscopy [118], effusion experiments [114], photoluminescence [115], nuclear reaction [119]. Since more than 15 years, the nature of the sites occupied by hydrogen is still under debate, partially because of the variability of sources of samples and used sample treatments. The possibilities include interstitial atoms (H_i in the so-called bond centred position in between Zn and O atoms) [105, 118, 120] or molecules ($H_{2,i}$) [117, 121], bounded to Zn [113, 119, 122] or O [110, 123] vacancies, substitutional H on O site [105], a combination of sites [115] and even H bounded with other intrinsic defects or impurities such as Li [124] [2]. Surprisingly, infra-red inactive hidden hydrogen (up to a concentration of 10^{19} cm^{-3}) was also suggested to be converted to infra-red active and dopant active hydrogen as a function of annealing in the absence of any external source of H [117, 121]. This hidden hydrogen was predicted to be trapped at oxygen vacancy sites in the form of molecules [125]. The residual concentration of hydrogen in ZnO single crystals depends strongly on the supplier [108, 122] and was quantified by Electron Paramagnetic Resonance, inductively coupled mass spectrometry, nuclear reaction, effusion and infra-red measurements (from 6×10^{16} cm^{-3} to 10^{19} cm^{-3} [107, 108, 114, 121]). In sputtered ZnO films, the determined amount of hydrogen can be found even 4 orders of magnitude higher [123]. Surprisingly, nuclear reaction analysis of hydrogen gave 0.02-0.04 at.% [126] and even up to 0.3 at.% [119, 122] of H in some as-grown crystals with a slow recovery due to room storage after effusion. The observed H concentrations are several orders of magnitude higher than that of other impurities [122]. Loading up to 30 at.% could even be achieved electrochemically with more than a half of it chemically bounded to the ZnO lattice. On pristine surfaces prepared by sputtering-annealing, a subsurface enrichment in hydrogen by one order of magnitude compared to the bulk value was also observed over a depth of 10 nm in single crystals [126]. Hydrogen is found to very rapidly diffuse in bulk ZnO for H_2-plasma exposed surfaces with an activation energy of 0.17-0.34 eV (0.5 eV from theory), with a strong variation of the prefactor and an interstitial mechanism of diffusion [116, 126, 127, 128].

Beyond extrinsic point defects due to impurities, native points defects can be formed and act as dopants depending on the position of the Fermi level. It is out of the scope of this thesis to review the literature about point defects in ZnO and their spectroscopic fingerprints – a work already done in Refs. [95, 96, 97, 98, 99, 100, 129]. However, it is worth mentioning the thorough theoretical work of Janotti and Van de Walle [98, 101], who derived a phase diagram and a trend concerning their formation and stability. They demonstrated that oxygen deficiency manifested through O vacancies or Zn interstitials is unlikely to be the cause of n-type conductivity, thus, hydrogen being the most probable candidate. In n-type samples, O vacancies act as deep donors with a high formation energy, while Zn-interstitials are shallow donors also with a high formation energy but a very fast diffusion with a migration barrier of 0.57 eV. Zinc vacancies are deep acceptors with a low formation energy while the formation of O interstitial is unlikely. In fact, all defects have modest migration barriers (in the order of an eV) which implies that they are highly mobile at temperatures at which crystals are annealed. Their migration was highlighted in the observed change of wetting of Cu particles upon annealing [94]. Unfortunately, literature gives no clear study about the effect of sputtering/annealing preparation on the profile of concentration of defects in the subsurface.

[2] Li also acts as a amphoteric dopant and is present in the hydrothermal synthesis of crystals [103]

2.1.2.2 Hydrogen at the surface

This section is limited to the effect of the chemistry of hydrogen on polar ZnO surfaces. The question of adsorbates (in particular H_2O and H) on polar and non-polar ZnO surfaces was reviewed by C. Wöll [52], who strongly contributed to the field with surface science approaches. Regarding H, the adsorption behaviour on the two polar faces of ZnO is quite different.

On pristine polar surfaces, the sticking coefficient of molecular H is rather poor [52, 82, 130]; it is barely dissociated or adsorbed. On ZnO(0001)-Zn, an early work of Becker [82, 131] already highlighted the instability of this surface upon atomic hydrogen exposure (provided by the hot filament technique). Whereas the substrate kept a (1×1) LEED pattern, Helium Atom Scattering evidenced the formation of OH groups through the breaking of Zn-O surface bonds. Hydroxyl fingerprints were also observed in the O $1s$ XPS peak. A prolonged exposure destroyed the periodicity, as seen by HAS, but not by LEED, proving that this surface reduction is limited to the top surface layers. This hydrogenated surface is chemically rather inert, as demonstrated by CO adsorption experiments [86]. Parallel observations were made by AFM and spectroscopic ellipsometry [132, 133], but with a harsher exposure using a plasma source of atomic hydrogen. These measurements revealed that the ZnO(0001)-Zn is easily etched by atomic hydrogen giving rise to metallic zinc signature in the dielectric function, a strong surface roughening/etching and photoemission signatures of OH and metallic Zn [61]. The same phenomenon [133] was also observed on non polar orientations, ZnO$(10\bar{1}0)$-M and ZnO$(11\bar{2}0)$-A, and thin films with pseudo-activation energies in the range of 0.2-0.25-0.5 eV for M, Zn and A faces [133]. These values match with measured diffusion energy of H in ZnO with Secondary Ion Mass Spectrometry or desorption (~ 0.2 eV) [116, 127, 130]. Even exposure to 10^{-5} mbar of H_2 during 0.5 h induced a strong roughening of the triangular reconstruction observed in vacuum [134]. At the opposite, the ZnO$(000\bar{1})$-O surface is passivated upon the formation of an H-covered surface. Wöll and co-workers [52, 131] found that a (1×1) surface, probably already hydroxylated by the residual vacuum, is insensitive to H, while the (1×3) reconstruction that is observed by HAS and LEED is lifted with H and H_2O (with appearance of a OH shoulder on the O $1s$ peak). Optically and in low resolution AFM, no changes are observed on the O-terminated surface [132, 133]. In the High Resolution Electron Energy Loss spectroscopy (HREELS) study of Qiu *et al.* [109], while the appearance of an OH stretching band directly confirmed the formation of OH groups upon hydrogenation of ZnO$(000\bar{1})$-O, its frequency ruled out bulk ones (compared to bulk measurements)[110, 112, 113, 114, 115, 116, 117]; no Zn-H hydride stretching band was observed.

The difference of reactivity of the two surfaces (see Fig. 2.29) results from the bonding strength between O-H and Zn-H [104]. The Zn-terminated surface is transformed into an OH-stabilized surface through the exothermic reaction [75]: ZnO + H $\rightarrow$ Zn + OH. H is able to break the back bond between Zn and O atoms. The order of stability of the various ZnO orientations towards H is related to a number of crystallographic sites available for H adsorptions: ZnO$(000\bar{1})$-O $\gg$ ZnO$(10\bar{1}0)$-M $>$ ZnO(0001)-Zn $>$ ZnO$(11\bar{2}0)$-A.

2.1.3 Surface electronic properties: conductivity, space charge layer, band bending and work function

Hydrogenation is an often employed way to passivate chemically active surfaces of semi-conductors like silicon. Inertness is provided by the quenching of the dangling bonds and of the surface or band gap states. However, many oxide semiconductors turn out to be metallic upon hydrogen adsorption [135, 136]. It has been recognized that hydrogen diffuses in the bulk of ZnO and increases its conductivity [106]. While not only H doping, but also adsorbed hydrogen can act as a donor and modify the surface transport properties. In their pioneering work, Heiland and Kuntmann [135] pointed at a strong variation of the sheet conductance of cleaved polar surfaces of ZnO by adsorption of atomic and molecular oxygen. H (and not H_2) increases the surface conductivity, and adsorbed O reduces it. The variation of surface conductivity by up to 8 orders of magnitude (Fig. 2.8) were assigned to the donor/acceptor character of H/O and to the variation of the direction of band bending that switches the space charge layer from accumulation to depletion regime. This observation was supported by the variation of reflectivity that goes along with the change of the electric field in the space charge layer (similar to electroreflectance) [137]. One problem of ZnO is that thermal treatment and exposure to atmosphere yields to a surface conductive channel that hampers reliable bulk-like transport measurements, in particular in poorly doped samples [138, 139].

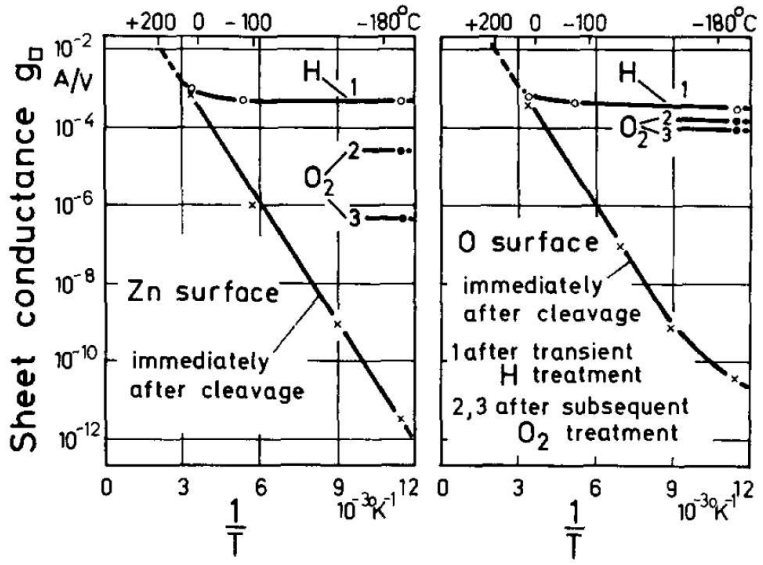

Figure 2.8: Sheet conductance measured by the Van der Pauw method in vacuum versus temperature on Zn- and O-terminated ZnO polar surfaces after cleavage, pretreatment with atomic H and exposure to O_2 [135].

The obtained surface charge in the accumulation zone at the ZnO surface [3] is in the range of $10^{12} - 10^{13}$ cm^{-2}, but it can increase up to 10^{15} cm^{-2} as determined by transport measurements. The accumulation zone can be produced by atomic hydrogen exposure [61, 109, 140, 141, 142, 143, 144, 145, 146, 147], UV-illumination [140, 141], plasma exposure [148], ion-bombardment or H_2^+ implantation [149, 150] (even at an electrolyte interface [151, 152] or on as-received substrates [139]), or hydroxylation [147, 153]. It is quite systematically destroyed by exposure to oxygen or ambient atmosphere. The problem of all these studies is the lack of knowledge on the effect of the treatment on the sample stoichiometry and diffusion of hydrogen. The electric field in the accumulation layer is so strong that electrons are constrained to move parallel to the surface in a narrow potential well, and their motion perpendicular to the surface is quantized. The resulting quasi-bidimensional confined electrons occupy energy levels that are split into two-dimensional subbands corresponding to different eigenstates of the potential well. Electrons are found to be mostly confined in the first one [152, 154]. As it appears at a free surface, this accumulation layer and the corresponding 2D electron gas was the playground of several studies aimed at understanding of the 2D confined behaviour:

- Hall mobility showed a complex modulated behaviour of the electron density [140, 141, 155, 156];
- a negative magnetoresitance was observed in such accumulation layers [142, 157];
- HREELS [143, 144] experiments pointed at two-dimensional plasmon quantizied excitations, which coupling with Fuchs-Kliewer phonons were called plasmarons; puzzlingly, the HREELS work of Qiu *et al.* [109] did not account for this accumulation layer and assigned the quasi-elastic peak broadening on ZnO(000$\bar{1}$)-O only to bulk doping through H diffusion and to surface metallization on ZnO(10$\bar{1}$0)-M [145];
- I-V STM curves revealed transitions between the different subbands on hydrogenated surfaces [158];
- parabolic band dispersion with quantized behaviour along the perpendicular direction was evidenced with angular resolved photoemission spectroscopy [61, 146, 147, 159].

The estimated extent of the accumulation layer has never been directly measured (see Sections 2.1.2.2 and 2.4); it has been estimated to be in the range of 1-2 nm (through simulations) [150, 152, 154]. Locally the carrier density corresponds nearly to a metallic one.

The increase of the carrier concentration in the accumulation layer was correlated: (i) to a variation of the band bending that induces the trapping well and (ii) to a decrease of the work function. These evolutions of the band levels that are adsorbate-dependent (and therefore time-dependent even under ultra-high vacuum conditions [160], not speaking about adventitious carbon contamination that changes the work function [161]) were characterized by optical measurements [135], macroscopic [162, 163] or local Kelvin methods using near

[3] Experiments were performed mainly on O-terminated surfaces in the earlier studies.

Reference	Sample preparation	ZnO(0001)-Zn	ZnO(000$\bar{1}$)-O	ZnO(10$\bar{1}$0)-M
UPS - present work	sput/UHV anneal 1200-1400 K	4.3	5	-
UPS - [61]	sput/O_2 anneal 1050-1100 K	4	5.1	4.5
UPS - [169]	sput/UHV anneal 900 K	4.49	-	-
UPS - [9, 147, 170, 171, 172]	sput/O_2 anneal 1050-1100 K	-	-	4.5-4.85
Kelvin - [139]	no preparation	4.52	4.70	-
XPS - [174]	sput/UHV anneal 850 K	-	5.18	-
UPS - [175]	sput/UHV anneal 723 K	3.9	4.6	4.3
UPS - [176]	sput/UHV anneal 800 K	4.3	4.6	-
UPS - [160]	sput/UHV anneal 700 K	3.7	6.0	5.05
Kelvin - [162, 163]	UHV cleavage	4.25	4.95	4.64
Photoelectric yield - [177]	UHV cleavage	-	-	4.68

Table 2.1: Compilation of data from the literature for the work function Φ_{ZnO} [eV] of ZnO surfaces.

Reference	Sample preparation	ZnO(0001)-Zn	ZnO(000$\bar{1}$)-O
UPS - present work	sput/UHV anneal (1200-1400 K)	0.9	1.1
Kelvin - [162, 163]	UHV cleaved and anneal at $\leq$800 K	$0.2 - 0.3$	$0.2 - 0.3$
UPS - [160]	sput/UHV anneal at 700 K	$-0.1 \underset{time}{\longrightarrow} -0.1$	$1.3 \underset{time}{\longrightarrow} 0.15$
AFM Kelvin - [164]	Air exposed samples	0.03 to 0.40	-0.08 to 0.3
UPS - [169, 178]	sput/UHV anneal at 1100 K	0.25	0.3
UPS - [139]	No *in situ* preparation	-0.61	-0.49
XPS - [61]	sput/UHV anneal at 1100 K + O_2	$\Delta_H V_{bb} = +0.6$	$\Delta_H V_{bb} = +0.4$
XPS - [167]	As-received / hydroxylated	-0.21	-0.42
XPS - [167]	UHV cleaved surface but still hydroxylated	-0.36	0.04
XPS - [153]	As loaded after atomic O treatment	-0.6	-0.3
XPS - [153]	Annealed at 1050 K	-0.2	0.5

Table 2.2: Absolute band bending V_{bb} (eV) at ZnO polar surfaces. $V_{bb} > 0$ corresponds to an upward band bending and $V_{bb} < 0$ to a downward one.

field microscopy [164], ultra-violet [160, 165], laboratory X-ray [139, 153, 166, 167, 168] or synchrotron [61, 146, 147, 153, 159] photoemission. Larger work function values were found on the native ZnO(000$\bar{1}$)-O than on the ZnO(000$\bar{1}$)-Zn surface (see Table 2.1), in agreement with the larger electronegativity of O [162].

Native surfaces after cleavage and annealing [4] or sputtering/annealing systematically show a depletion layer with upward band bending, the value of which decreases with time due to spurious adsorbates and therefore fluctuates from one experiment to another (see Table 2.2).

Atomic hydrogen adsorption systematically diminishes the work function, and bends the downward bands up to create an accumulation layer [61, 146, 147, 158, 159, 163]. It happens through creating H-related levels that donate electrons to the conduction band. The increase of conductivity proceeds much faster on the O-terminated surface than on the Zn one [163].

After the initial studies in 70-80s [162, 163], the origin of the accumulation/depletion zone has been quite intensively revised in the last 10 years, through photoemission [61, 139, 146, 147, 153, 159, 167, 168]. The accumulation layer seems to also appear on native crystals without special surface preparation [139]. In the work of Piper *et al.* [146], ZnO(000$\bar{1}$)-O was found (i) metallic with an accumulation layer of 2×10^{13} cm^{-2},

[4] Cleavage is not ideal, since fragments are present on the surface and sublimate during the first annealing irreversibly changing surface electronic properties [160, 162, 163].

as determined from the parabolic dispersion at the Fermi level and (ii) (1×1)-stabilized by a moderate hydrogen coverage even after intense sputtering/annealing cycles. Upon hydrogen exposure ZnO$(000\bar{1})$-O, Ozawa and co-workers [61, 147, 159] highlighted a metallization of all the polar faces of ZnO [61]. Same observations were made for the ZnO$(10\bar{1}0)$-M face after water and methanol exposure [147, 159]. This goes along with: (i) the appearance of a single free-electron-like metallic band just below the Fermi level with a Zn $4s$ character that disperses quadratically with $k_{\|}$ and (ii) the characteristic hydroxyl fingerprint in the O $2s$ core level. The donated and accumulated concentrations are in the range of $10^{12} - 10^{13}$ cm^{-2}. At the opposite, ZnO(0001)-Zn surface does not develop an accumulation zone, nor a sizeable variation of its work function or a clear state at the Fermi level – this fact was assigned to the specific etching of this surface by atomic H [61, 132, 133] (see section 2.3.2 and Fig. 2.29). UHV cleaved O-terminated surface shows flat bands, while the Zn-orientation bands are bent upwards [167]. But these latter have band gap-related defects and are know to contain easily desorbing fragments [179], and therefore, to evolve during the first heating [162, 163]. Heinhold *et al.* [153, 167, 168] used X-ray valence band photoemission to study the correlation between band bending, hydroxylation and thermal treatment on all the ZnO surfaces starting with as-loaded surfaces: polar ZnO(0001)-Zn and ZnO$(000\bar{1})$-O [153, 167] and non-polar ZnO$(10\bar{1}0)$-M and ZnO$(11\bar{2}0)$-A [168]. The band bending could be cycled reversibly on the O-,M- and A- surfaces by heating (1050 K, dosing H_2O or H, or vacuum-rehydroxylation). It was correlated to the OH coverage of the surface seen from O $1s$ peak decomposition, and a depleted surface could be prepared by vacuum annealing. The transition was observed at an OH coverage of 0.9 ML on the O-terminated surface. The Zn-surface was more resilient to heating keeping its upward band bending. However, these studies were performed on as-loaded samples cleaned with atomic O to remove carbon contamination, but with inherent polishing damage and poor LEED patterns.

Unfortunately, in most experiments, the absolute band bending was derived indirectly from the knowledge of the position of the Fermi level relative to the valence band through the bulk carrier concentration that may change upon sputtering/annealing cycles, or through the estimated accumulated charge [61, 139, 146, 147, 153, 159, 160, 167, 168]. No direct measurement was performed (see section 2.4). Finally, the assignment of the origin of the observed changes of the work function, band bending and conductivity is not settled, although there is an compelling correlation with the surface hydroxylation. Surface states [60, 180], donor characters of surface hydroxyl groups [61, 139, 146, 147, 153, 159, 164, 167, 168], hydrogen diffusion in the subsurface, subsurface defects diffusion [160, 163] have been all invoked. As in the case of the polarity healing (see section 2.1.1), these changes are somehow due to the variability of surface preparation (cleavage [162, 163, 167], sputtering/annealing [60, 61, 146, 147, 159], as-loaded state and thermal treatments [153, 168]) and surface hydroxylation.

2.1.4 Metals on ZnO and their electrical contact

2.1.4.1 Basics of electrical contact at metal-semiconductor interface

The general concepts of the band alignment and electrical contact at the metal/semiconductor interface can be found in numerous textbooks [3, 181, 182] and reviews [183, 184, 185, 186]. They are the heart of the rectifying behaviour in diodes. Only key points and definitions will be reminded here.

Ideal contact

Fig. 2.9 shows the ideal energy (band) diagram of the contact between a metal and an n-type semiconductor. (The case of p-type is reversed and holes replace electrons in the reasoning.) When the metal and the semiconductor are put in contact, the free electrons are transferred between them due to the work function difference. If the metal work function Φ_m is higher than that of the semiconductor Φ_s ($\Phi_m > \Phi_s$, Fig. 2.9-left), the electrons flow from the semiconductor to the metal. The electron transfer continues until the Fermi levels of the metal $E_{F,m}$ and semiconductor $E_{F,s}$ are aligned. Under equilibrium, a Helmholtz double layer is established at the interface, where the metal is negatively charged and the semiconductor is positively charged near the interface due to electrostatic induction. Because of the low concentration of free charge carriers n in the semiconductor, the induced electric field cannot be efficiently screened; the so-called Debye length $L_D \sim \sqrt{n}$ over which the screening happens is orders of magnitude higher than that in the metal (which is around a fraction of Å, as given by the Thomas-Fermi length). This causes the free charge carrier concentration near the semiconductor surface to be depleted compared with the bulk. This region is called the space charge region. In the n-type semiconductor, when $\Phi_m > \Phi_s$, electrons are depleted in

the space charge region (thus called depletion layer) which is characterized by excess positive charges due to ionized donors. When $\Phi_m < \Phi_s$ (Fig. 2.9-right), the electrons are accumulated in the space charge region due to the electron transfer from the metal to the semiconductor, and this region is called the accumulation layer. In general, when the Fermi level of the metal is below that of the semiconductor, charge flows to the metal causing the semiconductor Fermi level to decrease, and *vice versa*. It should be mentioned that the amount of surface charge is equal to the integral of the charge in the semiconductor taken with an opposite sign.

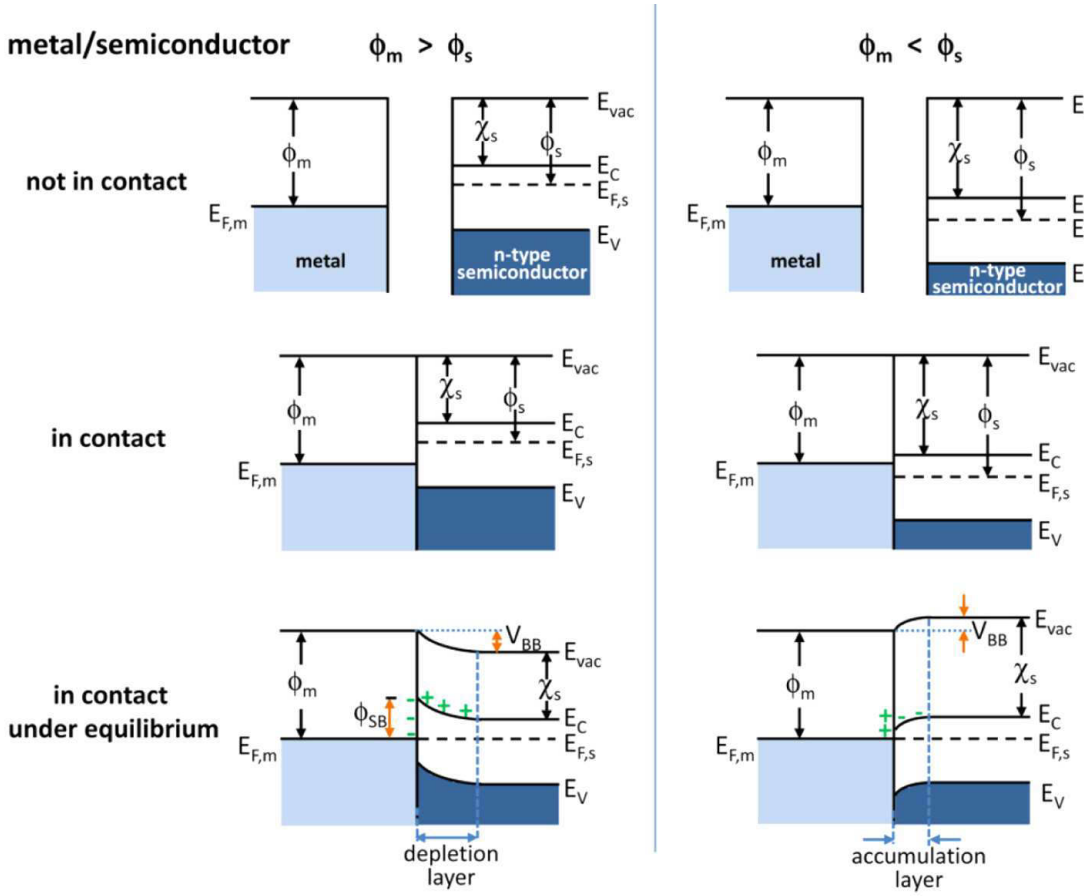

Figure 2.9: Schematic band diagrams of the metal and n-type semi-conductor contact: E_{vac} is the vacuum level, E_c is the energy of the conduction band minimum, E_v is the energy of the valence band maximum, Φ_m is the metal work function, Φ_s is the semi-conductor work function, χ_s is the electron affinity of the semiconductor, V_{bb} is the band bending, E_F is the Fermi level, ϕ_{SB} is the Schottky barrier [186].

In the space charge region, the band edges in the semiconductor are continuously shifted by the electric field between the semiconductor and the metal due to the charge transfer. This phenomenon is called band bending. The energy bands bend upwards towards the interface, when $\Phi_m > \Phi_s$, and downwards towards the interface, when $\Phi_m < \Phi_s$. As the electron in the semiconductor experiences repulsion from the negatively charged Helmholtz layer located in the metal, its potential energy rises and the bands bend upwards, and *vice versa*. Not only valence or conduction band, but also but also deeper levels are affected by the band banding, as the electric field is macroscopic. From Fig. 2.9, compared with the bulk, the degree of bending in the semiconductor equals the work function difference between metal and semiconductor, $V_{bb} = |\Phi_m - \Phi_s|$. When $\Phi_m > \Phi_s$ in an n-type semiconductor, there is also a energy barrier formed at the metal-semiconductor interface between the Fermi level and the bottom of the conduction band. It is called the Schottky barrier and is given by $\phi_{SB} = \Phi_m - \chi_s$, where χ_s is the electron affinity of the semiconductor (ideal Schottky-Mott contact). When $\Phi_m < \Phi_s$ in an n-type semiconductor, there is no Schottky barrier and the metal-semiconductor contact is ohmic.

For this ideal Schottky contact [181, 182, 3] (or Schottky-Mott limit), the potential $\Phi(z)$ within the semiconductor can be obtained as the solution of the Poisson equation along the perpendicular direction: $\nabla^2\Phi(z) + \rho(z)/\epsilon(0) = 0$, where $\rho(z)$ is the charge density in the surface space region and $\epsilon(0)$ the static dielectric function of the semiconductor. This equation is self-consistent, as $\rho(z)$ depends on the local potential $\Phi(z)$ [3, 182]. Using the abrupt approximation for $kT \ll V_{bb}$, $\rho = eN_d$ is given by the bulk concentration of ionized impurities with the space charge region for $z < W$ and $d\Phi/dz = 0$ for $z > W$. The analytic result is given by a parabolic dependence:

$$\Phi(z) = \Phi_0 + V_{bb}\left(1 - \frac{z^2}{W^2}\right) \quad \text{for} \quad z < W \quad \text{and} \quad \Phi(z) = \Phi_0 \quad \text{for} \quad z > W, \tag{2.1}$$

where $W = \sqrt{2\epsilon(0)V_{bb}/eN_d}$ and V_{bb} is the band bending. The application of a voltage across the interface gives rise to an asymmetric flow of current which is called the rectifying behaviour in diodes [181]. The corresponding I-V characteristic is of thermoionic type; it depends on the Schottky barrier, polarization and temperature.

Actual Schottky contact

The concepts developed for a metal/semiconductor interface, in particular that of band bending, can be applied to the surface states (intrinsic ones or those derived from surface defects) that are present at a free surface (Fig. 2.10a). Adsorbates can also play the role of metal [186]. Upward or downward band bending can occur depending on their donor or acceptor character, *i.e.* their relative position with respect to the Fermi level in the bulk. Usually, the density of surface states is large (10^{15} cm^{-2}) compared to the equivalent bulk dopant density in regions parallel to the surface ($10^8 - 10^{12}$ cm^{-2}). Therefore, the Fermi level of the semiconductor is almost independent of the bulk dopant concentration and is "pinned" by the surface states (the so-called Fermi level pinning).

In fact, the actual Schottky barrier [3, 182, 183] can be influenced by:

- intrinsic surface states present at the free surface before contact;
- states produced after contact, the wavefunction of which tails into to the semiconductor band gap (the so-called Metal Induced Gap States (MIGS));
- extrinsic surface states due to imperfections;
- interface-specific states due to interfacial reactions.

If the density of these surface states is large, the contact with the metal does not alter the surface Fermi position and thereby the band bending V_{bb} does not notably change (Bardeen limit). As depicted in Fig. 2.10b, most of the contact potential difference $\Phi_m - \Phi_s$ falls across a thin dipole region at the interface. Charge transfer occurs primarily due to the high density of surface states rather than from the surface charge region of the semiconductor. Instead of $\phi_{SB} = \Phi_m - \chi_s$, the barrier height is then given by: $\phi_{SB} = V_{bb} + E_C - E_F = \Phi_m - \chi_s - \Delta\chi$, where $\Delta\chi$ depends on the position of the surface states in the band gap. The dipole region is assumed to be thin enough, so that charges tunnel freely between the metal and the semiconductor. Due to charge neutrality, the charge Q_m per unit area on the metal side is balanced by the charge density $Q_s = Q_{is} + Q_{sc}$ in interface states and in the space charge layer in the semiconductor. Large band bending may induce a very narrow accumulation layer which traps a degenerated electron gas with a high surface electron density. The states of this 2D electron gas are quantified along the perpendicular direction into subbands. This phenomenon is known to happen on ZnO surface upon hydrogen exposure (as discussed in Section 2.1.3).

Methods to determine Schottky barrier height are mostly based on electrical measurements, such as current-voltage and capacitance techniques [3, 183, 184] or on photoabsorption (the so-called internal photoemission). Band bending, barrier height and work function changes upon adsorption [5] can be also estimated directly though photoemission, as done in this work. The question of band bending and electrical contact at the metal/semi-conductor interface has profound implications in the transport of all type of charges, not only electrons and holes, but also ions [6] (see Chapter 4), and in (photo)chemistry and catalysis [186].

[5] Kelvin probe and even microscopy are also used.

[6] The Cabrera-Mott model of oxidation is a good example of electric field driven diffusion of ions [187]

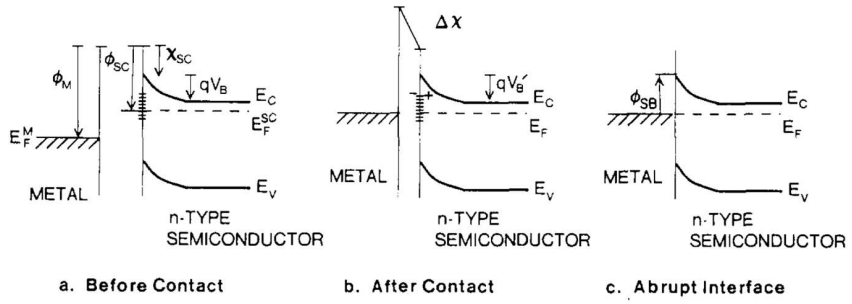

Figure 2.10: Schematic band diagram of a metal and a semiconductor with a high density of surface states: (a) before contact, (b) after contact, (c) after an ideal contact [183].

2.1.4.2 Metal on polar ZnO surfaces: from growth mode to electronic properties

Surface science studies of the epitaxy, morphology, charge transfer and electronic properties of metal deposits on the polar surfaces of ZnO are scarce, compared for instance to the TiO_2(110) surface reviewed by U. Diebold [188]. The only exception is Cu which drew a lot of attention because of the massive use of Cu-ZnO-supported catalysts for the synthesis of methanol [52]. The reason of this scarcity probably lies in the complex interplay between metal and polarity healing and the difficulty of routinely imaging the surface by near-field microscopy due to surface conductivity [189]. Theory often assumes an interface with a uncompensated surface leading to very strong adsorption [7]. But the often used vapour deposition requires the pre-existing healed surface, the nature of which remains under debates (see section 2.1.1). Besides the alkali metals, two metal categories can be defined: (i) noble metals (Cu, Ag, Au) and (ii) more reactive ones (Ti, Fe, Cr, Co, Ni) with the intermediate cases of Pt and Pd. All the below mentioned studies involved surface preparation by sputtering-annealing cycles similar to those employed in the present work.

Noble metals

Regarding epitaxial relationship at metal/ZnO(0001) surfaces, the hexagon/hexagon orientation corresponding to $M(111)[1\bar{1}0] \parallel ZnO(0001)[10\bar{1}0]$ was systematically observed by grazing incidence diffraction or electron diffraction (LEED, TEM): Au [190] (misfit -11%), Cu [174, 191, 192] (misfit -21%), Ag [193, 194] (misfit -11%), Pd [195] (misfit -15%), Pt [196, 197] (misfit -14%). In the case of silver, the preference over the 30° rotated epitaxy having a lower lattice mismatch (-3% compared to -11%, see section 2.2.3) was assigned to a nearly perfect coincidence between 8 unit cells of ZnO and 9 of Ag. The metal appears strained-free [192, 193, 194]. But, the rotated epitaxy $Ag(111)[1\bar{1}0] \parallel ZnO(0001)[21\bar{3}0]$ is prevailing at the interface between ZnO platelet-precipitates obtained by oxidizing ZnAg alloys [198]; these interfaces are expected to be close to thermodynamic equilibrium, really stabilized by polarity and show arrays of misfit dislocations. As shown in Section 2.2.3, steps edges on surfaces seems to play an important role in this hexagon/hexagon surprising generic orientation of metals.

The first experiments performed in the Campbell's group [174, 175, 191, 199, 200] on Cu/ZnO(0001) combined photoemission, LEED and Low-Energy Ion Scattering (LEIS), a technique highly sensitive to the surface coverage. A 2D growth which is at odd with the thermodynamics expectations [201] was observed in the submonolayer regime. The critical coverage for the nucleation of the second layer in the islands was found to be poorly temperature- (between 100 and 450 K) and flux- dependent, with a value around 0.3 ML for ZnO(0001)-Zn and 0.6 ML on $ZnO(000\bar{1})$-O. This pseudo layer-by-layer growth also concerns Pt and Pd to some extent and was tentatively explained by a kinetic model [174, 200, 201] involving upstepping and downstepping barriers at the cluster edge.

On the ZnO(0001)-Zn surface, Scanning Tunnelling Microscopy pointed at a preferential nucleation along step edges especially at the apexes of the triangular holes/pits [94, 202], although it may depend on surface preparation [203] and the ageing in vacuum [70]. The critical coverage of the transition from 2D to 3D clusters as determined by LEIS is also questioned by STM observations which pointed at 2D clusters only at very low coverages [203, 204]. On $ZnO(10\bar{1}0)$-M [70, 205], only step edges along [0001] direction, *i.e.* polar steps made of only Zn and O atoms, are decorated by 3D clusters. After ageing, nucleation on terraces is also observed. As seen by grazing incidence small-angle scattering for Ag [193, 194] or STM (Ag [206],

[7] Metal adsorption is a known mechanism of polarity healing [54, 55]

Cu [202], Au [205]), growth of thicker films proceeds through the formation of nearly percolated flat on top (111) particles covering a large fraction of the surface. A better Ag wetting was found on the O-termination face compared to the Zn-one [193, 194]. Cu clusters seen by STM appear more 2D on ZnO(000$\bar{1}$)-O than on ZnO(0001)-Zn [203, 204]

After an initial coarsening, heating of Cu below 400 K seems to induce a wetting enhancement [94] at the opposite to the usual sintering observed for all metal/oxide interfaces [201]. Migration of ZnO subsurface defects (in particular, positively charged O vacancies) due to the space charge layer induced by the charge transfer between Cu and ZnO was invoked [94]. Annealing of copper films above 570 K leads to a partial entrenching of the particles and the decrease of the apparent coverage [202, 205, 207]; this island thickening may also explain the decrease of LEIS signal with temperature [174, 199]. Based on photoemission, the formation of a actual alloy with copper in this regime was excluded [94, 208]. In parallel, an inwards diffusion of individual Cu atoms leading to shallow donors was seen through the broadening of the quasi-elastic peak in HREELS and confirmed by *ab initio* calculations [109].

At tiny coverages, cationic Cu is detected by ultra-violet photoemission on ZnO(0001), but its adsorption becomes rapidly neutral [174, 175, 200]. A downward band bending is also observed.

Reactive metals

As shown by photoelectron spectroscopy, room temperature deposition of transition metals gives rise to a good metal wetting and to complex band bending due to a partial interface reaction: Ti [209], Cr [210, 211], Fe [212], Co [213], Ni [176]. Further annealing of the film in a temperature range above 700 K give rise to sintering, reduction of ZnO, appearance of metallic Zn, interdiffusion and formation of a new interfacial compound, often assigned to spinel (see Chapter 4) but without very clear structural proofs. Metallic zinc Auger fingerprint was also found during Pt deposition on both Zn- and O- terminated surfaces and assigned to a partial reduction [214].

2.1.4.3 Electrical contact and Schottky barrier at metal/ZnO interfaces: a review

The question of electrical contact at metal/ZnO interface was extensively reviewed by Ozgur [95], Monakhov [103] and Brillson [102, 129]. It was revived by the potential or actual use of ZnO in wide band gap optoelectronics and microelectronics. The need to switch in a reliable way from ohmic to Schottky contact in many devices (blue diodes and lasers, high mobility transistors, UV photodetectors, spintronic devices) pushes forward the understanding of the electric contact at this interface. For instance, the technology of silver film used in low-emissive coatings could replace Indium Tin Oxide (ITO) films in transparent electronics or Organic Light Emitting Diodes (OLEDs). But this requires mastering the Ag/ZnO contact. The control of the barrier height at metal/ZnO still represents a considerable challenge and is far from being fully rationalized [8]. It does not obey the ideal contact descriprion that is dominated by the affinity of the oxide and the work function of the metal (see section 2.1.4.1 and Fig. 2.11). This indicates the important role played by interfacial states. For instance, in case of the unreactive Au metal, the barrier height ϕ_{SB} can go from 0.4 to 1 eV showing the sensitivity to extrinsic factors such a surface preparation and film growth.

A wide range of Schottky barriers has been observed for metals on ZnO (see Tables I and II in Ref. [102] which summarize all the values accessible in the literature, or Fig. 2.11) depending on:

- the nature of bulk defects and the growth method of ZnO crystals, in particular the H content; annealing changes the characteristics of diodes through defect diffusion/ionization [215];
- the surface preparation, in particular the removal of carbon contamination, and its morphology prior to metal deposition [102];
- the surface orientation [216]; ohmic contacts are sometimes observed on air-exposed ZnO(000$\bar{1}$)-O, and therefore, hydroxylated surfaces and have been associated with an accumulation layer induced by OH adsorbates [217, 218]; ZnO(0001)-Zn yields to higher barriers; H plasma treatment allows to switch from Schottky to ohmic contact by creating an accumulation layer [219];
- the reactivity and oxidation state of the metal; the performance of diodes is different if the silver is oxidized or not [220]; intentional formation of low resistance ohmic contacts requires the deposition of reactive elements such as Ti or Al and interface alloying;
- lateral inhomogeneities of barriers that impact C-V and I-V measurements [103].

[8] The extensive review of Brillson [102] remains quite descriptive.

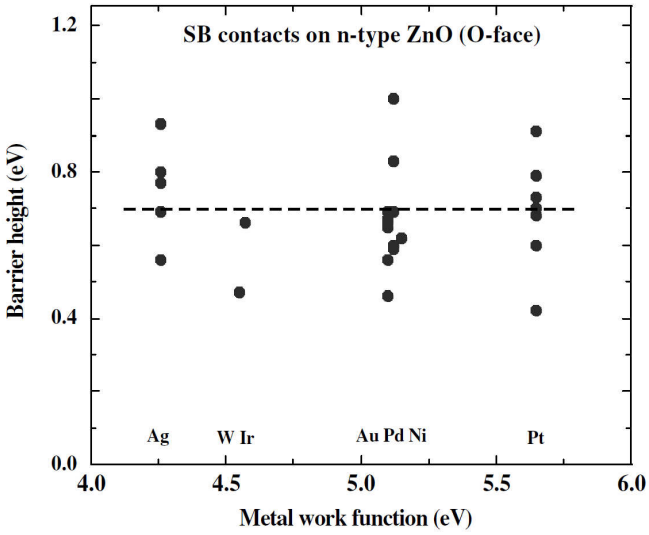

Figure 2.11: Compilation of Schottky barriers height on ZnO($000\bar{1}$) as a function of metal work function [103].

These fluctuations are not surprising, since (i) adsorbates easily alter the band bending and the surface conductive channel (see section 2.1.3) by transferring charges in a similar way as metals or the electric field applied to a gate of a transistor, (ii) a variety of defects act as dopants in ZnO [95, 96, 97, 98, 99, 100, 129], and (iii) surface preparation (if any) before diode formation on single crystals is not fully controlled (solvent cleaning, plasma exposure, annealing, etc.). There is a considerable evidence for suggesting that the Schottky barrier height depends heavily on density of native point defects in the crystal subsurface prior to interface formation [129] (see Section 2.3.6-2.4). Indeed, the ideality factor obtained from current/voltage measurements of diodes is typically above one implying that a pure thermoionic description of the current transport is not valid and that defects and/or tunnelling are involved [102, 103, 129]. As a rule of thumb, the contact at the metal/ZnO interface is driven by the heat of formation of the metal oxide relative to that of ZnO. Unreactive metals show I-V rectifying behaviour with barrier heights around 0.75 eV [129] (Fig. 2.11), while reactive ones form ohmic contacts. The Ag/ZnO interface presents most of the time a Schottky contact with an on-off ratio of 10^8, a barrier between 0.7 and 1.1 eV, and an ideality factor >1 [102, 215, 221, 222]. These observations match known expectations; as a noble metal, silver has a poor reactivity with ZnO and forms a Schottky barrier but the contact is still not ideal (see section 2.3.6).

Based on literature, Brillson [102] concluded that, in order to achieve a controllable Schottky barrier, one requires at minimum:

- high quality single crystals with low defect and impurity content;
- surface preparation that removes chemical contamination, such as hydroxides and hydrocarbons without creating surface roughness beyond the monolayer level,
- contact formation by metal deposition that does not introduce additional contamination and reaction,
- any subsequent thermal processing kept below temperatures at which reaction and diffusion occur.

All these requirements have been fulfilled in the present work.

2.1.5 Conclusions and goals

This chapter aims to revisit the interplay between polarity, hydrogen and electrical contact between Ag and the polar faces of ZnO. This question was never tackled in-depth in the literature, since it touches communities with different fields of interest. Also, the extreme surface in the studies on Schottky contacts is far from being fully mastered [102]. In the present study, state-of-the-art ultra-high vacuum and surface science techniques were employed to:

- prepare atomically smooth surfaces free of impurities, with an apparent low levels of hydrogen;
- grow silver thin film with a controlled epitaxy;

- characterize the changes of work function, band bending and Schottky barrier upon metal deposition as a function of orientation and hydrogenation.

One of the original points of this work is the combined use of UPS and HAXPES to measure the band alignment at the interface. We also aimed to switch from Schottky to an ohmic contact by using the accumulation layer created by hydrogenation of the surface, as it is done by doping the surface in the semiconductor industry [3, 183, 184].

2.2 Ag thin film growth on ZnO basal surfaces

2.2.1 ZnO surface preparation and its topography

As stated in the introduction part, the electrical contact at metal/zinc oxide interface is highly sensitive to the surface orientation (polar herein), surface preparation, impurity levels, roughness and metal deposition method. To date, many ways were reported to prepare suitable "clean and atomically smooth ZnO surfaces": immersion and soaking in acids [217]; ultrasonic cleaning in simple organic solvents [220]; exposure to oxygen (20%)-helium (80%) remote plasma [217]; cleavage [162]; sputtering-annealing cycles [70]. Only this last preparation was intensively used in surface science studies, in particular those employing scanning probe techniques which showed atomically flat surfaces. This procedure was adopted in the present work although the resulting atomic structures and mechanism of charge compensation of the polar faces are still highly debated, in particular on the O-face. Beyond that, the nature of subsurface defects and their concentration due to sputtering/annealing have never been explored but can play an important role, for instance towards metal wetting [94].

The substrates were ZnO single crystals having an (0001) orientation within less than 0.5° and a RMS surface roughness below 0.3 nm. Crystal supplied by Tokyo Dempa, Japan were grown by hydrothermal method with a special care on the level of impurities in particular Li coming from salts in the saturated growth solution, leading to high resistivity samples in the range of 0.05-50 Ω.cm [103, 223]. However, conductivity was enough to observe no sizeable charging effects in photoemission after *in situ* preparations. For instance, the absolute binding energy of Zn $2p_{3/2}$ core level was found at the same value of 1022.75 ± 0.05 eV with the laboratory Al Kα source ($h\nu = 1486.6$ eV) and a synchrotron photon energy of $h\nu = 2100$ eV on surface prepared in similar conditions; the two experiments differ by several orders of magnitude in terms of incident photon flux. Substrates were preheated by the supplier at temperature above 1400 K for several hours to improve crystallinity and reduced the level of hydrogen. At the opposite to earlier experiments with a crystal provided by Mateck-Gmbh, the Tokyo Dempa substrates desorbed much less hydrogen upon thermal annealing. Thermal desorption experiments [224] showed no significant H_2 signal up to 950 K at the opposite of Ref. [114].

Surface preparation and *in situ* characterization were performed in the ultra-high vacuum chamber shown in Fig. 1.1. Several cycles (above at least 5 and up to 40) of sputtering-annealing were required to achieve a surface with a sharp (1×1) LEED pattern [9] and free of any contaminant at the level of detection of photoemission (a few % of ML for surface species or a few at.% for bulk impurities). Attention was focused on C, Ar, Ca, Na, K, Si, Ag and Li. Although annealing is supposed to enrich the subsurface in Li [103], our XPS quantification of this latter rules out only its massive presence (above the monolayer range) because of the very low ionization cross section of Li 1s core level. Sputtering was performed with 1 keV Ar^+ ions ($p_{Ar} = 2.10^{-5}$ mbar, $I_{sample} > 10\mu A$) during at least 30 min and followed by annealing during 20-25 min under ultra-high vacuum ($p < 1.5\,10^{-9}$ mbar) at temperatures around 1200-1400 K as measured by optical pyrometry on the back plate [10]. These temperatures are higher than in all other studies (800-1000 K except Ref. [89]) but turned out to be efficient to achieve a sharp LEED pattern. At variance to substrates from other suppliers, no sizeable desorption of hydrogen was observed with mass spectrometry.

ZnO surfaces doped with H was obtained by exposing an as-prepared surface during 2-5 min to a mixture of molecular and atomic hydrogen provided by a gas cracker in line of sight of the sample at a total pressure of $p_{H2} = 1.10^{-7}$ mbar. This latter consist of a heated Ir tube (power 63 W) in which pure H_2 is flowing; dissociative adsorption and desorption without recombination is favoured on this catalytic material leading

[9] Although bulk ZnO unit cell has only a 3-fold symmetry, the hexagonal 6-fold symmetry of LEED pattern is due to the existence of 60°-rotated domains between different terraces [87, 225].

[10] An important thermal gradient may exist across the sample.

to a fraction of dissociation in the range of 50% as estimated by the supplier. This allows to estimate the actual exposition of the surface to a few Langmuir of atomic hydrogen (1 Langmuir corresponds to exposure to 10^{-6} Torr during one second and leads roughly to the adsorption of one monolayer if the sticking coefficient is close to one). Since the cracking efficiency is unknown, the total exposure (21 L) will be given hereafter. Although the actual exposure to atomic H is difficult to compare from one reference to the other, according to the literature [61, 130] intensive bulk diffusion is unlikely. Some surfaces were also exposed to molecular water directly in the analysis chamber which hosts the photoemission set-up. An equivalent of 25 L was dosed on the surface at room temperature.

After the cleaning cycles, the chemical state of the Zn- and O-terminated ZnO substrates was investigated by means of laboratory XPS. A wide spectrum (Fig. 2.12) obtained with the Al-Kα source ($h\nu = 1486.6$ eV, normal emission) for the ZnO-Zn sample shows the following features:

- O 1s, Zn 3s, Zn 2p, Zn 3p, and Zn 3d core levels. Zn 2p, Zn 3p, and Zn 3d are doublet peaks due to spin-orbit splitting, but Zn 3p and Zn 3d are not resolved due to the natural line width of the X-ray source;
- Zn LMM (inset of Fig. 2.12) and O KVV Auger transitions.

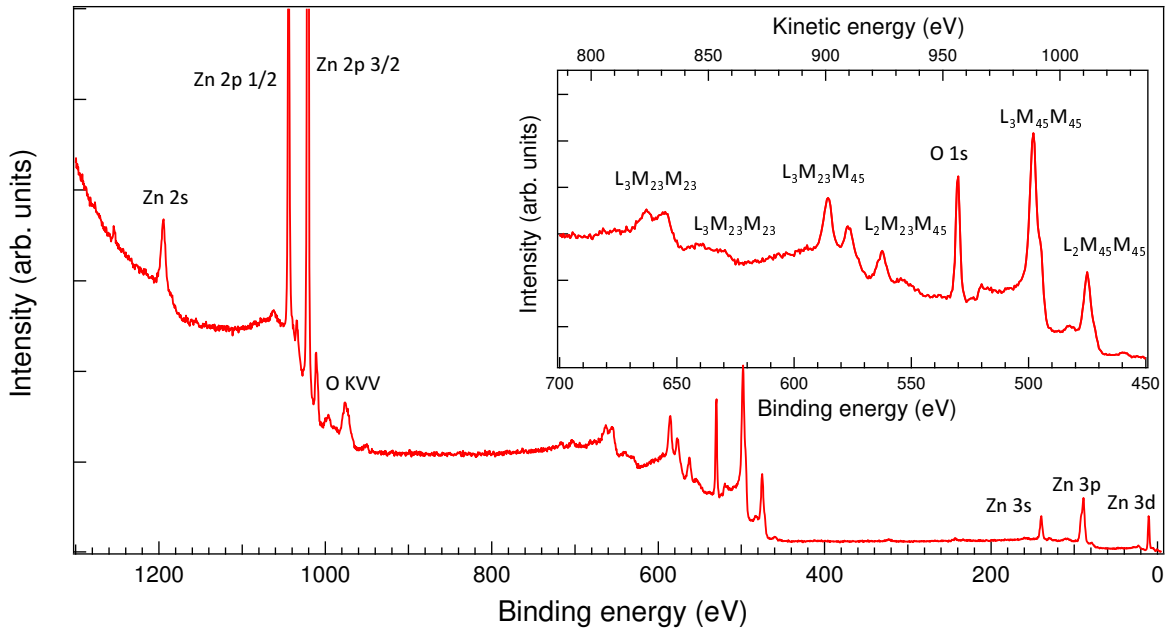

Figure 2.12: XPS spectrum (Al Kα, $h\nu = 1486.6$ eV; normal emission) of the ZnO-Zn sample. The inset shows the region of the ZMM Auger transition. Asides the core levels and Auger transitions from Zn and O, no impurities such as C, Ar, Ca, Na, K, Si are detected.

ZnO surface crystallinity and morphology were checked by LEED, RHEED and STM. All electron diffraction techniques (Fig. 2.13) showed (1×1) unreconstructed surface on both ZnO-Zn and ZnO-O surfaces with a good signal/noise ratio. Knowing the geometry of the set-up, this is confirmed by the determination of the surface lattice parameter (3.23 ± 0.16 Å) in close agreement with expectation of 3.23 Å [99].

The ZnO(0001)-Zn surface was imaged by scanning tunnelling microscopy (Figs. 2.14a,b). It consists in terraces of triangular shape, sizes of which are in between 10 and a few 100 nm separated by half-unit cell step (2.7 ± 0.1 Å) corresponding to half the unit call along the c-axis. This topography comes from the mechanism of polarity compensation through the formation of Zn vacancies in a reductive environment such as UHV [70]. As shown by counting in STM and numerical simulation, they provide exactly 1/4 of the charge required to stabilize the surface [70] (see section 2.1.1). The imaging of the ZnO$(000\bar{1})$-O surface turned out to be more difficult despite the very good surface crystallinity shown by electron diffraction techniques. The

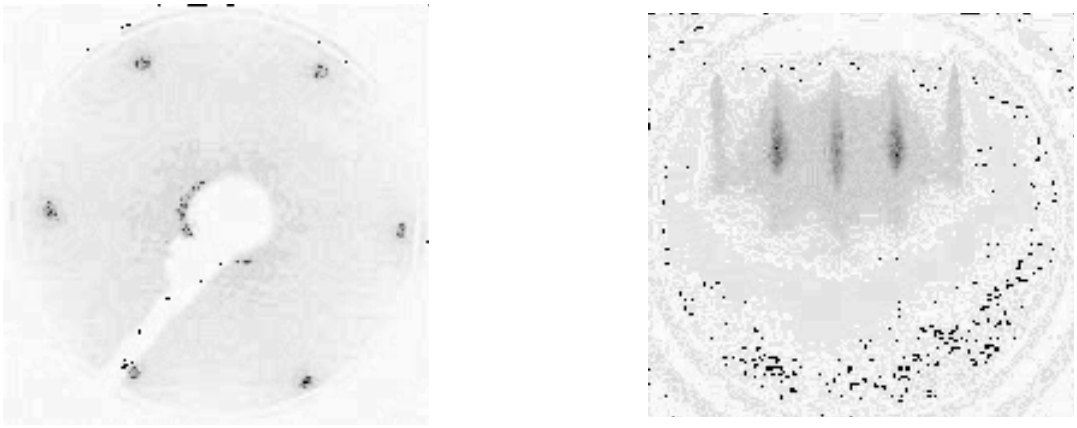

Figure 2.13: LEED pattern (beam energy 70 eV, left) and RHEED diagram (beam energy 7.5 keV) along $[1\bar{1}00]$ (right) of a clean ZnO(0001)-Zn surface after preparation.

surface is more heterogeneous with much smaller terraces and, at some places, puzzling patterns. Very few images have been published to date [70, 93]. The complexity of the theoretically predicted surface phase diagram, in passing controversial, as a function of temperature and chemical potential of oxygen and hydrogen renders the interpretation of the images quite difficult and beyond the scope of this work.

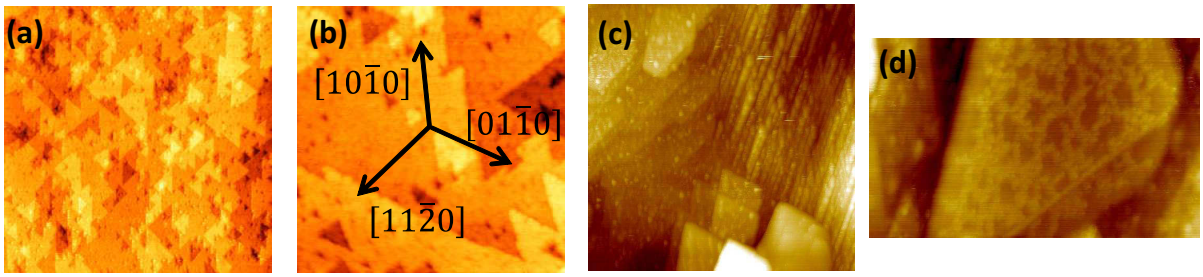

Figure 2.14: STM imaging (a,b) of the ZnO(0001)-Zn surface: (a) 800×800 nm^2, $U = 1.9$ V, $I_t = 10$ pA, (b) 200×200 nm^2, $U = 2.1$ V, $I_t = 200$ pA; (c,d) of the ZnO(0001)-O surface: (c) 150×150 nm^2, $U = 2.3$ V, $I_t = 200$ pA, (d) 60×33, $U = 2.3$ V, $I_t = 200$ pA.

2.2.2 Morphology, epitaxy and plasmonics of Ag films on ZnO

Ag thin films were grown by thermal evaporation (pressure $p \sim 5.10^{-10}$ mbar) on clean and atomically flat basal ZnO surfaces. Two types of samples were prepared:

- thin island Ag films having an equivalent thicknesses between 0.02 and a few nm to study the initial stages of the growth with XPS, UPS, LEED, RHEED, SDRS and STM.
- thicker films (around 12 nm) to protect from atmosphere the surface and study the band bending at the Ag/ZnO interface by synchrotron HAXPES measurements. Those films were deposited at low temperature (100 K) to kinetically favour the wetting and obtain earlier percolation than at room temperature. Film continuity was checked with laboratory photoemission; no Zn $2p$ signal could be detected showing the absence of holes. This thickness was chosen as a best compromise between percolation and sensitivity to substrate signal in HAXPES.

Films thicknesses have been calibrated *in situ* by a quartz microbalance and cross-checked with photoemission and *ex situ* X-Ray Reflectivity (XRR). Only during UPS measurements, film thickness was determined only through photoemission as the evaporator was directly mounted in the spectrometer chamber to avoid time-consuming transfers and sample repositioning. The chosen evaporation rates were between $0.0008 - 0.002$ nm/s and 0.03 nm/s for the thin and thick silver films respectively.

2.2.3 Atomic structure and epitaxy

The atomic structure and the epitaxy of the silver films was analysed *in situ* with electron diffraction technique (at 100 K and 300 K) and *ex situ* with X-ray diffraction on the thicker films.

The observed epitaxial plan is Ag(111)‖ZnO(0001) and corresponds to the preferred orientation observed in the industrial stacks. Two high symmetry orientations (in cubic notations) are expected for the in-plane directions. Either the dense row of silver is aligned along the $[10\bar{1}0]$ direction of ZnO *i.e.* (i) $Ag(111)_c[1\bar{1}0]_c$ ‖ $ZnO(0001)[10\bar{1}0]$, the so-called hexagon/hexagon epitaxy or is rotated by 30° *i.e.* (ii) $Ag(111)_c[1\bar{1}0]_c$ ‖ $ZnO(0001)[11\bar{2}0]$ [193, 194] (Fig. 2.15). Taking into account the lattice parameters of the surface unit cell of Ag(111) (in hexagonal notation: $a_{ZnO} = 3.25$ Å , $c_{ZnO} = 5.207$ Å , $a_{Ag,h} = 2.89$ Å , $c_{Ag,h} = 7.08$ Å), the lattice mismatch is -11% for the orientation (i) and +3% for the orientation (ii). Whatever the face, the film thickness or the temperature of growth and despite the apparent strong lattice mismatch, only the orientation (i) hexagon/hexagon was observed all along this study (in particular in LEED and RHEED and even at 100 K; Fig. 2.15), contrary to Refs. [193, 194] which pointed out the possible existence of orientation (ii) for poorly crystallized surfaces. The reason stems in the present preparation recipes which favour surface crystallinity.

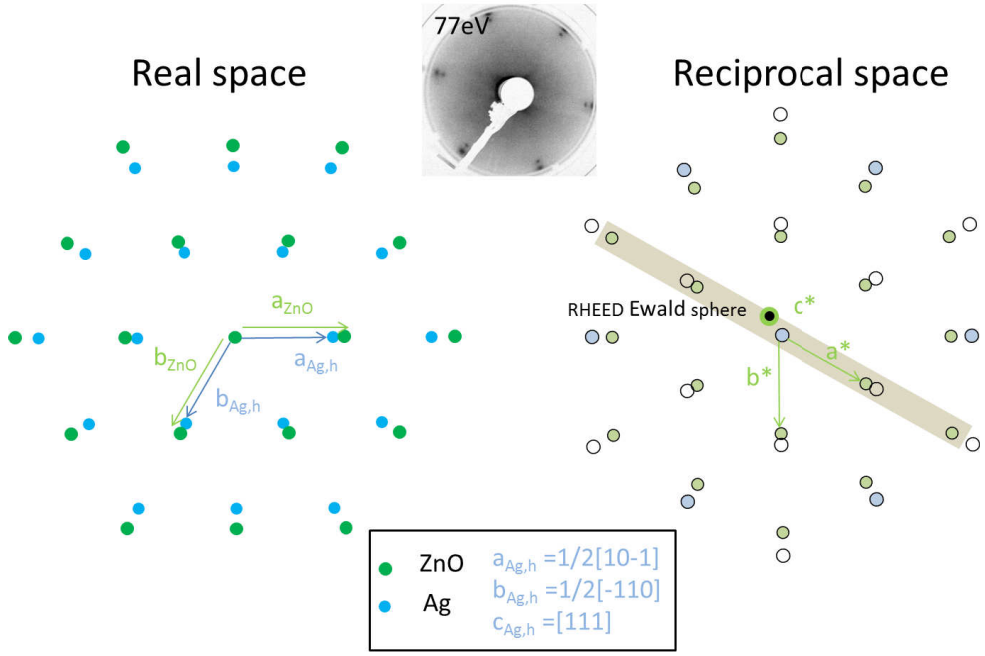

Figure 2.15: Scheme in the surface plane of the real space and reciprocal space (cut along the $l = 0$ plane) corresponding to the hexagon/hexagon epitaxy Ag(111)‖ZnO(0001)-Zn. On the left side, the LEED pattern for a 2.4 nm thick film of Ag on ZnO(0001)-Zn shows the 11% spot splitting of the hexagon/hexagon epitaxy. The shaded area corresponds to the portion of the Ewald sphere intercepted during the RHEED measurements.

In a coherent way with STM imaging and optical measurements (see below), the RHEED analysis (which probes the shaded area of reciprocal space shown in Fig. 2.15) confirms the 3D growth of silver in the hexagon/hexagon orientation with two variants rotated by 180° which correspond to the face-cubic-centred ABC and ACB stacking (Fig. 2.16-2.17). The RHEED pattern which is characteristics of a flat surface at the beginning of the growth goes through a spotty appearance in the middle of the deposition before sharpening again after film percolation. This latter was checked through photoemission which showed no detectable Zn $2p$ signals from the substrate at a film thickness of 12 nm.

However, the RHEED bulk Bragg peaks of Ag do not appear before a critical thickness around 0.16 nm (or 0.7 ML, the monolayer being defined as the atomic layer spacing along the [111] direction of silver). This signs the lack of ABC-ACB stacking of at least three monolayers; this finding agrees with the existence of a critical threshold for bidimensional growth of metals of the end of transition series on the polar faces of

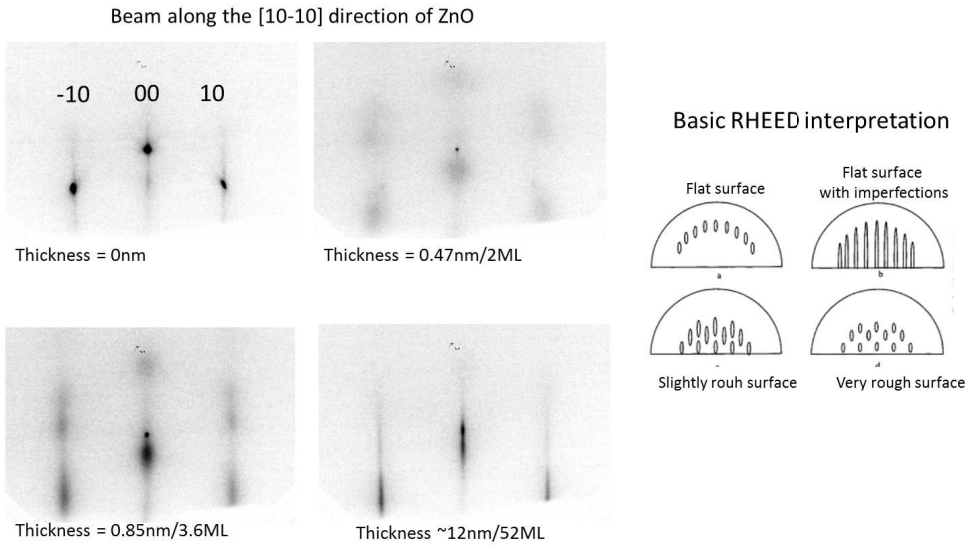

Figure 2.16: Sequence of RHEED patterns obtained during the growth of Ag on ZnO$(000\bar{1})$-O at 100 K. The electron beam of 7.5 keV is aligned along the $[10\bar{1}0]$ direction of ZnO. The right panel shows a schematic representation of the expected patterns for different surface roughness. The RHEED pattern of the bare surface is mainly made out of sharp rods drilling the Ewald sphere in out-of-plane positions as expected from a flat surface. The spotty pattern during silver growth is characteristic of transmission through 3D islands. Notice that the final positions of the Ag diffraction peaks are located at a lower l-value than those of ZnO.

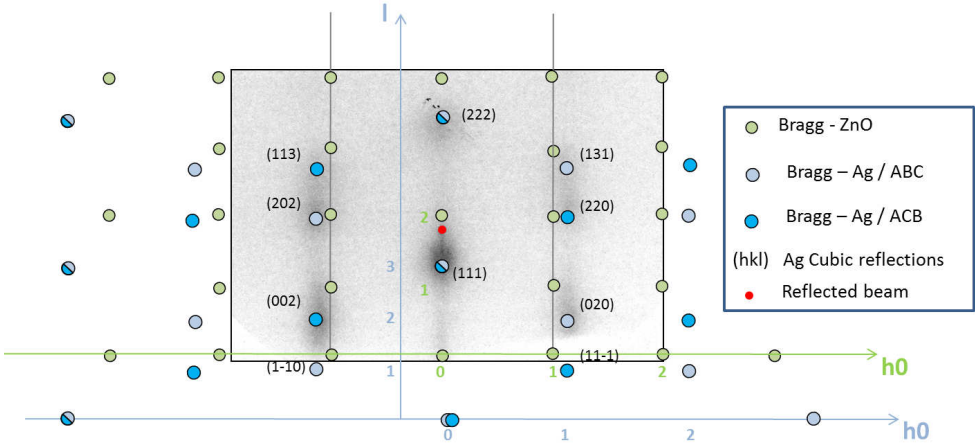

Figure 2.17: RHEED pattern extracted from the sequence of Fig. 2.16 at a film thickness of 0.5 nm (2.3 ML) superimposed with the bulk reciprocal space of Ag and ZnO. The two possible stacking variants ABC and ACB are highlighted. Notice the presence of only bulk Bragg peaks of silver which demonstrated a 3D growth. In the hexagonal surface unit cell, the ZnO bulk extinction conditions reads ($l = 2n + 1$ and $h - k = 3n$) while those of the two silver variants are ($h + 2k + l = 3n + 1$ and $2h + k + 2l = 3n' + 2$; $h + 2k + l = 3n + 2$ and $2h + k + 2l = 3n' + 1$), n, n' being relative integers.

ZnO [200]. This threshold parallels also the evolution of the in-plane lattice parameter of silver (Fig. 2.18a). The fit of RHEED intensity cuts demonstrates a contraction by $\sim 6\%$ of the metal lattice parameters at the first stages of the growth process. In a parallel way, the integrated intensity of the specular peak goes through a minimum at around 1 ML before recovering the initial intensity after 2-3 ML (Fig. 2.19a). The in-plane coherent domain sizes (Fig. 2.18b) deduced from the Full-Width at Half Maximum of Ag Bragg peaks ($L_{coh} = a_{ZnO}/\Delta h_{FWHM}$, see Sect. 1.2.3.3) increases from 1 nm to around 4 nm at the end of the growth. Assuming that the coherence length is mainly limited by particle size, the value determined by RHEED at the earliest stages of growth *i.e.* at a thickness below the monolayer agrees with the values found with near-field microscopy (1 nm at 100 K in RHEED *vs* 1.5 nm at 300 K in STM). The same coherent domain size along the perpendicular direction (Fig. 2.19b) ($L_{coh} = c_{ZnO}/\Delta l_{FWHM}$) confirms the formation of very flat clusters at the early beginning of the growth. In fact, it is possible to parallel the existence of this thickness threshold in RHEED with the nucleation of clusters along the step edges and the change of work function as seen by UPS (see below).

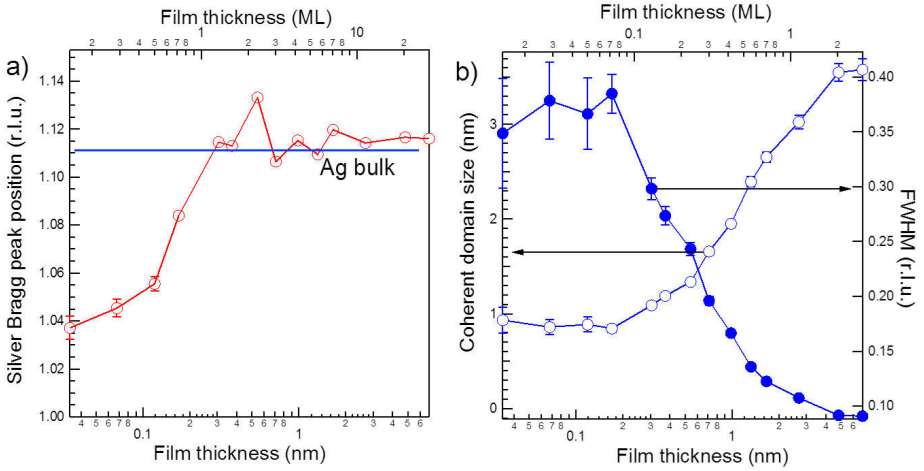

Figure 2.18: (a) Relative evolution of the in-plane lattice parameter of silver as deduced from the position of RHEED diffraction rod during Ag/ZnO(0001)-Zn deposition at 100 K. (b) Evolution of in-plane width of Ag Bragg peaks and of the size of the corresponding coherent domains. Here, r.l.u. stands for reciprocal lattice units, relative to ZnO (=1).

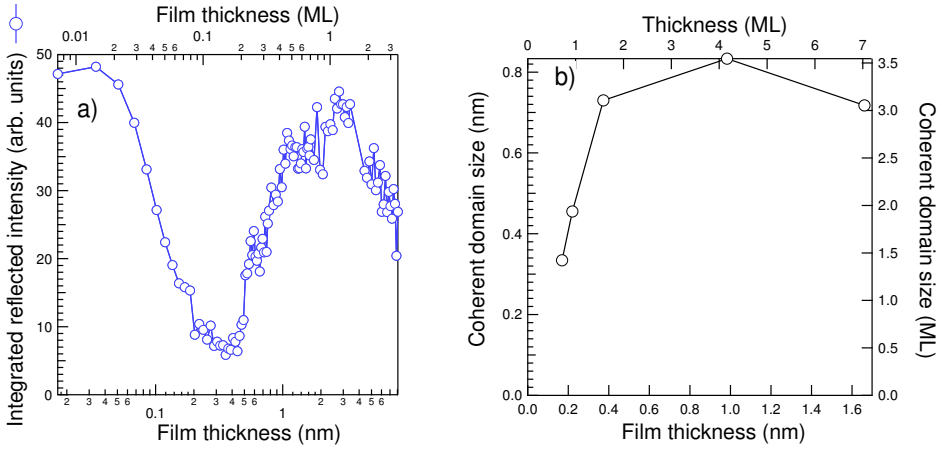

Figure 2.19: (a) Evolution of the integrated intensity of the RHEED reflected beam and (b) of the silver coherent domain sizes along the perpendicular direction as a function of the film thickness. Deposition at 100 K on ZnO(0001)-Zn. The reliability of analysis in Fig. (b) is limited only to low thicknesses.

To better understand the existence of such a counter-intuitive epitaxy in terms of lattice mismatch and lack of strain induced by the substrate above 1 ML, it was previously claimed that it was linked to the existence of a perfect coincidence between (9×9) bulk Ag unit cells on (8×8) ZnO ones [193, 194]. But, the early nucleated clusters are not large enough to develop such a coincidence and to favour the hexagon/hexagon epitaxy over the rotated one with a much lower lattice mismatch. Therefore to understand this behaviour which is similar to the case of copper, deposits have been performed on the ZnO$(10\bar{1}0)$ face which has a rectangular surface unit cell and shares the common $[10\bar{1}0]$ direction with the polar orientations. Silver deposits at room temperature have been analysed by LEED and showed a clear epitaxial relationship in particular after annealing (Fig. 2.20). The orientation which is $Ag(111)_c[1\bar{1}0]_c \parallel ZnO(10\bar{1}0)[0001]$ shares the alignment of the dense rows of silver with the direction $[10\bar{1}0]$ of ZnO. A likely explanation, which is confirmed by near-field microscopy, is that the initial nucleation and growth is driven by step edges. This is the case of polar faces (see below) but also on the ZnO$(10\bar{1}0)$-M as shows by the STM images of Fig. 9a extracted from the thesis I. Valenti [226] (Collaboration with University of Modena, Italy). Fig. 2.21a shows that particles are aligned only along the step edges of orientation [0001] as depicted in Fig. 2.21b. This alignment may be related to the polarity of the step edges themselves which are made out of only of type of atoms [54, 55, 70]. Similar preferential nucleation on only one type of step have already been observed in the case of Cu/ZnO$(10\bar{1}0)$ [70, 205].

Finally, thick films used in the HAXPES synchrotron measurements were also studied *ex situ* by XRD in the Bragg-Brentano $\theta-2\theta$ geometry. Similar observations were obtained on both ZnO terminations (Zn and O). All Ag films were found to have only one out-of-plane (111) orientation (Fig. 2.22a). All observed Ag diffraction peaks are modulated by the Kiessig fringes of the film due to its finite thickness and to interference on its parallel interfaces with air and ZnO substrate. These fringes demonstrate the low roughness of both interfaces as confirmed by AFM imaging of the surface (Fig. 2.22d). Pole figure diffraction measurement was performed in order to confirm the previously observed in-plane orientation. The pole figure of the Ag(002) reflection (Fig. 2.22c) shows clear peaks corresponding only to the hexagon/hexagon epitaxy [193, 194] without any measurable strain induced by the 11% misfit. Also, X-ray reflectivity as well as Electron Probe Micro-Analysis (EPMA) confirm the thickness of the film (Fig. 2.22b) calibrated by the quartz microbalance system. Surprisingly, Ag films deposited at 100 K were stable even after one month of exposure to the ambient atmosphere. AFM imaging shows that the surface has no pinholes (Fig. 2.22d is shown as an example).

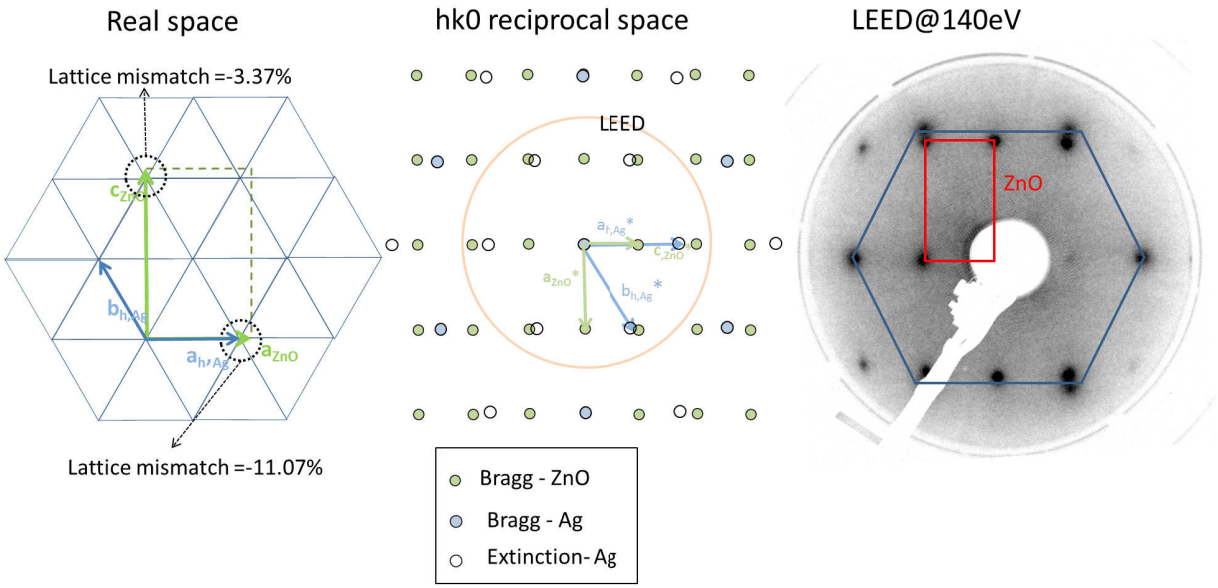

Figure 2.20: Same as Fig. 2.15 but on the ZnO$(10\bar{1}0)$-M face. The thickness of the film is 10 ML and it was annealed at 900 K to improve the visibility of the LEED pattern.

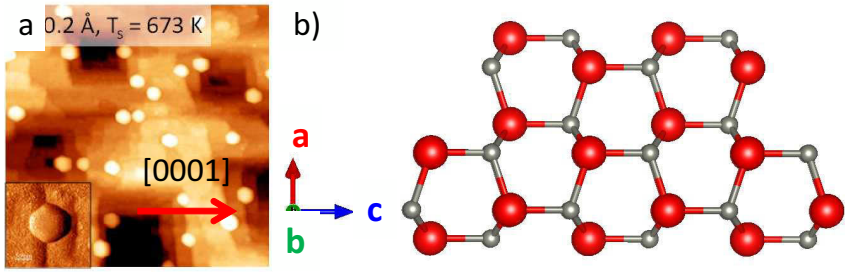

Figure 2.21: (a) STM image (100×100 nm) of a 0.1 ML of Ag/ZnO($10\bar{1}0$)-M after annealing at 673 K (From Ref. [226]. (b) Ball and stick models of the wurtzite structure along the [$01\bar{1}0$] axis.

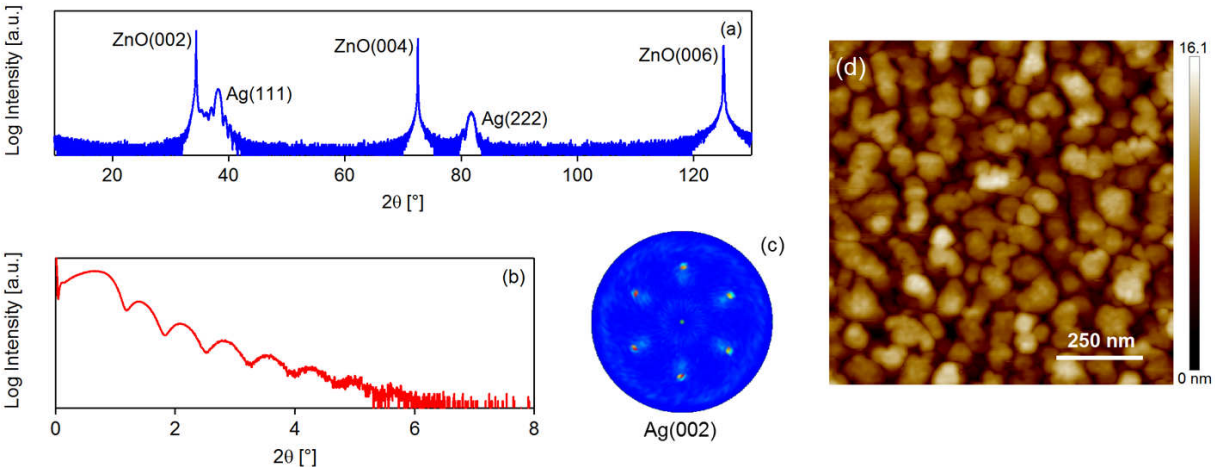

Figure 2.22: (a) Bragg-Brentano XRD, (b) X-ray reflectivity spectra, and (c) polar figure of the Ag (002) reflection obtained on a 12 nm of Ag/ZnO(0001)-Zn deposit done at 100 K. (d) AFM image of a 12 nm film of Ag deposited ZnO($000\bar{1}$)-O at 100 K. The image has been taken after a long ageing in ambient atmosphere. The root mean square roughness (2.4 nm) may be influenced by aging.

2.2.4 Film morphology as seen by STM

The question of film morphology was tackled by STM imaging for a few selected deposits which thicknesses were calibrated by photoemission. Due to tip tunnelling instabilities, only ZnO(0001)-Zn could be satisfactorily imaged (Fig. 2.23).

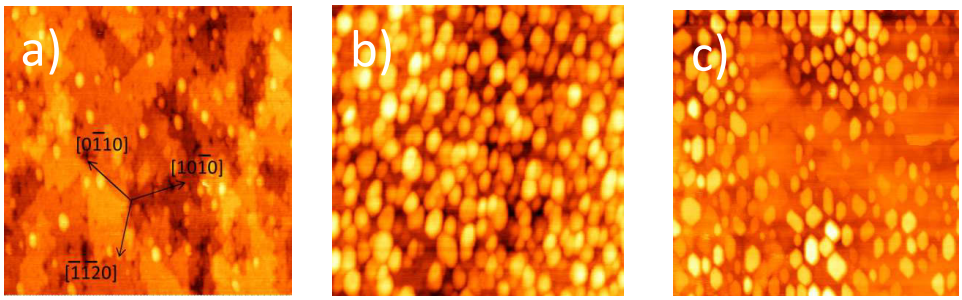

Figure 2.23: STM imaging of Ag deposits on ZnO(0001)-Zn face: (a) 0.02 ML (400×400 nm^2, 2.5 V, 30 pA), (b) 0.5 ML (200×200 nm^2, 2.2 V, 50 pA), (c) 1 ML (300×300 nm^2, -2.3 V, 200 pA).

At a coverage of 1 ML, the growth leads to flat top clusters with apparent size and height of the order of 25 ± 10 nm and 0.7 ± 0.1 nm; this later is very close to three silver atomic planes in agreement with the RHEED estimate (Fig. 2.19). The density of particles around $2.2\,10^{11}$ cm^{-2} is relatively lower than that obtained on wide band gap oxides such as alumina [227] ($10^{12}-10^{13}$ cm^{-2}). Their hexagonal shape matches the found Ag(111) orientation seen in diffraction. For a much lower coverage around 0.02 ML, the apparent size of the clusters is reduced down to 15.0 ± 3 nm for an apparent height relative to the substrate very close to one atomic layer. The clusters are found mainly close to step edges and their density is much lower than before $\sim\ 5.10^{10}$ cm^{-2}. The estimated thickness from STM findings matches that given by photoemission ($\sim$ 0.02 ML) if the lateral apparent size is corrected by a tip induced broadening of around $\sim$ 2 nm. The height close to one atomic plane is in line with the tendency of pseudo 2D growth seen by RHEED.

2.2.5 Film growth as determined by UV-visible spectroscopy

The dynamics of silver growth has been followed by UV-visible spectroscopy (1.5-5.5 eV), more precisely by Surface Differential Reflectivity Spectroscopy (SDRS) [228, 229]. The principle of the technique is to record the relative variation of the sample reflectivity while evaporating silver on the substrate. This spectroscopic technique is well-suited for metal deposit on dielectric substrates where the growth proceeds through 3D particles due the strong dielectric contrast between those materials. Typical spectra obtained on ZnO(0001)-Zn during the submonolayer deposition and above are shown in Fig. 2.24 in s and p-polarizations, *i.e.* with the electric field either perpendicular or parallel to the incident plane. In p-polarization, the dielectric behaviour of the film both parallel and perpendicular to the substrate is probed while only the parallel direction is excited in s-polarization. Similar spectra have been obtained on the O-terminated and hydrogenated surfaces. Spectra are characteristic of a 3D growth of particles; indeed, the incident electric field excite the so-called localized surface plasmon modes either parallel to the surface (feature that redshifts from 3 eV to below 1.5 eV in both polarizations) and perpendicular to it (feature around 4 eV only in p-polarization). To first order, those peaks correspond to the light absorptions associated to a vibrating damped dipole parallel and perpendicular to the surface [229, 49]. The location and intensity of such features are extremely sensitive to the morphology of the growing film [38] and, in particular to the particle aspect ratio [227, 48, 230, 36]. The excitonic nature of the band gap of ZnO lead to the feature around 3.2-3.3 eV [229]. It corresponds to a strong maximum of the abolute reflection coefficient of ZnO in p- and s-polarizations. When the incident plane was aligned along the [10$\bar{1}$0] or [21$\bar{3}$0] directions of the ZnO substrate, a clear anisotropy of the optical response was observed (not shown). It can be assigned to the preferential nucleation along steps but also to hexagonal platelet shape of the Ag(111) particles (see Fig. 2.23c).

As shown in Fig. 2.24a in the submonolayer regime, the plasmonic behaviour develops very rapidly since the early beginning of growth for the parallel dipole, and after 0.25-0.42 ML for the perpendicular one. This proves (i) the collective behaviour of the electron cloud and therefore the metallicity of the particles and (ii) the formation of clusters of less than 3 atomic layers below 0.25-0.42 ML, a minimal thickness which is required to develop a dipole along the perpendicular direction [231]. This observation of the formation of 2D clusters at the early stages of growth agrees with the RHEED technique, which gives somehow a larger

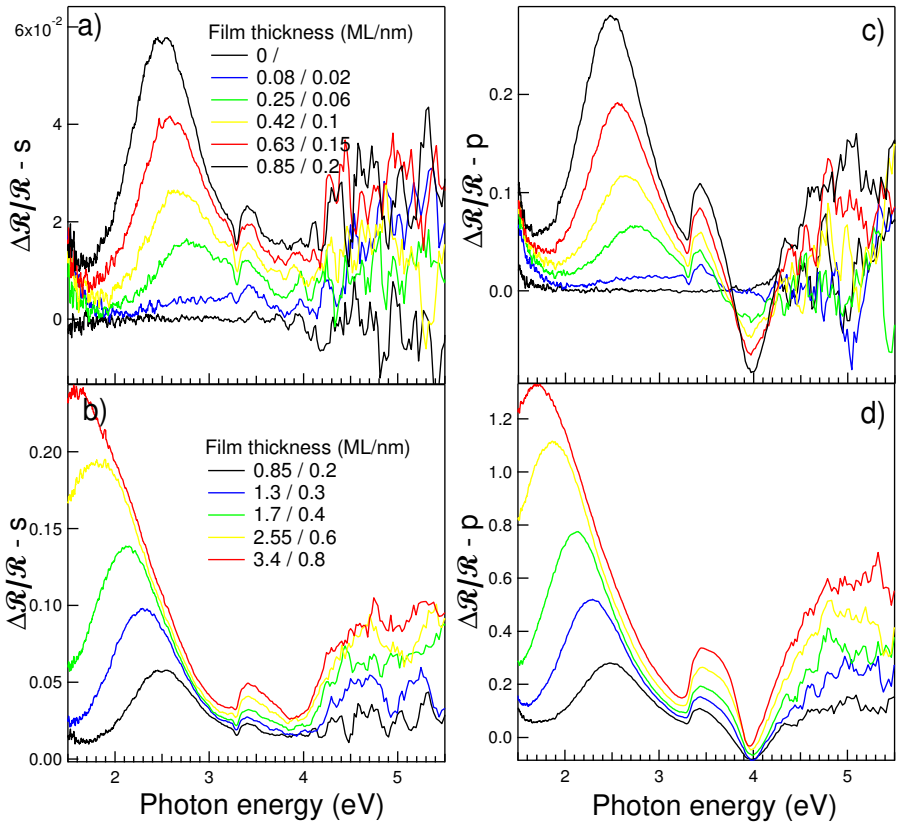

Figure 2.24: Evolution of SDRS spectra in (a,b) s- and (c,d) p-polarization during deposition of silver on ZnO(0001)-Zn at room temperature. Equivalent film thicknesses as calibrated by quartz microbalance are given in figures. The incident plane ($\Theta = 55°$) was aligned along the $[21\bar{3}0]$ direction of ZnO. Althoug plasmon resonances correspond to absorption (A), they appear as positive or negative peaks or dips; transmission (T) allows fulfilling the energy conservation, since $R + T + A = 1$.

threshold value of transition to 3D particles due to the lower temperature of growth (100[11] vs 300 K; see Fig. 2.19). The difference in terms of growth and wetting with previously studied wide band gap oxides (herein $Al_2O_3(0001)$) [227, 230] is fairly well illustrated in Fig. 2.25 through the plot of the integrated signal in s-polarization and the positions of the plasmon resonances in p-polarization. A much larger splitting of parallel and perpendicular resonances is observed between both substrates. The perpendicular mode tends towards the limit value of the surface plasmon frequency of bulk silver (3.85 eV) but from higher energies. This well known blue-shift [36, 231, 232], which is due to a reduced screening of free s-electrons by more localized d ones at the silver surface, is in line with the formation of much flatter clusters (see section 2.2.4). Moreover, as shown in depth in Ref. [229, 233, 234], the main growth stages can be highlighted through the integrated intensity defined by:

$$\mathcal{A}_s(t) = \frac{1}{t}\int \frac{1}{\omega}\left(\mathrm{Re}[\epsilon(\omega)] - 1\right)\frac{\Delta\mathcal{R}_s}{\mathcal{R}_s}(\omega)d\omega \tag{2.2}$$

where $\frac{\Delta\mathcal{R}_s}{\mathcal{R}_s}(\omega)$ is the differential reflectivity signal in s-polarization at frequency ω, t the average film thickness and $\epsilon(\omega)$ the dielectric function of the substrate. For small particles, $\mathcal{A}_s(t)$ is proportional the oscillator strength of the parallel plasmon mode of the particle normalized by its mass; it is driven to first order only by the evolution of the particle shape. The higher the quantity the higher the aspect ratio. Similarly to $Ag/Al_2O_3(0001)$ [227, 36], $\mathcal{A}_s(t)$ decreases during nucleation, then stays constant during the growth stage at constant particle density and increases again during coalescence due to hindrance of particle reshaping upon contact. While, coalescence hardly starts on alumina in the explored range of thickness, the onset is much earlier in the case of ZnO. This roots into the formation of much flatter clusters. The apparent decrease of $\mathcal{A}_s(t)$ above 3 ML is an artefact; it is mainly due to the limited spectral range of integration in Eq. 2.2(see Fig. 2.24b).

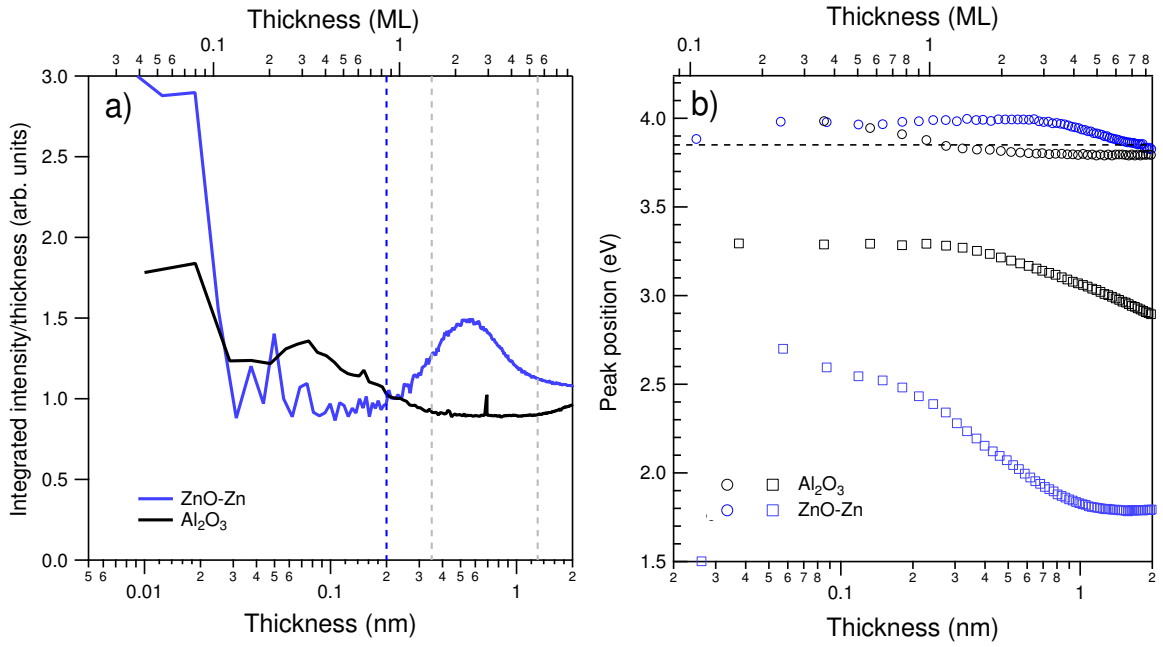

Figure 2.25: Evolution with Ag deposited thickness of (a) the integrated signal $\mathcal{A}_s(t)$ in s-polarization and (b) of the position of the extrema in p-polarization. Deposition on ZnO(0001)-Zn (blue) and $Al_2O_3(0001)$ [227] (black) are compared. Incident angle ($\Theta = 55°$).

The quantitative analysis of such spectra within the framework of surface susceptibilities [44] using truncated spherical [47] or spheroidal shapes [48] as done in the past, for instance in the case of wide band gap insulating substrates [227, 230, 36] is beyond the scope of this thesis. It has been performed during the internship of S. Castilla [235] (INSP/UPMC). The scenario of the formation of high aspect ratio particles was confirmed as well as the early percolation in the case of ZnO.

[11] A lower temperature was chosen in order to obtain a continuous thin film.

2.3 Work function, band bending and Schottky barrier at Ag/ZnO interface

2.3.1 Experimental

The nature of the electrical contact at Ag/ZnO interface was probed *in situ* through ultra-violet photoemission spectroscopy (UPS). To a lesser extent, similar measurements were performed in the literature for Pt/ZnO [169, 178]. The excitation energy is that of the He I emission line at 21.2 eV. Most spectra have been collected in the normal emission geometry. The spectra of the valence band up to the cut-off of secondary electrons were recorded during sequential and cumulative deposition of Ag at room temperature directly in the analysis chamber to avoid errors due to sample positioning and transfer. The film thickness was calibrated through the ratio of Ag $3d$/Zn $2p$ core level intensities on a film with a submonolayer thickness (to assume no damping of signal through the overlayer) by taking into account ionization cross sections, damping of the signal in the substrate and analyser transmission [236]. For thicker deposits, the equivalent thickness was extrapolated with the evaporation time and assuming a constant silver flux and a sticking coefficient of one. The estimated evaporation was $5.5\,10^{-4}$ nm/s. During UPS measurements, the sample was systematically biased at -15 V in order to accelerate the electrons of low kinetic energy and to correctly measure the emission cut-off of secondary electrons and therefore the work function. As no states are present at the Fermi level in the oxide substrate, this latter was determined on the metallic sample holder which was in electrical contact with the substrate and the spectrometer. This alignment was confirmed by the appearance of Ag $5sp$ states at the Fermi level for the thickest metal deposit (8.4 ML = 2 nm; 1 ML corresponds to (111)-plane in silver *i.e.* 0.235 nm or $2.38\,10^{15}$ cm^{-2}). The resolution for a pass energy of 20 eV was around 0.3 eV as determined on the Fermi edge of the holder. Experiments were performed at a He pressure of $6.\,10^{-8}$ mbar in the main chamber and spectra recorded with a step of 0.05 eV.
The two polar terminations ZnO(000$\bar{1}$)-O and ZnO(0001)-Zn were studied after standard vacuum preparation procedure or after on-purpose exposure to atomic hydrogen provided by a thermal gas cracker in the preparation chamber or to molecular water directly in the analysis chamber.

2.3.2 Spectroscopic fingerprints of hydrogenation and hydroxylation: hydroxyl groups and etching

The measured valence bands of ZnO surfaces are shown in Fig. 2.26. Their detailed description in terms of hybridization of atomic orbitals and the corresponding dispersion is far from being settled in the literature because of the complex contribution of $3d$-$4s$ electrons of zinc [60, 147, 160, 180, 237, 238, 239, 240, 241]. The valence band is roughly characterized by a two-peak structure (3-5 eV and 10-12 eV). The first one is mainly derived from O $2p$ contributions. Cation orbitals contribute particularly to the higher binding-energy feature (10-12 eV) which is mainly derived from Zn $3d$ levels and to a lesser extend to the lower binding energy feature (3-5 eV) through Zn $4sp$ levels. Further splitting of these two structures was also evidenced in the literature [60, 237, 238, 239]. On the clean surfaces, a residual density of states is present between 0.5 eV and the onset of the upper valence band derived from O $2p$. The origin of those states, which are clearly enhanced in grazing emission and related to the near-surface, is unknown and poorly commented in the literature. Observed on cleaved Zn-terminated surface [167] or annealed polar surfaces [153], these states were assigned to hydrogen related reduction of Zn and diffusion of impurities. Except for different values of work function and band bending that will be analysed later in Section 2.3.4-2.3.6, the UPS valence band differences between surfaces are minute. The hydrogenation induces (i) a huge decrease of the work function (*i.e.* an increase of the binding energy of the onset of emission of secondary electrons) and (ii) a downward band bending (*i.e.* a decrease of the binding energy onset of O $2p$ derived valence band). This latter phenomenon is further confirmed by core levels shifts (see Fig. 2.27-2.28). An enhancement of the intensity of the band gap states is also observed mainly on the Zn-terminated surface (Fig. 2.26c,d) showing different reactivity towards hydrogen between both surfaces. These states are assigned to metallic Zn [176] that is formed upon etching of the Zn face. This hypothesis is further confirmed by the photoemission analysis of O $1s$ core level and Auger $L_3M_{45}M_{45}$ transitions (Fig. 2.27-2.28) that are sensitive to the surface chemistry of ZnO. As for metal induced reduction of ZnO (Pt [169], Ti [209, 224]), the Auger transition was used as a reporter of the chemical state of Zn and was preferred over Zn $2p$ or Zn $3p$ level due to the chemical shift between Zn^0 and Zn^{2+} [242]. On both ZnO surfaces, the hydrogenation is accompanied by a sizeable increase of the high energy shoulder of the O $1s$ core level; it is shifted by ~ 1.9 eV on ZnO-Zn and ~ 2.1 eV on ZnO-O compared to the bulk component. A very similar chemical shift and uptake of intensity

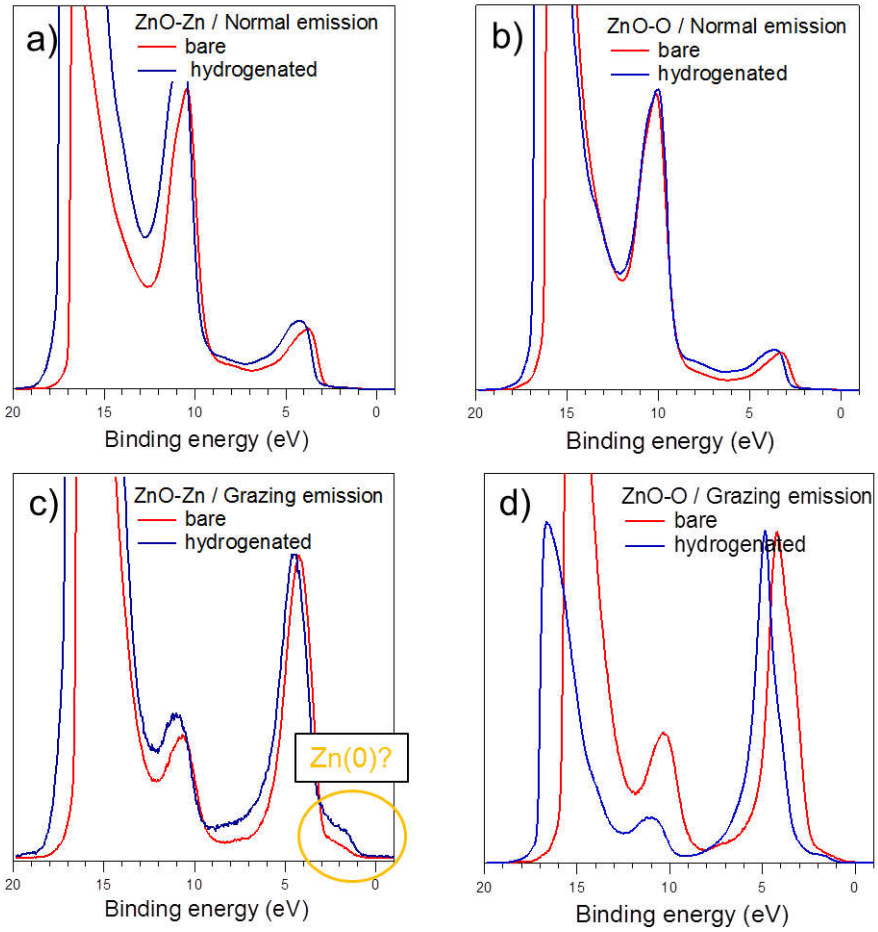

Figure 2.26: Valence bands of polar faces of ZnO before and after hydrogenation (21 L) taken at normal (a-b) and grazing emission (c-d) (take-off angle 70°: (a,c) ZnO(0001)-Zn and (b,d) ZnO(000$\bar{1}$)-O. Spectra have been normalized to the maximum of the O 2p derived peak; the variation of intensity is due to sample transfer between analysis and preparation chamber.

is found upon exposure to water. according to literature, this extra-component (ZnO($000\bar{1}$)-O: 1.9 eV [81], 1.9 eV [93], 1.9-2.5 [243]; 1.4 eV [132, 153, 167, 168] on as loaded/annealed surface of Zn and O-terminations) is usually assigned to the formation of hydroxyl groups [52]. But the expected valence band fingerprints of hydroxylation upon H-exposure are difficult to unravel. Indeed, the characteristic two-peak structure of 1π and 3σ bonding orbitals of hydroxyl groups [244, 245] separated by 3-4 eV at binding energies of 5-7 eV (1π) and 9-11 eV (3σ) overlaps with the emission peak of the valence band of as-prepared ZnO. These latter are hardly visible in Ref. [61, 246] but, owing to the mode of exposure to atomic hydrogen, the amount of adsorbed hydrogen, not speaking about its location at the surface or in the subsurface region, is difficult to compare from one study to the other. In a similar way, the free-electron like states observed by Ozawa *et al.* [61, 147, 159] close to the Fermi level are absent in our data; the reason stems from their strong photon energy dependence with a resonant behaviour at 64 eV which corresponds to the probing of the Γ-point of the surface Brillouin zone where lies most of its spectral weight.

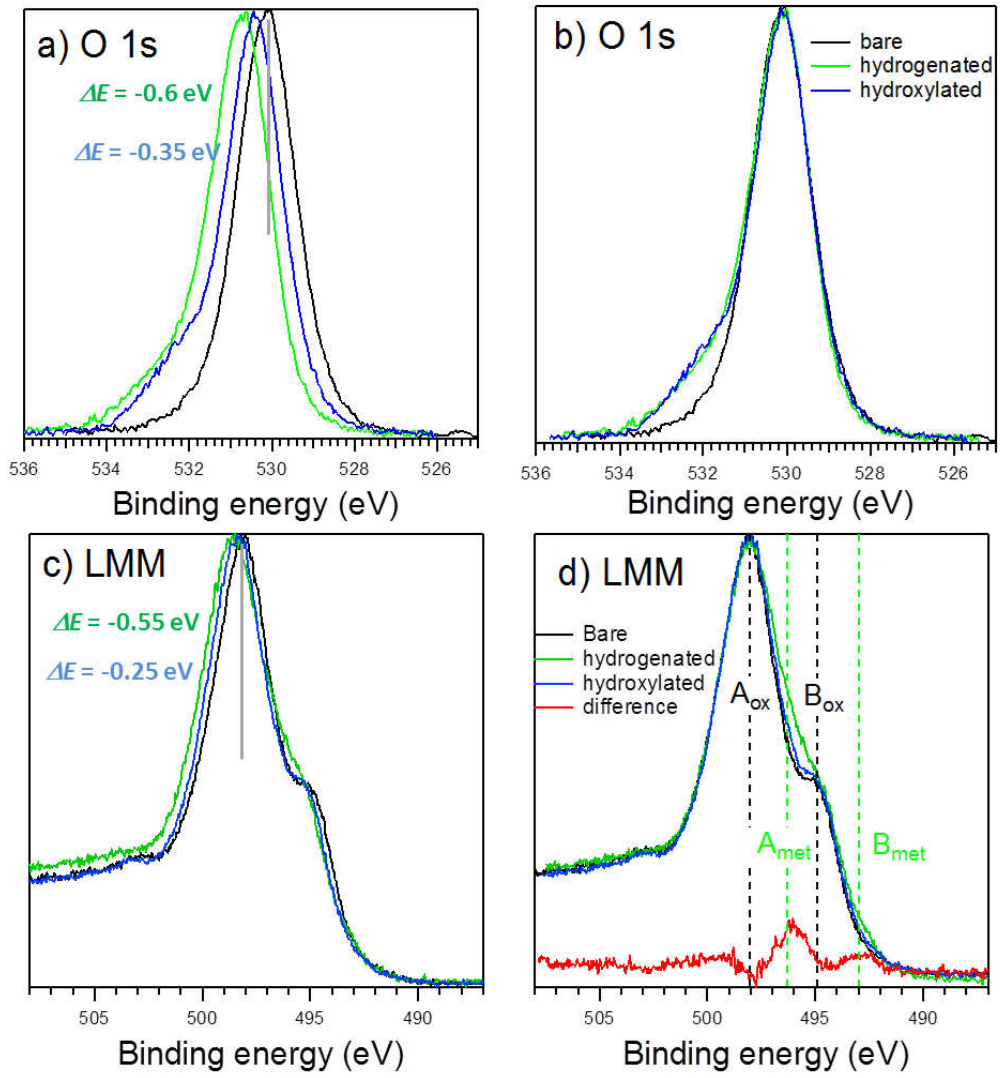

Figure 2.27: ZnO(0001)-Zn: Effect of hydrogenation (21 L) and hydroxylation by water (25 L) at room temperature on (a,b) O 1*s* core level and c)d on $L_3M_{45}M_{45}$ Auger transitions. Spectra have been collected in grazing emission geometry (take-off 70°) Figs. (a-c) show data uncorrected from band bending (given in figure) and Figs. (b-d) after realignment on the as-prepared surface. peaks. The red line corresponds to the difference spectrum after and before hydrogenation. The vertical lines points at the positions of the oxide (A_{ox}, B_{ox}) and metallic (A_{met}, B_{met}) components of the Auger line.

In parallel to the formation of hydroxyl groups, H adsorption impacts the Zn chemical state of both

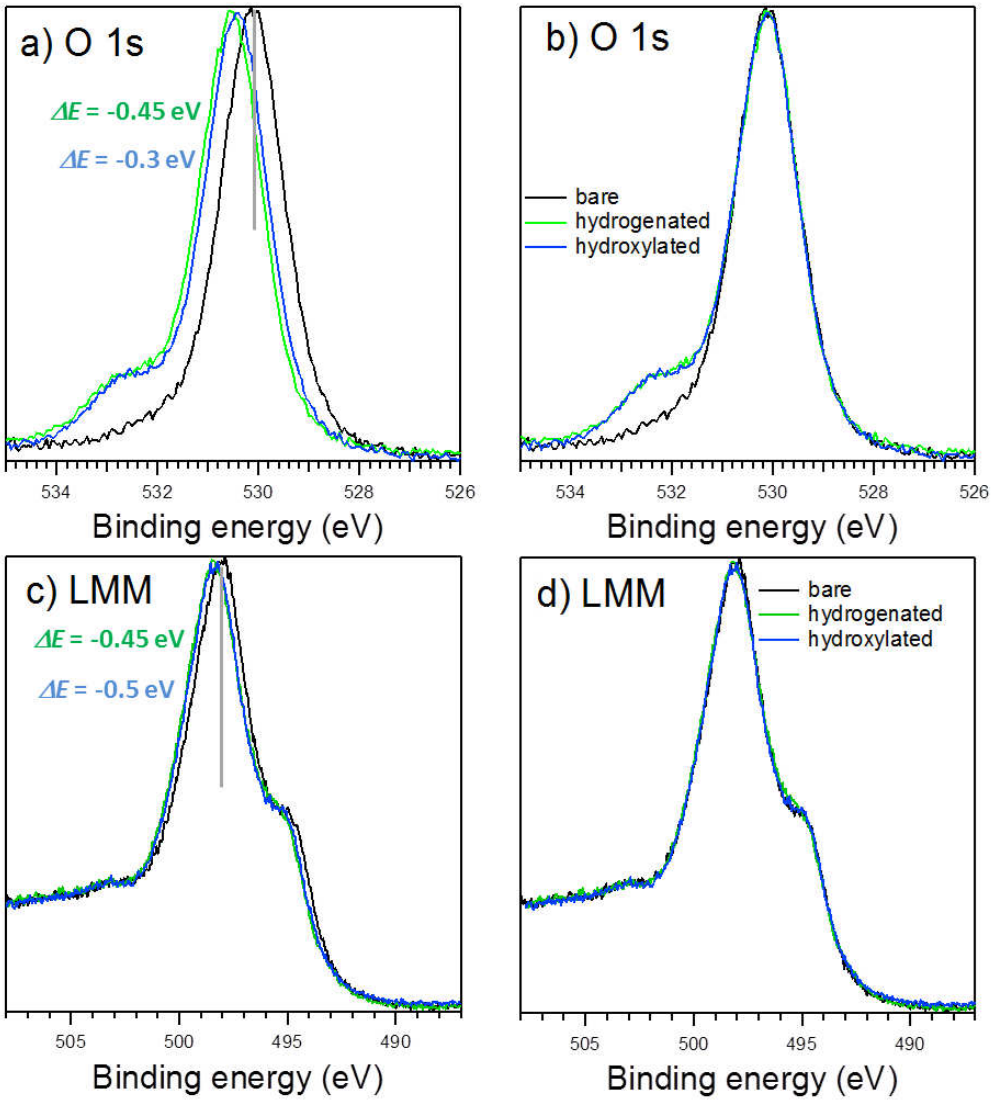

Figure 2.28: ZnO(0001)-O: Same as Fig. 2.27.

surfaces in a very different way. In the absence of sizeable zinc core level shifts in particular of Zn $2p$, the chemical state of zinc is efficiently tracked by means of the Zn $L_3M_{45}M_{45}$ Auger line, the most intense Zn LMM transition. In this transition, the core-hole in the Zn $2p_{3/2}$ level (L_3) is filled by an electron decaying from the Zn $3d$ level (M_{45}), and the difference in energy between those two levels is used to emit an electron from the Zn $3d$ level (M_{45}). The Zn $L_3M_{45}M_{45}$ profile is dominated by two intense features separated in energy by around 3-4 eV (peaks A and B in Fig. 2.27). The oxidation of the metal results in a shift toward lower kinetic energy (or higher binding energy), a broadening of the Zn LMM profile and a change in A/B ratio [233, 247]. Peak A of pristine ZnO (A_{ox} in Fig. 2.27) and peak B of metallic Zn (B_{met} in Fig. 2.27) are separated in energy by ~ 5 eV, which allows the identification the metal and oxidized states of Zn. Water adsorption and the resulting hydroxyl groups do not modify the lineshape of the LMM Auger transition (Fig. 2.27d and Fig. 2.28d). At the opposite, H-exposure clearly leads to a reduction of the surface on the Zn-terminated surface (Fig. 2.27d) but not the O-terminated one (Fig. 2.28d). This findings already highlighted in some previous works through ellipsometry [132, 133] and OH photoemission fingerprint [61] was assigned to a different etching behaviour due atomic hydrogen (Fig. 2.29). On the Zn-terminated surface, H breaks the back-bonds between Zn and O atoms and binds to subsurface O atoms leaving behind a free metallic zinc Zn^0. Its fingerprint is detected in the Auger transition (Fig. 2.27d) and UPS spectra (Fig. 2.26c). At the opposite on ZnO$(000\bar{1})$, only hydrogenation of terminal O-atoms happens without any reduction of zinc. But up to now, despite the OH peak and the appearance of states in the band gap (see Fig. 2.26), there was no clear evidence in the literature of metallic zinc. Similar conclusions were also reached upon deposition of reactive metals: Ti [209], Cr [210, 211]. A quantification of the relative intensities of A_{met}-B_{met} and A_{ox}-B_{ox} of Fig. 2.27d gives a coverage of metallic zinc of the order of 0.4 ML.

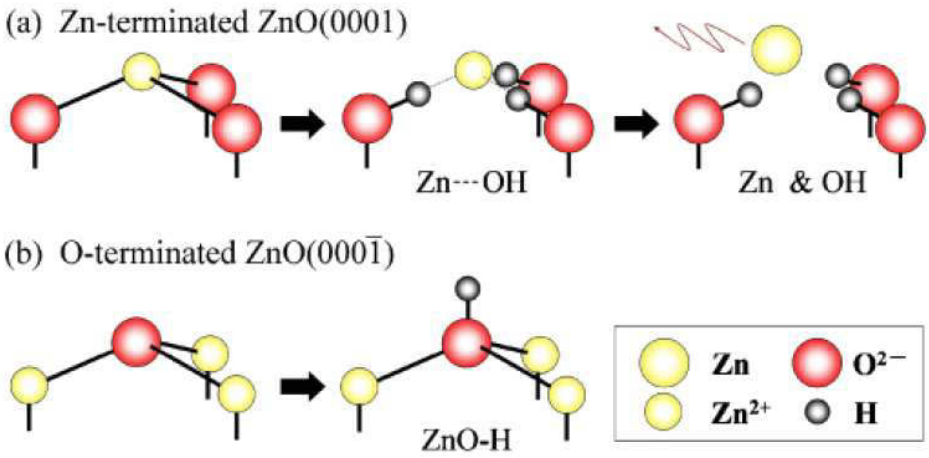

Figure 2.29: Schematic representation of the different etching behaviours induced by H exposure: (a) ZnO(0001)-Zn and (b) ZnO$(000\bar{1})$-O. From Ref. [61].

According to a quantitative decomposition of the O $1s$ spectra, our sample and preparation lead to a nearly OH free surface on the photoemission point of view. A literature overview showed that only Lindsay and co-workers [89] obtained a similar symmetric O $1s$ peak on ZnO$(000\bar{1})$-O. This explains why the as-prepared surfaces are extremely sensitive, in terms of band bending and uptake of O $1s$ shoulder, to the residual atmosphere of the vacuum chamber (mainly composed of H and H_2O)[12]. Once hydroxylated or hydrogenated, surfaces are much less prone to this phenomenon. Water and hydrogen compete for the formation of hydroxyl groups; similar coverages are reached with both adsorbates (Table 2.3 - 10-12% at grazing emission). Using an electron mean free path of $\lambda_{O1s,ZnO} = 19.5$ Å [23, 248] an taking into account the grazing take-off angle, this ratio amounts to 0.25-0.3 monolayers of Zn or O. Quantitative LEED analysis [87] led to a similar coverage (1/3 ML of OH) in the form of a disordered layer. However, this coverage of hydroxyl groups does not correspond to the charge required by electrostatic consideration to heal the polar divergence [53, 54]. according to *ab initio* calculations, a (1×2) OH covered surface should be the most

[12] Band bending evolves over several tenths of eV at a time scale of one hour at a base pressure in the high 10^{-11} mbar making absolute comparison of band bending difficult between different studies. Therefore, all spectroscopic characterization were performed as fast as possible to avoid this problem.

Sample treatment	ZnO(0001)-Zn	ZnO(000$\bar{1}$)-O
As-prepared	0.7	1.3
H (21 L)	10.5	10.5
H_2O (25 L)	12.5	11.2
H_2O (25 L) + H (21 L)	$10.5 \rightarrow 16.7$	-
H (21 L) + H_2O (25 L)	$14.9 \rightarrow 13.7$	-

Table 2.3: Ratio (%) of the O 1s shoulder peak shifted by 1.9 eV (ZnO-Zn) and 2.18 eV (ZnO-O) over the total O 1s area as a function of sample treatment and exposure. Data corresponds to grazing emission (70°). The fits have been made with pseudo-Voigt functions with Gaussian and Lorentzian FWHM of 1 eV. Total exposures to gases are given. Typical error bars are in the range of 1%.

stable configuration [85, 88]. Anyway, one could envision that adsorption of hydrogen induces, on both polar orientations, an OH-stabilized O-terminated surface, accompanied with metallic Zn^0 on the ZnO(0001)-Zn. If hydrogen may involve similar adsorption sites than water, the reciprocal is not true at least on the Zn-terminated surface. While an uptake of the shoulder of O 1s core level occurs (Table 2.3), further band bending and reduction are observed on a hydroxylated ZnO(0001)-Zn surface (not shown), an hydrogenated surface seems to be passivated regarding water adsorption (Table 2.3). Unfortunately, data are missing to comment on the behaviour of O-terminated surface. The observed H-etching process of the Zn-face seems to be limited, at least in our experimental conditions since a multiplication of the total exposure by 4.5 hardly affects the observed fingerprints on both surfaces. The same limitation was found in Ref. [61] for O 2s, band bending and work function evolutions. This finding favours only surface hydroxylation but does not fully rule out bulk diffusion of hydrogen. Finally, the adsorption of water or hydrogen are accompanied by no specific reconstruction as seen by LEED which keeps its (1×1) sharp pattern.

In the absence of atomic scale identification of the adsorption sites, the difference between hydroxylation and hydrogenation can not be further rationalized. Anyway, both induce a sizeable downward band bending of several tenths of eV accompanied by the formation of OH groups. Nevertheless, their role, and more generally that of hydrogen an the reduction it induces, on the electrical contact with silver will be further explored.

2.3.3 Valence band evolution during silver deposition

The evolution of the UPS spectra on the clean ZnO(0001)-Zn surface alongside a zoom on the region of the Fermi level and of the cut-off of emission of secondary electrons are shown in Fig. 2.30. Qualitatively, the scenario is the same on all the studied surfaces. Upon deposition, progressively appear the Ag 4d states beyond 4 eV and Ag 5sp states in the band gap of the oxide. In a parallel way, the onset of the zinc oxide valence band and the energy of the cut-off of secondary electrons shift. Those trends will be analysed in the following in terms of work function, band bending and Schottky barrier changes (see section 2.3.4 and 2.3.6).

For the thickest deposit, metallic Ag 5sp states are clearly visible at the Fermi level (Fig. 2.30b), confirming its calibration on the metallic support. The peak just below the Fermi level for the thickest films (8.4 ML) reminds the surface state of Ag(111) [250]. The onset of the appearance of these states is above 0.5 ML for all studied surfaces (*i.e.* Zn and O-terminations and bare and hydrogenated). This observation parallels the findings about the growth mode (*i.e.* flat islands), the contraction of the lattice parameter and the growth at step edge. At a first glance, the absence of these states at the Fermi level below roughly 0.5 ML seems to indicated that the clusters are non-metallic and have a special electronic structure due to a charge transfer at Ag/ZnO. This interpretation is apparently confirmed by the strong variation of the work function in this thickness range and the strong shift of the apparent Ag 5sp Fermi step of the cluster (up to -0.7 eV). But this initial state interpretation is inconsistent with the existence of a pronounced plasmon resonance (see section 2.2.5) which proves the collective motion of s-electrons and therefore of the metallicity of the particles in this size range. The discrepancy lies in a final state effect due to the existence of a positive charge after the photoionization process which shifts upwards and broadens the apparent Fermi level of the clusters in a way that depends on the coupling between the substrate and the particle. The time scale over which the photoelectron interact with the positive hole is governed by the neutralization by the substrate conductivity. This phenomenon that happens on the femto-time scale was already demonstrated in the case of silver or gold clusters supported on vitreous carbon or graphite [251, 252, 253], gold particles on

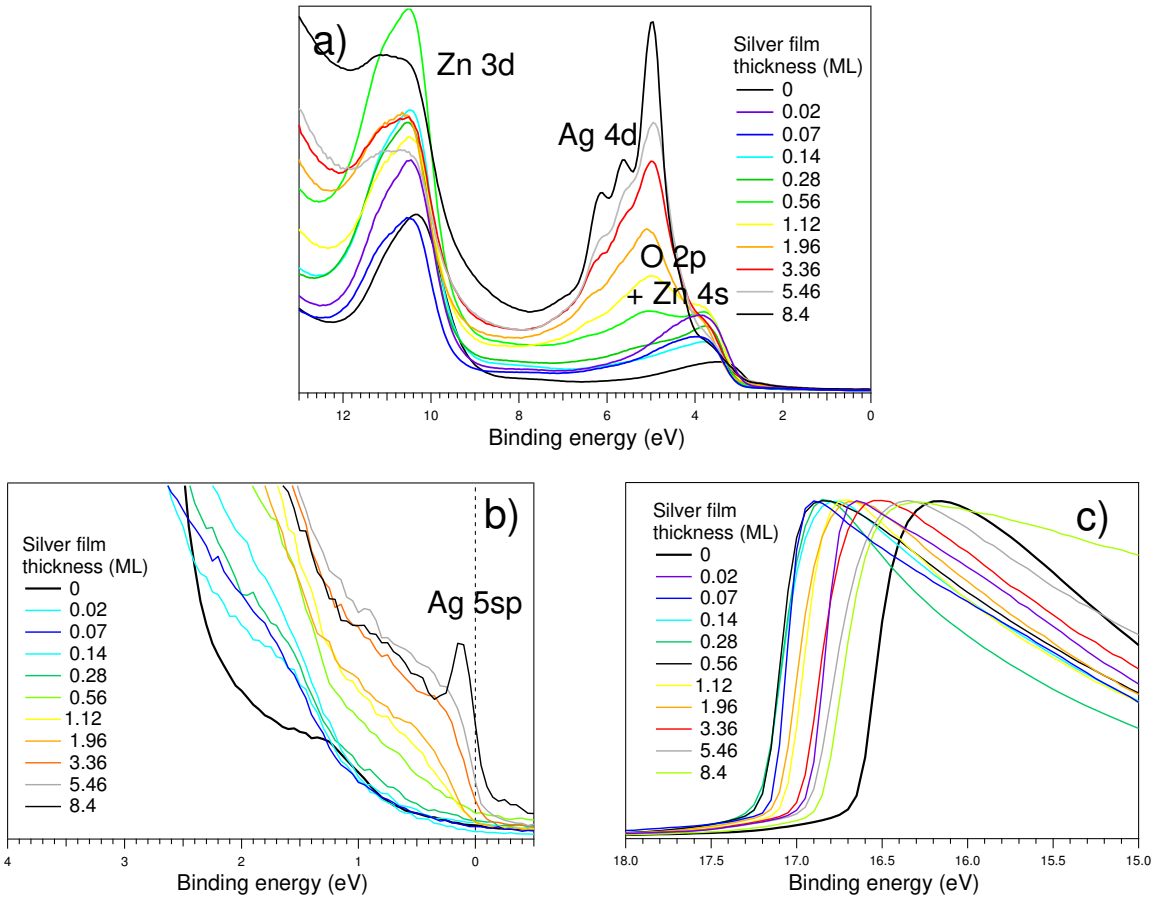

Figure 2.30: UPS spectra of Ag/ZnO(0001)-Zn at 300 K as a function of the film thickness given in Ag(111) monolayer (1ML = 0.235 nm): (a) Evolution of the valence band showing the main contributions from the orbitals of the elements. Spectra have been rescaled to the same counting rate. (b) Zoom on the region of the Fermi level. Notice progressive shift of Ag 5*sp* metallic level towards the Fermi level. (c) Zoom on the cut-off of emission of secondary electrons. Spectra have been normalized to the maximum.

$TiO_2(110)$ [254] or Ag/ZnO($10\bar{1}0$))-M [172]. The observed shift is much larger than ZnO($10\bar{1}0$)-M [172] at the same equivalent thickness suggesting either a very different cluster morphology on polar and non polar surfaces or a different sample conductivity and hole relaxation dynamics. The maximum expected shift is given by $E_{B,max} = \alpha e^2/4\pi\epsilon_0 R$ where R is the radius of the particle, ϵ_0 the vacuum permittivity and α a constant value around 0.5 [253, 254]. The observed shift of around -0.7 eV at an equivalent thickness of 0.28 ML corresponds to a particle size of around 2 nm which matches the SDRS estimate.

As the surface is covered with silver, the Ag $4d$ peaks (peaks A-E) grow at 4-8 eV and the emission from the substrate is gradually damped. Their positions were determined by taking the second derivative of the spectra and indicated by dotted lines in Fig. 2.31a. Those features were already observed by synchrotron angle-resolved photoemission measurements for Ag/ZnO($10\bar{1}0$)-M deposits [172] at exactly the same energies: $E_A = 4.3$ eV, $E_B = 4.93$ eV, $E_C = 5.62$ eV, $E_D = 6.2$ eV, $E_F = 7.2$ eV. Ozawa *et al.* [172] demonstrated that those features have a clear bidimensional dispersive character as shown by the absence of dispersion by changing the photon energy (perpendicular direction); this was interpreted as Ag $4d$ states confined in 2D islands or very thin 3D islands with a few atomic layer thickness. This conclusion matches the present plasmonics findings and earlier grazing incidence scattering measurements [193, 194] about the formation of flat top Ag(111) particles. Those states are reminiscent of quantum-well states observed on Ag/metal films [250] but for *sp* electrons. Through polarization dependent measurements [172], peak B was assigned to $d_{x^2-y^2}$ orbitals and peal A and C to $d_{3z^2-r^2}$. Peaks A-E sharpen upon deposition above 1 ML (Fig. 2.31b) due to particle lateral growth but are less visible on hydrogenated surfaces even at the highest coverage (Fig. 2.31c). This suggests a different particle morphology on hydrogenated surfaces.

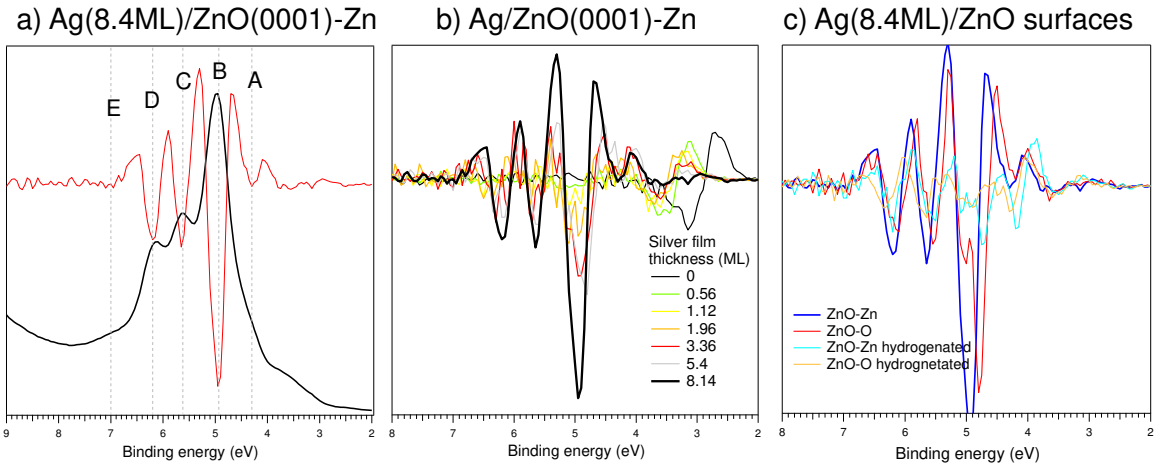

Figure 2.31: Double differentiated UPS spectra: (a) comparison with the corresponding actual spectrum for 8.4 ML Ag deposit on ZnO(0001)-Zn surface, (b) evolution as a function of the silver thickness on ZnO(0001)-Zn, and (c) for a deposit of 8.4 ML on bare and hydrogenated ZnO(0001)-Zn/ZnO($000\bar{1}$) surfaces.

2.3.4 Work function evolution upon silver deposition: bare versus hydrogenated surfaces

Only normal emission data have been considered for work function determination to avoid the pitfalls due to the distortion of field lines between a polarized sample and a grounded analyser nose [255]. The position of the cut-off of the emission of secondary electrons (Fig. 2.32a) was determined as the intersection of the linear extrapolation of the noise level and the tangent line at the inflexion point of the sharp decrease of intensity [256]; this defines the work function Φ which is plotted in Fig. 2.33 for all the studied surfaces as a function of silver film thickness.

The measured work functions of the as-prepared surfaces ($\Phi_{ZnO-Zn} = 4.3$ eV and $\Phi_{ZnO-O} = 5$ eV) agrees with previous determinations (see Table 2.1) for samples prepared in similar conditions by sputtering/annealing or by cleavage under ultra-high vacuum. The sensitivity to adsorbates (in particular hydrogen) and to the subsurface contents in intrinsic defects may explain the observed sizeable variations.

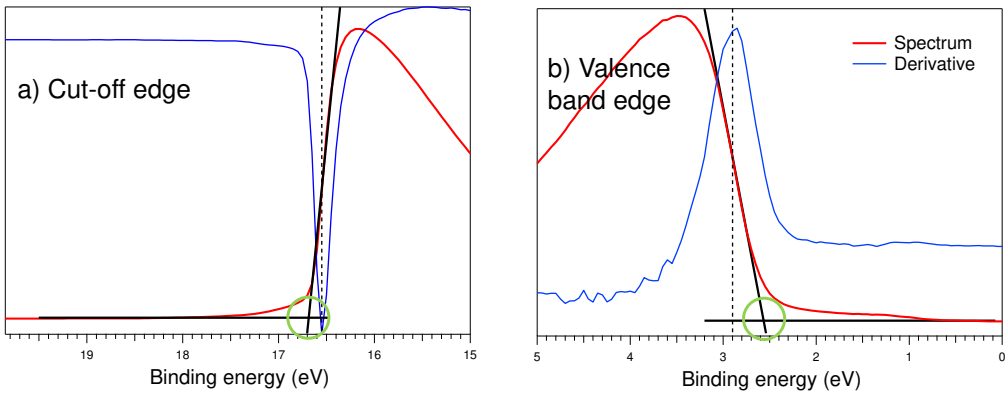

Figure 2.32: Tangent method to determine from the actual experimental data (a) the cut-off position and the work function and (b) the edge of the valence band of ZnO relative to the Fermi level. The inflexion point of the curve is obtained at the maximum of the derivative; the sought binding energy (green circle) is obtained as the intersection of the linear part of the edge at this point and a linear extrapolation of the background. For the valence band edge similar method has been applied on the upper part of the valence band edge, in order to avoid the influence of Ag $5sp$ states. The accuracy of such determination is around 0.1 eV.

Upon hydrogen exposure (Fig. 2.33), the work function is drastically reduced down to a value of $\Phi_{ZnO-Zn+H} = \Phi_{ZnO-O+H} = 3.65$ eV. Exactly, the same similar effect was found on vacuum cleaved crystals exposed to atomic hydrogen (produced by the hot filament method) in the seminal work of Moorman *et al.* [163] for both polar surfaces; the variation was correlated to an increase of the surface electron density as determined by Van der Pauw resistivity measurements through the formation of an accumulation layer on both polar surfaces. But more recently, Ozawa *et al.* [61] revisited the problem with photoemission (using a hot tungsten filament to produce atomic hydrogen); the authors found a similar decrease of the work function on ZnO$(000\bar{1})$-O ($\Phi_{ZnO-O} = 5.1$ eV; $\Phi_{ZnO-O+H} = 3.9$ eV) but not the ZnO(0001)-Zn ($\Phi_{ZnO-Zn+H} = 4$ eV; $\Phi_{ZnO-Zn+H} = 3.95$ eV) for the smallest exposures. While in the former case, a surface metallization was evidenced through a downward band bending, an accumulation layer and the formation of a partial filled metallic band at the Fermi level (with a 2D free-like carrier parabolic dispersion seen by angle-resolved photoemission spectroscopy), no such states were found on the other termination. Only, states well below the Fermi level (< 0.5 eV) were evidenced and assigned to the formation of metallic zinc clusters due to etching by hydrogen as in Fig. 2.29. Their position in the band gap of the oxide was explained by the same final state effect due the partial screening of the photohole evoked in the case of silver particles (section 2.3.3). However, it rather difficult to compare various experiments since the cracking efficiency of H_2 and the adsorption on the surface are unknown. In the work of Ref. [61], total hydrogen dose is far larger than ours and the way of producing H is different (2000 L instead of 21 L herein). But, in our study (section 2.3.2) and Ref. [61], hydrogenation is accompanied by a similar hydroxyl coverage close to 0.25-0.3 ML as determined by O-core level analysis.

Work function evolutions upon silver deposition Φ_{ZnO+Ag} have a very similar trends on both faces O and Zn: a sharp decrease until a value close to 4 eV for a thickness below half a monolayer and then a slow increase up the limit value to 4.2 eV at the largest film thicknesses. But this value is still well below the expected work function of a bulk Ag(111) crystal ($\Phi_{Ag(111)} = 4.73$ eV; $\Phi_{Ag(100)} = 4.64$ eV; $\Phi_{Ag(110)} = 4.52$ eV [257, 258, 259] [13]) or that of polycrystalline Ag-(111)-oriented thick films [257, 260]. Beyond the existence of stacking faults along the [111] direction (see section 2.2.3) that is expected to slightly reduce the value from 4.73 to 4.64 eV [260], a likely explanation is the effect of partial coverage of the substrate and an incomplete image effect in a film of 8 ML which is reduced compared to a semi-infinite substrate.

[13] The work function of a silver surface increases when it gets more compact.

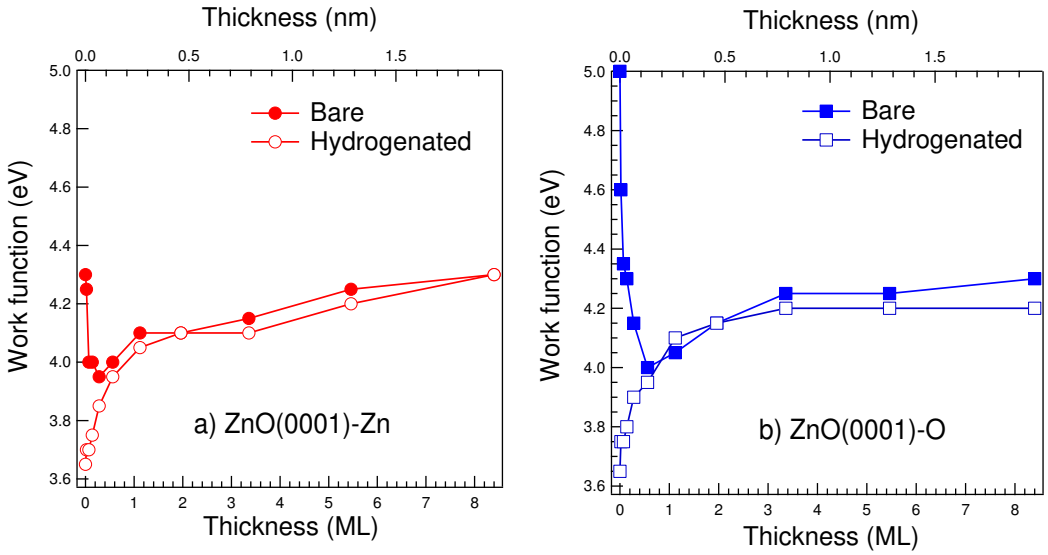

Figure 2.33: Evolution of the work function of the Ag/ZnO interface as a function of the deposited thickness, orientation and hydrogenation of the substrate.

2.3.5 Changes of work function, band bending and ionization energy upon silver deposition: the charge transfer

For a semiconductor it is convenient to decompose the work function Φ as the sum of three terms [3, 4, 182] (see Fig. 2.9):

$$\Phi = I + V_{bb} - (E_F - E_V) = \chi + V_{bb} + (E_C - E_F) \tag{2.3}$$

where V_{bb} is the band bending, χ the electron affinity, I the ionization energy which is the difference between the valence band and the vacuum level, E_F the Fermi level and E_C, E_V the positions of the conduction and the valence bands. The effect of an adsorbate (herein hydrogen or silver) is assumed (i) to create a dipole layer at the surface that change the electron affinity by $\Delta\chi$ or the ionization energy by ΔI and (ii) to induce a change in band bending ΔV_{bb} in the semiconductor. The concomitant change of the work function is given by $\Delta\Phi = \Delta I + \Delta V_{bb} = \Delta I + \Delta V_{bb}$ since the position of the Fermi level relative to the valence and conduction bands is fixed by the bulk doping only. The dipole contribution is often calculated on a simplifying assumption about the nature and the magnitude of the dipole. It is described by an electric double layer which induces a voltage drop for emitted electrons in a similar way as a parallel plate capacitor: $\Delta I = \Delta\chi = eN_{dip}p_\perp(\theta)/\epsilon_0$. N_{dip} is the surface density of created dipole of strength $p_\perp(N_{dip})$ (perpendicular to the surface) which may evolve with the coverage through dipole-dipole interaction [3, 182].

The variation of the band bending ΔV_{bb} was obtained by measuring directly the shift relative to the Fermi level of the flank of upper oxide valence edge extrapolated to background (see Fig. 2.32b). No other emission band characteristic of the oxide is accurate enough for such an analysis; the Zn $4s$ and Ag $4d$ levels overlap while the Zn $3d$ band is biased by the evolving background of secondary electrons (Fig. 2.30) at the opposite of the photoemission measurements for Cu/ZnO of Ref. [175] performed at higher photon energy. Unfortunately, because of the appearance of Ag $4d$ and $5sp$ states close to O $2p$ levels of ZnO, the determination of the valence band onset is less accurate above an equivalent thickness of 6 ML (1.4 nm). Fig. 2.34 gathers the variations $\Delta\Phi$, ΔV_{bb}, ΔI during Ag growth as obtained from UPS spectra analysis of both Zn- and O-terminated surface, as-prepared and hydrogenated surface.

Hydrogenation of the as-prepared surfaces induces large downward band bending ($\Delta V_{bb} < 0$) (open symbols in Fig. 2.34a,c) as seen directly from the shifts of the O 2p and Zn 3d bands in UPS (Fig. 2.26) or the O 1s core level or $L_3M_{45}M_{45}$ Auger transitions (Figs. 2.27-2.28). Absolute values differ slightly from one measurement to another because of the reactivity of the surface towards residual background [160]. Water produces somehow similar downward band bending. This implies (i) that bands are bent upwards on the as-prepared surface (see Set. 2.4) and (ii) adsorbed H, at first sight in the form of OH-groups (see

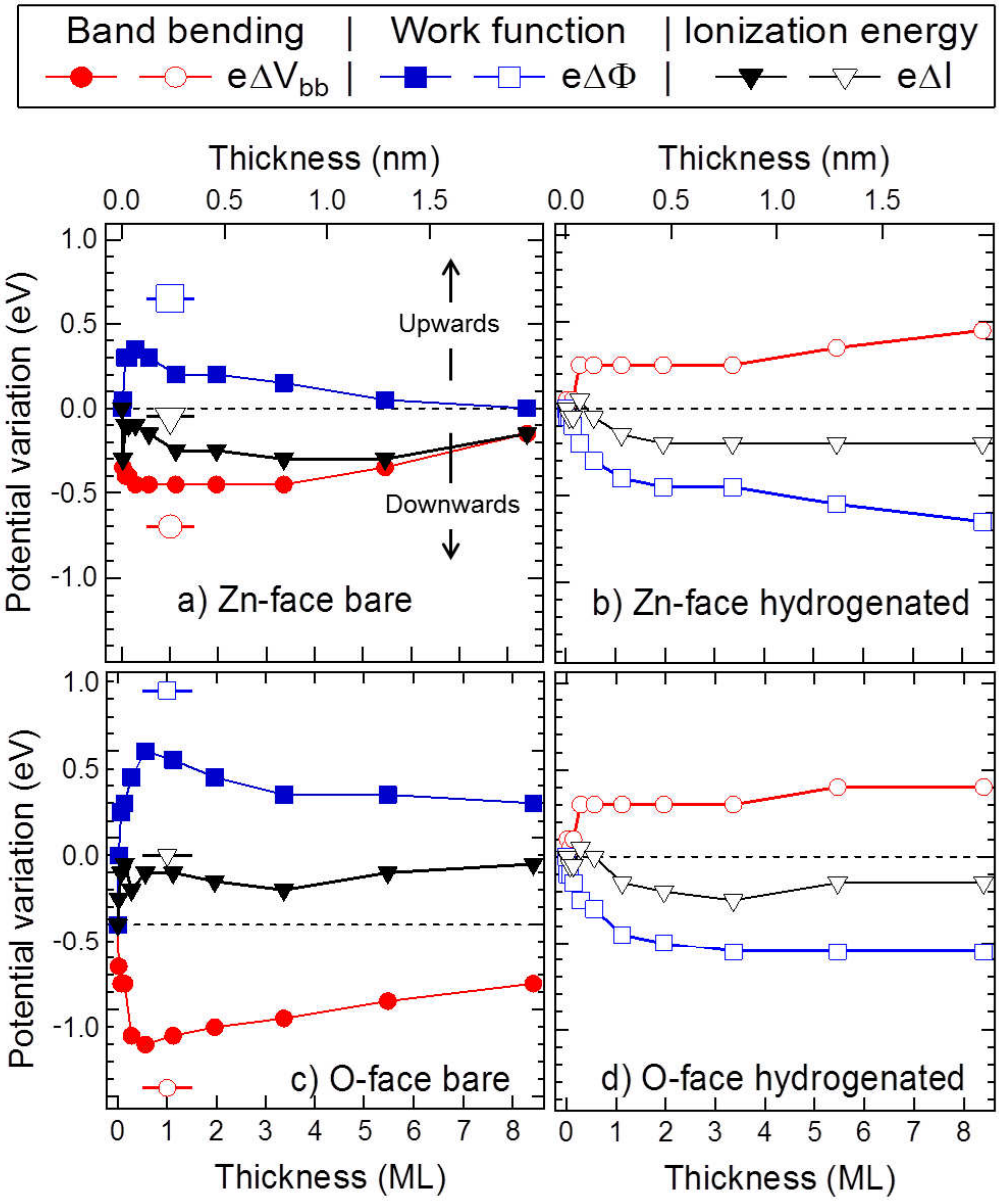

Figure 2.34: Variation of band bending ΔV_{bb} (circles), work function $\Delta\Phi$ (squares), ionization energy ΔI (triangles) during silver deposition on (a) as prepared ZnO(0001)-Zn surface, (b) hydrogenated ZnO(0001)-Zn surface, (c) as prepared ZnO(000$\bar{1}$)-O surface, (b) hydrogenated ZnO(000$\bar{1}$)-O surface. The horizontal bars in Figs. (a,c) stand for the corresponding variations after hydrogenation of the bare surface.

section 2.3.2), acts as a charge donor. On the O-face, the donor character can be inferred also from positive ΔI value, meaning the formation of a surface dipole moment with a positive end pointing at the vacuum as expected from cationic hydrogen. The lack of surface states and of reconstruction after hydrogenation rule the other basics interpretations of ΔI change [182]. On the Zn-face, band bending and work function change compensate nearly perfectly leading to a ΔI value close to zero. The etching of the surface and the formation of metallic zinc might screen or quench the surface dipole on ZnO(0001)-Zn surface. Assuming a hydroxyl coverage of 0.25 ML as deduced from the O 1s analysis after hydrogenation of ZnO($000\bar{1}$), the variation of ionization energy give a dipole moment of $p_\perp = 0.4$ Debye. Of course, one should keep in mind that, not only the contribution of OH, but also inwards diffusion of hydrogen (see section 2.1.2) Finally, in the presently explored conditions, hydrogenation does not produces an accumulation layer and a metallization of the surface since the Fermi level is always found by UPS slightly below the surface conduction band (see Fig. 2.36-2.37). The bands bend downwards upon hydrogenation but do not cross the Fermi level at the opposite of Refs. [61, 146, 147, 158, 159, 163] (see section 2.1.3). But, hydrogenation conditions are difficult to compare from one experiment to the other because of diffusion even if similar apparent OH coverage are reached [61].

On the as-prepared surfaces, silver deposition induces a sizeable sharp downward band bending ($\Delta V_{bb} < 0$). It is larger on the O-face than on Zn-face, peaks in the submonolayer range at coverage of ~ 0.56 ML before decreasing down to a value around 0.4 eV. As already stated, the work function follows a parallel but opposite behaviour. But their sum, the so-called band bending corrected function [174, 201] or the variation of the ionization energy [3, 4, 182] ΔI, has an opposite sign on the two orientations. This translates an opposite interface dipole on the two surfaces. On the other hand, the variation of band bending and work function follow opposite trends on the hydrogenated surfaces *i.e.* an upward band bending and an increase of work function. However, the interface dipole has an orientation similar to the deposition on the as-prepared ZnO(0001)-Zn.
On ZnO($000\bar{1}$)-O, downward band bending and $\Delta I < 0$ is consistent with charge donation from Ag to ZnO to make cationic Ag species. These electrons go partially into the space-charge region of the semiconductor causing the band bending and are at the same time partially localized on the surface atoms creating a local surface dipole. At the earliest stage of deposition, the corresponding dipole $p_\perp(N_{Ag})$ (Fig. 2.35) amounts to 1.5 Debye. It corresponds to ~ 0.1 elementary charge per silver atom assuming a charge separation of around 2 Å, the sum of Ag atomic radius and O^{2-} ionic radius [261]. However, the results are more puzzling on the Zn-terminated surface. While downward band bending ($\Delta V_{bb} < 0$) favours a charge transfer to the bulk of the substrate, the surface dipole ($\Delta I > 0$) is oriented towards the substrate suggesting anionic silver. Similar charge transfer have been obtained for Cu [94]. The obtained dipole amounts to ~ 3 Debye at the beginning of the growth; the corresponding polarization charge is ~ 0.3 electron per silver atom assuming a charge separation of 2.5 Å, the sum of Ag atomic radius and of Zn^{2+} ionic radius. On hydrogenated surfaces the upward variation of band bending ($\Delta V_{bb} > 0$) as well as that of the ionization energy agree with a charge transfer from the substrate to the metal *i.e.* anionic silver. Hydrogenation makes both Zn- and O-terminates surfaces similar in terms of band diagram evolution during silver deposition. This is inline with the XPS findings of the formation of an OH-stabilized surface with (ZnO(0001)-Zn) or without (ZnO($000\bar{1}$)-O) Zn etching. On all surfaces, the curves $\Delta V_{bb}, \Delta\Phi$ and ΔI nearly stop changing above ~ 0.56 ML and the local dipole decreases below 0.05 Debye, showing that the adsorbtion of Ag is nearly neutral and unpolarised, in the expected form of nanoparticles.

The formation of ionic-like species in the first 0.5 ML is to be brought together with the STM and RHEED findings that shows a peculiar growth process in the same thickness range. A likely hypothesis is either a strong chemical interaction with the under-coordinated step atoms and/or an extra-stabilization brought by the metal of the polarity of the surface or of the polar edges of surface nanostructures. Indeed, polarity healing rule requires removal of positive (negative) charge on the ZnO(0001)-Zn (ZnO($000\bar{1}$)-O) termination that can be partially provided by anionic (cationic) silver atoms. Being partially ionized, silver seems to play a similar role as hydrogen at the early beginning of deposition.

The comparison with Cu is interesting since Cu atoms have electron affinity and ionization energies similar to Ag [261] and Cu(111) has a work function not so far from that of Ag(111) ($\Phi_{Cu(111)} = 4.94$ eV vs $\Phi_{Ag(111)} = 4.73$ eV) [258, 259]. A similar tendency to cationic absorption up to 0.3 ML was observed for Cu on ZnO($000\bar{1}$)-O [174, 175, 201]. Results on the ZnO(0001)-Zn surfaces are more contradictory. Didziulis and coll. [175, 201] and Beinik *et al.* [94] found the first atoms as negatively charged while the results of Yoshihara and Campbell pointed at cationic silver [199] below 0.1 ML followed by a change of band bending

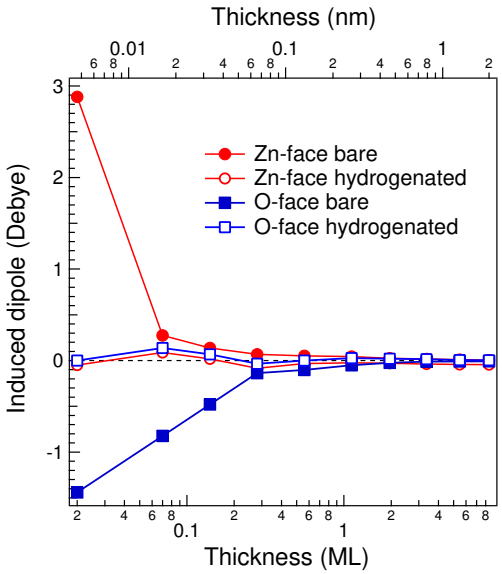

Figure 2.35: Evolution with silver film thickness of the surface dipole deduced from the variation of the ionization energy extracted from UPS data.

from downwards to upwards above 0.5 ML.

2.3.6 Schottky barrier and band alignment

2.3.6.1 The ideal contact

The ideal Schottky barrier (see section 2.1.4.1) at the Ag/ZnO interface between semi-infinite media was determined from UPS measurements of the bare surface, data from the literature and a drawing of the alignment of the bands at the interface. On the as prepared surface, the angular measurements between normal and grazing emission (up to 70°) showed a slight shift of 0.1 eV [14] of the positions of the core level line (in particular O 1s and Auger LMM). This means, that by changing the escape depth of electrons from around 2 nm to 0.7 nm, an slight upward band bending can be detected. This conclusion will be confirmed later on by the HAXPES measurements in the next section by changing more drastically the probing depth.

Figs. 2.36-2.37 show, for both orientations after vacuum annealing and after exposure to hydrogen, the band alignment before and after an ideal Schottky contact *i.e.* a simple theoretical alignment of the Fermi level assuming the lack of surface state or reactivity that may impart the charge transfer between the metal and the semiconductor. On the one hand, the values of the band gap ($E_g = 3.38$ eV) and the work function of silver along the (111)-orientation ($\Phi_{Ag(111)} = 4.73$ eV) are taken from literature [262]. On the other hand, ZnO work function and the position of the Fermi level relative to the conduction band have been obtained directly from the UPS data of the bare surfaces. In theory for an ideal Schottky contact, a charge transfer from ZnO to Ag is to be expected on the Zn-terminated face leading to an upward band bending. Exactly the opposite should happen on the O-face because of the difference of work function between the two orientations. But hydrogenation makes both surfaces in principle completely identical. The ideal Schottky barriers of Ag/ZnO interface should be $\phi_{SB,ZnO-Zn} = 1.16$ eV, $\phi_{SB,ZnO-O} = 0.76$ eV and $\phi_{SB,ZnO-H} = 1.21$ eV.

2.3.6.2 Actual Schottky contact

In fact, the situation is much more complex than the ideal one for several reasons among which the modification of interface states, the charge transfer with the metal, the chemical bond at the interface and the finite thickness of the film. Regarding isolated silver atoms, the small electronic affinity and the large ionization energy of Ag do not really favour a charge transfer but it seems to occur according to work function change.

The actual Schottky barrier could be determined directly from UPS profiles by using the method of Ref. [256] that is to say by measuring the distance between the upper oxide valence edge extrapolated to

[14] A special care was taken to measure normal and grazing emission one after the other to avoid hydrogen uptake from residual atmosphere which changes the band bending.

background and the Fermi level (Fig. 2.32b). Unfortunately, because of the appearance of Ag $4d$ and $5sp$ states in this energy range, the determination could only be made accurately up to an equivalent thickness of 6 ML (1.4 nm). It allows positioning the conduction band relative to the Fermi level knowing the band gap of the oxide. Fig. 2.38 gathers all the measurements for all studied surfaces of this Schottky barrier. This quantity should be taken with caution since, in principle, it is ill-defined for a discontinuous film in which metallic states are not necessarily present at the Fermi level. according to the UPS data of Fig. 2.30b, silver states show up at the Fermi level E_F only above 0.5 ML. The different surfaces distinguish from each other only at the first stages of the deposit. For the thickest deposit, an average value of around $\phi_{SB,ZnO} = 0.5 - 0.7$ eV is found, a value much lower than that expected for an ideal contact but, also slightly lower than the literature ones (0.7-1 eV [102, 215, 221, 222]). The hydrogen treatment does affect the barrier height only for film thicknesses below 0.3 ML in the range of the change of work function. It is worth noticing that in all situations studied herein the metal/oxide is of Schottky type.

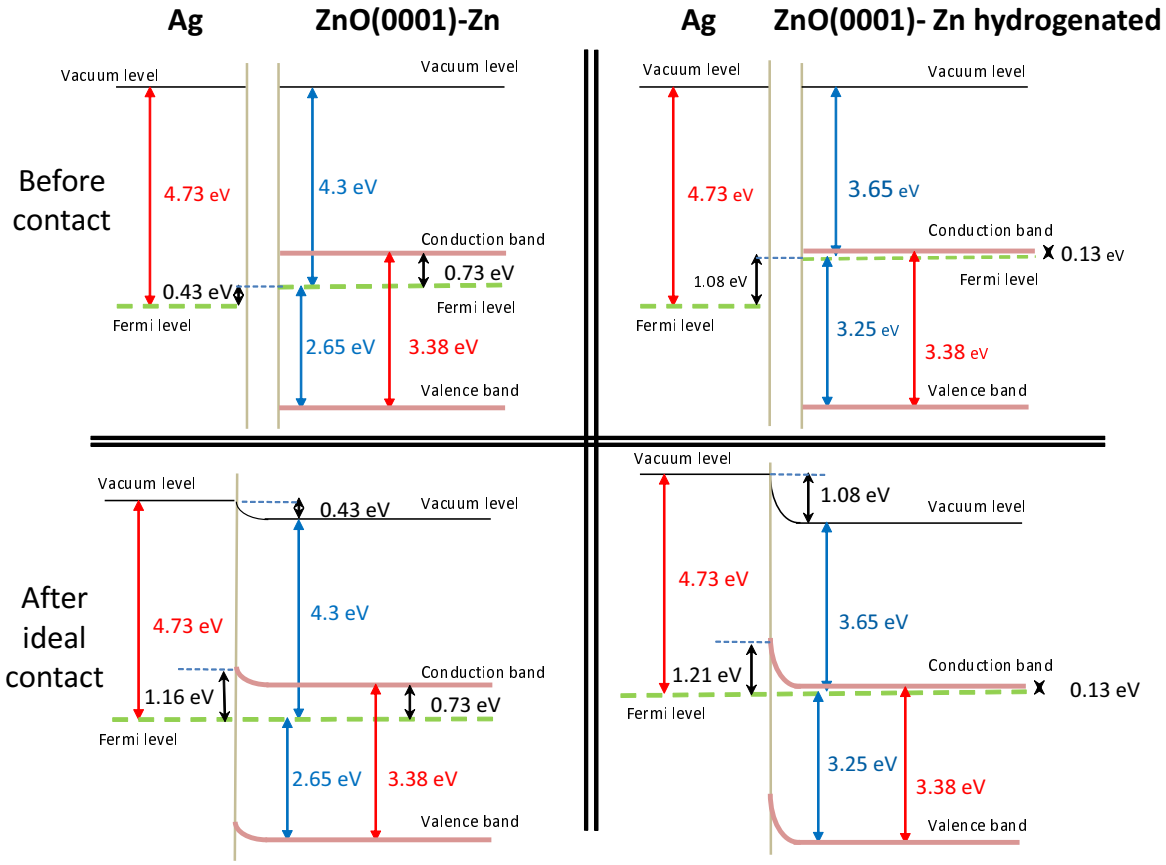

Figure 2.36: Band diagram alignment before (upper panels) and after (lower panels) a theoretical contact between Ag(111) and ZnO(0001)-Zn for substrates vacuum annealed (left column) or hydrogenated (right column). Values in red are extracted from the literature [257, 258, 259, 262] and those in blue are obtained from the present UPS measurements. They corresponds to "surface" values that is to say over the probing depth of UPS. The diagram after contact corresponds to an ideal Schottky contact without formation of an interface dipole due to the metal.

2.4 Band bending at the ZnO-Ag interface studied by HAXPES

The previous UPS analysis of the band alignment at the interface Ag/ZnO is highly surface sensitive because of the used photon energy. It does not bring any information on how the surface electronic structure connects to the bulk one, in particular the actual band bending and the position of the Fermi level relative to the conduction band. Moreover, direct determination of Schottky barrier with UPS is limited to the first stages of growth due to the progressive appearance of the silver states close to the edge of the valence band of

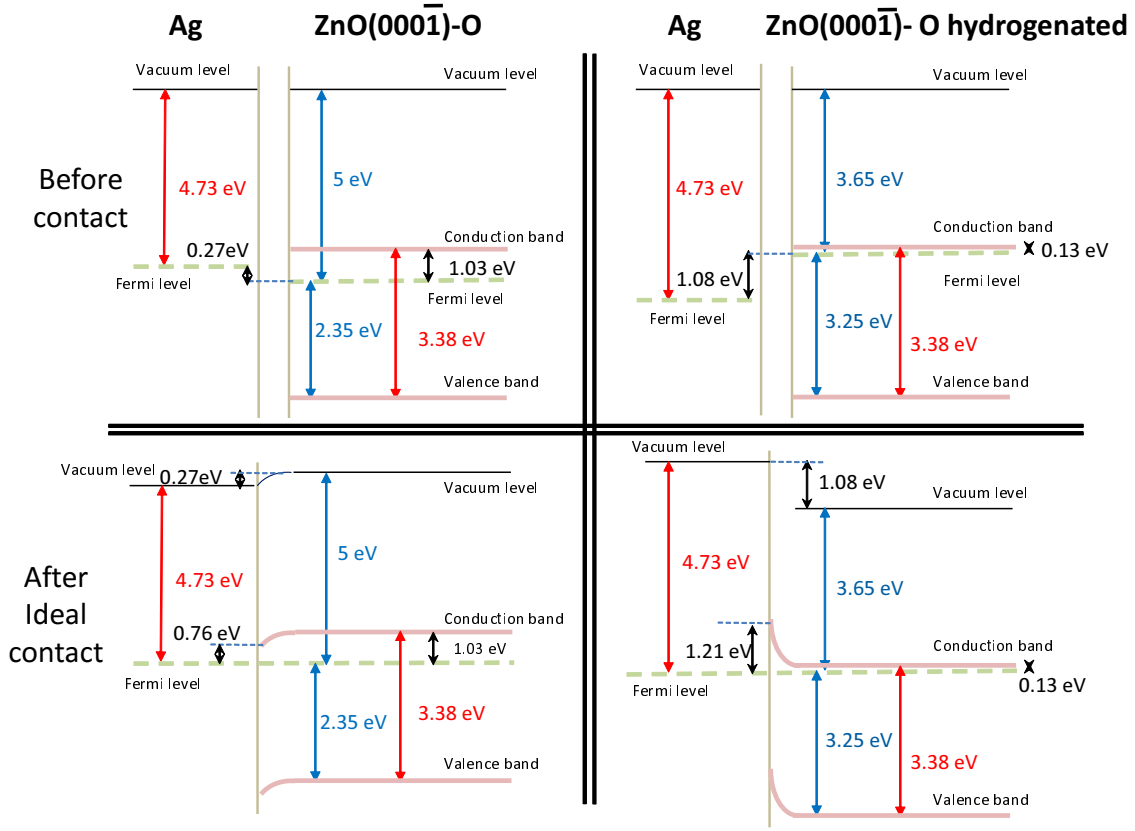

Figure 2.37: Same as Fig. 2.36 but for the ZnO(000$\bar{1}$)-O orientation.

the substrate. As shown previously, a slight upward bending of 0.1 eV was suspected through laboratory photoemission at a photon energy of Al-Kα (*i.e.* 1486.6 eV between normal and grazing emission); but the corresponding variation of escape depth is modest (typically from 2 nm down to 0.7 nm). To overcome this limitation, experiments at higher photon energy were undertaken at synchrotron on specially designed samples. The principle of band bending determination sketched in Fig. 2.39 is to go deeper in the bulk by increasing the photon energy according to the universal curve, the inelastic mean free path of photoelectrons. The shift of the binding energy Zn $2p$ core level was analysed with a suitable model to extract quantitative information relative to the band bending, the screening length, the carrier density and the Fermi level position.

2.4.1 Zn $2p$ core level evolution with photon energy

2.4.1.1 Experimental

Experiments have been performed on the KMC-1 beam line of BESSY II synchrotron (Berlin) by HAXPES by focusing in particular on the Zn $2p$ core level line shape as a reporter of band bending. O $1s$ core level was not used due to surface contamination. Designed 12 nm thick film of silver were grown on the polar faces of ZnO (see section 2.2) to obtain (i) a continuous protective capping for the sample transport which is (ii) electrically percolated and (ii) thin enough to have a reasonable counting rate during the photoemission measurements. One ZnO(0001)-Zn bare surface was also analysed *in situ* after a few cycles of sputtering and annealing but at a slightly lower temperature (T =1100 K) compared to capped ZnO (T =1400 K) due to technical limitations of the beamline furnace and in a poorer vacuum (a few 10^{-9} mbar). By varying the photon energy from 2.1 to 8.4 keV and using take-off angles of $82-87°$ and $50°$, core level spectra were taken at different escape depths in ZnO ranging from 2.1 to 10.1 nm. The corresponding inelastic mean free path have been obtained from the well-known Tanuma, Powell and Penn formula [23, 248]. But one has to keep in mind that the probing depth is much higher since electrons go through the 12 nm thick silver overlayer. The binding energy scale was corrected with respect to the Ag $3d$ and Au $4f$ core levels used as references to define the position of the Fermi level. Electrical contact between the metallic sample holder and the

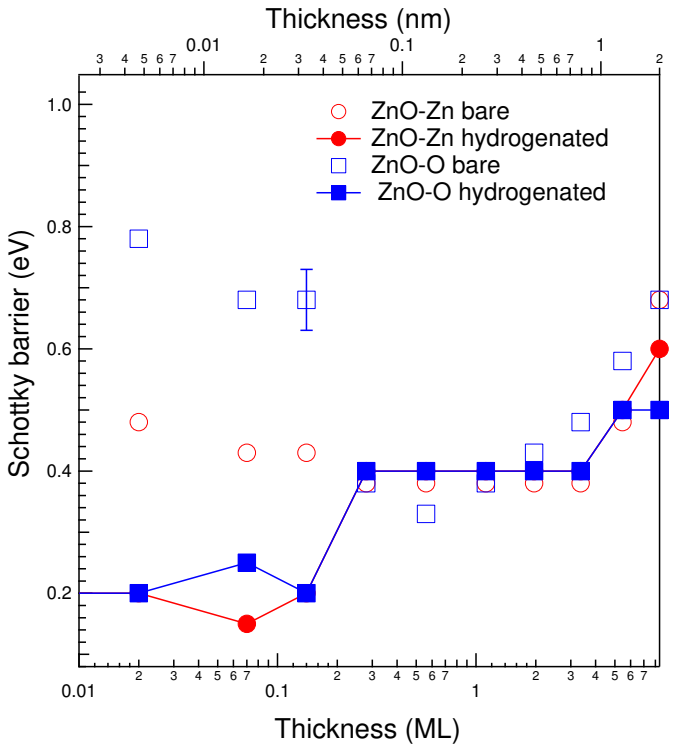

Figure 2.38: Variation of the Schottky barrier height as a function of silver film thickness on ZnO polar crystals. The value is determined through the difference between the oxide valence band edge and the Fermi level position. The typical error bar of such a determination is 0.05 eV.

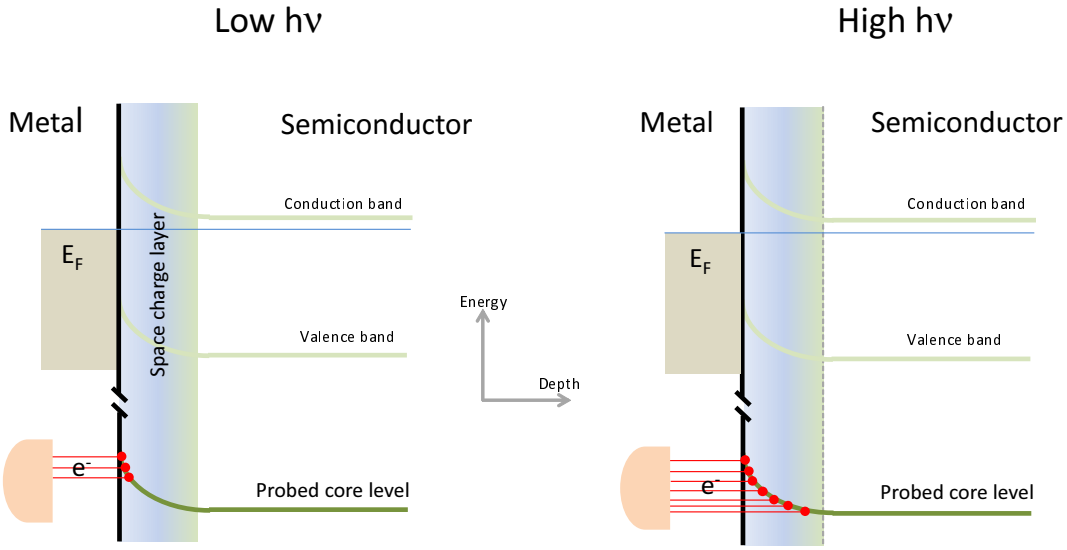

Figure 2.39: Principle of band bending measurements using HAXPES. Due to the electric field, bands and core levels are bent, here upwards. Photoelectrons coming from deeper layers are therefore shifted to lower binding energy. This shift is probed by changing the photon energy $h\nu$ and the photoelectron inelastic mean free path.

silver films was ensured by metallic clamps and/or conductive paste while the Au $4f$ core level spectra were recorded on an ancillary gold foil reference electrically connected to the sample holder. These calibration of binding energy scale were found to be fully consistent, as shown in Fig. 2.40.

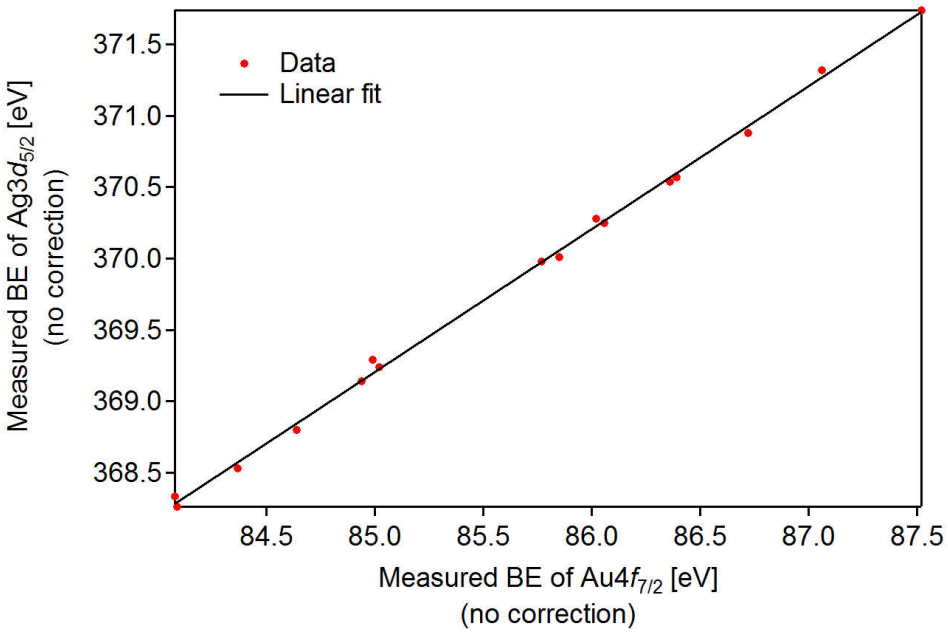

Figure 2.40: Comparison of references used for binding energy calibration: measured positions of the Ag 3 $d_{5/2}$ and Au $4f_{7/2}$ core levels positions.

2.4.1.2 Data analysis: band bending-dependent peak position and broadening

An HAXPES core level peak can be fitted by a Voigt function, *i.e.* the convolution of Lorentzian and Gaussian peak shapes. The former is determined by the lifetime of the core level while the latter encompasses various phenomenon among which the instrumental resolution of the analyser and of the monochromator and potential heterogeneities in the sample. When charge transfer occurs at an interface of a semi-conductor with a metal or even due to surface states, the resulting macroscopic electric field build up shifts the band structure with depth leading to the so-called band bending. In photoemission, it induces a depth-dependence of the core level positions as well as an extra-broadening of peak width. For the sake of the present analysis, it will be assumed in this section that the band bending contribute to the Gaussian broadening of the peak, even if the peak shape cannot be fully reproduced by the Voigt shape in presence of the band bending (see section 4.2). Given the constant Lorentzian width for the same core level, one is left with the Gaussian width which varies for different photoelectron escape depths.

In order to extract broadening related to the band bending, one has to estimate the other contributions and subtract them from the total Gaussian width. If inhomogeneities of potential can be neglected in the case of a ZnO monocrystals, the main contribution stems from instrumental resolution given by: (i) the width of the monochromator line and (ii) the resolution of the analyser. In the present measurements, the analyser settings (slit aperture/pass energy) were kept constant for all experimental points but the resolution of the monochromator varied for the different crystals (Si(111) and Si(311) and the harmonics) and photon energies used. Since those values have not been tabulated for all photon energies, the total experimental resolution had to be evaluated with the help of the gold foil reference spectra. Within negligible potential inhomogeneity in the foil, the Gaussian width of the Au $4f$ peaks is a good estimate of the experimental resolution. The case of a 2.1 keV photon energy is a good illustration. For slit width of 0.5 mm and pass energy of 200 eV, the analyser resolution is 0.25 eV. At a photon energy of 2.1 keV, the monochromator resolution using the Si(111) crystal is about 0.21 eV according to the beamline calibration [15, 16]. This gives a total experimental resolution of 0.33 eV very close to the Gaussian FWHM$_G$ of the Au $4f$ doublet that varies from 0.33 to 0.38 eV at beam energies of 2.05-2.1 keV. Therefore, the values of Gaussian contribution

to FWHM of the Au $4f$ core level (Fig. 2.41) were used systematically as the experimental resolution and subtracted from the Gaussian widths of the Zn $2p_{3/2}$ peak in order to obtain the peak width related to the band bending.

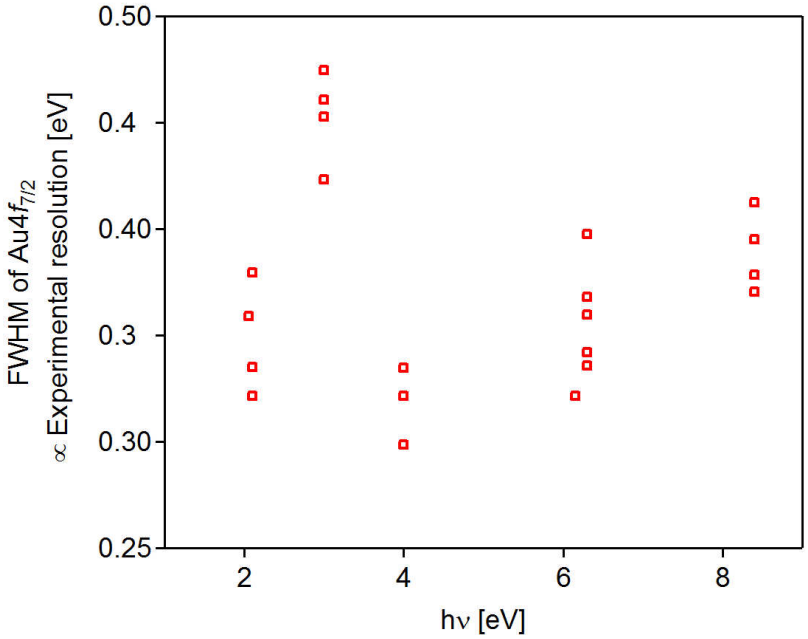

Figure 2.41: FWHM of the Gaussian contribution of the Au $4f_{7/2}$ core level as a function of the selected photon energy. It is used herein as the experimental resolution for the different studied samples.

The results of the band bending measurements that is to say of the evolution of the Zn $2p$ peak position and its FWHM after subtraction of the experimental resolution are gathered in Fig. 2.42. Data have been plotted as a function of the escape depth of the photoelectron in ZnO. All the studied samples exhibit a decrease by ~ 0.5 eV of the Zn $2p$ binding energy when increasing the probing depth corresponding to an upward band bending close the interface and a depleted region in the ZnO semiconductor. The measured binding energies for the largest escape depth overlap at a value of 1021.5 eV corresponding to the bulk value. A change in peak width goes with the observed shift: the peak widths are larger near the interface where the band bending is the most significant. The difference between all samples is however within the error bars with a tendency of larger band bending on ZnO-O than ZnO-Zn and on hydrogenated surface than on native ones.

Finally, beam induced surface photovoltage could bias the measurements [263, 264]; the photo-excitation of an electron-hole pair creates dynamically carriers that are split by the electric field in the charge space layer and that screen it whatever the bending direction. However, it can be excluded since (i) by changing the photon flux by 50%, no shift of Zn $2p$ was observed, (ii) that UPS (section 2.3.6) and HAXPES (section 2.4.3) lead to similar Schottky barriers values and (iii) that photovoltage impacts much more p-type doped materials at low temperature [264].

2.4.2 Modelling of band bending effects on photoemission

Band alignment at Ag/ZnO interface and charge transfer lead to the formation of a space charge layer and to a bending of bands the profile of which is indirectly probed by the position of the Zn $2p$ core level in HAXPES. In a similar way to previous works HAXPES performed on semi-conductors [265, 266, 267], to extract quantitative information from Fig. 2.42, the photoemission line shape was simulated by taking into account the damping of the emitted photoelectron signal and the shift with depth of the core level due to band bending:

$$I_t(E) = \frac{1}{\lambda}\int_0^{+\infty} e^{-z/\lambda} I(z,E)dz \tag{2.4}$$

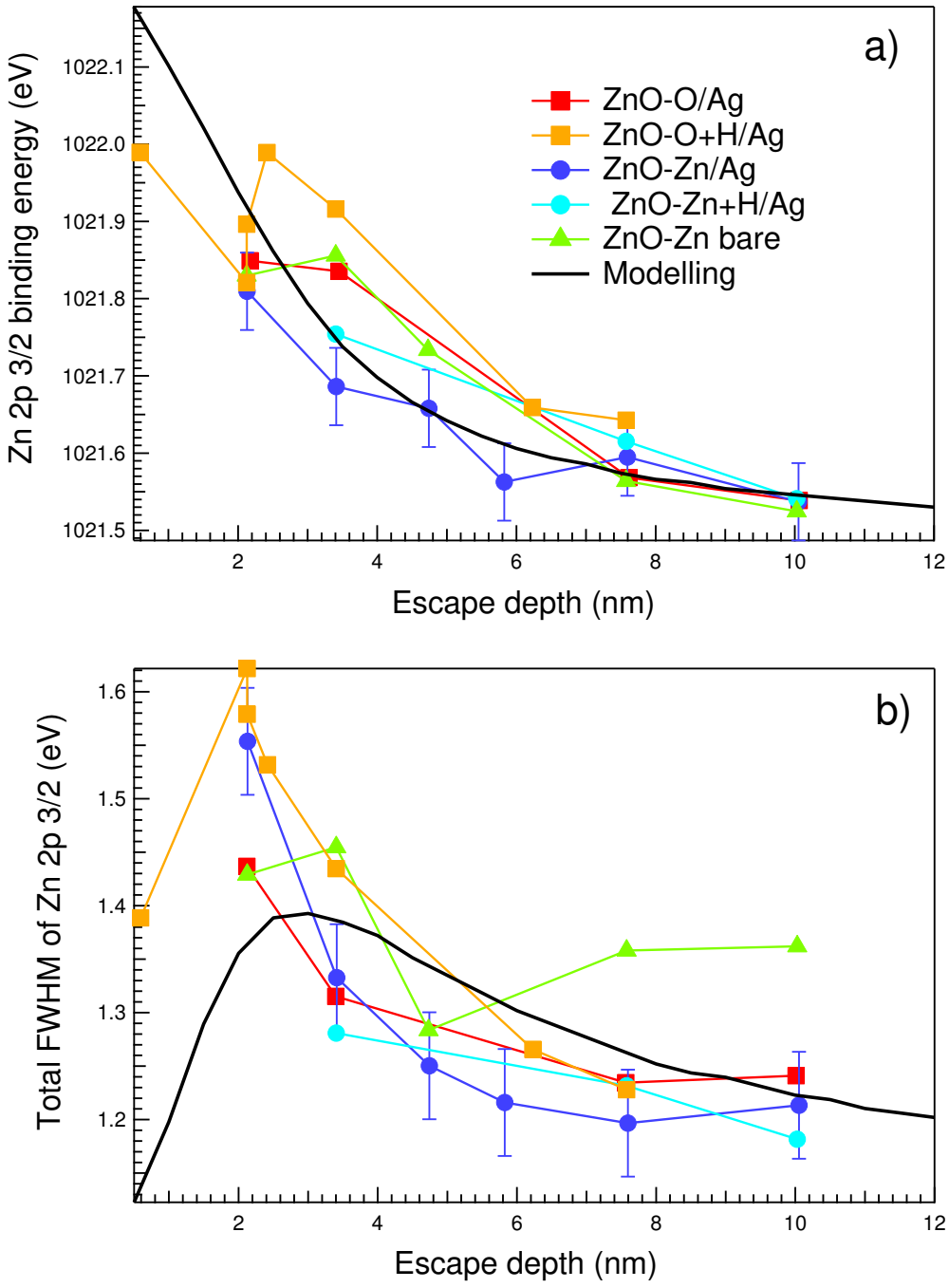

Figure 2.42: Band bending as measured by high energy photoemission: (a) change of the Zn $2p$ peak position and (b) FWHM after subtraction of the experimental contribution derived from Au $4f$ core level analysis for different samples: Ag/ZnO-O, Ag/ZnO-Zn, Ag/ZnO-O (H-doped) and Ag/ZnO-Zn (H-doped) and for bare ZnO-Zn. Bold black line corresponds to modelling (see Section 2.4.2). The error bars are of the order of 0.05 eV.

where E is the binding energy, λ is the escape depth of the photoelectron and $I(z,E)$ is the chosen line shape of the core level. It has been chosen herein to be Gaussian or Lorentzian:

$$I(z,E) = \frac{1}{\sigma_i\sqrt{2\pi}} e^{-\frac{(E-E_0(z))^2}{2\sigma_i^2}}, \quad I(z,E) = \frac{\pi}{\sigma}\frac{1}{(E-E_0(z))^2+\sigma_i^2}. \tag{2.5}$$

The corresponding FWHM are given by $\mathrm{FWHM}_{G,i} = 2\sqrt{2\ln 2}\sigma_i$ for the Gaussian peak and $\mathrm{FWHM}_{G,i} = 2\sigma_i$ for the Lorentzian peak; σ_i will be called hereafter intrinsic broadening. $E_0(z)$ is the depth dependent position of the core level which depends on the detailed characteristics of the charge distribution near the surface. It is assumed herein to be given by the solution of the Poisson equation for an homogeneous semiconductor with a depletion layer empty of carriers up to a thickness W and a constant ionized donor density N_d. Although questionable according to UPS measurements, the depth impacted by interfacial states (or their density) is assumed to be negligible at the length scale probed by HAXPES. This leads to the following parabolic dependence:

$$E_0(z) = E_0 + V_{bb}\left(1 - \frac{z^2}{W^2}\right) \quad \text{for} \quad z < W \quad \text{and} \quad E_0(z) = E_0 \quad \text{for} \quad z > W. \tag{2.6}$$

E_0 is the binding of the photoemission potential reached in the bulk above the depth W of the space charge layer which is assumed to be fully depleted and homogeneously filled with ionized doping centres N_d. V_{bb} is the value of band bending *i.e.* the difference of level position between surface and bulk. Positive $V_{bb} > 0$ values correspond to an upward band bending and negative $V_{bb} < 0$ to a downward one. In this model of parabolic band bending, the width of the space charge layer is given by: $W = \sqrt{2\epsilon(0)V_{bb}/eN_d}$, where $\epsilon(0)$ is the static dielectric function of the semiconductor.

2.4.3 Fit of experimental data and simulation of line shapes

The analysis focused only on the two indicators of Fig. 2.42 , namely the dependency with escape depth of the Zn $2p$ core level position and of the extra-contribution to broadening induced by band bending.

Because of the moderate dependency on the sample preparation which parallels the UPS conclusions, only main trends were reproduced without trying to distinguish samples. For each set of parameters (W,V_{bb},E_0,FWHM_{iG}) and for a given escape depth λ, the expected profile of the peak was calculated according to Eqs. 2.4-2.6; the obtained position of the peak and its FWHM were directly compared to experimental results of Fig. 2.42. The best qualitative agreement that could be obtained is shown in Fig. 2.42 as a bold black line and corresponds to the following parameters: $W = 2.75 \pm 1$ nm, $V_{bb} = 0.75 \pm 0.1$ eV, $E_0 = 1021.47 \pm 0.05$ eV, $\mathrm{FWHM}_{iG} = 1.1 \pm 0.05$ eV ($\sigma_i = 0.47 \pm 0.02$ eV). Results are given for an intrinsic Gaussian base lineshape for which definitively better agreement could be obtained compared to Lorentzian. E_0 acts mainly as an offset of the curve. The corresponding simulated spectra are compared to the experimental ones in Fig. 2.43 after normalization to maximum.

To reinforce these findings, to demonstrate the sensitivity of the analysis and to derive reasonable error bars, sets of theoretical curves were calculated, convoluted with a Gaussian peak of FWHM of 0.35 eV to mimic the experimental resolution and compared to simulations with the best set of parameters. Fig. 2.44 gathers the calculated evolution of the first three moments that characterize the peak namely:

- its centroid $\mu = \int E I_t(E) dE$,
- its standard deviation $\sigma = \int (E-\mu)^2 I_t(E) dE$,
- its skewness $\gamma = \int (E-\mu)^3 I_t(E) dE/\sigma^3$.

Skewness quantifies the peak asymmetry; positive value $\gamma > 0$ corresponds to peak with a tail on the right side of the peak and negative values on the left side. For moderate $\gamma < 0$ values, the centroid μ is very close to the position of the peak maximum and the standard deviation σ is directly connected to its FWHM.

Besides the expected shift of the peak with probing depth, the present modelling of band bending leads to a complex dependence with λ of its broadening (standard deviation) and of its asymmetry (skewness). Depending on W, V_{bb} and FWHM_{iG}, the peak can be left side or right side asymmetric (or sometimes nearly symmetric) with a transition as a function of λ. This is fairly well illustrated with the three examples of Fig. 2.45 that correspond to extreme cases of Fig. 2.44. An apparent peak doublet is sometimes observed

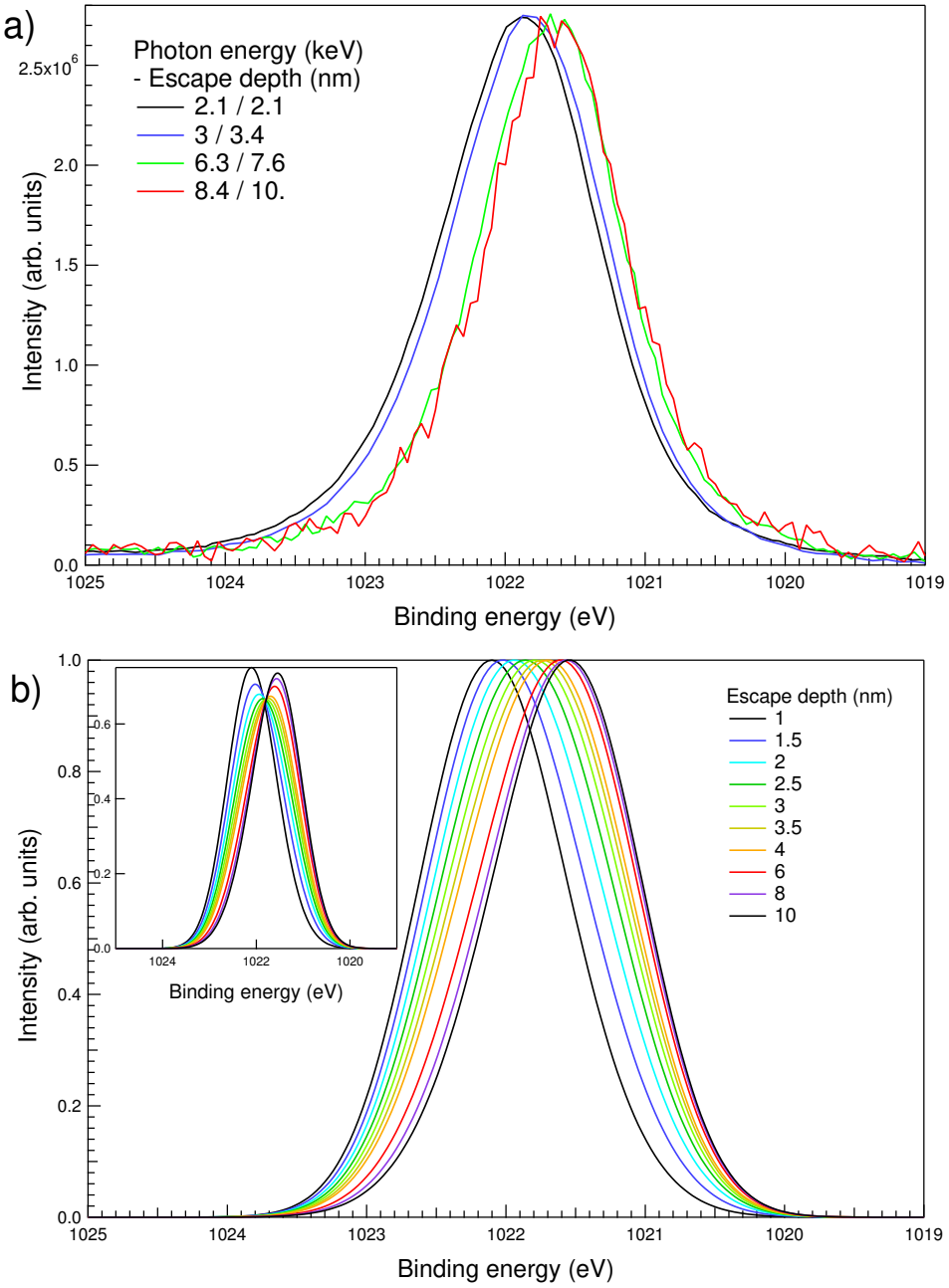

Figure 2.43: Evolution with escape depth of (a) the Zn $2p_{3/2}$ profile of the Ag/ZnO(0001)-Zn and (b) the simulated one normalized to their maxima. The inset shows the unnormalized peak.

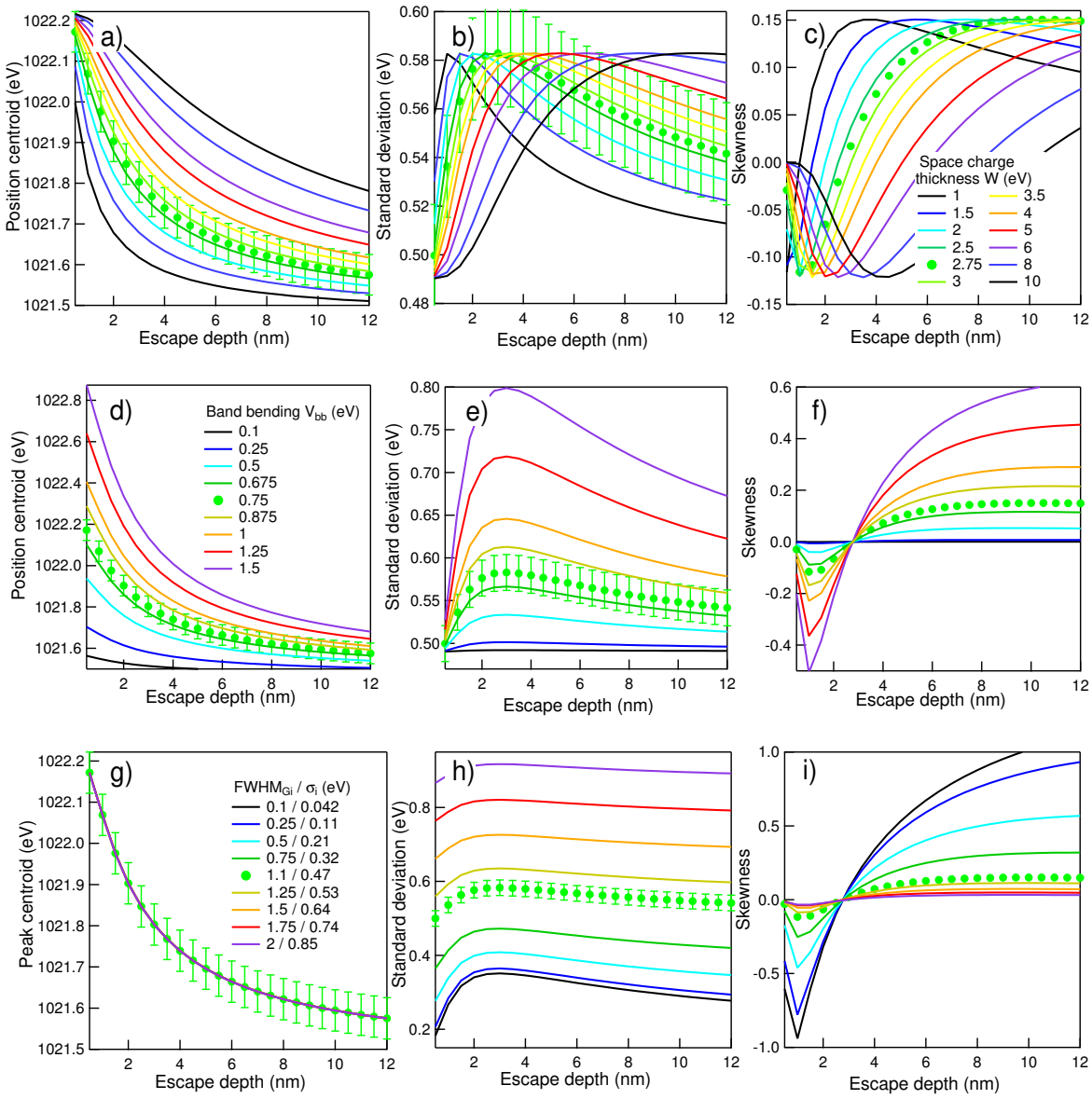

Figure 2.44: Simulation of band bending effects on the three first moments of spectral line shape: (a,d,g) centroid μ; (b,e,h) standard deviation σ; (c,f,i) γ skewness. The role of (a,b,c) space charge layer W, (d,e,f) of the amplitude of band bending V_{bb}, and (g,h,i) of the intrinsic broadening $\mathrm{FWHM}_{Gi} = 2\sqrt{2\ln 2}\sigma_i$ are compared to the best agreement (filled circles) to data (Fig. 2.42) that is to say to $W = 2.75 \pm 1$ nm, $V_{bb} = 0.75 \pm 0.1$ eV, $E_0 = 1021.47 \pm 0.05$ eV, $\mathrm{FWHM}_{iG} = 1.1 \pm 0.05$ eV ($\sigma_i = 0.47 \pm 0.02$ eV). Notice that the centroid of the peak (g) is completely independent of the intrinsic broadening σ_i contrary to the peak maximum.

(see Fig. 2.45a-c) with a transfer of intensity from surface to bulk-like peak position with probing depth. This asymmetry can be much more moderate (see Fig. 2.45a) as in the experimental cases. In passing, this is an extra-constraint to be fulfilled when seeking the best agreement with experiments

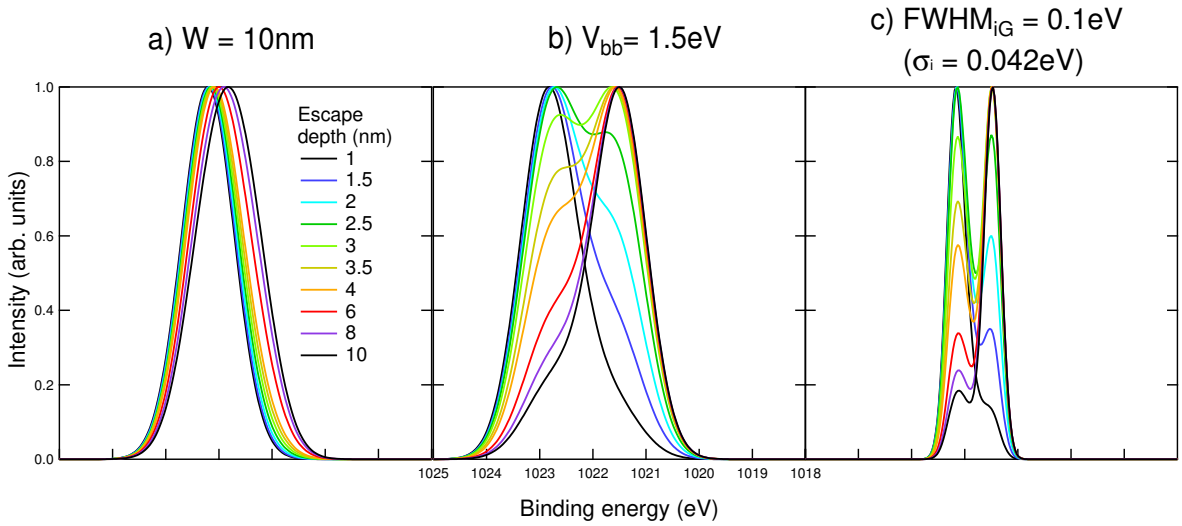

Figure 2.45: Evolution of simulated peak profile versus the escape depth illustrating extreme cases of band bending: (a) $W = 10$ nm, $V_{bb} = 0.75$ eV, FWHM$_{iG} = 1.1$ eV , (b) $W = 2.75$ nm, $V_{bb} = 1.5$ eV,FWHM$_{iG} = 1.1$ eV, (c) $W = 2.75$ nm, $V_{bb} = 0.75$ eV, FWHM$_{iG} = 0.1$ eV. Peaks have been convoluted by a Gaussian that accounts for experimental resolution FWHM$_S = 0.35$ eV. Peaks have been normalized to their maximum.

2.4.4 Position of the Fermi level and discussion

Using tabulated static dielectric function of ZnO $\epsilon(0) = 8.65$ [96], the band bending ($V_{bb} = 0.75 \pm 0.1$ eV) and space charge layer width ($W = 2.75 \pm 1$ nm) values obtained from HAXPES analysis give a large ionized donor concentration of $N_D = 2V_{bb}\epsilon_0\epsilon(0)/eW^2 = 1 \pm 0.8\, 10^{20}$ cm^{-3}. This value is greater than the density of states in the valence band at $T = 300$ K in the parabolic band model $N_c = 2(2\pi m_e m^* kT/h^2)^{3/2} = 3.\, 10^{18}$ cm^{-3} with a known effective mass of $m^* = 0.24$ [96, 262]. according to the semi-conductor theory [181, 182], this would put the Fermi level of ZnO in the conduction band of the material, leading to a degenerated semiconductor. Somehow, this finding agrees with the value of the Schottky barrier ($\phi_{SB,Ag-ZnO} = 0.5-0.7$ eV; see Fig. 2.38) found by UPS for the thickest studied deposit; indeed, if one assumes that the HAXPES measured band bending of $V_{bb} = 0.75$ eV is already achieved for the last deposit studied in UPS (8 ML; Figs. 2.33-2.34), the Fermi level would again lie in the conduction band. By referring only to the variation of the band bending ΔV_{bb} measured from the position of the ZnO valence band edge upon deposition (Fig. 2.34), the same hypothesis would lead to an absolute upward band bending of $V_{bb,ZnO-O} = 1.1$ eV, $V_{bb,ZnO-Zn} = 0.9$ eV for the as-prepared surfaces and of $V_{bb,ZnO-O+H} = 0.35$ eV, $V_{bb,ZnO-Zn+H} = 0.3$ eV for the hydrogenated ones. This band bending which corresponds to roughly of 1/3 of the band gap is among the largest found in the literature (see Table 2.2). This depleted surface may explain the poor surface conductivity and the imaging difficulties invoked in tunnelling spectroscopy. From the UPS position of the conduction band relative to the Fermi level (Fig. 2.36-2.37), this band bending of the bare surface put indeed the Fermi level in the conduction band at $E_{F,ZnO} - E_C = 0.17$ eV for the as-prepared surface and at $E_{F,ZnO+H} - E_C = 0.3$ eV for the hydrogenated ones. Within the error bars of such a determination which is at least of 0.1 eV, those values are in good agreement and show the consistency of the measurements on the various substrates. In a regime of degenerated semiconductor[181, 182], one can not any more approximate the Fermi distribution, that accounts for the thermal occupancy of carriers in the conduction band, by the Boltzmann function. Actually, in the parabolic band model, the expression of the carrier density is given by:

$$n = N_c \mathcal{F}_{1/2}(\eta) \quad \text{with} \quad \mathcal{F}_{1/2}(\eta) = \frac{2}{\sqrt{\pi}} \int_0^\infty \frac{\sqrt{\epsilon}}{1 + e^{\epsilon - \eta}} d\epsilon, \tag{2.7}$$

where $\eta = (E_F - E_C)/kT$ and $\epsilon = (E - E_C)/kT$. The tabulated function $\mathcal{F}_{1/2}(\eta)$, known as the Fermi-Dirac integral of half-order, gives for $\eta = 9.5 \pm 3$ (an average value between bare and hydrogenated surfaces) a

carrier density of $n = 0.7 \pm 0.3\, 10^{20}$ cm^{-3}, an order of magnitude that matches with the ionized donor density found from Debye length and band bending. This value is higher than the measured carrier concentration in as-received crystals of the same supplier, which is in the range of 10^{15-17} cm^{-3} according to literature [103, 139, 168, 268]. Such an increase by several orders of magnitude can only be explained by the method of crystal preparation by sputtering and vacuum annealing which should induce a under-stoichiometry and a large quantity of bulk defects. Compared to bulk atomic density of $N_{ZnO} = 4.2\, 10^{22}$ cm^{-3}, assuming one electron released per defect, the found donor density corresponds to approximately one atom over 400 or to a stoichiometry of $ZnO_{0.9975}$, not a surprising value compared to other reducible oxides such as TiO_2 prepared in similar conditions [188, 269]. Therefore, determination of absolute band bending from assumed bulk carrier concentration is questionable if sample preparation is involved [61, 139, 146, 147, 153, 159, 160, 167, 168]. Finally, from the HAXPES analysis, one can deduce the corresponding screening charge in the space charge layer: $Q_D \simeq WN_D = 2.5 \pm 3.\, 10^{13}$ cm^{-2}. The absence of accumulation layer after hydrogenation at the opposite of some results of the literature may be explained by the degeneracy of the bulk of the ZnO substrate [61, 146, 147, 158, 159, 163] (see section 2.1.3).

Within the uncertainties of the measurements, the band alignment of the contact between a thick Ag film and ZnO (Fig. 2.46) is independent of the surface orientation [222] or preparation and seems to be dominated by the interface states induced by metal deposition (see Fig. 2.36-2.37) and not really by a pinning of the Fermi level by intrinsic defects (oxygen vacancies) as already suggested [103, 268]. This finding agrees with all the Ag/ZnO Schottky barriers (0.7-1 eV) of the literature [102, 215, 221, 222]; the measured $\phi_{SB,Ag-ZnO}$ are around 0.2-0.3 eV higher than ours but are measured on a semiconductor with a native doping (10^{15-17} cm^{-3}) which sets the Fermi level 0.2-0.3 eV below than our.

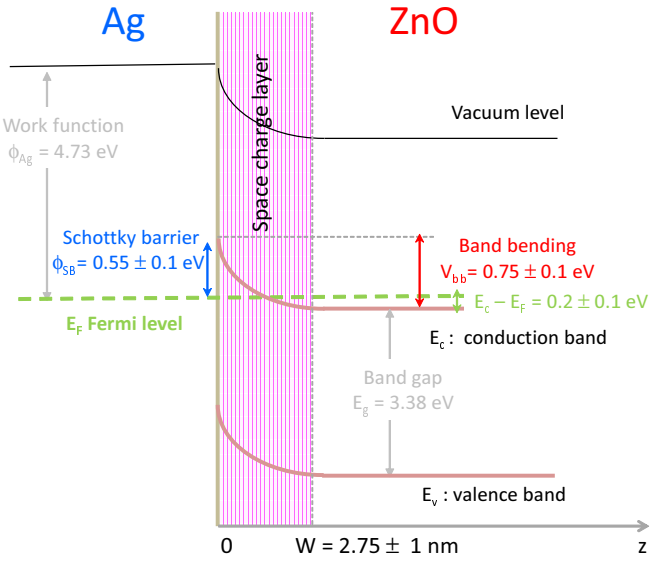

Figure 2.46: Band alignment of Ag/ZnO as deduced from the present photoemission study. The contact is of Schottky type with a barrier height of 0.55 ± 0.1 eV.

2.5 Summary and conclusions

Using a surface science approach, the present chapter focused on the electrical contact between the polar surfaces of ZnO.

Silver films from submonolayer to percolated thick films were grown by thermal evaporation on O- and Zn-terminated surfaces. Surfaces, clean on a spectroscopic point of view, with sharp (1×1) LEED pattern were prepared by sputtering-annealing cycles in vacuum.

Electron diffraction techniques showed that silver grow epitaxially with (111) hexagon-on-hexagon orientation. At least on ZnO(0001)-Zn, through STM and a comparison with ZnO$(10\bar{1}0)$, this orientation is explained by a preferential nucleation and alignment of dense rows of silver along the polar $[10\bar{1}0]$ step edges of the triangular/pits morphology of this surface. In the sub-monolayer thickness range, 2D clusters partially

strained are formed up to a critical coverage. Above, ABC and BCA stacking variants appear. While this scenario of growth process is partially confirmed by differential reflectivity, the existence of the plasmon resonance since the early stage of growth demonstrate the metallicity of the particles.

Different photoemission techniques from ultraviolet to hard X-ray excitations were combined to determine the evolution of work function, band bending, ionization energy and Schottky barrier during silver growth and the influence of the hydrogenation.

While as prepared surfaces seem hydroxyl free, hydrogen etches the ZnO(0001)-Zn surface by breaking Zn-O back bonds, creating hydroxyl groups and releasing metallic zinc which is detected by its Auger fingerprint and by the states it induces in the band gap. On the O-terminated surface, only hydroxylation occurs. A final coverage in the range of 0.3 ML is achieved on both orientations. The hydrogenation process is accompanied by a strong downward band bending and a reduction of the work function which is assigned to the donor character of OH groups although subsurface diffusion is not to be excluded. Bands are bent upwards by around 1 eV on as-prepared surface and only by around 0.3 eV after hydrogenation. Surface preparation leads to a defective degenerated substrate with a Fermi level above the conduction band. Therefore, the performed hydrogenation does not allow to switch from a depleted to an accumulation layer as expected from literature.

In the submonolayer regime, silver induces strong variations of band bending and work function, similar to hydrogen adsorption in terms of direction. But the variation of ionization energy suggests a different surface dipole orientation and charge transfer on the two terminations in agreement with their surface polarity: cationic on ZnO-O and anionic on ZnO-Zn. These findings parallel the preferential nucleation along step edge. But after this initial stage, the adsorption of silver is neutral. Hydrogenation makes both surfaces identical. The progressive shift of the Ag $5sp$ states towards the Fermi level is assigned to a final-state effect in nanoparticles. In parallel, the confinement along the perpendicular direction in flat top particles generates confined Ag $4d$ states. The electrical contact at Ag/ZnO is of Schottky type with a barrier height around 0.5-0.7 eV which is independent of the surface termination or its hydrogenation for thick films. It seems to be dominated by the metal induced gap states.

Chapter 3

ZnO thin films with controlled orientation grown by radio frequency magnetron sputtering

In this chapter, the growth and properties of ZnO films deposited on Si wafers by Radio Frequency (RF) magnetron sputtering are studied. Deposition parameters, namely substrate temperature and bias voltage are explored with the goal to control the orientation of the ZnO layers.

The chapter is structured as follows. A brief overview of ZnO applications, as well as different ways to detect the polarity of ZnO monocrystals and thin films are reviewed in Section 3.1, which ends with a description of a RF magnetron sputtering method that can be used to produce ZnO thin films with a chosen orientation. Section 3.2 presents the details of depositions and characterization tools used. Phenomena influencing the ZnO growth on Si are discussed in Section 3.3. The resulting film microstructure (crystallinity and grain size) and defects are presented in Section 3.4. Section 3.5 is dedicated to the exploration ZnO orientation diagram. The chapter ends with the Conclusions (Section 3.6).

3.1 Introduction: ZnO thin films and polarity

3.1.1 Context

Peculiar physical and reactive properties of ZnO have found a wealth of applications in multiple material forms (powders, layers, nano-objects) and in numerous fields from electronics, detectors and sensors to catalysis [95, 96, 99]. ZnO is used as a UV absorber in sunscreens due to its relatively large band gap; its bio-compatibility and transparency for visible light is exploited in contact lenses. Its rather high electrical conductivity when doped with Al or F results in a wide use of ZnO layers as transparent electrodes (in solar-cells, for example). ZnO piezoelectric properties are also exploited in transducers. Finally, nowadays, ZnO is seen as the next generation optoelectronic material due to its large exciton binding energy.

Due to the relatively easy control of its microstructural properties and transparency, ZnO is also used in optical coatings developed by the glass industry. This chapter concerns the use of ZnO thin films as a seed layer for the growth of silver in low-emissive coatings. Such products are elaborated by sputter-deposition on glass plates. Beyond its versatility in terms of deposited material (metals, oxides, nitrides), this growth technique allows for a reliable control of thickness homogeneity, oxidation, density and flatness of complex stacks on large area (see Section 1.1.2 for more details). In low-emissive silver-based coatings, the metal film should be thin enough (below 15 nm) to be transparent for the visible light but conductive enough to effectively reflect the infrared radiation. Over the years ZnO layer was found to be the best candidate in terms of silver adhesion, crystallization and optical properties. Sputter-deposited ZnO films satisfy a number of requirements. The weak roughness of thin ZnO layers ($\sim$5nm) is an advantage for a smooth Ag over-layer growth. Favoured by the low band gap [201], the adhesion between Ag and ZnO is ensured by a local epitaxy between ZnO(0001) and Ag(111) planes [193, 194] (see Chapter 2). Fortunately, ZnO films are naturally crystallized even on amorphous substrates and textured with their c-axis perpendicular to the surface. Of course, mastering the properties of the ZnO layer is a key to further control the performance of the whole product. Unlike evaporation, sputter-deposition leads to higher deposition rates and film microstructures

which are highly out-of-equilibrium. Film growth and properties can be influenced by a large number of deposition parameters (see Section 1.1.2). In this study, ZnO film polarity (introduced next in Section 3.1.2), unknown and, thus, neglected in case of sputtered films so far, is explored.

3.1.2 ZnO thin film polarity detection and control

Zinc oxide is a II-VI semiconductor crystallizing under ambient conditions in the hexagonal wurtzite structure [95]. The alternation along the c-axis of planes of Zn cations and O anions charged positively and negatively results in a dipole moment in the bulk unit cell. As a result of this ion stacking, one of the surfaces of a bulk sample should expose a Zn-plane while the other side should be terminated by an O-plane. The two surfaces are called the c+, Zn-terminated or ZnO(0001)-Zn and the c-, O-terminated or ZnO$(000\bar{1})$-O. Such surfaces are polar; they are unstable due to the macroscopic electric field that develops across the sample and they require a mechanism of charge compensation to avoid surface energy divergence, as detailed in Chapter 2 and in Refs. [53, 54, 55]. The compensation mechanism can be face-dependent. Cation vacancy formation or adsorption of foreign atoms such as hydrogen have often been invoked for the Zn-face and O-face of ZnO single crystals (see review in Chapter 2).

It is not surprising that the two polar surfaces have remarkably different properties and that their nature impacts the bonding strength to the neighbouring layer [270]. Before controlling and exploiting the polarity of thin films, the first question that arises is the way to characterize it. The etching rate by acid solutions is dramatically different for the two faces [271, 272]. The difference in roughness of the resulting faces became even a standard method to differentiate the two surfaces of a single crystal. It is important to notice that this macroscopic test does not work on nano-crystalline films due to the important reactivity of ZnO grain boundaries. As reviewed in Ref. [270], apart from the wet chemical attack, structural and mostly spectroscopic methods were developed to distinguish the two surfaces. Transmission electron microscopy techniques are able to determine the orientation of ZnO crystals with a high spatial resolution. The necessary sensitivity to orientation can be reached with diffracted electrons (in convergent beam electron diffraction or in the low energy electron diffraction techniques) or by direct high resolution imaging with atomic resolution and by channelling-enhanced microanalysis (electron energy loss spectroscopy). Scanning probe microscopy can also be sensitive enough to differentiate the two surfaces based on their particular properties by simultaneously recording some specific tip-surface interactions. X-Ray Diffraction (XRD) technique is relatively insensitive to the orientation, while synchrotron resonant diffraction at a specific edge was used successfully. X-ray photoelectron diffraction was also applied to single crystals and polycrystalline ZnO films [273, 274], but this technique should be coupled with extensive calculations. Finally, low energy ion scattering which is tremendously sensitive to the mass of the atoms of the last atomic plane was also employed but the quantification in the case of a mixed surface termination is not obvious.

Recently, another approach to distinguish the two polar surfaces was proposed based on photoemission spectroscopy of the valence band [275, 276]. It was shown that a characteristic sub-peak appears in the region of Zn $3d$-O $2p$ valence band spectra of the (0001) surface but not in that of the $(000\bar{1})$ surface under X-ray excitation, as shown in Fig. 3.1. This feature was also observed on other wurtzite structures, namely, GaN and InN [277, 278], thus confirming that the nature of the discussed sub-peak is intrinsic to the structure itself. Extensive *ab initio* calculations suggested that the polarity dependence of the valence band feature is associated with a polarization-related photoemission phenomena [277]. If the exact origin of the sub-peak is still not fully understood, it can anyway be used as a fingerprint of the orientation. Interestingly, this spectroscopic method was successfully applied to nano-crystalline films of ZnO deposited by sputtering [279], where the ZnO films had a preferential orientation with either Zn- or O-terminated surfaces exposed to vacuum.

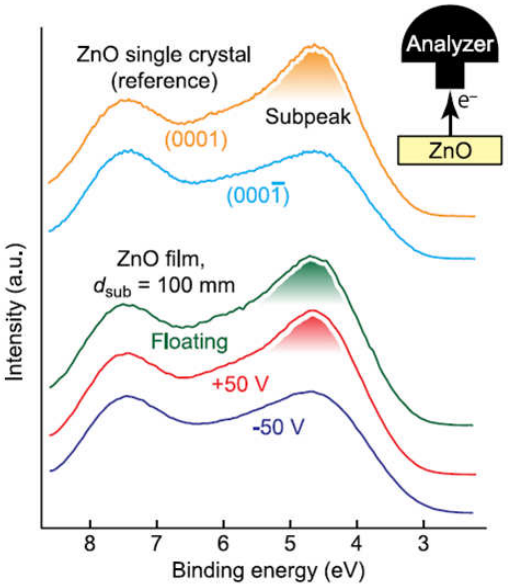

Figure 3.1: X-ray photoemission (Al Kα, $h\nu$ = 1486.6 eV; normal emission) valence band spectra of a ZnO single crystal and of deposited films of different orientations. An enhancement of intensity appears on Zn-terminated surfaces compared to O-terminated ones [279]

The growth of ZnO films by a number of techniques appeared to be rather straightforward as the wurtzite structure is stable under ambient conditions. However, the control of the orientation and polarity of the films is not as easy. When growing epitaxial layers, the polarity can be predetermined either by the crystallographic orientation of the substrate (Al_2O_3 single crystal for instance) or by a crystallized template layer [270]. The nucleation of one or another polarity can also be favoured by doping [280]. But sputtering deposition is rarely used for growth of controlled polarity ZnO films, as poor vacuum conditions are believed to lead to contaminated films. Another reason lies in the rather energetic flow of atoms/ions causing point defects and implantation. One of the parameters which is usually accessible in sputter-deposition is the application of a bias potential to the substrate. Recently, it was shown that a reasonable bias voltage can promote the formation of one of the orientations under certain conditions [279] (Fig. 3.1) even on amorphous substrates. The proposed interpretation of such control is the initial orientation of the dipole of the ZnO molecules by the applied electric field at the moment of nucleation. With this method, the orientation of the ZnO grains in the nano-films is driven not by the structure of the substrate (which can be amorphous), but by the deposition conditions. In addition, Williams *et al.* showed that once the film starts growing with a chosen orientation, this orientation is conserved even if the sign of the substrate bias changes [279].

In this chapter, the growth of ZnO films by Radio Frequency (RF) sputtering is studied, and the deposition conditions to master the ZnO film orientation [279] are systematically explored and extended. Valence band photoemission is used for polarity identification. The use of a silicon wafer as a substrate already introduced some difficulties into the control of deposition. But the work ended up with a diagram along the temperature and bias axes predicting the orientation of ZnO films. Therefore, this study paves the way to the use of a new level, namely polarity, in the control of Ag/ZnO interface used in optical coatings.

3.2 Samples and experimental protocol

ZnO samples were deposited onto 280 µm thick 2 inches Si(001) wafers, covered by SiO_x native oxide; no specific cleaning procedure was applied before deposition. Intrinsic ZnO films were deposited in MISSTIC chamber (Section 1.1.2) by RF magnetron sputtering from an undoped ceramic ZnO target in Ar plasma (Ar pressure p_{Ar} =9.7 µbar) – pure or with 10% of O_2, at a target-sample distance of 11 cm. The power of the magnetron was kept at 50 W for all depositions. The sample holder was mounted on an electrically isolated arm which allowed applying an external bias voltage and heating. The sample holder temperature was measured and controlled by a thermocouple (see Section 1.1.2) and a pyrometer set on the emissivity of Si. The recipe reported by Williams *et al.* as a way to predefine the polarity of ZnO thin films – substrate

temperature of 500 °C and substrate bias of +50 and -50 V [279] – was chosen as a starting point of this study. Film thickness was measured either by Electron Probe MicroAnalysis (EPMA) (Section 1.2.4) or by X-Ray Reflectivity (XRR) (Section 1.2.3.3) relying on the standard ZnO bulk density.

3.3 ZnO deposition rate and growth mechanism

Fig. 3.2 shows the ZnO thickness as function of deposition time for several growth conditions. Such a graph can be used to deduce the deposition rate and its variation in time. When zinc oxide is grown at room temperature, the growth rate appears to be stable (2.78 nm/min=0.05 nm/s) as the thickness increases linearly with the deposition time.

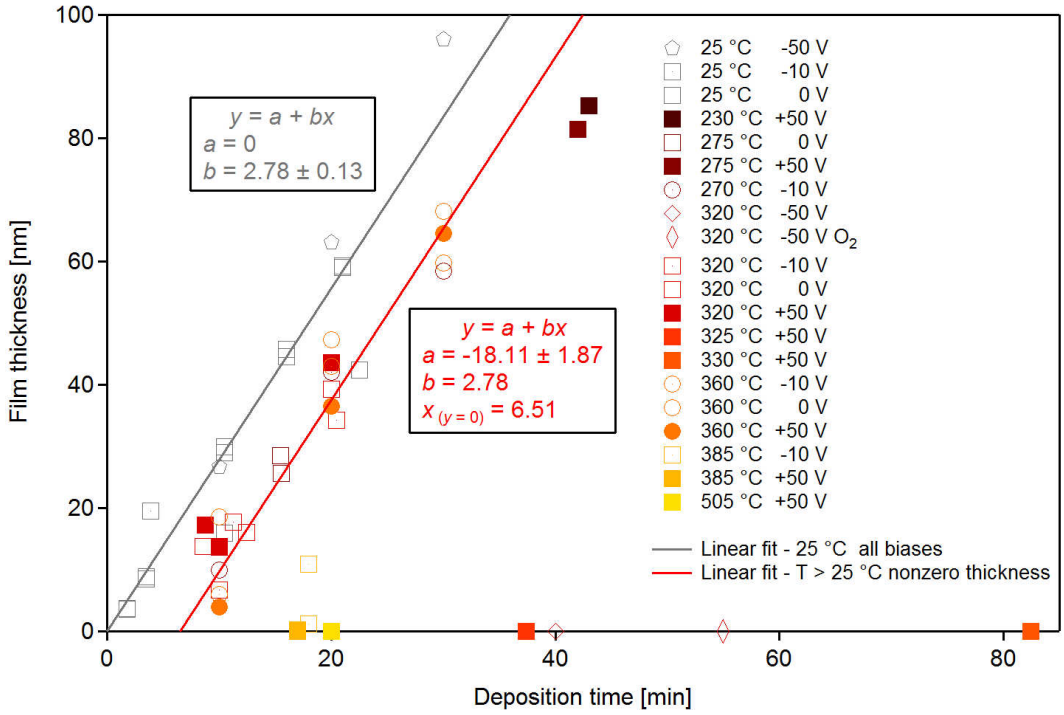

Figure 3.2: Film thickness versus deposition time for all studied samples. Thickness was determined either by EPMA (squares and diamonds) or XRR (pentagons and circles).

However, at elevated temperatures (230-320±70 °C[1]) and for the bias ranging from -10 to +50 V, the deposition rate is much slower at the beginning of deposition (during approximately 7 minutes), before switching to a value close to 0.05 nm/s corresponding to the room temperature value. When the deposition is performed at an elevated temperature (320±70 °C) and at a high negative bias (-50 V), no ZnO is observed on the substrate. The addition of O_2 (10%) does not improve the deposition rate at these conditions (see Fig. 3.2). However, a linear time dependence is observed for a room temperature growth at a -50 V bias.

The reduced deposition rate at the beginning of ZnO growth and the absence of the layer when deposited at -50 V bias pointed at specific mechanisms occurring during deposition. Several additional experiments were carried out with the aim to identify them and to explain such a behaviour. At the first attempt ZnO growth was performed in two steps (Fig. 3.3). The first layer was deposited at 320±70 °C and +50 V for 20 minutes resulting in a ∼30 nm thick film in accordance with results shown in Fig. 3.2. Then, during the next 20 minutes the deposition was continued at the same temperature but at a reversed substrate bias of -50 V. As a result, the thickness of the layer was reduced down to 7 nm.

[1]Hereafter temperature errorbars are given based on temerature calibration results (see Section 1.1.2). Errorbars vary as function of temperature, they are higher at higer temperatures due to the imperfect thermal contact between the substrate and the sample holder.

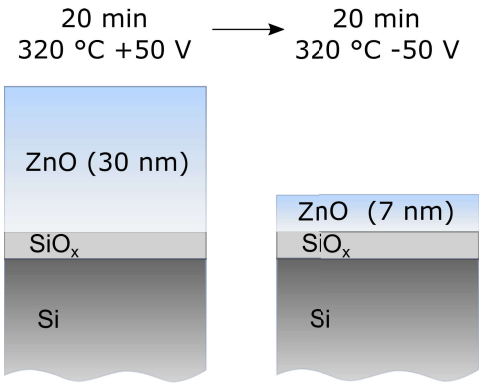

Figure 3.3: Scheme of a stepwise ZnO deposition.

This layer thinning can be explained by a re-sputtering of the existing layer by positive ions (Ar, Zn) accelerated by the sample potential. The process of re-sputtering can be probably set in or intensified due to increased temperature by the following mechanism. Light O atoms are known to be re-sputtered preferentially and this could lead to a Zn-rich surface. Also, at 320 °C the vapour pressure of zinc is of the order of 0.1 mbar [281], which leads to an intense evaporation of Zn atoms and to a complete loss of the layer. At room temperature Zn atoms do not evaporate easily (the vapour pressure of zinc at 25 °C is 10^{-16} mbar) and re-sputtered O atoms can be refilled by the newly arriving atoms.

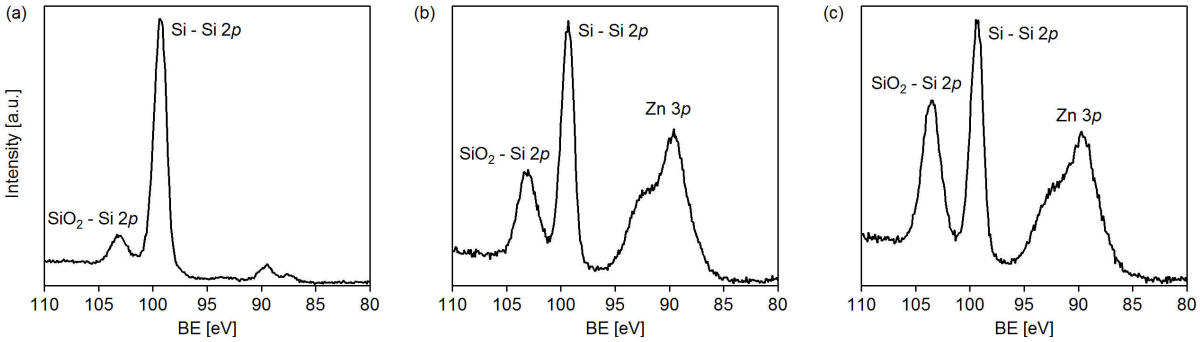

Figure 3.4: XPS spectra (Al Kα, $h\nu = 1486.6$ eV; normal emission) of Si $2p$ and Zn $3p$ regions: (a) a bare Si wafer, (b) a Si wafer after 5 min of ZnO deposition at 360±30 °C and a bias of +50 V, and (c) a Si wafer after 10 min of ZnO deposition at the same conditions.

Since the reduced deposition rate of ZnO at elevated temperatures was also observed for biases from -10 up to +50 V, the above mechanism of re-sputtering cannot be invoked. At this point the knowledge of the composition of the surface after a few minutes of deposition can provide a hint to the governing phenomenon. A ZnO layer deposited at 360±30 °C and +50 V was studied by X-ray Photoemission Spectroscopy (XPS) after several minutes of deposition. Fig. 3.4 shows the region of the Si $2p$ and Zn $3p$ core levels of a clean Si wafer and of ZnO films after 5 and 10 min of deposition. A monotone increase with time of the component corresponding to oxidized Si shifted by ~4 eV from the bulk Si one is obvious. The thickness of SiO_2 layer was estimated from the peak areas assuming an idealized layered structure ZnO / SiO_2 / Si without intermixing. According to Eq. 1.12 and 1.14, XPS intensities I_{SiO_2} and I_{Si} of Si- and SiO_2-related Si $2p$ components can be written as:

$$I_{SiO_2} \propto \rho_{SiO_2}\lambda_{SiO_2} \cdot (1 - \exp(-d_{SiO_2}/\lambda_{SiO_2}))\,, \tag{3.1}$$

$$I_{Si} \propto \rho_{Si}\lambda_{Si} \cdot \exp(-d_{SiO_2}/\lambda_{SiO_2})\,, \tag{3.2}$$

where d_{SiO_2} is the thickness of the SiO_2 layer, $\lambda_{SiO_2} = 3.8$ nm and $\lambda_{Si} = 3.1$ nm are the inelastic mean free paths of Si $2p$ photoelectrons in the corresponding materials excited at a photon energy of 1486.6 eV [249], and ρ_{Si} and ρ_{SiO_2} are the bulk atomic densities of Si and SiO_2 ($\rho_{Si}/\rho_{SiO_2} = 2.2$). The photoionization cross

section σ and the analyser transmission function T are advantageously identical for these peaks. Si $2p$ peak areas were determined by fitting with two Voigt peaks corresponding to Si- and SiO_2-related components, and a Shirley background. Based on the found area fractions, the SiO_2 thickness was derived from Eq. 3.1 and 3.2 as a numerical solution of the following equation:

$$\frac{\rho_{SiO_2}\lambda_{SiO_2}}{\rho_{Si}\lambda_{Si}} \cdot \frac{1-\exp\left(-d_{SiO_2}/\lambda_{SiO_2}\right)}{\exp\left(-d_{SiO_2}/\lambda_{Si}\right)} \cdot \frac{I_{Si}}{I_{SiO_2}} = 1. \tag{3.3}$$

As shown in Table 3.1, the SiO_2 thickness increased by 1.6 nm after the first 5 minutes of deposition and then by additional 1 nm after the next 5 minutes. At the same time the area of the Zn $3p$ peak did not evolve much during the second 5 minutes period (see Fig. 3.4).

Sample	Si [%]	SiO_2 [%]	SiO_2 thickness [nm]
Clean Si wafer	89	11	~0.8
After 5 min	67	33	~2.4
After 10 min	55	45	~3.4

Table 3.1: Fractions of Si-Si $2p$ and SiO_2-Si $2p$ components in the total Si $2p$ area for the Si wafer and ZnO deposited on Si during 5 and 10 min at 360±30 °C and a bias of +50 V, and the estimated SiO_2 thickness.

Oxidation of Si wafer at this elevated temperature is not surprising, since the enthalpy of oxidation is large $\Delta G\,(SiO_2)$ = -880 kJ / mole O_2 [282]. Apparently the rate of this oxidation process is rather high at the beginning of the process and then it is reduced as SiO_2 layer becomes thicker, in a similar way as in Cabrera-Mott description of surface oxidation [187]. The substrate oxidation in combination with Zn evaporation may therefore explain the reduced apparent deposition rate.

However, interfaces between layers may be far from the idealized ones assumed for XPS analysis. The morphology of ZnO layers was studied *ex situ* by AFM (Section 1.2.2.2). AFM topographies of ZnO samples deposited during 5, 10, and 30 min on a hot substrate corresponding to equivalent thicknesses of <1, 13.8, and 64.6 nm (Fig. 3.5) have been scrutinized. After 5 and 10 minutes of deposition, the film was composed of isolated islands, and a large part of the wafer was still uncovered. Therefore, the observed variation of the Si/SiO_2 XPS signal is likely due to the actual thickening of the wafer oxide. Though, an alloying with Zn cannot be excluded.

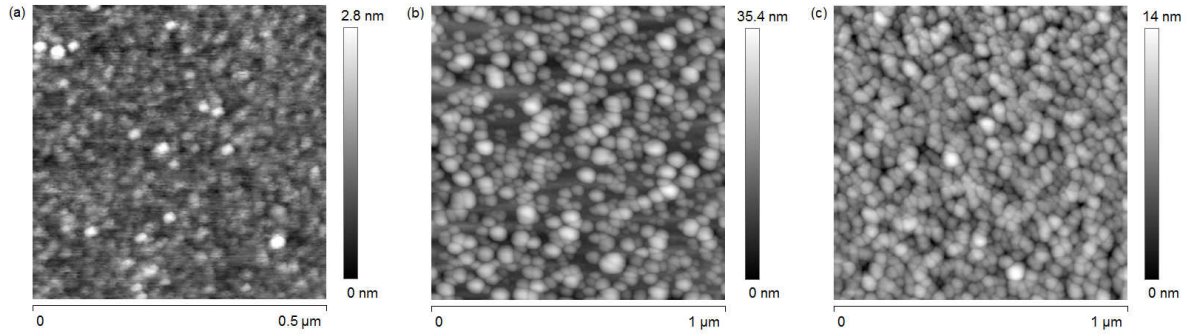

Figure 3.5: AFM images of a ZnO sample after (a) 5, (b) 10 and (c) 30 min of deposition on a Si wafer at 360±30 °C and a bias of +50 V. Corresponding surface rougnesses R_a are 0.26, 4.55, and 1.57 nm.

For comparison purposes an additional ZnO sample was deposited on a bulk fused SiO_2 substrate at 360±30 °C and a bias of +50 V. After 5 minutes of deposition, the film should be about 13 nm thick in case of a constant deposition rate as observed for RT samples. The AFM image (Fig. 3.6b) shows that grains cover the substrate rather well. The XPS scan (Fig. 3.6a) shows no trace of Si $2p$ peaks. Knowing that IMFP of Si $2p$ photoelectrons in ZnO is 2.6 nm [249], this means that the SiO_2 wafer is covered by at least 8 nm of ZnO, in accordance with the constant deposition rate suggestion. These results are consistent with the previous hypothesis. The absence of mechanisms driving oxygen away from the surface of the growing film in case of the SiO_2 substrate (neither oxidation of the substrate nor re-sputtering due to a negative bias) ensures a steady formation of the film and a linear thickening.

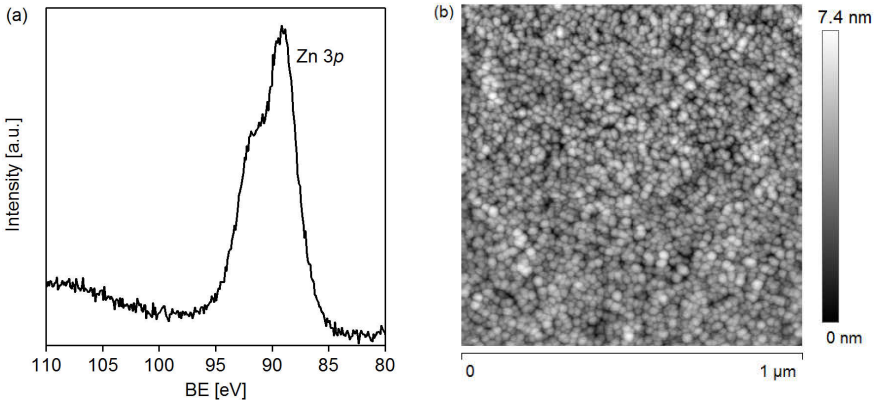

Figure 3.6: (a) XPS spectrum (Al Kα, $h\nu = 1486.6$ eV; normal emission) around Si $2p$ and Zn $3p$ core levels showing the lack of Si $2p$ signal, (b) AFM image of a ZnO film on a bulk SiO_2 substrate after 5 min of deposition at 360±30 °C and a bias of +50 V.

Regarding possible interfacial reactions with the Si wafer, the distribution of species through the film was explored by SIMS (Section 1.2.6). Fig. 3.7 shows a comparison (i) of a 29.9 nm thick sample deposited at RT and a bias of 0 V (Fig. 3.7a) and (ii) of a 28.5 nm thick sample deposited at 275±70 °C and 0 V (Fig. 3.7b). The time scale in this graph is proportional to the sputtered depth into the sample. In both cases, O^- and ZnO^- ions are readily detected all through the layer thickness. For the sample deposited at 275±70 °C the Si-ZnO interface is wider, with a thicker SiO_2 layer. SiO_2Zn^- cluster ions are detected at the interface in both samples. In the ZnO film deposited at 275±70 °C these ions are also detected in the ZnO layer which points at a more extensive interdiffusion at an elevated temperature. Interestingly, the H^- and OH^- levels are almost 10 times higher in the RT-deposited sample suggesting a reduced trapping of these species during deposition on a hot substrate[2], or once exposed to atmosphere.

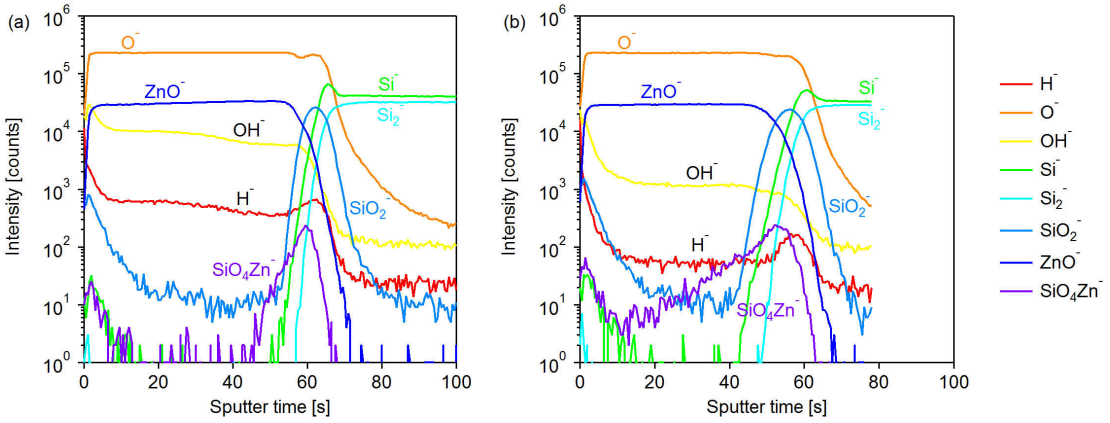

Figure 3.7: SIMS profiles of (a) 29.9 nm ZnO deposited at RT, (b) 28.5 nm ZnO deposited at 275±70 °C both at 0 V bias. H^-, O^-, OH^-, Si^-, Si_2^-, SiO_2^-, ZnO^-, SiO_4Zn^- signals are followed versus sputtering time.

This study shows that heating the sample during deposition can lead to a cascade of phenomena. O re-sputtering, probably present at any substrate temperature, leads to an increase of the time t_{ZnO} needed for a Zn atom to meet an O atom to form a ZnO molecule at the surface and to condense. This time is to be compared to the time a Zn atom resides at the surface before re-evaporation, t_{Zn}. At RT $t_{Zn} \gg t_{ZnO}$ seems to be always true. At a higher temperature the balance is shifted, which results in a reduced growth rate. Oxidation of the substrate itself is another mechanism increasing t_{ZnO} and reducing the probability of formation of a stable ZnO nucleus. However, the O migration into the substrate reduces, as the thickness of the SiO_x oxide increases. At a certain point (after about 7 minutes), this self-limited oxidation allows for the formation of ZnO film. In addition, the presence of SiO_4Zn^- ions in the SIMS analysis indicates the

[2]The residual H^- and OH^- levels in the SIMS chamber are $\sim 10^2$.

formation of a mixed interfacial $ZnSiO_x$ compound, especially for high temperature deposition. Formation of such mixed oxides at the interface between silicon substrate and ZnO has already been reported in the literature for samples deposited [286] or annealed at 1000 °C [283].

3.4 Thin film microstructure and defects

The XRD analysis (see Section 1.2.3.3) performed on all samples shows only the peaks belonging to the ZnO(0002) family (as shown in Fig. 3.8) demonstrating the preferential crystalline texture with the *c*-axis of the wurtzite structure perpendicular to the sample surface. Rocking curves for (0002) and (0004) peaks (not presented) show similar peak widths in the range of 3.3-5.0° corresponding to low grain misorientation. The diffraction peaks for the RT-deposited ZnO are $\sim 10^3$ times less pronounced, although the sample thicknesses is only 2.9 times lower, suggesting a poorer crystallinity or less pronounced texture in this case. For continuous films, peak widths match the film thickness (that corresponds to the grain size in the perperdicular direction) through the Scherrer equation [24]. When the deposition temperature is higher, the XRD peak position approaches the bulk ZnO value (marked by a vertical line in the inset of Fig. 3.8). This might be related to a stress relaxation due to the deposition on a hotter substrate. So, for example, the RT-deposited ZnO film is in compression, with the corresponding in-plane strain of ~0.6% (evaluated from the XRD peak position).

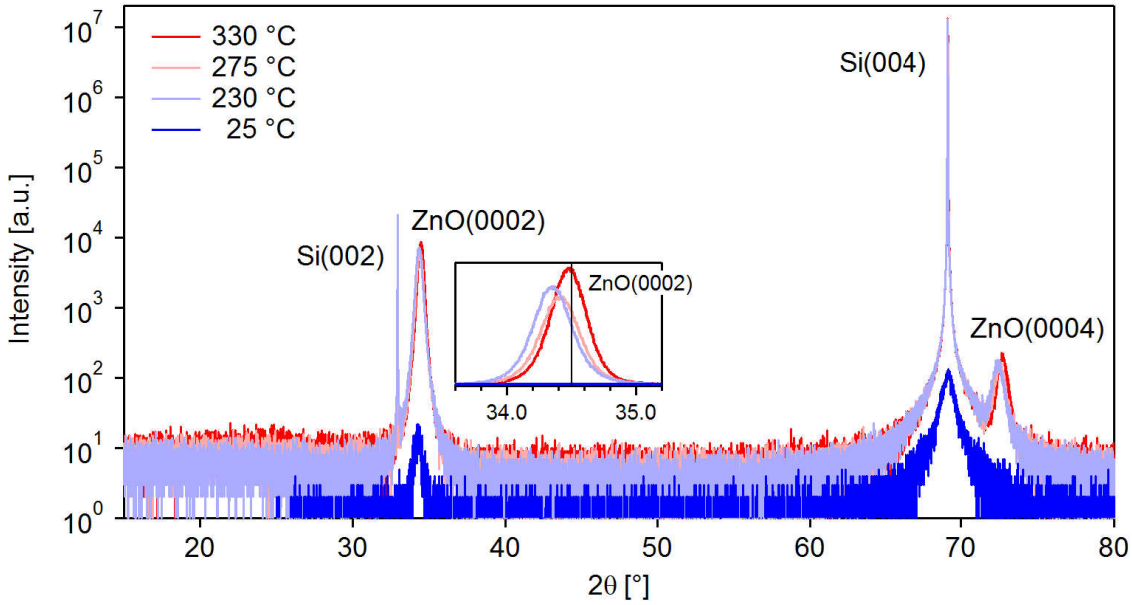

Figure 3.8: XRD θ-2θ scans taken in Bragg-Brentano geometry on ZnO samples deposited (i) at 330, 275, and 230±70 °C and a bias of +50 V (corresponding sample thicknesses: 82.4, 81.4, and 85.3 nm) and (ii) at 25 °C and a 0 V bias (29.9 nm). The inset shows a zoom on the ZnO(0002) reflection, with a vertical line corresponding to the bulk ZnO Bragg peak position. The measurement on the RT-deposited sample was performed with a 0.2° offset, in order to suppress the Si substrate peaks.

The average grain size at the surface of the film could be estimated from AFM images (see, for example, Fig. 3.5). Fig. 3.9 presents its evolution with film thickness for ZnO samples deposited at various temperature and bias conditions. Clearly, the grain size increases with film thickness in a way that is typical for a competitive grain growth. For the samples deposited at higher temperatures the grains appear larger. This tendency stays true if extrapolating the curves to the beginning of the deposition that is to the zero thickness. Apparently, the grain size at the nucleation stage is already smaller for the RT sample either because of the phenomenon of the substrate oxidation (which would increase the grain size at elevated temperature) or due to more intense ion bombardment due to bias conditions at RT (which would increase the nucleation density and decrease the grain size).

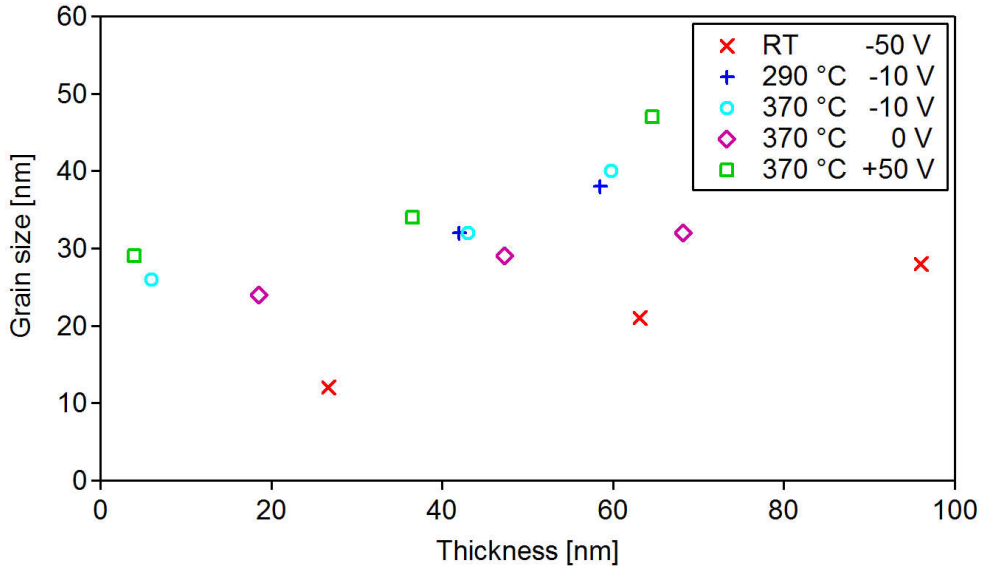

Figure 3.9: ZnO average grain size retrieved from AFM topography as a function of film thickness for five different deposition conditions: (i) RT and bias of -50 V (red crosses), (ii) 290±30 °C and -10 V (blue pluses), (iii) 370±30 °C and -10 V (cyan circles), (iv) 370±30 °C and 0 V (violet diamonds), (v) 370±30 °C and +50 V (green squares).

The stoichiometry of ZnO is an important parameter which is expected to impact the oxygen diffusivity and titanium oxidation (discussed in Chapter 4). Unfortunately, neither EPMA (due to insufficient sensitivity), nor XPS (due to extreme surface sensitivity), nor HAXPES (due to poor selectivity between the layers) provided a reliable value. To our experience, the transparency of the film alone can be a good criterion for nearly stoichiometric films, which is often checked for samples on glass. Thus, we assume that all our ZnO samples were roughly stoichiometric, independently of the deposition conditions.

Fig. 3.10 shows PhotoLuminescence (PL) spectra of ZnO thin films deposited at various conditions. The spectrum of a sample grown at high temperature (43.6 nm thick sample deposited at 320±70 °C and +50 V, red curve in Fig. 3.10) is composed of an intense peak around 380 nm corresponding to the band gap of ZnO and a defect band at ∼550 nm with much lower intensity. This indicates a rather good crystalline quality of the film. When the ZnO layer is deposited at the same temperature of 320±70 °C, but at a negative bias of -10 V, an extra band appears in the PL spectrum around 416 nm (blue curve in Fig. 3.10). The RT sample and the thinner sample deposited at higher temperature and +50 V bias have a much less intense peak at 380 nm while the broad peak at ∼550 nm is always present (blue and black curves in Fig. 3.10).

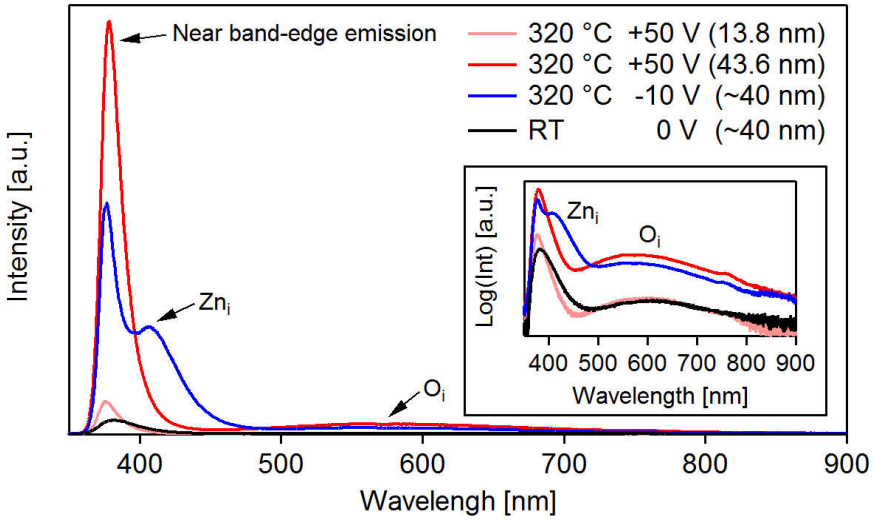

Figure 3.10: PL spectra of various ZnO samples: (i) 13.8 nm, 320±70 °C and +50 V (pink), (ii) 43.6 nm thick, deposited at 320±70 °C and bias of +50 V (red), (iii) ∼40 nm, 320±70 °C and -10 V (blue), (iv) ∼40 nm, RT and 0 V (black). The inset shows the same spectra in a logarithmic scale.

In case of a ZnO monocrystal, the PL spectrum consists of an intense peak in the ultra-violet at around 380 nm that corresponds to inter-band transitions (see *e.g.* [284]). The spectrum of a 44 nm thick ZnO deposited at 320±70 °C and a bias of +50 V (pink curve in Fig. 3.10) resembles closely the one of a monocrystalline zinc oxide, with an additional low-intensity defect band at around 550 nm usually assigned to O interstitials [284]. Curiously, a 3 times thinner sample deposited at the same conditions shows a 10 times less intense PL band gap peak. This difference can be explained by the fact that thinner films consist of smaller grains and the interface with the substrate is somewhat impacted by a mixed $ZnSiO_x$ phase discussed above. When shifting from the +50 V bias to -10 V, an extra defect band around 416 nm appears corresponding to Zn interstitial defects [284].

The comparison between PL spectra of samples deposited at low and high temperatures suggests that the electronic structure of the RT ZnO is far from being perfect due to microstructural defects, in agreement with the XRD study. The defects density and crystalline quality can be significantly improved by a deposition on a hot substrate.

3.5 ZnO orientation as a function of bias and temperature

As it was shown earlier by Williams *et al.* [279], ZnO film polarity can be controlled by choosing the substrate bias voltage (-50 V for ZnO-O and 0 or +50 V for ZnO-Zn termination when depositing at 500 °C). Authors suggested that the polarity control is achieved through the orientation of the dipole of the ZnO molecule by the electric field at the substrate surface during the nucleation stage. Such effect was not observed at room temperature.

In order to verify the effect of temperature, three ZnO films were deposited on Si(001) at substrate temperature of 330, 275, and 230±70 °C, and a bias of +50 V. As explained in the introduction, the XPS valence band measurement was used to identify the orientation. Fig. 3.11 compares such measurements for the three films and for ZnO(0001)-Zn and ZnO(000$\bar{1}$)-O single crystals used as references. The ZnO films deposited at 330 and 275±70 °C are Zn-terminated while the sample deposited at 230±70 °C has a ZnO-O surface. Thus the control of polarity requires a substrate temperature of somewhat above 230 °C.

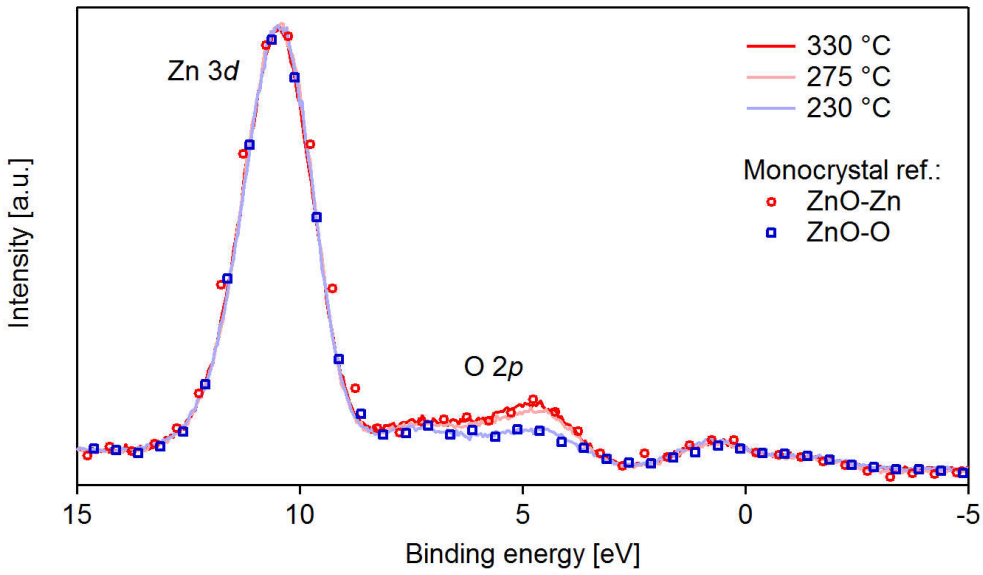

Figure 3.11: Valence band photoemission spectra of ZnO samples (Al Kα, $h\nu = 1486.6\,\mathrm{eV}$; normal emission) showing Zn $3d$ and O $2p$ core levels. Data from ZnO(0001) and ZnO(000$\bar{1}$) single crystals are compared with ZnO thin films deposited at temperatures from 230 to 330 ± 70 °C and a bias of +50 V. Intensity at negative binding energies is due to X-ray source satellites.

Using this valence band identification of the orientation, two parameters (temperature and substrate voltage) were tested in order to define a diagram (Fig. 3.12) relating the deposition parameters and the orientation of the ZnO film. The conditions for obtaining the ZnO-Zn orientation appear to be rather narrow. Negative bias voltage or the decrease of the temperature systematically lead to the formation of ZnO-O films. The higher temperatures range is also limited: over ~500 °C the oxidation of the Si wafer is rather intense and the sticking of Zn to the surface is close to zero[3]. Changing other conditions (O_2 partial pressure, magnetron-substrate distance, etc., not studied in the present work) can also impact the boundaries of such a diagram. The origin of the limits of the diagram remains unknown, since the actual mechanism of orientation selection is still hypothetical. The preferential alignment of the ZnO molecule dipole in an electric field is a possible mechanism, but the interplay with the piezoelectric properties of ZnO should not be excluded. While the phenomenon of re-sputtering sets a clear limit, knowing (or rather guessing) the mechanisms behind the transition between the two orientations could provide a way to systematically master the film polarity and study its impact on silver growth.

[3] However, a prolonged deposition ($\gg$30 minutes) might still result in the formation of ZnO.

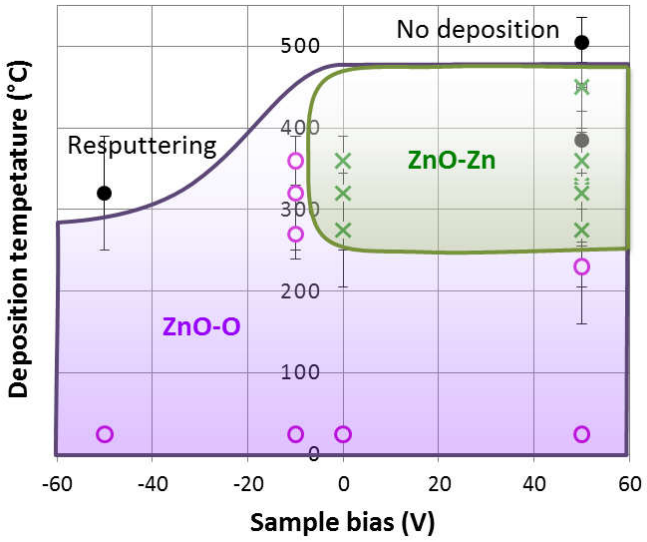

Figure 3.12: Schematic diagram of the ZnO film orientation as a function of the substrate temperature and substrate bias voltage during deposition.

3.6 Conclusions

Properties of ZnO films deposited by magnetron sputtering were studied as function of substrate temperature and bias voltage. At room temperature films grow with a constant deposition rate of 0.05 nm/s. At higher temperatures (230-320±70 °C), the beginning of growth is delayed. An XPS study revealed that the substrate is first oxidized by O arriving from the target. This observation is coherent with the SiO_2 and ZnO enthalpies of formation [282], heats of formation of metallic Zn and ZnO [285], and Zn vapour pressure [281]. The comparison of SIMS profiles of two ZnO samples deposited at RT and on a hot wafer confirms the thickening of Si oxide layer and indicates the formation of a mixed interfacial $ZnSiO_x$ compound [283, 286]. Once a sufficiently thick SiO_x passivation layer is formed, ZnO growth starts. Immediate ZnO growth on a hot bulk SiO_2 substrate further confirms this scenario. At high substrate temperature (320±70 °C) and high negative bias (-50 V), sample re-sputtering is observed, most likely due to positive ions attracted by the electric field.

All prepared samples were polycrystalline and ZnO{0001} textured. The crystallinity of the RT-deposited ZnO was much poorer than that of ZnO deposited on a hot substrate. The shift of the ZnO diffraction peak as a function of the deposition temperature suggests that residual stress in the film is progressively relaxed. In parallel, grain size increases with thickness, and is larger for higher deposition temperatures, as expected from a higher mobility. Photoluminescence measurements showed that in terms of the electronic structure RT-deposited samples were much more defective, while the films deposited at 320±70 °C showed an intense bulk-like band gap emission, like in the case of single crystal ZnO.

As it was shown earlier by Williams *et al.*, ZnO thin film polarity can be controlled by choosing a bias voltage applied to the sample [279]. Authors suggested that the polarity control is achieved through the orientation of the dipole of the ZnO unit cell by the electric field at the substrate, which becomes possible at high temperature. No evidence was though provided for this substrate temperature effect on polarity control. We demonstrated that for a bias of +50 V the control over the ZnO orientation is lost at 230±70 °C. Also, the three experimental points reported in Ref. [279] were expanded into a complete parameter space of substrate temperatures and bias voltages during deposition. Three distinct zones were discovered corresponding to ZnO-Zn, ZnO-O, and re-sputtering / no deposition zone, as discussed in Section 3.3. Some of the explored deposition conditions (substrate biases of -10, 0, and +50 V, and substrate temperatures of 25 °C, 300±100 °C, and 500±30 °C) were used in the study of the reactivity between ZnO and Ti thin films (Chapter 4).

Chapter 4

Reaction at the Ti-ZnO thin film interface

This chapter deals with the chemical reaction at the interface between Ti and ZnO films deposited by magnetron sputtering as a function of temperature, film thickness and stoichiometry. HArd X-ray PhotoEmission Spectroscopy (HAXPES) performed at BESSY II synchrotron (Helmholtz Zentrum Berlin) on specially designed samples was the main tool for observation of chemical transformations at a buried interface. Combined with Thermal Desorption Spectroscopy (TDS) and bulk phase diagram simulation, it was used to propose a reaction mechanism. It allowed understanding the path of the reaction and its rate limiting factors.

This chapter is structured as follows. It starts with a general introduction on chemical interactions at metal-oxide interfaces (Section 4.1). Then, a literature review is presented on the reactions in the Zn-Ti-O system, in the bulk and interfacial cases (Section 4.2). The typical sample structure and HAXPES experimental protocol are described in Section 4.3. Section 4.4 presents the details of the HAXPES data treatment as well as the interpretation of the observed trends. HAXPES results are presented and discussed in Sections 4.5-4.8. Section 4.9 treats the TDS data collected from similar samples. The final discussion (Section 4.10) supported by thermodynamic simulations proposes a mechanism of the interface reaction.

4.1 Chemical reaction at the metal/oxide interface

Chemical reaction and mass transport at interfaces play a paramount role in a wide variety of multiphase inorganic systems including composite materials, coatings, thin films or catalysts, in particular upon thermal treatment [201, 287, 288, 289]. The term "chemical reaction" is well suited in the framework of interfaces when interdiffusion occurs over length scales larger than a single monolayer or/and when new phases are formed with a thickness larger than one atomic layer. Chemical reaction involves mass transport at the solid state which is driven by a gradient of electrochemical potential, consisting of either a gradient of electrical potential provided by space charge layer and/or of chemical potential.

Depending on the reactivity of the compounds and the nature of the formed products, several phenomena can occur at a metal (A) // oxide (BO_x) interface [288]:

- Redox reaction: It will occur by oxidizing the metal overlayer and reducing the oxide substrate and is driven mainly by the difference of electronegativity of the constituting elements. It can be schematically written as $A//BO_x \rightarrow AO_y//BO_{x-y}$ and proceeds mostly through diffusion of oxygen.
- Alloy formation: At some interfaces, stable intermetallic alloys may be formed according to: $A//BO_x \rightarrow AB_y//BO_z$ or $A//BO_x \rightarrow AO_y//AB_z//BO_x$. An example is the formation of aluminides or silicides upon reductive conditions. In this case, cations from the substrate are extracted from the oxide and incorporated into the metal overlayer.
- Encapsulation: Found in particular in the case of oxide supported nanoparticles, it involves mass transport from the oxide onto the surface of the metal. Particles are physically covered by a thin layer of reduced oxide following $A//BO_x \rightarrow BO_{x-\delta}//A//BO_x$. The so-called Strong Metal Support Interaction (SMSI) which occurs for reducible oxides and which is deleterious for particle catalytic properties requires the outward diffusion of cations from the bulk to the interface. It is driven by the

difference in work function between the metal and the oxide and therefore the doping, the Fermi level position, the charge transfer, and the electric field in the created space charge layer. A well-known example is the case of late transition metals on rutile TiO_2 [290].

- Interdiffusion: Metal may diffuse into the oxide or vice-versa leading to the formation of interdiffusion zones or mixed oxides at the interfaces (ternary compounds, oxide solid solutions) according to: $A//BO_x \rightarrow ABO_y$.
- (De)wetting: From an energetic point of view, wetting at metal/oxide interface is not favoured since the interface energy $\gamma_{M/Ox}$ does not overcome the sum of the surface energies of the metal γ_M and the oxide γ_{Ox} [201, 288]. The Bauer criterion [291] for 2D film growth is never really encountered; metallic films on oxides are formed in out-of-equilibrium conditions and have a strong tendency to dewet even when encapsulated. In contrast, oxides wet metals well.
- Crystallization: Grain growth and defect healing are strongly thermally activated processes.

All these phenomena can alter in a drastic way the initial properties of the system through, for example, the change of its electronic and optical properties, the stress build-up or the modification of adhesion [292]. The occurrence of one event compared to the others is dictated by thermodynamics and its extend is driven by kinetics considerations, mostly given by diffusion of species and mass transport [287, 288].

Bulk thermodynamic calculations of solid state reaction provide already a relevant starting point to predict the driving forces of an interfacial reaction [288]. For a redox reaction $A + BO_x \rightarrow AO_y + BO_{x-y}$, the sign of the Gibbs free energy:

$$\triangle G = \triangle H - T\triangle S \tag{4.1}$$

will suggest the feasibility of the reaction. In the solid state, changes in entropy $\triangle S$ are negligible so that enthalpy changes $\triangle H$ can be used as a first criterion. Therefore, the heat of formation of oxides $\triangle H_f^{Ox}$ turns out to be a key parameter in the description of reactivity [201]. For instance, at metal/TiO_2 interfaces, the overall direction of the reaction can be reliably predicted by comparing the reactivities of Ti and the other metal involved [288]. However, for interfaces and in thin films, extra energetic contributions have to be accounted for. Metal γ_M and oxide γ_{Ox} surface energies as well as the interface energy $\gamma_{M/Ox}$ may play a critical role in some reaction processes (*e.g.* encapsulation). For instance, Campbell demonstrated that the adhesion energy:

$$E_{adh} = \gamma_M + \gamma_{Ox} - \gamma_{M/Ox} \tag{4.2}$$

at metal/oxide interface provides an extra stabilization which lowers the pressure required for oxide stability as a thin film below that needed for bulk oxide stability by a factor:

$$\exp\left[-\left(2\gamma_{M/Ox} - E_{adh}\right) / \left(t \cdot N_{Ox} \cdot RT\right)\right], \tag{4.3}$$

where t is the oxide film thickness and N_{Ox} is the oxygen concentration in the bulk oxide [293]. For nanometric films, this correction can be of many orders of magnitude. Beyond this restriction specific to interfaces, most of the time thermodynamic data of interfaces are not known, not speaking about composition gradients which blur the accurate phase determination. Therefore, most of the time bulk data are used on defined compounds assuming that thermodynamic equilibrium is reached which may be not the case at moderate temperatures for solid state reactions ($T < 1000$ °C).

Kinetics may be limited either by the progress of the reaction itself or by mass transport. The growth rate of the new formed interface is expected to be linear with time in the first case and quadratic in the second case. Most reactions at metal/oxide interfaces are diffusion limited. In model systems, two main driving forces have been pointed out and are at work in the mass transport, either the spatial concentration gradients or the electric field [288, 292]. In the first case, the concentration flux follows Fick's law:

$$J = -D\frac{dC}{dx}, \tag{4.4}$$

with a diffusion coefficient:

$$D = a^2\nu \exp\left[-\frac{E_a}{kT}\right], \tag{4.5}$$

which has an Arrhenius-like temperature dependence. E_a, ν, a are respectively the activation energy, the attempt frequency and the typical hopping length. Such a mechanism dominates at high temperature and

low electric field. However, macroscopic electric fields, such that encountered in space charge layer, can deeply modify the ionic diffusion by lowering / increasing the apparent activation energy, in a similar way to thermoionic emission. This field-driven diffusion is at the heart of the well-known Cabrera-Mott description of surface oxidation of metals [187] that can be generalized to interfaces [288]. Pathways of ionic diffusion can be bulk-like as in the case of model systems (metal/single-crystal) [288] or can involve grain boundaries, as in the case of polycrystalline systems [292]. Film crystallinity, defect concentration as well as porosity may dramatically impact the process kinetics. For example, Mühlbacher *et al.* compared three systems: (i) monocrystalline Cu on monocrystalline TiN, (ii) polycrystalline Cu on dense TiN films deposited on Si(001) by magnetron sputtering at 700 °C, and (iii) polycrystalline Cu on under-dense TiN films deposited on Si(001) at room temperature [294]. In the monocrystalline thin film system Cu diffusion over a length of 7-12 nm was observed after 12 h annealing at 1000 °C. For Cu on dense polycrystalline TiN film the diffusion length reached 30 nm after 1 h annealing at 900 °C. For Cu on under-dense polycrystalline TiN film the diffusion length already exceeded 500 nm after annealing at 700 °C. Finally, it is also known that if a diffusion process is accompanied by a redox reaction, the diffusion length is limited by the reaction (see *e.g.* Ref. [295]). An in depth description of ionic transport across an interface is far beyond the scope of this introduction chapter. But the question of diffusion of species is partially addressed at the end of this chapter through Thermal Desorption Spectroscopy.

Up to now, the effect of ambient atmosphere was ignored since our experiments have been performed in vacuum on closed systems; but it should be kept in mind that diffusion of oxidizing agents from the atmosphere can play a role in the solid state reaction, even for encapsulated layers [287].

4.2 Reaction between ZnO and Ti

4.2.1 Bulk phase equilibria in the Zn-Ti-O system

Bulk thermodynamics is already a relevant starting point to predict the evolution of a Ti/ZnO stack. Ti has a much higher affinity for oxygen than Zn, as seen by the enthalpies of formation of the various corresponding oxides: $\triangle H_f^{Ox}(Ti_3O_5)$ = -2459.1 kJ/mol, $\triangle H_f^{Ox}(Ti_2O_3)$ = -1520.9 kJ/mol, $\triangle H_f^{Ox}(TiO_2)$ = -944 kJ/mol, and $\triangle H_f^{Ox}(TiO)$ = -542.7 kJ/mol against $\triangle H_f^{Ox}(ZnO)$ = -350 kJ/mol [296, 297, 298]. Therefore, the reduction of ZnO by Ti is thermodynamically favoured in the ZnO-Ti system. But, unfortunately, the pathway of reduction and the expected intermediates are not known since there is no available ternary Zn-Ti-O phase diagram in the literature. Most of the results concern the reaction between ZnO and TiO_2 oxides. Therefore, thermodynamic simulations using databases were performed at the end of this study to predict the evolutions in the ZnO-Ti systems (see Section 4.10).

Regarding the ZnO-TiO_2 system, three stable defined compounds can be formed as a result of solid state reactions (see Fig. 4.1):

- Zn ortho-titanate Zn_2TiO_4 which is a cubic spinel ($Fd\bar{3}m$; a = 8.46080 Å) [299];
- Zn polytitanate $Zn_2Ti_3O_8$, which is a defect spinel ($P4_332$; a = 8.39200Å) [300, 301];
- Zn meta-titanate $ZnTiO_3$ having a hexagonal $FeTiO_3$ ilmenite structure ($R\bar{3}$; a = 5.49270 Å, α = 55.0831°) [299].

Three more or less consistent phase diagrams (gathered in Fig. 4.2) were reported in the literature [299, 301, 302]. The one by Dulin and Rase [299] covers the temperature range from 600 to 1600 °C. While the authors claimed that only $ZnTiO_3$ and Zn_2TiO_4 ternary oxides are possible in the system, Qian *et al.* extended these results to lower temperatures down to 400 °C and found the same phases [302]. Kim *et al.* reported a diagram for 700-1400 °C also updating the Dulin and Rase's one by adding: (i) the $Zn_2Ti_3O_8$ phase that exists for 50-60% of TiO_2 in the mixture and decomposes at ∼945 °C, and (ii) a solid solution of TiO_2 and Zn_2TiO_4 existing above ∼945 °C for the compositions containing 40 to 100% of TiO_2 [301]. Authors claimed that TiO_2-Zn_2TiO_4 solid solutions are also possible for 33-40% of TiO_2 at 800-1400 °C.

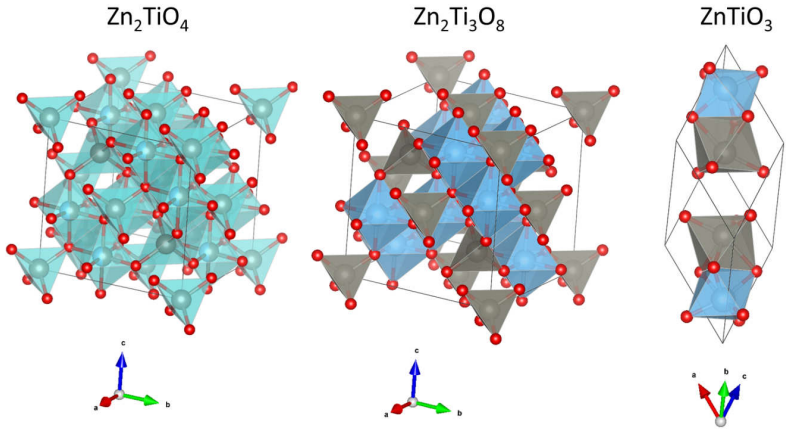

Figure 4.1: Ball model of the three main $ZnTiO_x$ atomic structures. Coordination polyhedra are shown around Zn (blue) and Ti (grey). Oxygen is displayed as red balls. In the spinel structure, the site occupancy is random.

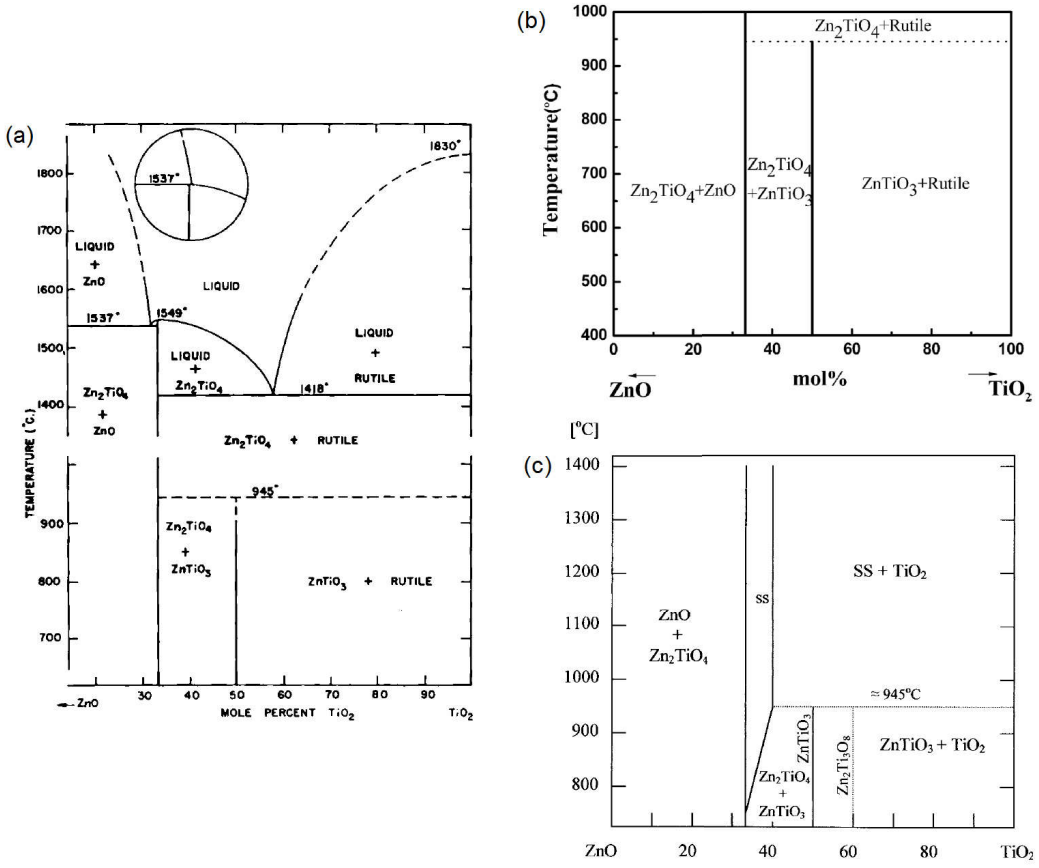

Figure 4.2: ZnO-TiO_2 phase diagrams retrieved from: (a) Dulin and Rase [299], (b) Qian *et al.* [302], and (c) Kim *et al.* [301].

Lee *et al.* detected the co-existence of $Zn_2Ti_3O_8$ and TiO_2 phases at 800 °C [303, 283]. Bartram and Slepetys reported that Zn polytitanate can be observed for compositions with 50-90% of TiO_2 [300]. Between 600 and 800 °C, $Zn_2Ti_3O_8$ should coexist with anatase TiO_2 for 67-90% of TiO_2 in the mixture, and with Zn_2TiO_4 for 50% of TiO_2. The $Zn_2Ti_3O_8$ phase is transformed to Zn_2TiO_4 and rutile TiO_2 at 800-1000 °C. In agreement with these findings, Steinike and Wallis reported that the mixed oxide formation is overlapped

with the transformation of TiO_2 from the anatase to rutile which takes place between 530 and 830 °C [304]. We suggest that the presence or absence of anatase TiO_2 in some phase diagrams [299, 301, 302] can be related to the actual TiO_2 phase used in sample preparation (in most of the cases – in powder form).

A phase diagram alternative to the one by Dulin and Rase [299] was proposed by Yang and Swisher [305]. In agreement with Bartram and Slepetys [300], and Lee *et al.* [303, 283], they confirmed the existence of the $Zn_2Ti_3O_8$ phase and its stability up to ~800 °C [305]. Authors claimed that $Zn_2Ti_3O_8$ is subsequently transformed into $ZnTiO_3$ and then into Zn_2TiO_4.

By unifying the available information, a new phase diagram can be proposed as shown in Fig. 4.3a, with possible alternatives for the region between 600 and 945 °C and compositions with more than 50% of TiO_2 (Fig. 4.3b and c).

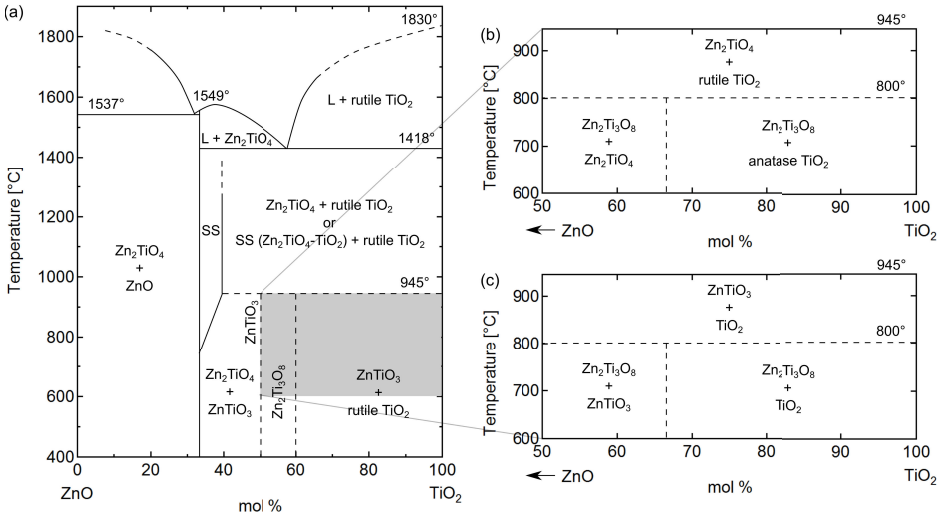

Figure 4.3: (a) Phase diagram for bulk Zn-Ti-O systems based on Ref. [299, 301, 302], and alternative diagrams for the 600-945 °C region for compositions with >50% of TiO_2, based on Ref. [300, 303] (b) and [305] (c).

4.2.2 Reaction at the interface

Reaction at ZnO/TiO_2 or ZnO/Ti interfaces in the form of thin films or nanopowders was addressed in several studies. Just like in the bulk case, they showed or suspected the formation of a mixed compound at the interface, and/or appearance of metallic Zn.

Steinike and Wallis mixed ZnO and TiO_2 nanopowders and annealed them at 600-950 °C [304]. They found that, at the beginning of the reaction, there was an abundant presence of Zn at the surface of the TiO_2 particles, which, in mixtures with well-crystallized TiO_2, resulted in formation of the Zn_2TiO_4 compound. Yang *et al.* studied ZnO nanowires covered by TiO_2 films [306]. They showed that, after annealing at 700 °C, the ZnO surface became covered by Zn_2TiO_4 nanocrystallites. Manik *et al.*, based on Rietveld's powder structure refinement, concluded that during the reaction between ZnO and TiO_2, Zn atoms are preferentially substituted by Ti atoms [307].

Lee *et al.* observed the effect of the film stabilization on the phase transition of zinc titanate [303, 283]. The authors found that $ZnTiO_3$ thin films deposited by magnetron sputtering decomposed into Zn_2TiO_4 and TiO_2 not at 945 °C, like in the case of a bulk mixture, but at 900 °C.

Several recent studies were carried out on Ti films evaporated on bulk ZnO. Kerjan, Søndergård, Jupille *et al.* studied ultrathin Ti films evaporated on ZnO(0001) monocrystals in vacuum [308]. LEED patterns showed the lack of clear epitaxy in coverages ranging from 0 to 2 nm. But XPS analysis revealed the occurrence of an interfacial reaction happening even during the deposition at room temperature; oxidation of Ti and reduction of ZnO to a more metallic state continued even after deposition of 2 nm of Ti. When the system was annealed in vacuum at 300-400 °C, a structural transition occurred; the authors detected the formation of an epitaxial cubic spinel Zn_2TiO_4 film through the appearance of its (111) diffraction peak.

Borghetti, Mouchaal, and Lazzari explored the same system, during deposition and after annealing [224, 209]. Experiments on Zn- and O-terminated basal surfaces of ZnO were carried out in ultra-high vacuum,

and oxidation states were monitored through Ti $2p$ core levels, and Zn $L_3M_{45}M_{45}$ Auger transition. Like Kerjan *et al.* [308], the authors found that Ti and ZnO reaction during the deposition is limited below a Ti thickness of 1 nm. At the early stages of growth, Ti^{4+}, Ti^{3+}, Ti^{2+} species were formed on the bare surface of ZnO before being rapidly dominated by metallic Ti^0 above 1 nm. Zn- and O-terminated surfaces of ZnO showed similar trends. In parallel, Zn LMM spectra clearly demonstrated the presence of metallic Zn. A possibility of a ZnO-TiO_2 ternary compound formation was suggested for the ZnO-O surface, based on the Zn LMM Auger line shape that could not be accounted for as a simple superposition of those of ZnO and metallic Zn. These Ti / ZnO(0001) samples were annealed under vacuum at temperatures ranging from 200 to 700 °C which promoted the ZnO-Ti reaction. ZnO-O surfaces were more prompt to react with Ti than ZnO-Zn. Already after annealing at 200 °C Ti^0 was no longer the dominant oxidation state of Ti on ZnO-O. After annealing at 450 °C most of the Ti atoms were in the Ti^{4+} state. Surprisingly, the reaction between ZnO-Zn and Ti started only at 400-500 °C giving rise to oxidation states of Ti higher than Ti^0.

Rahman and Narusawa studied the interface stability of Ti thin films (16 nm) grown on monocrystal ZnO(0001) by Rutherford backscattering and channelling spectroscopy [309]. They stated that the reaction between Ti and ZnO started already during the deposition and observed a significant amount of Zn metal on the sample surface after annealing at 400 °C.

Knut, Grachev, Søndergård, *et al.* [310] were the first to study the reactivity of a Ti and ZnO thin films – a Ti (5 nm) / ZnO (50 nm) stack deposited under vacuum by magnetron sputtering on Si wafers, and in most of the experiments encapsulated by a top Mo layer. As in the present work, chemistry was probed by the HAXPES technique (see Section 1.2.1.2) on a complete stack through the evolution of Ti $2p$, Zn $2p$, and Zn LMM Auger spectra for a few uncovered samples. The authors showed that the reaction started already during the deposition, similarly to the case of Ti films on ZnO monocrystals [308, 224, 209]. The 5 nm Ti film was already slightly oxidized, and metallic Zn was detected at the interface. Then the system was gradually annealed in vacuum at 200, 350, and 550 °C. After annealing at 200 °C a large increase of Ti^{2+} was observed, and the presence of metallic Zn became more prominent as seen not only from the Zn LMM Auger line, but also from the shape of the Zn $2p$ peak. After annealing at 350 °C Ti oxidation further progressed, while the Zn signal recovered the ZnO characteristics. Knut *et al.* assumed that metallic Zn produced in the reaction with Ti was re-oxidized by O diffusing from the bulk of the ZnO film towards the surface [310]. After annealing at 550 °C the Ti layer was almost completely oxidized to Ti^{4+}. At the same time the Zn $2p$ peak shifted towards higher binding energies, and its intensity increased suggesting ZnO intermixing with Ti or TiO_2. Authors suggested that the Zn_2TiO_4 compound was formed at the interface. A posteriori XRD analysis indicated the formation of new nanocrystalline phases, but the peaks were too broad to conclusively confirm the spinel structure.

Kim *et al.* [311] also investigated the thin film ZnO-Ti interface. In their work, Ti (30 nm) / Au (50 nm) contacts were e-beam evaporated onto ZnO:Al (1000 nm) films RF-sputtered on (0001) sapphire substrates. The authors observed the influence of annealing in N_2 on the ZnO-Ti interface evolution by using Auger Electron Spectroscopy (AES) depth profiling. For the as-deposited sample, there was already some amount of O that diffused from ZnO into the Ti layer. When the sample was annealed at 300 °C, O diffusion into Ti continued, and the extent of ZnO dissociation increased. After annealing at 500 °C O diffused into the totality of the Ti film, most likely forming a TiO oxide. Significant amounts of Ti and O out-diffused through Au to the sample surface. According to the *a posteriori* XRD analysis, TiO_2 (rutile and srilankite) and TiO peaks were identified.

Ip *et al.* studied the effect of annealing in N_2 on Ti (20 nm) / Al (80 nm) / Pt (40 nm) / Au (80 nm) contacts e-beam deposited on ZnO(0001) monocrystal [312]. AES profiling after annealing at 250 °C showed that an interfacial reaction started between ZnO and Ti leading to the formation of Ti-O phases. After 600 °C, the ZnO-Ti contact became "completely intermixed".

In the light of the state of the art, this study aims at elucidating the pathway of the ZnO-Ti reaction as a function of annealing temperature, film stoichiometry and crystallinity. The puzzling behaviour of Zn and the formation of a defined compound have been revised by combining HAXPES and TDS analysis in a systematic way.

4.3 Model stack structure and experimental protocol

In order to study the reactivity between ZnO and Ti films, model samples were prepared, with the typical sample structure shown in Fig. 4.4.

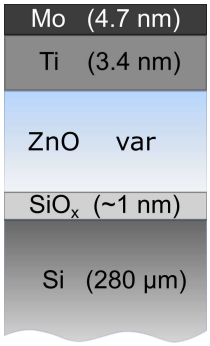

Figure 4.4: Schematic of the studied stack structures: Si substrate / ZnO (8.5-29.7 nm) / Ti (3.4 nm) / Mo (4.8 nm).

Unless stated otherwise, the samples were deposited by magnetron sputtering on 280 µm thick Si wafers covered with a native oxide layer (∼1 nm). The Mo film (∼5 nm) was used as a capping layer in order to protect the Ti layer from external atmosphere [1], but also to approach the case of the encapsulated industrial stacks. The thickness of the Mo layer was optimized to be thick enough to ensure a good protection of Ti and thin enough to allow for detection of the HAXPES signal (see Section 1.2.1.2 for details) from the deeper layers of the stack. As described previously, ZnO layers were deposited by Radio Frequency (RF) sputtering from an undoped ceramic target at the Ar pressure of 9.7 µbar without or with oxygen (0 or 2%), at substrate biases of -10, 0, and +50 V, and substrate temperatures of 25 °C, 300±100 °C, and 500±30 °C. Ti and Mo layers were deposited at room temperature (RT) at Ar pressures of 3.6 and 1.5 µbar, respectively, by direct current sputtering. The deposition rates were 0.04 nm/s for ZnO, 0.11 nm/s for Ti, and 0.48 nm/s for Mo films. Film thicknesses were measured by EPMA (see Section 1.2.4 for details), taking into account ZnO, Ti, and Mo bulk densities. Typical EPMA error of thickness evaluation is of the order of 0.5 nm. Thickness variations over different depositions performed at the same conditions were in the range of 7%. An additional source of error is the thickness inhomogeneity over the sample surface, which for magnetron sputtering deposition could reach 5-10% between the centre and the edge of the sample. This explains unintended variations of Ti and Mo thickness.

Reactivity of Ti and ZnO thin films was studied as a function of the following modifications of the stack: (i) ZnO thickness, (ii) improved ZnO crystallinity by deposition at higher temperature, and (iii) Ti replaced by a TiO_x film (by Ti deposition from an oxygen-poisonned target) [2] . The corresponding samples are listed in Table 4.1.

[1] According to the phase diagram, Mo and Ti do not form alloys up to 695 °C [313].

[2] The effect of ZnO film termination (O or Zn) was also studied, but no significant difference in ZnO-Ti reactivity was observed – most probably due to the fact that the grain boundaries play a more important role – and, therefore, these results are not presented.

Stack	ZnO deposition conditions	ZnO thickness [nm]	Ti thickness [nm]	Mo thickness [nm]
ZnO (RT, 14.4) / Mo	RT 0 V O_2: 0%	14.4	0	4.7
ZnO (RT, 29.7) / Ti / Mo	RT 0 V O_2: 0%	29.7	3.6	4.8
ZnO (RT, 10.5) / Ti / Mo	RT -10 V O_2: 0%	10.5	3.4	4.4
ZnO (RT, 8.5) / Ti / Mo	RT 0 V O_2: 0%	8.5	3.5	4.8
ZnO (300 °C, 26.6) / Ti / Mo	300±100 °C 0 V O_2: 0%	26.6	3.7	5.1
ZnO (300 °C, 16.0) / Ti / Mo	300±100 °C 0 V O_2: 0%	16.0	3.3	4.5
ZnO (300 °C, O_2, 19.5) / Ti / Mo	300±100 °C -10 V O_2: 2%	19.5	3.4	4.3
ZnO (500 °C, O_2, 28.2) / TiO_x / Mo	500±30 °C +50 V O_2: 2%	28.2	3.0	5.1

Table 4.1: List of the studied ZnO / Ti / Mo samples deposited on Si wafers with native oxide. Deposition conditions for the ZnO layers, as well as the thicknesses of all the films in the stack are given in nm. For samples containing TiO_x the Ti thickness corresponds to the equivalent quantity of Ti.

The oxidation states in these samples were investigated by means of HAXPES (see Section 1.2.1.2 for details) as-deposited and after subsequent annealing in vacuum ($p \sim 10^{-9}$ mbar) at 250, 350, and 550 °C (10 min at each temperature plateau value[3], reached with a heating at a rate of 20 °C/min). Before each HAXPES measurement the samples were cooled down to temperatures $\leq$ 90 °C. Unless stated otherwise, the spectra were recorded at a photon energy of $h\nu = 4\,\text{keV}$ and take-off angles close to normal emission (81-87°). The analyser pass energy was fixed at 500 eV for survey scans and at 200 eV for detailed scans of particular core levels. Some samples were also studied by TDS (see Section 1.2.5). The thicknesses of the thin film layers were controlled by EPMA before and after annealing cycles. No change of Ti and Mo quantity was observed, while ZnO thickness systematically decreased after the thermal treatment, as it will be shown in the following.

4.4 HAXPES data interpretation

4.4.1 Spectra overview

Fig. 4.5 shows a survey HAXPES spectrum of a ZnO (RT, 29.7) / Ti / Mo sample for binding energies ranging from 1300 to 0 eV (corresponding electron kinetic energies range from 2700 to 4000 eV). The following core level features (single peaks or doublets due to spin-orbit splitting) are present on the widescan:

- Zn 2*s*, Zn 2*p*, Zn 3*s*, Zn 3*p*, Zn 3*d*;
- Ti 2*s*, Ti 2*p*, Ti 3*s*, Ti 3*p*;
- O 1*s* peak;

[3] After an extra annealing at the same temperature and doubling the annealing duration, HAXPES spectra did not evolve any more.

- Mo $3s$, Mo $3p$, Mo $3d$, Mo $4p$;
- Si $2s$, Si $2p$;
- C $1s$ corresponding to the surface contamination.

No trace of other elements is observed.

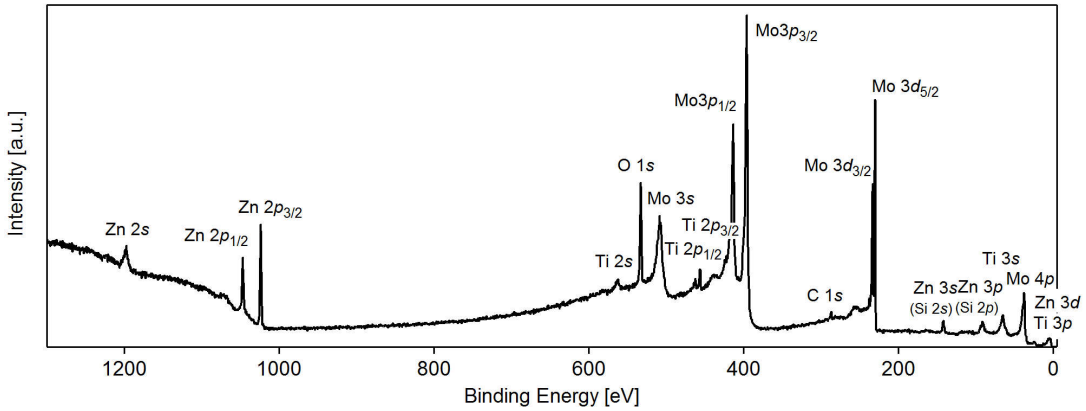

Figure 4.5: HAXPES wide scan of a ZnO (RT, 29.7) / Ti / Mo sample showing Zn, Ti, O core levels, and the C $1s$ peak corresponding to the surface contamination of the sample.

Zn, Ti, O, Mo, Si, and C have the following Auger peaks (with corresponding kinetic energies):

Zn: Zn LMM (987.6 eV), see *e.g.* [314] and Zn LVV (51.2 eV), see *e.g.* Ref. [315];

Ti: Ti LMM (354 eV), Ti LMV (418 eV), Ti LVV (451 eV) [316];

O: O KLL (512 eV) [315] and O KVV (506.9 eV) [317];

Mo: Mo LMM (2032.2 or 2038.8 eV for pure Mo or MoO_x, respectively), Mo MVV (222.8 eV for pure Mo) [314];

Si: Si KLL (1615.7 eV for pure Si [318], 1609 eV for SiO_x [319]), Si LMM (1615.5 eV or 1605 eV for pure Si or SiO_x, respectively), Si LVV (88.5 eV or 72.5 eV for pure Si or SiO_2, respectively) [315];

C: C KLL (265 eV) [320].

But their kinetic energies range from 72.5 to 1615.7 eV, therefore these peaks are not visible in the HAXPES spectra taken at a photon energy of 4 keV.

For analysis, all spectra were normalized by the number of scans and by the area of Mo peak, either Mo $3p_{3/2}$ or Mo $3d_{5/2}$, used as a reference, knowing that the Mo quantity and its localization in the sample remained unchanged after annealing. This normalization allowed taking into account possible changes in overall signal intensity due to the sample position and beam flux variations (although it was monitored during each measurement). The binding energy was corrected with respect to the Au $4f$ core level used as a reference. The Au $4f$ core level spectra were recorded on a gold foil reference electrically connected to the sample holder. The Fermi level of different materials was aligned through the electrical contact between the sample holder, conductive Si substrate, and thin film layers. No significant charging effect was noted for these samples.

In the following a specific attention will be paid to the Zn $2p$ and Ti $2p$ core levels as they reflect the changes in the sample caused by the reaction between the ZnO and Ti layers.

4.4.2 Ti $2p$ core level analysis

4.4.2.1 Fitting the Ti $2p$ background

The observed changes of the spectra were quantified through fitting. As shown in Fig. 4.6a, Ti $2p$ peaks are located in between Mo $3s$ and Mo $3p$ core levels in the spectrum. This leads to a complicated shape of the Ti $2p$ background.

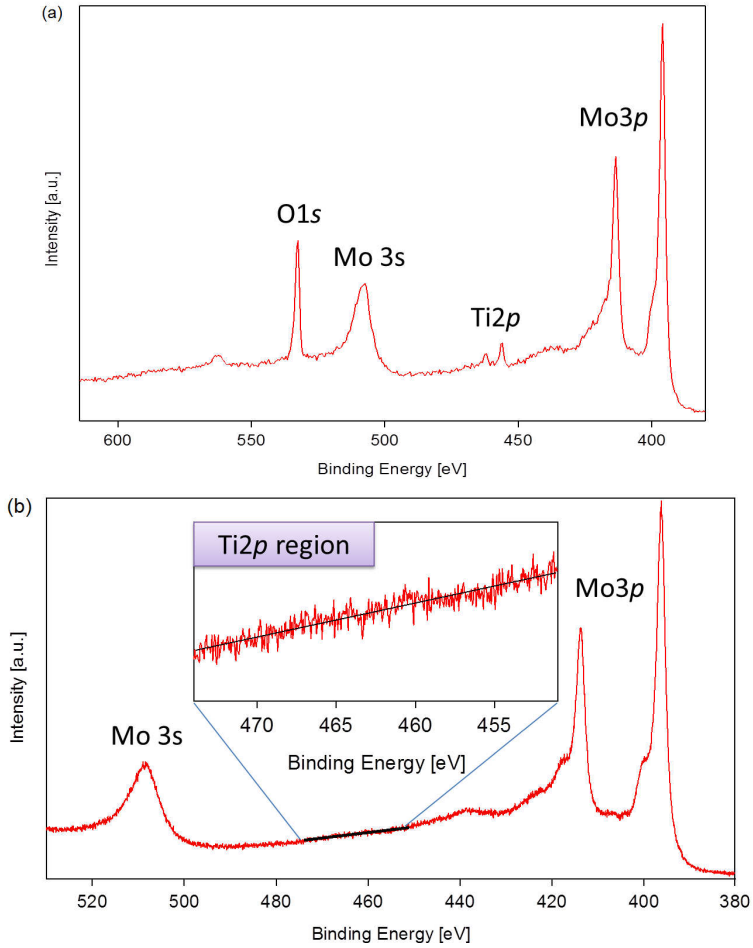

Figure 4.6: (a) HAXPES spectra region showing O $1s$, Mo $3s$, Ti $2p$, and Mo $3p$ peaks of the ZnO (RT, 29.7) / Ti / Mo sample recorded at a photon energy of 4 keV in the normal detection geometry. (b) Similar HAXPES spectra of a sample without Ti. The inset shows the linear fit of the background in the Ti $2p$ region.

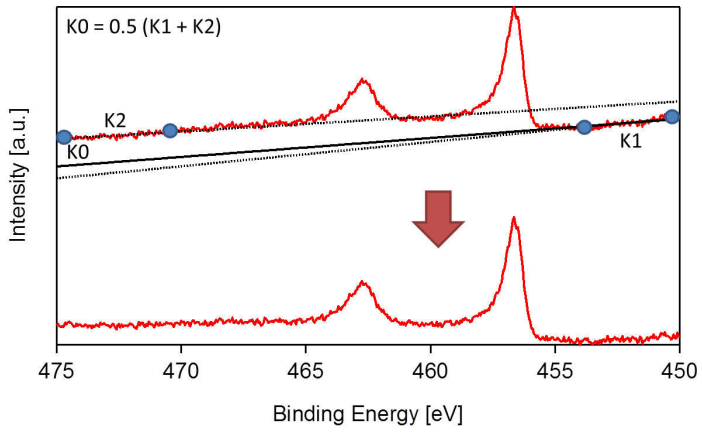

Figure 4.7: Zoom on the Ti $2p$ HAXPES spectra of the as-deposited ZnO (RT, 29.7) / Ti / Mo sample recorded at a photon energy of 4 keV in the normal detection geometry. The slope K_0 of the linear part of the background can be defined as an average of the linear fit of the baseline at lower (K_1) and higher binding energy (K_2) sides of the Ti $2p$ spectra.

A pure Mo (5 nm) sample on Si wafer with native oxide was deposited as a reference to identify the shape of the background "under" Ti $2p$ peaks. The zoom on the region between Mo $3s$ and Mo $3p$ peaks for the Mo reference is shown in the inset of Fig. 4.6b. The shape of the background seems to be linear in the Ti $2p$ region, in the first approximation. Nevertheless, a reliable fit of the Ti $2p$ background as a combination of linear and Shirley shapes (see Section 1.2.1.3 for details) could never be achieved using a spectra decomposition software. It turned out to be more efficient to manually subtract a linear background which slope K_0 is the average of the linear baselines at lower (K_1) and higher binding energy (K_2) sides of the Ti $2p$ spectra, as shown in Fig. 4.7.

4.4.2.2 Ti $2p$ fitting parameters from literature

In order to fit Ti $2p$ core level, all possible oxidation states of Ti (Ti^0, Ti^{2+}, Ti^{3+}, and Ti^{4+})[4] should be considered. That means fitting the spectrum using 8 components (4 Ti $2p$ doublets), each having 5 parameters: peak position, peak maximum intensity, Gaussian and Lorentzian broadening (Full Widths at Half Maximum, FWHMG and FWHML), and peak asymmetry, which amounts to 40 fitting parameters in total. Therefore, constraints have to be applied to the parameters, in particular, according to references found in the literature [242, 310, 322, 323], as shown in Table 4.2.

Oxidation state	Average Ti$2p_{3/2}$ binding energy [eV]	Number of references used	Average spin-orbit splitting [eV]	Number of references used
Ti^0	453.9±0.3	15	6.1±0.1	5
Ti^{2+}	455.2±0.5	4	5.8±0.2	2
Ti^{3+}	457.1±0.4	5	5.6±0.5	2
Ti^{4+}	458.7±0.3	48	5.8±0.1	13

Table 4.2: Fitting parameters for the 4 doublet components of the Ti $2p$ spectra corresponding to the Ti^0, Ti^{2+}, Ti^{3+}, and Ti^{4+}oxidation states compiled from the NIST XPS database [242] and several chosen publications [310, 322, 323]. When reported, the branching ratio was 0.5.

4.4.2.3 Ti $2p$ core level parameters determined from the reference samples

In order to validate the known parameters and determine the unknown ones, the following reference samples were prepared and analysed by HAXPES:

- Si substrate / Ti (44.1 nm) / Mo (4.9 nm) denoted as Ti-S,
- Si substrate / TiO_2 (20 nm) [5] / Mo (5 nm)[5] denoted as TiO_2-S [6].

Oxidation state	Ti $2p_{3/2}$ binding energy [eV]	Ti $2p$ spin-orbit splitting [eV]	Ti $2p$ branch. ratio	Ti $2p_{3/2}$ FWHML [eV]	Ti $2p_{1/2}$ FWHML [eV]	Ti $2p_{3/2,\,1/2}$ FWHMG [eV]	Ti $2p_{3/2}$ asym-metry.	Ti $2p_{1/2}$ asymm.
Ti-S	453.75	6.11	0.46	0.39	0.78	0.35	0.60	0.38
TiO_2-S	458.65	5.73	0.52	0.39	1.28	0.82	0	0

Table 4.3: Fitting parameters obtained for Ti $2p$ spectra of Ti-S and TiO_2-S reference samples.

Fig. 4.8 shows the fits of the Ti $2p$ spectra of Ti-S and TiO_2-S reference samples. The minor Ti^{2+} peak in the Ti-S spectra accounts for the residual oxygen in the chamber adsorbed between the deposition of Ti and Mo layers. The Ti^{3+} peak in the TiO_2-S corresponds either to a slight under-oxidation of the TiO_2 film, or to the reduction of TiO_2 at the interface with Mo. The obtained fit parameters for the Ti^0 and Ti^{4+} peaks are shown in Table 4.3. The fitting details are described in the following (see Section 4.4.2.4).

[4] There is crystallographic and Raman data on Ti_2O (see, *e.g.* Ref. [321]), but no data concerning oxidation states of Ti other than Ti^0, Ti^{2+}, Ti^{3+}, and Ti^{4+} is available in the literature.

[5] Value estimated based on the deposition rate.

[6] A supplementary sample of TiO_2 / Ti / Mo was prepared in order to verify the effect of the metallic layer in contact with TiO_2(either Mo or Ti) on the $Ti^{4+}2p$ peak position possibly influenced by the band bending. For TiO_2 in contact with Ti the $Ti^{4+}2p_{3/2}$ binding energy was 458.81 eV, *i.e.* slightly shifted by 0.16 eV with respect to that for TiO_2 in contact with Mo.

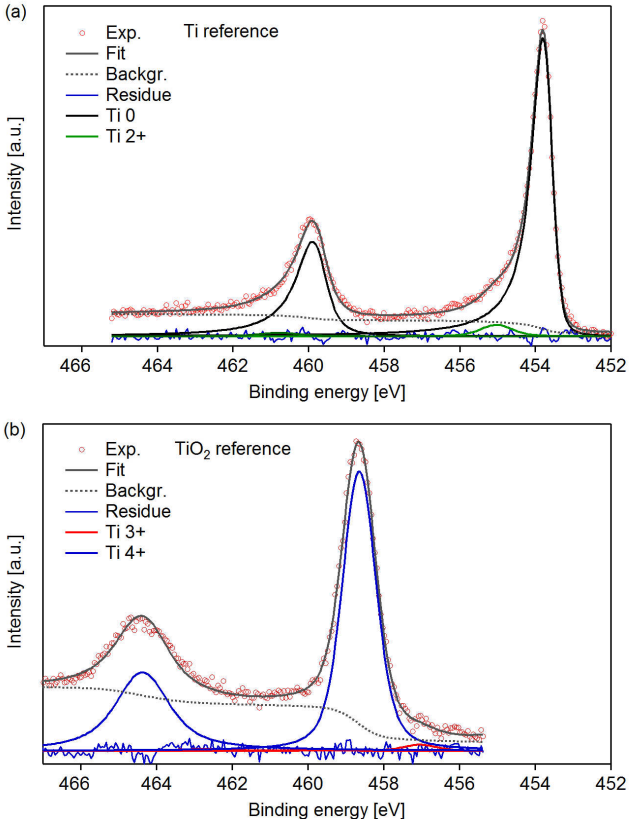

Figure 4.8: Ti $2p$ core level fits for the Ti-S and TiO_2-S reference samples showing the experimental HAXPES data, fit, Ti^0, Ti^{2+}, Ti^{3+}, and Ti^{4+} components, background, and residue.

4.4.2.4 Ti $2p$ fitting details

Based on the analysis of the pure Ti-S and TiO_2-S references, fitting parameters for Ti^0 and Ti^{4+} were determined (see Table 4.3). These parameters as well as the parameters found in the literature for Ti^0, Ti^{2+}, Ti^{3+}, and Ti^{4+} (Table 4.2) were used to fit the complex Ti $2p$ spectra of ZnO / Ti / Mo samples. The symmetric peaks corresponding to oxidized Ti (Ti^{2+}, Ti^{3+}, and Ti^{4+}) were fitted with Voigt profiles, and the asymmetric metallic peak (Ti^0) – with the PCI-curve (see Section 1.2.1.3 for details). In order to account for possible band bending effects, the position of Ti^0 $2p_{3/2}$ with respect to Ti^{2+} $2p_{3/2}$, Ti^{3+} $2p_{3/2}$, and Ti^{4+} $2p_{3/2}$ peaks was set free. But binding energy shifts between the Ti^{2+}, Ti^{3+}, and Ti^{4+} components were kept fixed as follows: 1.61 eV between Ti^{2+} $2p_{3/2}$ and Ti^{3+} $2p_{3/2}$, and 1.60 eV between Ti^{3+} $2p_{3/2}$ and Ti^{4+} $2p_{3/2}$, in agreement with literature values (Table 4.2). The spin-orbit splitting of the Ti^0 $2p$ doublet determined on the reference Ti sample, was fixed at 6.11 eV. The spin-orbit splitting of the Ti^{2+}, Ti^{3+}, and Ti^{4+} oxide Ti $2p$ components were fixed at 5.73 eV – the value found for the TiO_2 reference sample. The FWHML of Ti $2p_{3/2}$ was set to 0.39 eV, equal for all oxidation states, in agreement with the Ti $2p$ fit results for the references. The FWHML of Ti^0 $2p_{1/2}$ was fixed at 0.78 eV, and at 1.28 eV for all oxide Ti $2p_{1/2}$ peaks.[7] The Gaussian contribution was set free but constrained to be equal for both peaks within each doublet. It varied between different fits, but was not less than 0.35 eV which corresponds to the experimental resolution. The PCI-asymmetry was fixed at 0.60 for Ti^0 $2p_{3/2}$, at 0.38 for the Ti^0 $2p_{1/2}$, and at 0 for all the other components. The peak intensities within each doublet were chosen in a way that the branching ratios, *i.e.* ratios of areas were of 0.5 ± 0.1. The background was described as a combination of linear and Shirley shapes.

[7] The Ti $2p_{1/2}$ peaks have larger Lorentzian width due to the Coster-Kronig transition [324].

4.4.3 Zn $2p_{3/2}$ core level analysis

4.4.3.1 Zn $2p_{3/2}$ fitting parameters from literature

Compound	Average Zn $2p_{3/2}$ binding energy [eV]	References used
Zn	1021.8±0.2	[325, 326, 327, 328, 329]
ZnO	1022.1±0.2	[325, 326, 327, 328, 329]

Table 4.4: Zn $2p_{3/2}$ peak positions for metallic Zn and ZnO compiled from the NIST XPS database [242].

As in the case of Ti, changes of Zn chemical environment impacts the Zn $2p$ peak position and peak shape. The binding energies of the Zn $2p_{3/2}$ peak of ZnO and metallic Zn found in the literature [242] are presented in Table 4.4. The chemical shift between the ZnO-Zn $2p_{3/2}$ (symmetric) and Zn-Zn $2p_{3/2}$ (asymmetric) peaks is quite small, 0.3±0.1 eV. Experimentally, when a mixed $ZnTiO_x$ compound is formed, the peak stays symmetric, but shifts. Unfortunately, no data on Zn $2p_{3/2}$ binding energies for Zn_2TiO_4 is available in the literature. The following values can be found in the literature as examples of the Zn $2p_{3/2}$ peak shift with respect to ZnO-Zn $2p_{3/2}$ for mixed oxides: 0.5 eV for Zn_2AlO_4 [330], 0.3 eV for Zn_2SiO_4, -0.9 eV for $ZnFe_2O_4$ [331].

4.4.3.2 Zn $2p_{3/2}$ core level parameters determined from the reference samples

The following reference samples were studied by HAXPES:

- Si substrate / Zn (>15 nm) denoted as Zn-S,
- Si substrate / ZnO (29.9 nm) deposited at RT denoted as ZnO-S.

Oxidation state	Zn $2p_{3/2}$ binding energy [eV]	Zn $2p_{3/2}$ FWHML [eV]	Zn $2p_{3/2}$ FWHMG [eV]	Zn $2p_{3/2}$ asymmetry
Zn-S	1021.80	0.49	0.44	0.12
ZnO-S	1021.91	0.49	1.30	0

Table 4.5: Fitting parameters obtained for Zn $2p_{3/2}$ spectra of Zn-S and ZnO-S reference samples.

The fitted spectra and found fitting parameters are shown in Fig. 4.9 and Table 4.5. The fitting details are described in the following (see Section 4.4.3.3). The Zn $2p$ spectrum of the Zn reference contains a surface component corresponding to the surface oxide and contamination. The spectrum of the ZnO reference also exhibits a (minor) surface peak at a higher binding energy corresponding to the surface contamination.

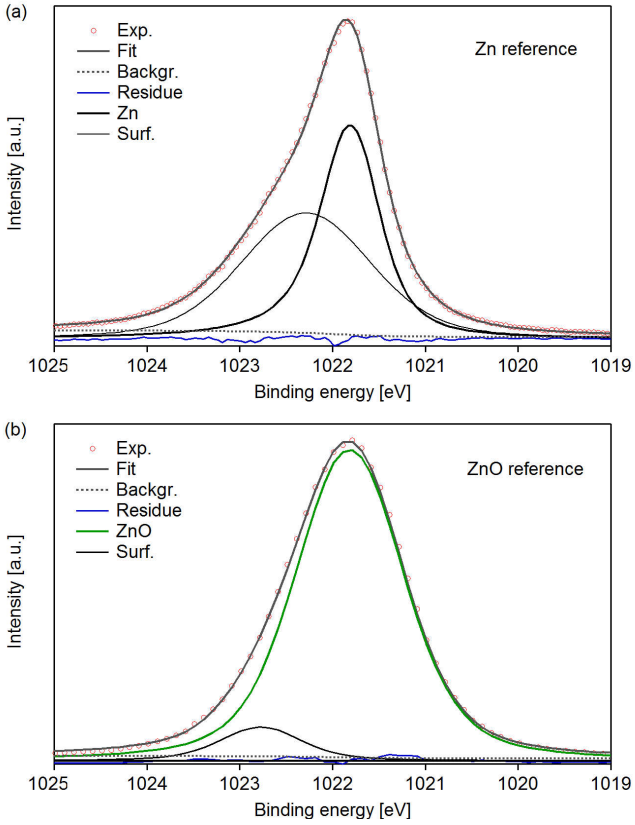

Figure 4.9: Zn $2p$ fits for the Zn and ZnO reference samples showing the experimental HAXPES data, fit, Zn- and ZnO-related components, background, and residue.

4.4.3.3 Zn $2p$ fitting details

In order to quantify the changes of the Zn chemical environment in the ZnO / Ti / Mo samples, Zn $2p_{3/2}$ peaks were fitted with 3 components corresponding to metallic Zn (Zn), ZnO (ZnO), and mixed ZnO-TiO_2 compound ($ZnTiO_x$). Fit results obtained for the reference samples (Table 4.5) as well as the data from literature (Table 4.4, [242]) were used to fix some of the fitting parameters. The ZnO- and $ZnTiO_x$-related symmetric peaks were fitted with Voigt profiles, while the asymmetric Zn-related peak was fitted with the PCI-curve. The binding energy shift of the ZnO component with respect to the Zn one was set to 0.26 eV. The shift between the components corresponding to ZnO and the unknown $ZnTiO_x$ compound was determined from the best Zn $2p_{3/2}$ fit for the ZnO (RT, 29.7 nm) / Ti / Mo sample after annealing at 550 °C and fixed at 0.26 eV in all fits. The FWHML was fixed at 0.49 eV for all the 3 components. The FWHMG was set free for all components and varied in different fits from 0.69 to 2.72 eV. The asymmetry of the Zn-related PCI peak was set to 0.12, and to 0 for the other two peaks. The background was described as a combination of linear and Shirley shapes.

4.5 Ti $2p$ and Zn $2p$ spectra evolution in the ZnO (RT, 29.7) / Ti / Mo sample after annealing in vacuum

4.5.1 Observation of core level evolution as a function of annealing

The reaction between the ZnO and Ti layers starts already during deposition of the Ti layer at room temperature. When the ZnO (RT, 29.7) / Ti / Mo sample is annealed at 250, 350, and 550 °C, the reaction goes on, activated by temperature. The interaction between the layers leads to the sizeable evolution of the Ti $2p$, O $1s$, and Zn $2p$ core levels.

Fig. 4.10 presents Ti $2p$ spectrum of the as-deposited ZnO (RT, 29.7) / Ti / Mo sample, as well as its evolution after subsequent annealings at 250, 350, and 550 °C under high vacuum ($p \sim 10^{-9}$ mbar).

Before thermal treatments, spectrum is represented by an asymmetric doublet at 454.05 eV corresponding to Ti^0 $2p_{3/2}$ and Ti^0 $2p_{1/2}$ separated by the spin-orbit splitting of 6.1 eV [310]. After annealing at 250 ˚C the Ti^0 component decreases, and a wide shoulder appears at higher binding energies. After 350 ˚C multiple peaks are observed, with an intensity maximum at 458.99 eV corresponding to the Ti^{4+} component. After annealing at 550 ˚C only one symmetric peak corresponding to Ti^{4+} [310] is visible.

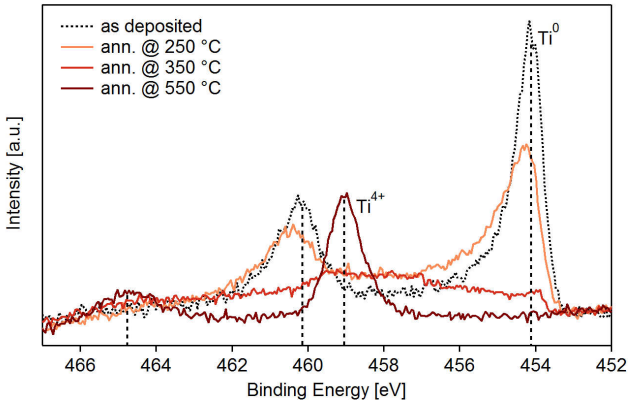

Figure 4.10: Ti $2p$ spectra of the ZnO (RT, 29.7) / Ti / Mo sample recorded at a photon energy of 4 keV in the normal detection geometry, as-deposited and after annealing at 250, 350, and 550 ˚C.

Fig. 4.11a shows O $1s$ peaks for the ZnO (RT, 29.7) / Ti / Mo sample, as-deposited and after annealing at 250, 350, and 550 ˚C. The intense peak for the as-deposited sample corresponds to the surface oxide of the Mo capping layer. Subpeaks corresponding to MoO_3 surface oxide [332] [8] are visible on the Mo $3d$ spectra together with the intense asymmetric peaks of metallic Mo [334], as shown in Fig. 4.11b, but they disappear after annealing at 250 ˚C.[9] Therefore, after annealing at 250 ˚C the O $1s$ core level represents oxygen in deeper layers of the stack, mostly in the ZnO film. After further annealing at 350 and 550 ˚C O $1s$ intensity gradually increases, as the reaction between ZnO and Ti goes on. Knut *et al.* [310] observed similar evolution of the oxygen core level with annealings.[10]

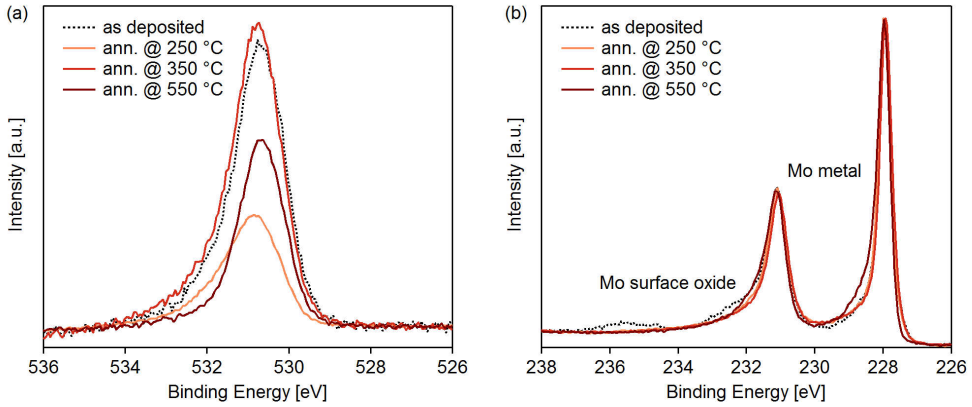

Figure 4.11: (a) O $1s$ spectra of the ZnO (RT, 29.7) / Ti / Mo sample recorded at a photon energy of 4 keV in the normal detection geometry, as-deposited and after annealing at 250, 350, and 550 ˚C. (b) Mo $3d$ spectra of the same sample normalized to the intensity maximum.

Fig. 4.12a shows Zn $2p_{3/2}$ spectrum evolution of the same sample, ZnO (RT, 29.7) / Ti / Mo , as-deposited

[8] The enthalpies of formation of Mo(III) and Mo(IV) oxides: $\triangle H_f^{Ox}(MoO_3) = -744.8$ kJ/mol, $\triangle H_f^{Ox}(MoO_2) = -589.5$ kJ/mol [333].

[9] The shape of the Mo $3d$ doublet remained unchanged after further annealings, except for a slight evolution after annealing at 550 ˚C, probably due to a reaction at the interface with Ti.

[10] O $1s$ peak for the as-deposited sample in case of Knut *et al.* [310] was less intense, because the part of the Mo film containing the native oxide was sputtered off prior to HAXPES measurements.

and after subsequent annealings at 250, 350, and 550 °C. Fig. 4.12b shows the same spectra normalized to the same intensity to make it easier to follow the changes in peak position and shape. The Zn $2p_{3/2}$ peak for the as-deposited sample is symmetric, as in the case of bulk ZnO. After annealing at 250 °C its intensity increases, and it becomes more asymmetric. After 350 °C the intensity drops, and the peak symmetry is recovered. Finally, after 550 °C the peak intensity further decreases, and it shifts towards higher binding energies.

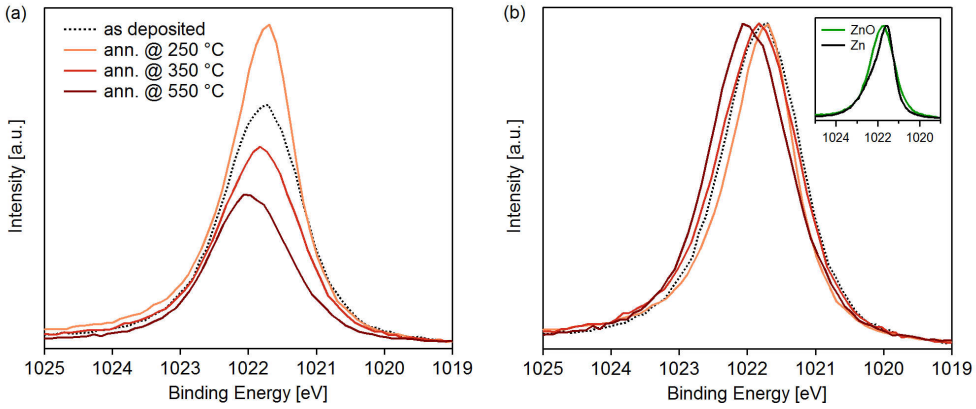

Figure 4.12: (a) Zn $2p_{3/2}$ spectra of the ZnO (RT, 29.7) / Ti / Mo sample recorded at a photon energy of 4 keV in the normal detection geometry, as-deposited and after annealing at 250, 350, and 550 °C. (b) Same spectra normalized by the peak intensity maxima. The inset shows the comparison of the Zn $2p$ peak shapes for the metallic Zn and ZnO references discussed in Section 4.4.3.2.

4.5.2 Ti oxidation state evaluation

To follow the evolution of all oxidation states, HAXPES spectra were decomposed according to parameters described in Section 4.4.2. Fits of the Ti $2p$ spectra of the ZnO (RT, 29.7) / Ti / Mo sample , as-deposited and after annealings at 250, 350, and 550 °C are given in Fig. 4.13 as an example. The spectrum of the as-deposited sample is represented by a metallic component Ti^0 (94% of the total Ti $2p$ area) and a small Ti^{2+} residue. After annealing at 250 °C the intensity of Ti^0 decreases giving rise to oxidized Ti states. The amount of Ti^{2+} increases, and higher oxidation states appear in the spectrum. After annealing at 350 °C a mixed oxidation state is observed, with the most intense peak being Ti^{4+}. After 550 °C the Ti film is almost completely transformed into Ti^{4+} (97% of the total area), except for a tiny Ti^{3+} residue.

Based on the areas of the Ti^0 $2p$, Ti^{2+} $2p$, Ti^{3+} $2p$, and Ti^{4+} $2p$ components the oxidation state of the Ti film could be quantified. The fractions of Ti^0, Ti^{2+}, Ti^{3+}, and Ti^{4+} components in the Ti $2p$ spectrum can be defined as:

$$c_i = \frac{I_i}{\sum_k I_k}, \tag{4.6}$$

where i =0, 2, 3, 4 corresponding to Ti^0, Ti^{2+}, Ti^{3+}, and Ti^{4+}, and I_i are the areas of the Ti^0, Ti^{2+}, Ti^{3+}, and Ti^{4+} components. If Ti^0, Ti^{2+}, Ti^{3+}, and Ti^{4+} species are homogeneously distributed, these fractions could correspond to respective atomic concentrations. In this case the fraction of oxidized Ti atoms in the film is equal to $(1 - c_0)$, and the average oxidation state of Ti can be calculated as:

$$n = 0 \times c_0 + 2 \times c_2 + 3 \times c_3 + 4 \times c_4. \tag{4.7}$$

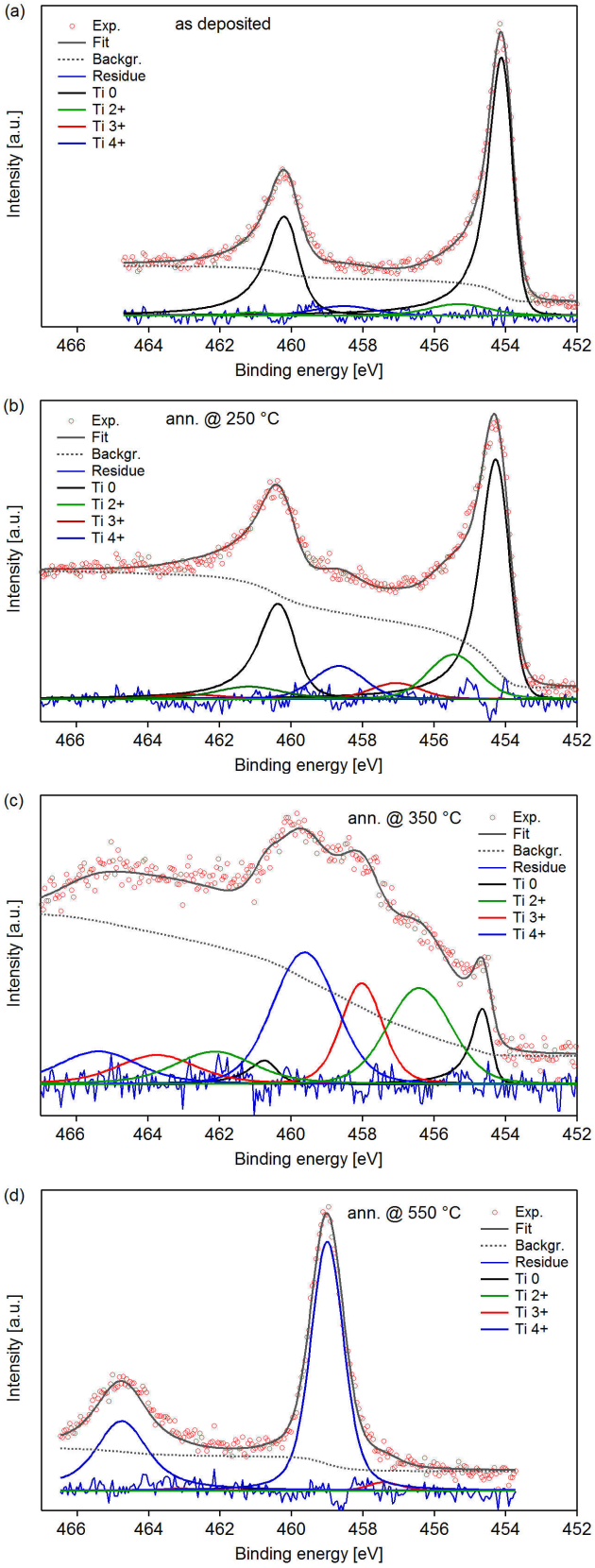

Figure 4.13: Ti $2p$ fit examples for the ZnO (RT, 29.7) / Ti / Mo sample: (a) as deposited and after annealing at (b) 250, (c) 350, and (d) 550 °C, showing the experimental data, fit, background, residue, Ti^{0}, Ti^{2+}, Ti^{3+}, and Ti^{4+} components of the fit.

In reality, the oxidation states of Ti should have a non-homogeneous distribution in the stack. As shown earlier by Knut *et al.* [310], if some Ti metal is left in the sample after annealing of a ZnO / Ti / Mo sample, it should be situated on top of the Ti layer, close to Mo. As shown in Fig. 4.14, a change of photon energy confirms this distribution of the Ti oxidation states. Ti $2p$ spectra of a ZnO (250 °C, 30) / Ti / Mo sample (not discussed in details in this work) were recorded at two different photon energies: 2.1 and 6 keV, corresponding to IMFPs of Ti $2p$ electrons of 2.4 and 6.4 nm in Mo, and 3.1 nm and 8.4 nm in Ti, respectively [335]. Thus, at a photon energy of 2.1 keV the probing depth is much smaller than at 6 keV. At 6 keV Ti^{4+} having a Ti^{3+} shoulder is visible in the spectrum, while at 2.1 keV lower oxidation states and even the Ti^0 component appear.

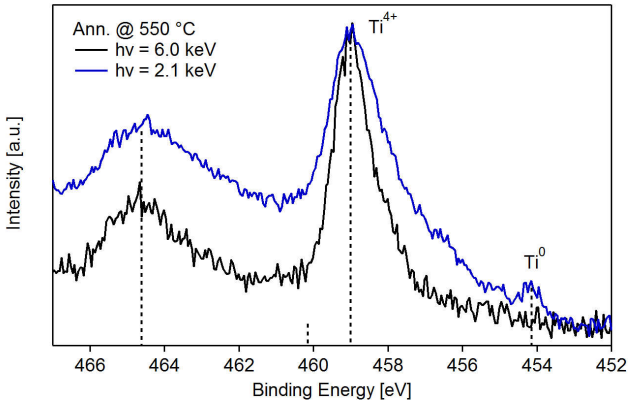

Figure 4.14: Comparison of Ti $2p$ spectra of the same sample, ZnO (30, 250 °C) / Ti / Mo acquired at the photon energies of 6 and 2.1 keV.

In order to evaluate the error done by using the simplified approach of the homogeneous mixture of the oxidation states of Ti, two ideal and extreme cases were compared: a homogeneous mixture of Ti^0, Ti^{2+}, Ti^{3+}, and Ti^{4+} atoms in the film and a layer by layer configuration, with Ti^{4+} at the bottom and Ti^0 on top, as shown in Fig. 4.15.

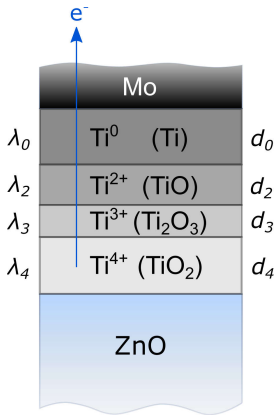

Figure 4.15: Schematic layer by layer distribution of the oxidation states of Ti in a ZnO / Ti / Mo sample, with Ti^{4+} (TiO_2) near the interface with ZnO and Ti^0 (metallic Ti) near the Mo capping layer.

In this configuration, according to Eq. 1.12 and 1.14, the Ti $2p$ intensities corresponding to different oxidation states can be expressed as:

$$I_0 \propto \lambda_0 \rho_0 \cdot (1 - \exp(-d_0/\lambda_0)) \,, \tag{4.8}$$

$$I_2 \propto \lambda_2 \rho_2 \cdot (1 - \exp(-d_2/\lambda_2)) \cdot \exp(-d_0/\lambda_0), \tag{4.9}$$

$$I_3 \propto \lambda_3 \rho_3 \cdot (1 - \exp(-d_3/\lambda_3)) \cdot \exp(-d_2/\lambda_2) \cdot \exp(-d_0/\lambda_0), \tag{4.10}$$

$$I_4 \propto \lambda_4 \rho_4 \cdot (1 - \exp(-d_4/\lambda_4)) \cdot \exp(-d_3/\lambda_3) \cdot \exp(-d_2/\lambda_2) \cdot \exp(-d_0/\lambda_0), \tag{4.11}$$

where I_i is the area of the i component, d_i and ρ_i are the thickness and the density of the corresponding i layer, and λ_i is the inelastic mean free path of the Ti $2p$ electrons in the i phase. Photoionization cross section σ and analyser transmission function T are identical for all peaks.

To be able to compare the two cases, one has to associate the Ti^0, Ti^{2+}, Ti^{3+}, and Ti^{4+} atoms with chemical compositions. For this evaluation, we assumed that Ti^{2+}, Ti^{3+}, and Ti^{4+} oxidation states correspond to the TiO, Ti_2O_3, and TiO_2 oxides, respectively, and Ti^0 corresponds to metallic Ti. Respective TiO_x thicknesses could be then evaluated, knowing the initial thickness of the Ti layer (~3.5 nm), bulk densities of Ti, TiO, $TiO_{1.5}$, and TiO_2 (4.51, 4.95, 4.49, and 4.23 g/cm^3, respectively), their atomic masses (47.87, 143.73, 71.87, and 79.87 g/mol, respectively), and corresponding IMFP values. The IMFP data was available only for metallic Ti ($\lambda_0 = 5.09$ nm) and TiO_2 ($\lambda_4 = 4.94$ nm) [335]. But since these IMFP values are close, for the sake of simplicity we considered that $\lambda_0 = \lambda_2 = \lambda_3 = \lambda_4 \simeq 5$ nm (with an error of 2%).

The spectrum for the ZnO (RT, 29.7) / Ti / Mo sample after annealing at 250 °C shown in Fig. 4.13b was taken as an example for evaluation. Here, the Ti^0 $2p_{3/2}$, Ti^{2+} $2p_{3/2}$, Ti^{3+} $2p_{3/2}$, and Ti^{4+} $2p_{3/2}$ components represent 65, 17, 6, and 12% of the total Ti $2p_{3/2}$ area, respectively. Based on the fitting results, equivalent TiO_x thicknesses were evaluated in the approximation of the homogeneous mixture: 2.3 nm of Ti, 0.7 nm of TiO, 0.3 nm of $TiO_{1.5}$, and 0.8 nm of TiO_2. These thicknesses were used to recalculate the areas in the approximation of a layer by layer distribution of Ti oxidation states (Fig. 4.15), using Eq. 4.8-4.11. The obtained partial areas were then compared with the partial areas from fitting results. The difference between the two estimations varied from 0 to 2% for the Ti^0, Ti^{2+}, Ti^{3+}, and Ti^{4+} oxidation states, as expected from the small magnitude of the initial Ti layer thickness compared to IMFP. It was therefore chosen to hereafter use the simplified approach.

The average oxidation state of Ti, and the fraction of Ti^0 and Ti^{4+} in the Ti layer in ZnO (RT, 29.7) / Ti / Mo was thus evaluated for the as-deposited sample and after annealings at 250, 350, and 550 °C (Table 4.6).

Thermal treatment in vacuum	Ti average oxidation state	Ti^0 [%]	Ti^{4+} [%]
As deposited	0.23	94	6
250 °C	1.24	56	14
350 °C	2.79	11	39
550 °C	3.96	0	97

Table 4.6: The average oxidation state of Ti, Ti^0 and Ti^{4+} fractions for the ZnO (RT, 29.7) / Ti / Mo sample, as-deposited and after annealings at 250, 350, and 550 °C.

4.5.3 Zn oxidation state and chemical environment evaluation

An example of the fit for the ZnO (RT, 29.7) / Ti / Mo sample, as-deposited and after annealing at 250, 350, and 550 °C – is given in Fig. 4.16. One can see that in the as-deposited sample ZnO is already slightly reduced during deposition. The spectrum of the as-deposited sample is represented mainly by the ZnO component, with a small Zn shoulder, corresponding to ZnO that is reduced during Ti deposition. After annealing at 250 °C the intensity of the Zn metal component increases and dominates the spectrum. After annealing at 350 °C the Zn intensity drops, so that ZnO again becomes the most intense contribution in the Zn $2p$ spectrum. After annealing at 550 °C the Zn component disappears, but an extra component emerges in the spectrum at higher binding energy. It is associated with the $ZnTiO_x$ compound.

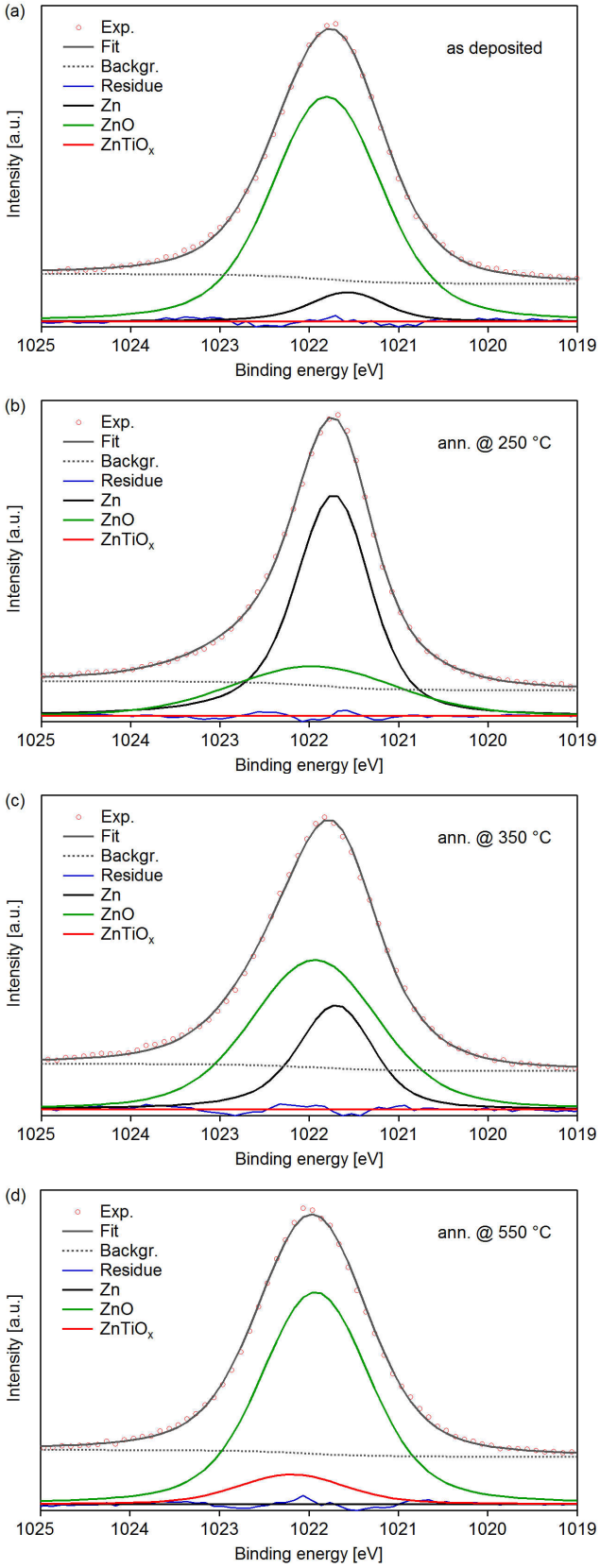

Figure 4.16: Zn 2p fit examples for the ZnO (RT, 29.7) / Ti / Mo sample: (a) as deposited and after annealing at (b) 250, (c) 350, and (d) 550 °C, showing the experimental data, fit, background, residue, ZnO-, Zn-, and $ZnTiO_x$-related components of the fit.

Fit results for the as-deposited sample, as well as after annealing at 250, 350, and 550 ˚C are gathered in Table 4.7. Fractions of each of the three Zn $2p_{3/2}$ components (Zn, ZnO, and $ZnTiO_x$) are given with respect to the total Zn $2p_{3/2}$ peak area.

Thermal treatment in vacuum	Zn [%]	ZnO [%]	$ZnTiO_x$ [%]
As deposited	9	91	0
250 ˚C	69	31	0
350 ˚C	31	69	0
550 ˚C	0	88	12

Table 4.7: Fractions of Zn-, ZnO-, and $ZnTiO_x$-related Zn $2p_{3/2}$ components for the ZnO (RT, 29.7) / Ti / Mo sample, as-deposited and after annealings at 250, 350, and 550 ˚C.

4.5.4 Discussion on the observed evolutions

Fig. 4.17 shows fractions of Ti $2p$ and Zn $2p$ components in the corresponding spectra, as well as the evolutions of the total Ti $2p$ and Zn $2p$ areas for the ZnO (RT, 29.7) / Ti / Mo sample as a function of the annealing temperature.

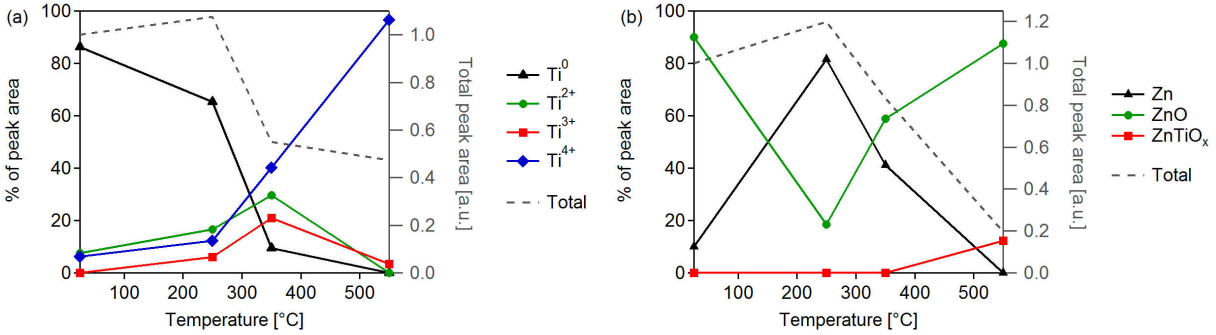

Figure 4.17: (a) Fractions of each of the Ti $2p$ components (Ti^0, Ti^{2+}, Ti^{3+}, and Ti^{4+}) with respect to the total Ti $2p$ peak area, (b) fractions of the Zn $2p$ components (Zn-, ZnO-, and $ZnTiO_x$-related) with respect to the total Zn $2p$ peak area for the ZnO (RT, 29.7) / Ti / Mo sample, as-deposited and after annealing at 250, 350, and 550 ˚C, and the evolution of the total area (dotted curve – right scale).

The evolution of Ti $2p$ spectra with annealings corresponds to gradual oxidation of the Ti film from metallic Ti (Ti^0) to fully oxidized Ti^{4+}. In the meanwhile, ZnO reduction is observed. Before annealing, the ZnO component is dominating the spectrum, but ZnO is slightly reduced already after the deposition. After annealing at 250 ˚C, the ZnO component decreases, while the Zn component becomes dominant. This corresponds to further ZnO reduction, and the diffusion of the produced Zn to the upper part of the sample, as suggested by the increase of its absolute intensity (dotted line in Fig. 4.17b). It is followed by the disappearance of Zn metal from the spectrum after annealing at 350 ˚C, and formation of a $ZnTiO_x$ mixed compound during annealing at 550 ˚C. A likely hypothesis is the formation of the Zn_2TiO_4 compound, as suggested by Kerjan *et al.* [308].

The loss of Zn after annealing in vacuum at 600 ˚C was *a posteriori* confirmed by EPMA. The Zn quantity decreased from 29.7 nm to 21 nm after annealing at 550 ˚C, while a reference sample of the same thicknesses without Ti showed no loss of ZnO. Therefore, the loss of Zn is clearly linked to the chemical reaction between ZnO and Ti layers. Table 4.8 lists ZnO thicknesses for all samples determined before and after thermal treatments.

Stack	ZnO thickness [nm]				
	As deposited	After 550 °C	Delta after 550 °C	After 650 °C	Delta after 650 °C
ZnO (RT, 14.4) / Mo	14.4	-	-	13.6	-0.8
ZnO (RT, 29.7) / Ti / Mo	29.7	-	-	21.0	-8.7
ZnO (RT, 10.5) / Ti / Mo	10.5	1.7	-8.8	-	-
ZnO (RT, 8.5) / Ti / Mo	8.5	0.5	-8.0	-	-
ZnO (300 °C, 26.6) / Ti / Mo	26.6	-	-	17.0	-9.6
ZnO (300 °C, 16.0) / Ti / Mo	16.0	9.7	-8.3	-	-
ZnO (300 °C + O_2, 19.5) / Ti / Mo	19.5	12.2	-7.3	-	-
ZnO (500 °C + O_2, 28.2) / TiO_x / Mo	28.2	22.1	-6.1	-	-

Table 4.8: ZnO thicknesses in ZnO / Ti / Mo samples, as-deposited and after annealing in vacuum at 550 and 600 °C. Thickness values were estimated by EPMA based on the Zn quantity, using ZnO bulk density.

The quantity of produced Zn and Zn_2TiO_4 (as suggested) was estimated based on the quantification of the Zn $2p$ HAXPES spectra of ZnO (RT, 29.7) / Ti / Mo (Fig. 4.12). The inelastic mean free path of the Zn $2p$ electrons excited by the photon energy of 4 keV (the corresponding kinetic energy of the electrons is ~2980 eV) in ZnO is ~4.7 nm, corresponding to a probing depth of ~14 nm. Thus, we can assume that in the beginning the spectra represented ~14 nm of ZnO. By making a proportional calculation and taking into account standard densities of Zn, ZnO, and Zn_2TiO_4 (7.14, 5.61, and 5.28 g/cm^3, respectively) and their molecular masses (65.38, 81.38, and 242.62 g/mol, respectively) the thicknesses of the created phases were evaluated. This gave ~6 nm of metallic Zn[11] produced during annealing at 250 °C, and 2.8 nm of Zn_2TiO_4[12] created during annealing at 550 °C. The estimated ~6 nm of Zn produced during annealing at 250 °C which left the sample during annealing at 350 °C correspond to an equivalent ZnO thickness of ~11 nm. Although this estimation does not take into account the exact location of Zn within the stack, the obtained values are comparable with those measured by EPMA.

The background of the Zn $2p$ doublet also provides noteworthy information, as shown in the zoom on HAXPES widescans in the Zn $2p$ region (Fig. 4.18a). After annealing at 250 °C the background at higher binding energies exhibits a different trend compared to the other spectra. Tougaard showed that the background shape depends critically on the in-depth distribution of the element [336]. As electrons pass through a material, some scatter inelastically, lose energy and end up at a lower energy in the spectrum. The measured energy spectrum is then sensitive to variations in chemical composition on the nanometre-depth scale. Fig. 4.18b is an adaptation from Ref. [336], showing the shape of the XPS background of the Cu $2p$ doublet as a function of the position of copper in gold: (i) placed on top of gold, (ii) distributed in volume, (iii) buried in a form of a thin layer, and (iv) situated underneath gold in a "bulk"-like form. By comparing the shapes of the background for the untreated sample and after annealing at different temperatures, it can be suggested that for the as-deposited sample the background corresponds to the case (iv) in Fig. 4.18b, and the change of the Zn $2p$ background after annealing at 250 °C corresponds to a part of Zn atoms that are either situated in the pre-surface region in a form of a thin layer (case (iii) in Fig. 4.18b), or distributed in the pre-surface region (case (ii)), or diffused onto the sample surface (case (i)). According to the Zn-Ti phase diagram (see Ref. [313] and Section 4.10.2), Zn and Ti are miscible at 250 °C. At this temperature $ZnTi_2$, ZnTi, Zn_2Ti, Zn_3Ti, Zn_5Ti, $Zn_{10}Ti$, and $Zn_{15}Ti$, can be formed for 33-100% of Zn in the mixture. Zn is also miscible with Mo [337]. Depending on the Zn fraction, it is possible to form either $MoZn_7$ or $MoZn_{22}$. Therefore, during annealing at 250 °C Zn can form an alloy with Ti or Mo.

[11] IMFP on Zn $2p$ electrons in Zn is ~4.1 nm [335].

[12] No data on $ZnTiO_x$ IMFP was available, therefore, if was considered to be equal to that of ZnO (4.7 nm) [335].

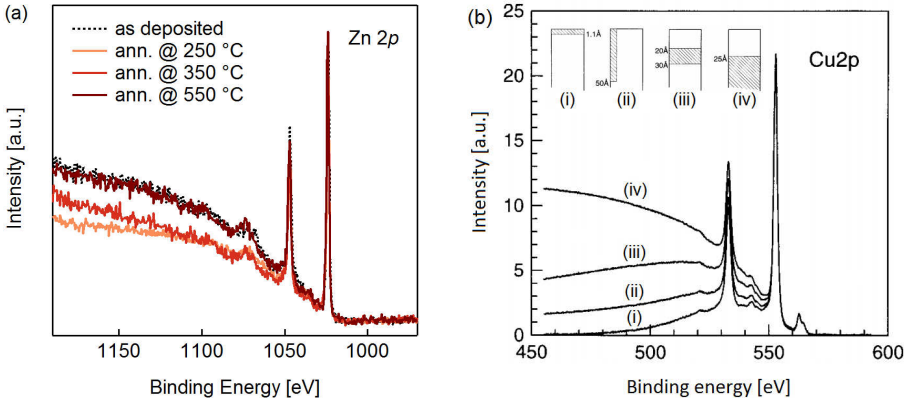

Figure 4.18: (a) Zoom on HAXPES widescans Zn $2p$ region normalized by Zn $2p$ maxima showing the background evolution as a function of annealing for the ZnO (RT, 10.5) / Ti / Mo sample. (b) Adaptation from Tougaard *et al.* [336], showing the shape of the XPS background of the Cu $2p$ doublet as a function of the position of copper in gold: (i) placed on top of gold, (ii) distributed in volume, (iii) buried in a form of a thin layer, and (iv) situated underneath gold in a "bulk"-like form.

The surface of a similar sample, ZnO (RT, 10.5) / Ti / Mo was observed by electron microscopy before and after annealing cycles up to 550 °C (Fig. 4.19). No cracks are observed on the surface. Therefore, Zn had to diffuse either through the bulk of the Ti and Mo or through the grain boundaries to leave the sample.

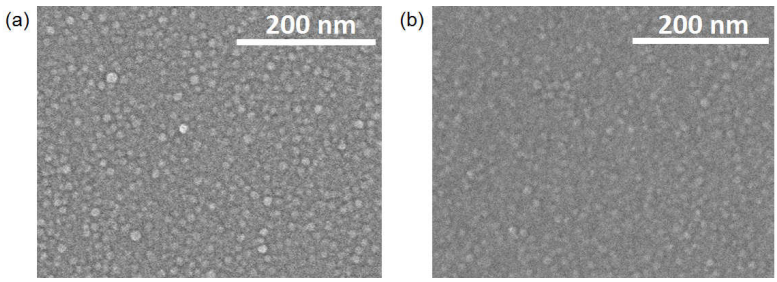

Figure 4.19: Electron microscopy images before and after annealing cycles up to 550 °C for the ZnO (RT, 10.5) / Ti / Mo sample showing its surface morphology.

4.6 Effect of ZnO thickness on Ti-ZnO reaction

In order to study the effect of the ZnO thickness on Ti oxidation, three samples were compared, containing different thicknesses of ZnO and same Ti thicknesses (3.4 nm): ZnO (RT, 29.7) / Ti / Mo (presented above), ZnO (RT, 10.5) / Ti / Mo, and ZnO (RT, 8.5) / Ti / Mo.

4.6.1 Ti $2p$ spectra evolution

Ti $2p$ spectra of the ZnO (RT, 8.5) / Ti / Mo sample as well as the evolution of the Ti^0, Ti^{2+}, Ti^{3+}, and Ti^{4+} components as a function of annealing are shown in Fig. 4.20a.b. Up to the annealing temperature of 350 °C it evolves in a similar way as the Ti $2p$ spectrum of the ZnO (RT, 29.7) / Ti / Mo sample (see Fig. 4.10). In the beginning the dominant component of the spectrum is metallic Ti (Ti^0). After annealing at 250 °C the Ti^0 component becomes less intense and higher oxidation states appear in the spectrum as a growing shoulder. After 350 °C oxidized states of Ti prevail over Ti^0, with Ti^{4+} becoming the most intense component. After annealing at 550 °C, in contrast to the ZnO (RT, 29.7) / Ti / Mo sample, the spectrum does not evolve much. The Ti^{4+} becomes slightly larger, but the other oxidation states remain quite intense. This is confirmed by spectra deconvolution (Fig. 4.20b): the components almost do not evolve after annealing at 550 °C. Not an extra annealing step at 550 °C (not shown), nor annealing at higher temperature, 650 °C does result in a full conversion of Ti into Ti^{4+}: the Ti $2p$ spectra remains the same.

The results for the ZnO (RT, 10.5) / Ti / Mo sample closely resembled those for ZnO (RT, 29.7) / Ti / Mo for all annealing temperatures.

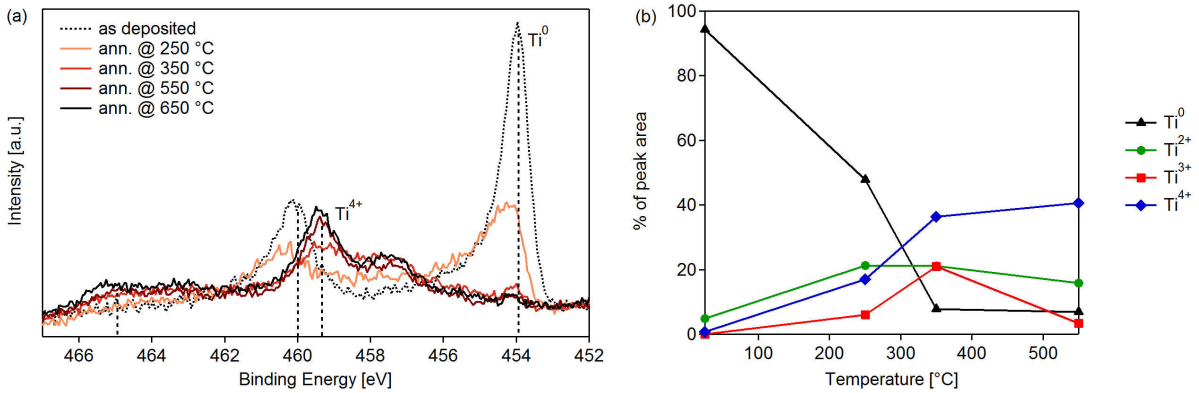

Figure 4.20: (a) Ti $2p$ spectra of the ZnO (RT, 8.5) / Ti / Mo sample recorded at a photon energy of 4 keV in the normal detection geometry, as-deposited and after annealing at 250, 350, 550, and 650 °C. (b) Evolution of the Ti^0, Ti^{2+}, Ti^{3+}, and Ti^{4+} components as a function of annealing.

4.6.2 Zn $2p_{3/2}$ spectra evolution

Zn $2p_{3/2}$ spectra of the ZnO (RT, 8.5) / Ti / Mo sample and the evolution of the Zn-, ZnO-, and $ZnTiO_x$-related components are shown in Fig. 4.21a,b. It evolves similarly to that of ZnO (RT, 29.7) / Ti / Mo (see Fig. 4.12) and ZnO (RT, 10.5) / Ti / Mo (not shown), although the evolution of the peak shape and position is more spectacular for the sample with a thinner ZnO layer. The fractions of the Zn, ZnO, and $ZnTiO_x$ components in the Zn $2p_{3/2}$ peak (Fig. 4.21b) almost do not evolve after annealing at 650 °C (Fig. 4.21a).

Zn $2p_{3/2}$ spectra of the ZnO (RT, 10.5) / Ti / Mo sample behaved in the same way as those of ZnO (RT, 8.5) / Ti / Mo and ZnO (RT, 29.7) / Ti / Mo.

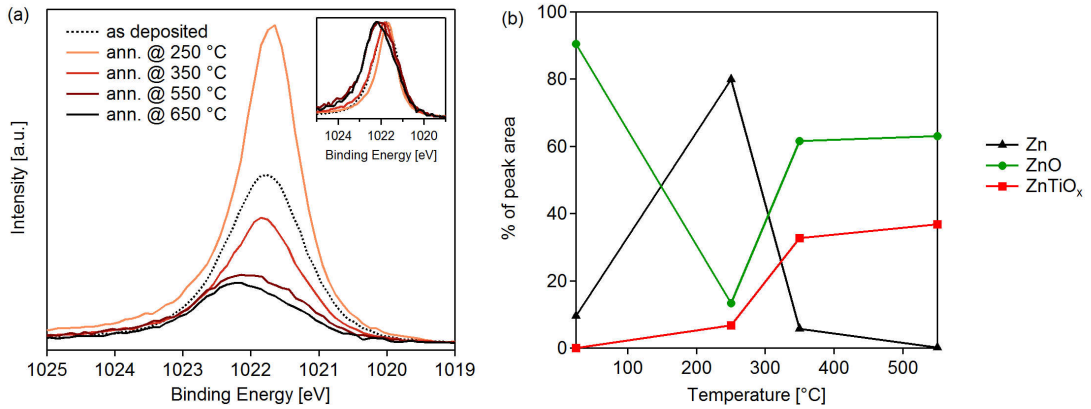

Figure 4.21: (a) Zn $2p_{3/2}$ spectra of the ZnO (RT, 8.5) / Ti / Mo sample recorded at a photon energy of 4 keV in the normal detection geometry, as-deposited and after annealing at 250, 350, 550, and 650 °C. The inset shows the same spectra normalized by the peak intensity maxima. (b) Evolution of the Zn, ZnO, and $ZnTiO_x$ components as a function of annealing.

4.6.3 Discussion

After annealing of the ZnO (RT, 8.5) / Ti / Mo sample at 550 °C the Ti film was largely under-oxidized (average oxidation state of 3.04 against 3.96 for the ZnO (RT, 29.7) / Ti / Mo sample), with 7% of Ti being in the metallic state Ti^0 and 41% of Ti^{4+}. Since the Ti $2p$ spectra did not evolve after further annealing, we can conclude that the reaction between ZnO and Ti could not progress further. A ZnO (RT, 10.5) / Ti / Mo sample, also containing room temperature deposited ZnO, but 10.5 nm thick, showed a behaviour similar to

the one of ZnO (RT, 29.7) / Ti / Mo. The average Ti oxidation state after annealing at 550 °C was 3.97 compared to 3.96 for ZnO (RT, 29.7) / Ti / Mo. It was thus concluded that, contrary to 8.5 nm, 10.5 nm of ZnO was enough to fully oxidise 3.5 nm of Ti.

Like in case of the ZnO (RT, 29.7) / Ti / Mo sample, one can relate the changes of the peak intensity and shape to the creation of metallic Zn which moved towards the top of the sample during annealing at 250 °C. Again, we suggest that Zn started leaving the stack between 250 and 350 °C. In turn, the shift of the peak position towards higher binding energies revealed the formation of a mixed $ZnTiO_x$ phase after 550 °C. The departure of Zn was confirmed *a posteriori* by EPMA: the Zn quantity in ZnO (RT, 8.5) / Ti / Mo after annealing was equivalent to 0.5 nm of ZnO against 8.5 nm before annealing (see Table 4.8). In case of the ZnO (RT, 10.5) / Ti / Mo sample the equivalent ZnO loss was of 8.8 nm.

In a simplified approach, one can consider a reaction between ZnO and Ti that goes as follows:

$$2ZnO + Ti \rightarrow TiO_2 + 2Zn. \tag{4.12}$$

Taking into account standard densities of ZnO and Ti and their atomic masses, one can evaluate the quantity of ZnO (supposing it is stoichiometric) needed to completely oxidise 3.5 nm of Ti: 9.4 nm. This corresponds well to the ZnO loss in the ZnO (RT, 29.7) / Ti / Mo and ZnO (RT, 10.5) / Ti / Mo samples after annealing at 550 °C. Since 9.4 nm can be indeed considered as a minimal thickness of ZnO needed to oxidise the whole 3.5 nm Ti film, we can conclude that the reaction between ZnO and Ti in ZnO (RT, 8.5) / Ti / Mo did not end by a complete oxidation of Ti due to the lack of ZnO reactant.

4.7 Effect of the ZnO crystalline quality on the Ti-ZnO reaction

In the previous chapter it was suggested that the ZnO film would have a better crystalline quality (and less defects) if prepared at an elevated temperature. This hypothesis was confirmed by X-ray diffraction and photoluminescence spectroscopy (see Section 3.4 for more details). In order to study the effect of the ZnO crystallinity, the previously discussed sample, ZnO (RT, 29.7) / Ti / Mo containing room temperature deposited ZnO was compared with ZnO (300 °C, 26.6) / Ti / Mo containing a similar amount of ZnO deposited at an elevated temperature (300±100 °C), and with a ZnO (300 °C, 16.0) / Ti / Mo sample, with the ZnO layer also deposited at higher temperature, but with a smaller thickness (16 nm).

4.7.1 Ti 2*p* spectra evolution

Ti 2*p* spectra of the ZnO (300 °C, 26.6) / Ti / Mo sample and the evolution of the Ti^0-Ti^{4+} components are shown in Fig. 4.22a,b. Again, at the beginning the spectrum is principally composed of the Ti^0 2*p* doublet. After annealing at 350 °C[13], in contrast with the case of ZnO (RT, 29.7) / Ti / Mo (see Section 4.5), the Ti^0 component is still the most intense in the spectrum. After 550 °C Ti^{4+} becomes the major component of the spectrum. Nevertheless, lower oxidation states are still visible. The average oxidation state of Ti after annealing at 550 °C is 3.37, with 4% of Ti^0 and 64% of Ti^{4+} in the film.

Analogous results were obtained for the ZnO (300 °C, 16.0) / Ti / Mo sample: at the end of the annealing cycle the average oxidation state of Ti was 3.40. This sample also showed a shifted onset temperature of oxidation.

[13] The sample was not measured after annealing at 250 °C.

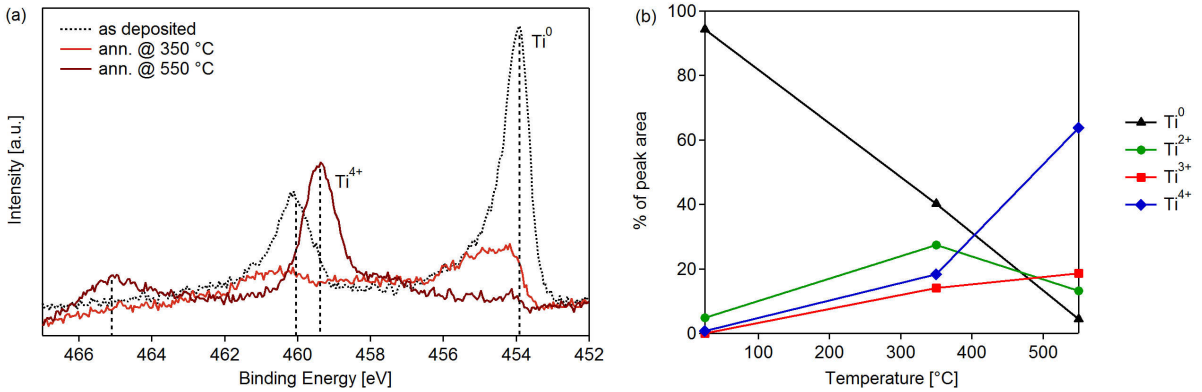

Figure 4.22: (a) Ti $2p$ spectra of the ZnO (300 °C, 26.6) / Ti / Mo sample recorded at a photon energy of 4 keV in the normal detection geometry, as-deposited and after annealing at 350 and 550 °C. (b) Evolution of the Ti^0, Ti^{2+}, Ti^{3+}, and Ti^{4+} components as a function of annealing.

4.7.2 Zn $2p$ spectra evolution

Zn $2p_{3/2}$ spectra of the ZnO (300 °C, 26.6) / Ti / Mo sample and the results of the peak decomposition as a function of annealing are shown in Fig. 4.23a,b. ZnO in the as-deposited sample is slightly reduced. After annealing at 350 °C, in contrast with ZnO (RT, 29.7) / Ti / Mo (Section 4.5), the Zn $2p_{3/2}$ peak becomes more intense and asymmetric due to the presence of Zn metal. After 550 °C the intensity drops, the symmetric shape of the peak is recovered, and, like in case of the ZnO (RT, 29.7) / Ti / Mo sample, the peak shifts towards higher binging energies.

Analogous results were obtained for ZnO (300 °C, 16.0) / Ti / Mo: Zn was produced during annealing at 350 °C and left the sample after 550 °C. A $ZnTiO_x$ compound was created during annealing at 550 °C.

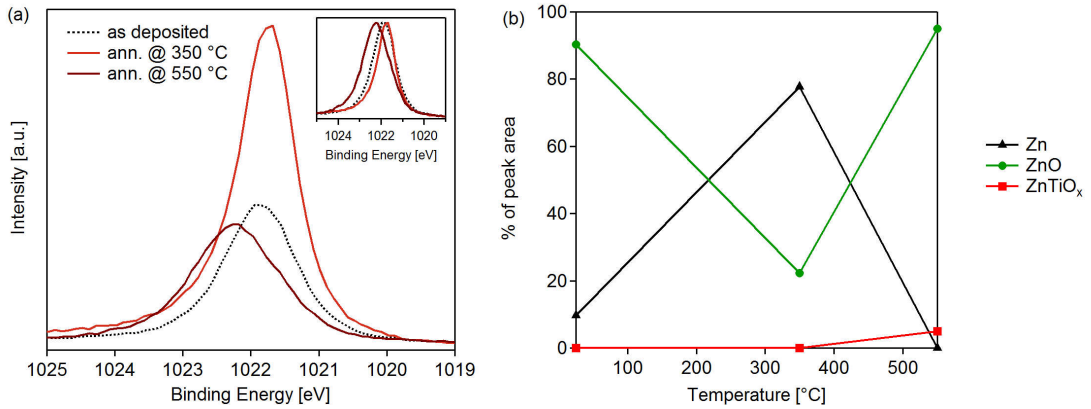

Figure 4.23: (a) Zn $2p_{3/2}$ spectra of the ZnO (300 °C, 26.6) / Ti / Mo sample recorded at a photon energy of 4 keV in the normal detection geometry, as-deposited and after annealing at 350 and 550 °C. The inset shows the same spectra normalized by the peak intensity maxima. (b) Evolution of the Zn, ZnO, and $ZnTiO_x$ components as a function of annealing.

4.7.3 Discussion

First, a higher deposition temperature of the ZnO layer led to a shift of the threshold of Ti oxidation to temperatures higher than 350 °C. Second, although the quantity of ZnO was sufficient, the oxidation degree of Ti in contact with a ZnO film deposited at 300 °C was significantly reduced (average oxidation state 3.37). That is to say, that the improved ZnO quality has limited its reactivity with Ti.

In contrast with the samples containing RT-deposited ZnO, metallic Zn was formed and moved upwards in the sample during annealing at 350 °C. After annealing at 550 °C Zn disappeared from the Zn $2p$ spectrum, and a mixed $ZnTiO_x$ compound was formed. *A posteriori* EPMA measurement confirmed the departure of

Zn in the ZnO (300 °C, 26.6) / Ti / Mo sample: the Zn quantity after thermal treatment at 600 °C was equivalent to 17 nm of ZnO against 26.6 nm in the as-deposited sample (see Table 4.8). Similar results were obtained for ZnO (300 °C, 16.0) / Ti / Mo, with an equivalent ZnO loss of 8.3 nm.

4.8 Effect of a TiO_x passivation layer on the Ti-ZnO reaction

As an attempt to further limit the ZnO-Ti reactivity, two samples were prepared: ZnO (300 °C + O_2, 19.5) / Ti / Mo and ZnO (500 °C + O_2, 28.2) / TiO_x / Mo. Here, the ZnO layers were deposited at 300±100 °C and at 500±30 °C, respectively, in 2 sccm of oxygen added to the Ar plasma. Ti layers were deposited without target pre-sputtering (cleaning), so that they were contaminated with oxygen, leading to a formation of TiO_x layer at the interface with ZnO.

4.8.1 Ti 2p spectra evolution

Ti 2p spectra of the ZnO (500 °C + O_2, 28.2) / TiO_x / Mo sample and the evolution of the Ti^0-Ti^{4+} components are shown in Fig. 4.24. Before annealing the spectrum shows the metallic Ti^0 state – the most intense peak in the spectrum, as well as higher oxidation states appearing as a pronounced shoulder. The average oxidation state of Ti in the as-deposited sample is 1.19. The spectrum doe not evolve after annealing at 200 °C. After annealing at 350 °C the Ti^0 component slightly decreases, giving rise to higher oxidation states. Only after annealing at 550 °C the spectrum drastically changes: Ti becomes almost completely oxidized to Ti^{4+} (0% of Ti^0 and 82% of Ti^{4+} in the spectrum), although the corresponding average oxidation state is 3.79.

Analogous results were obtained for ZnO (300 °C + O_2, 19.5) / Ti / Mo, while it was deposited at a lower temperature (300 compared to 500 °C). In this case the average oxidation states of Ti in the as-deposited sample and after annealing at 550 °C were 1.33 and 3.31, respectively.

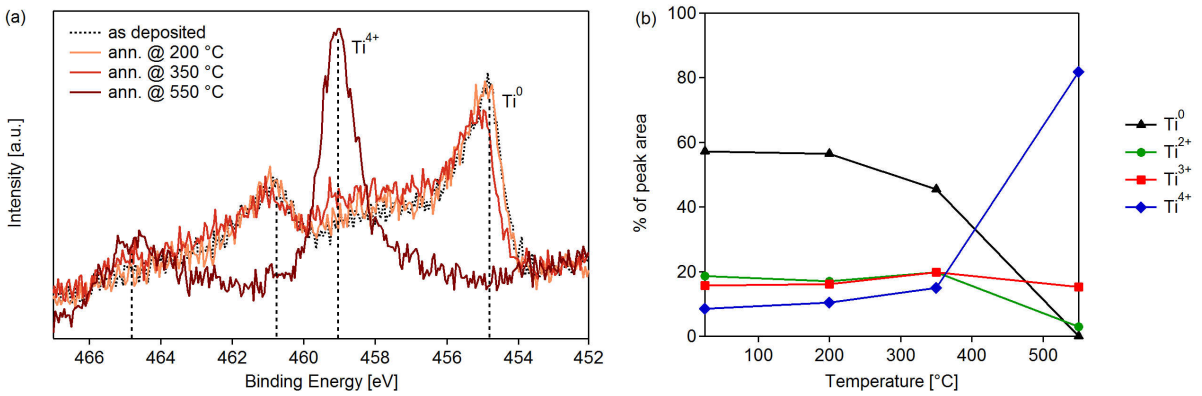

Figure 4.24: (a) Ti 2p spectra of the ZnO (500 °C + O_2, 28.2) / TiO_x / Mo sample recorded at a photon energy of 4 keV in the normal detection geometry, as-deposited and after annealing at 200, 350 and 550 °C. (b) Evolution of the Ti^0, Ti^{2+}, Ti^{3+}, and Ti^{4+} components as a function of annealing.

4.8.2 Zn 2p spectra evolution

Fig. 4.25 shows Zn $2p_{3/2}$ spectra of the ZnO (500 °C + O_2, 28.2) / TiO_x / Mo sample and the results of the peak decomposition as a function of annealing. Spectra does not evolve after annealing at 200 °C. After annealing at 350 °C Zn 2p intensity drops. After annealing at 550 °C the peak slightly shifts to lower binding energies. Spectra decomposition for the as-deposited sample shows that ~90% of the peak corresponds to ZnO, and the rest ~10% – to Zn. This ratio remains until annealing at 550 °C, which leads to a slight decrease of the ZnO component and to an increase of the Zn fraction.

Zn 2p spectra of the ZnO (300 °C + O_2, 19.5) / Ti / Mo sample showed a similar evolution.

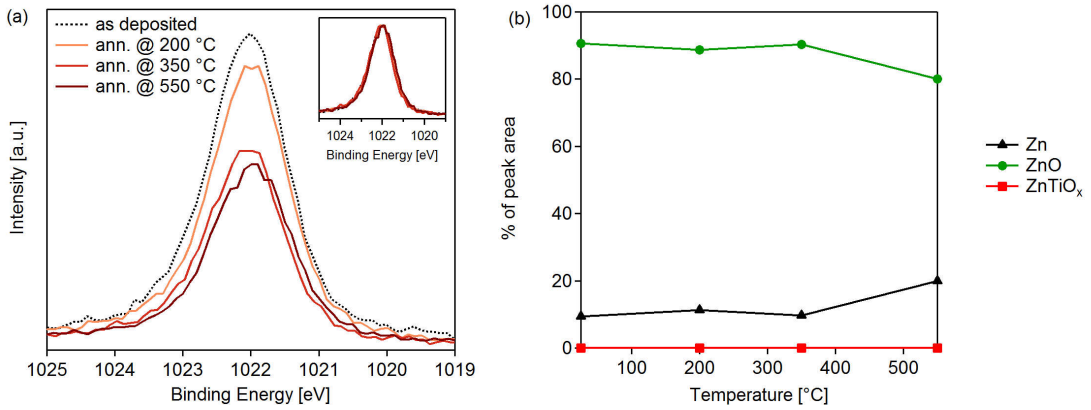

Figure 4.25: (a) Zn $2p_{3/2}$ spectra of the ZnO (500 °C + O_2, 28.2) / TiO_x / Mo sample recorded at a photon energy of 4 keV in the normal detection geometry, as-deposited and after annealing at 200, 350 and 550 °C. The inset shows the same spectra normalized by the peak intensity maxima. (b) Evolution of the Zn, ZnO, and $ZnTiO_x$ components as a function of annealing.

4.8.3 Discussion

Several parameters were modified in the ZnO (500 °C + O_2, 28.2) / TiO_x / Mo and ZnO (300 °C + O_2, 19.5) / Ti / Mo samples, compared to ZnO (300 °C, 26.6) / Ti / Mo. First, deposition conditions of ZnO, namely, the oxygen content during deposition and substrate temperature in one of the samples, were changed. Second, in both samples the Ti layer was replaced by an under-oxidized TiO_x film. The obtained ZnO-Ti interface had an improved resistance to thermal treatments: no change of Ti $2p$ spectra was observed up to annealing at 350 °C. Both samples showed similar behaviour in terms of the ZnO-TiO_x reactivity.

Both ZnO (500 °C + O_2, 28.2) / TiO_x / Mo and ZnO (300 °C + O_2, 19.5) / Ti / Mo were deposited in presence of oxygen, so it is difficult to conclude on the role of this parameter on the reactivity. The ZnO layer in ZnO (300 °C + O_2, 19.5) / Ti / Mo was deposited at the same temperature as that in ZnO (300 °C, 26.6) / Ti / Mo. Therefore, the major role of the deposition temperature in limiting the reactivity was rejected. Interestingly, a correlation was observed between the oxidation state of Ti in as-deposited samples and after annealing at 550 °C: the higher is the initial oxidation state of Ti, the less is the oxidation state after annealing at 550 °C (1.19 and 1.33, and 3.79 and 3.31 in ZnO (500 °C + O_2, 28.2) / TiO_x / Mo and ZnO (300 °C + O_2, 19.5) / Ti / Mo, respectively).

Based on these findings, we suggest that the main factor limiting the reaction between ZnO and TiO_x was the presence of TiO_x itself. It served as a protective diffusion barrier and started loosing its property only when the samples were annealed at 350 °C.

We suppose that the drop of the Zn $2p$ intensity after annealing at 350 °C corresponded to the thickening of the TiO_x layer due to the progressed oxidation. Although no evidence for strong ZnO reduction was observed, *a posteriori* EPMA showed that 6.1 nm of ZnO was lost after thermal treatment at 550 °C.

4.9 TDS study of the Ti-ZnO reaction

For ZnO deposited both at RT and at 300 °C, Zn formation in ZnO / Ti / Mo samples during annealing under vacuum was evidenced by HAXPES – during annealing at 250°C for the samples containing RT-deposited ZnO, and at 350 °C for the samples with ZnO deposited at 300±100 °C (see Sections 4.5 and 4.7). Based on the Zn signal which disappeared from the HAXPES spectrum after annealing at 350 and 550 °C in case of ZnO deposited at RT and 300±100 °C, Zn desorption was suggested and then confirmed by EPMA. The equivalent loss of ZnO was of 8.7 and 9.6 nm, respectively (see Table 4.8).

Given that the number of temperature points studied by HAXPES was limited to 3-5 (RT, 200 or 250, 350, 550, and 650 °C), it was not possible to conclude on the exact temperature of Zn desorption from the sample. A TDS study was therefore performed allowing for a continuous temperature scan while monitoring the desorbing species (see Section 1.2.5 for details). Two previously studied samples were examined: ZnO (RT, 29.7) / Ti / Mo containing room temperature deposited ZnO was compared with ZnO (300 °C, 26.6) / Ti / Mo containing a similar quantity of ZnO deposited at an elevated temperature (300±100 °C). According to the HAXPES results, the difference in the ZnO quality led to the following

differences in the ZnO-Ti reaction: change of the average oxidation state of Ti after annealing at 550 °C, shift of the onset temperature of Ti oxidation, and, as a consequence, of the temperature of Zn production and desorption.

The as-deposited samples were heated up to 600 °C under vacuum with a starting base pressure of 10^{-9} mbar at a heating rate of 0.5 K/s. The following m/q ratios were measured by TDS: 2 (H_2^+), (14) CO^{2+}, 16 (O_2^{2+}, O^+), 18 (H_2O^+), 28 (CO^+, N_2^+), 32 (O_2^+, $^{64}Zn^{2+}$), 40 (Ar^+, ZnO^{2+}, TiO_2^{2+}), 44 (CO_2^+), 48 (Ti^+), 64 ($^{64}Zn^+$, TiO^+), 66 ($^{66}Zn^+$), 80 (ZnO^+, TiO_2^+), and 98 (Mo^+) corresponding to the most likely fragments (given in parenthesis) to be expected. The measurements were performed several times for each sample, and were reproducible.

The TDS signal (detected ionic current) of the ZnO (RT, 29.7) / Ti / Mo sample is presented in Fig. 4.26 as an example. Spurious intense H_2, CO, O_2, H_2O, CO, and CO_2 desorption corresponding to the surface contamination is detected, since the sample was stored for a long time in air and was not cleaned prior to the TDS measurement. Nevertheless, Zn desorption is clearly visible. The signals from the two main Zn isotopes (^{64}Zn and ^{66}Zn) were systematically measured, in order to be sure that the $m/q = 64$ ratio did correspond only to desorbing Zn atoms.[14] One can also see a broad but not intense desorption band of Ar in the TDS spectrum[15]. For the ZnO (300 °C, 26.6) / Ti / Mo sample an additional narrow desorption peak of Ar was repeatedly observed around 400 °C. Ar is an unavoidable minor impurity trapped in thin films produced by magnetron sputtering in Ar plasma. Its quantification would require a calibration of the mass spectrometer. On the contrary, no desorption of Ti or TiO_x, nor Mo is observed for all the studied samples showing the absence of volatile species containing Ti or Mo. ZnO^+ is also absent showing that the Zn ($m/q = 64$ and 66) signals come from Zn atoms and are not fragments of the ZnO molecule.

Zn desorption was absent in a reference sample without Ti. This confirmed that ZnO films by themselves were thermally stable, and did not decompose upon annealing at temperatures up to 600 °C. Therefore, the Zn was produced and desorbed while heating only due to the presence of the Ti layer near ZnO.

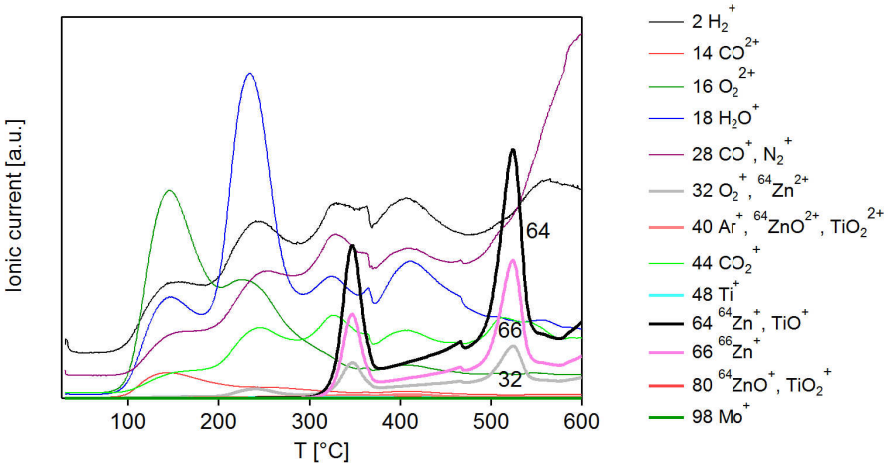

Figure 4.26: TDS spectra of H_2^+ (m/q =2), CO^{2+} (14), O_2^{2+} and O^+ (16), H_2O^+ (18), CO^+ and N_2^+ (28), O_2^+ and $^{64}Zn^{2+}$ (32), Ar^+, ZnO^{2+}, and TiO_2^{2+} (40), CO_2^+ (44), Ti^+ (48), $^{64}Zn^+$ and TiO^+ (64), $^{66}Zn^+$ (66), ZnO^+, TiO_2^+ (80), and Mo^+ (98) recorded on the as-received ZnO (RT, 29.7) / Ti / Mo sample. The heating rate is 0.5 K/s.

Fig. 4.27 shows ^{64}Zn TDS signals for the ZnO (RT, 29.7) / Ti / Mo and ZnO (300 °C, 26.6) / Ti / Mo samples as a function of temperature. For both samples, two peaks are clearly visible in the spectrum. The first one (i) shifts from 350 to 380 °C, and the second one (ii) – from 525 to 515 °C while switching from the ZnO (RT, 29.7) / Ti / Mo to the ZnO (300 °C, 26.6) / Ti / Mo sample, respectively. In terms of the integrated peak area after background subtraction, the ratio between the two peaks is 35/65% for ZnO (RT, 29.7) / Ti / Mo and 51/49% for ZnO (300 °C, 26.6) / Ti / Mo.

[14]The ratio between the ^{64}Zn and ^{66}Zn curves was 1.73 which corresponds to the natural abundance of these isotopes (48.3 and 28.0%, respectively).

[15]ZnO^{2+} does not contribute to the $m/q = 40$ signal, as ZnO^+ ($m/q = 80$) is absent.

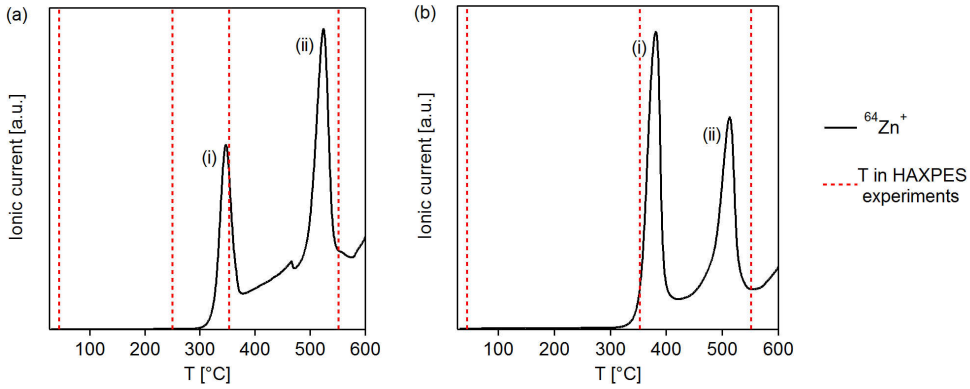

Figure 4.27: ^{64}Zn TDS signals (heating rate 0.5 K/s) for the (a) ZnO (RT, 29.7) / Ti / Mo and (b) ZnO (300 °C, 26.6) / Ti / Mo samples, as a function of temperature.

The activation energies of the desorption peaks were determined by a quantitative analysis. The rate of desorption is usually expressed through the Polaniy-Wigner equation [32, 338]:

$$r_d = -\frac{\mathrm{d}\theta}{\mathrm{d}t} = v\left(\theta\right)\theta^{n(\theta)}\exp\left(-\frac{E_a\left(\theta\right)}{kT}\right), \tag{4.13}$$

where θ is the surface coverage, $v\left(\theta\right)$ is the characteristic frequency, $n\left(\theta\right)$ is the order of the desorption reaction, $E_a\left(\theta\right)$ is the activation energy, $k = 1.38 \times 10^{-23}$ J/K the Boltzmann constant. Time t and temperature T are related through the linear heating ramp of slope α (0.5 K/s) as:

$$\frac{\mathrm{d}T}{\mathrm{d}t} = \alpha. \tag{4.14}$$

The introduced activation energy corresponds to the limiting step in the process of desorption. Since all the above listed parameters depend on the amount of desorbing species and vary with time, the accurate quantitative analysis of desorption spectra is relatively complex [32, 338, 339, 340] and requires a complete set of measurements at various heating rates. But several approximate approaches were developed in the past [32, 338, 339, 340, 341], among which the simplest one was provided by Redhead [32]. It relates the activation energy of desorption E_a with the temperature of the TDS peak maximum T_p within a hypothesis of a first order desorption ($n = 1$) which is coverage independent:

$$E_a = kT_p\left[\ln\left(\frac{\nu_1 T_p}{\alpha}\right) - 3.46\right], \tag{4.15}$$

where ν_1 is the characteristic frequency (10^{13} s^{-1} in the classical case). In the following, the activation energy deduced from the peak position T_p using Eq. 4.15 will be denoted as $E_a^{(1)}$.

The second approach is the linearisation of the desorption peak in order to determine the order of desorption as well as the activation energy. Under the hypothesis of coverage independent v, n, and E_a quantities, the detected ionic current, which is proportional to the desorption rate (see Section 1.2.5):

$$i\left(T\right) \propto r_d = -\alpha\frac{\mathrm{d}\theta}{\mathrm{d}T}, \tag{4.16}$$

is given by:

$$i\left(T\right) \propto \left(\int_{T_0}^{T} i\left(T'\right)\mathrm{d}T'\right)^n \exp\left(-\frac{E_a}{kT}\right). \tag{4.17}$$

In the $n = 0$ case the activation energy is the slope of $\ln\left[i\left(T\right)\right]$ as a function of $1/T$:

$$\ln\left[i\left(T\right)\right] \propto Const - \frac{E_a}{kT}. \tag{4.18}$$

Otherwise, since:

$$\ln\left[i\left(T\right)\right] \propto n \ln\left[\int_{T_0}^{T} i\left(T'\right) \mathrm{d}T'\right] - \frac{E_a}{kT}, \tag{4.19}$$

one can try to find the order of desorption n that linearises at best the quantity:

$$I\left(T\right) = \ln\left[i\left(T\right)\right] - n \ln\left[\int_{T_0}^{T} i\left(T'\right) \mathrm{d}T'\right] \propto -\frac{E_a}{kT} + \text{Const.} \tag{4.20}$$

as a function of $1/T$. The activation is the corresponding slope; it will be hereafter denoted $E_a^{(2)}$. Of course, the linearisation will never cover the whole peak, in particular, because of the dependence of all quantities on coverage which cannot be neglected. The approach is therefore limited at the onset of desorption for which the quantity of matter does not change significantly. This approach is often called desorption threshold analysis. An example of such a linearisation for Zn desorption is shown in Fig. 4.28.

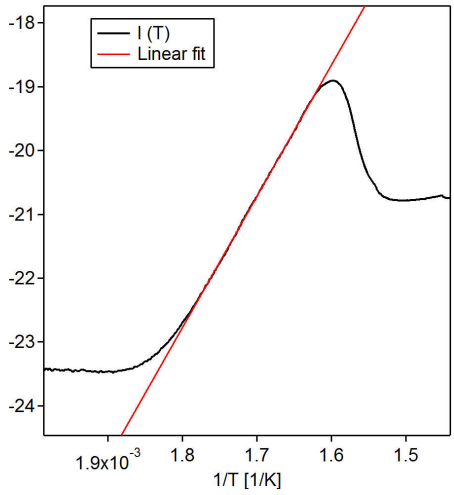

Figure 4.28: Example of linearisation of the $I\left(T\right)$ term (Eq. 4.20) for the ZnO (RT, 29.7) / Ti / Mo sample.

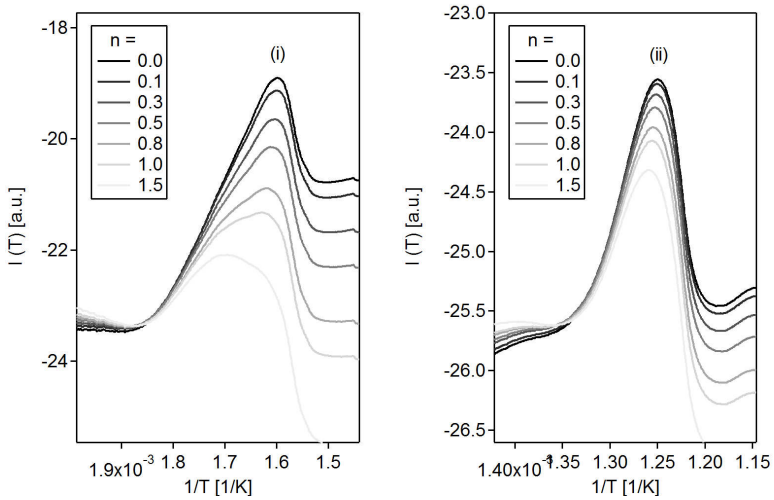

Figure 4.29: Desorption order analysis for the two Zn desorption bands observed for the ZnO (RT, 29.7) / Ti / Mo sample.

For both peaks (i) and (ii), a desorption order $n = 0$ was found (Fig. 4.29) except for the first peak (i) of the ZnO (300 °C, 26.6) / Ti / Mo sample which is better described by an order $n = 1.5 - 2$. This finding is in

line with the well-known asymmetric shape of the zero-order desorption [32]. The corresponding activation energies $E_a^{(2)}$ for both desorption bands (i) and (ii) are gathered in Table 4.9 and compared with those obtained using the Readhead method, $E_a^{(1)}$. The good agreement between the two quantities is somehow astonishing or fortuitous, since the found desorption order does not match the Readhead's hypothesis (*i.e.* $n = 1$). A higher $E_a^{(2)}$ value for the (i) peak of ZnO (300 °C, 26.6) / Ti / Mo is explained by the higher desorption order meaning that the desorption rate is limited by both the reaction and diffusion.

Sample	Zn desorption peak (i)				Zn desorption peak (ii)			
	T_p [°C]	$E_a^{(1)}$[eV]	$E_a^{(2)}$[eV]	n	T_p [°C]	$E_a^{(1)}$[eV]	$E_a^{(2)}$[eV]	n
ZnO (RT, 29.7) / Ti / Mo	350	1.79	1.75	0	525	2.33	2.43	0
ZnO (300 °C, 26.6) / Ti / Mo	380	1.90	2.37	1.5-2	515	2.29	2.31	0

Table 4.9: Apparent activation energies corresponding to the Zn TDS peaks (i) and (ii) evaluated either based on the peak position ($E_a^{(1)}$) [32] or by the near-threshold analysis ($E_a^{(2)}$) [32, 338, 339, 340, 341], and desorption orders of the respective peaks for the ZnO (RT, 29.7) / Ti / Mo and ZnO (300 °C, 26.6) / Ti / Mo samples.

In order to verify, whether the desorption was limited (or not) by the diffusion through the different layers, three additional samples containing metallic Zn were analysed by TDS:

- Si substrate / Zn (1.3 nm) / Mo (3.0 nm) denoted as Zn / Mo-S,
- Si substrate / Zn (1.6 nm) / Ti (3.3 nm) / Mo (3.0 nm) denoted as Zn / Ti / Mo-S,
- Si substrate / Zn (1.8 nm) / TiO_{2-x} (4.0 nm) / Mo (3.0 nm) denoted as Zn / TiO_2 / Mo-S.

A part of the Mo film containing the native oxide was sputtered off prior to TDS measurements, leading to a reduced Mo thickness compared to usual samples. As shown in Fig. 4.30, Zn desorption through Mo starts at around 200 °C and continues at higher temperatures. The first peak of Zn desorption through Ti is situated around ∼350 °C, and two more desorption peaks are observed: at ∼450 and 550 °C. Desorption through TiO_x is observed at ∼450-500 °C. In all the samples all Zn was desorbed.

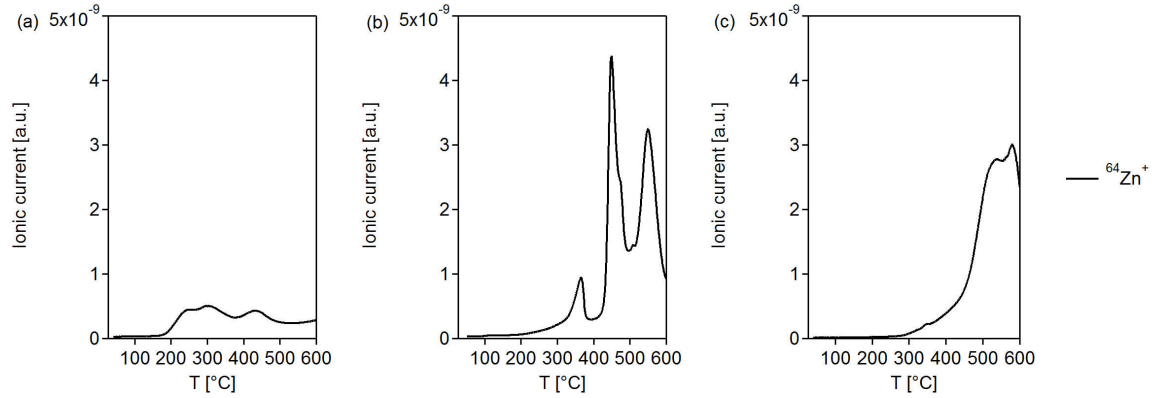

Figure 4.30: ^{64}Zn TDS signals for the (a) Zn / Mo-S, (b) Zn / Ti / Mo-S, and (c) Zn / TiO_2 / Mo-S samples, as a function of temperature.

4.9.1 Discussion of the TDS results

The TDS results obtained on ZnO / Ti / Mo thin film samples were compared with the results obtained by Mouchaal, Borghetti, and Lazzari [224] for 0.4-1.1 nm deposits of Ti evaporated on two polar surfaces of ZnO single crystals, ZnO-Zn and ZnO-O. Zinc desorption is observed only when ZnO is in contact with Ti. The second desorption band (ii) observed for the thin film samples appears in the same region, as for Ti evaporated on both surfaces of the monocrystal ZnO. The first band (i) is observed only for the ZnO-O surface. Interestingly, it shifts to lower temperatures with the increasing Ti coverage, as for a fractional desorption order. The high temperature peak (ii) is quenched for the smaller amount of Ti.

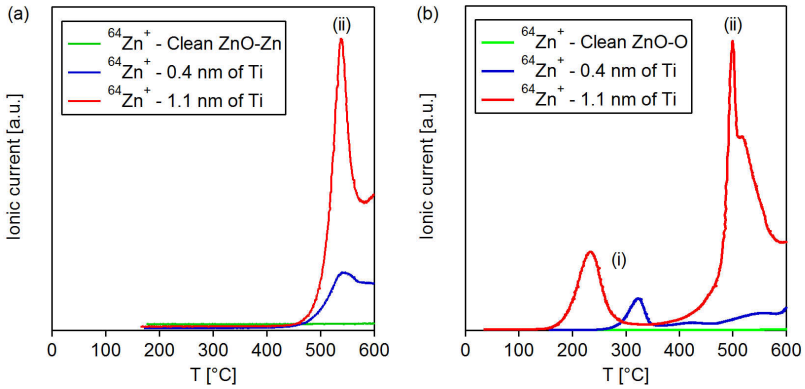

Figure 4.31: ^{64}Zn TDS signals for the (a) ZnO-Zn and (b) ZnO-O monocrystals, clean and covered by 0.4 and 1.1 nm of Ti, as a function of temperature. Interpreted from Ref. [224].

Based on these observations on the samples with and without Ti and the comparison with the results on ZnO monocrystals and evaporated Ti films, it was concluded that the Zn desorption was related to the interaction between the ZnO and Ti layers. It was suggested that the band (ii) around 520 °C is intrinsic to the reaction between ZnO and Ti, because it did not shift or disappear as a function of the nature of ZnO (monocrystal *vs* thin film), surface termination of monocrystal ZnO, or the ZnO layer preparation (RT *vs* 300 °C). By coincidence, $E_a^{(2)}$ of the peak (ii) matches with the enthalpy of the ZnO-Ti reaction (Eq. 4.12) which is:

$$\triangle H_f = \triangle H_f^{TiO_2} - 2\triangle H_f^{ZnO} = -244\,\mathrm{kJ/mol} = -2.53\,\mathrm{eV}. \tag{4.21}$$

However, it should be kept in mind that $E_a^{(2)}$ is an apparent activation energy that combines barriers of reaction between Ti and ZnO and of diffusion through the overlayers. But, as shown in Fig. 4.30, neither Mo nor Ti overlayers seem to really limit the desorption.

Absent for monocrystals except for the sub-monolayer deposit that can react with surface defects (such as hydroxyl groups), the peak (i) is thought to be related to the defects, stoichiometry or crystalline quality of ZnO layer. Its temperature position and activation energy are most probably related to diffusion through the Ti overlayer. Indeed, the shape of peak (i) of the ZnO (RT, 29.7) / Ti / Mo sample corresponds to a 0-order desorption which means that the rate of desorption is not limited by the available amount of Zn. A likely hypothesis is that Zn is already available (*i.e.* produced) at the moment of desorption, and the desorption is limited by the diffusion through the Ti layer which becomes possible only above ∼350 °C, according to Fig. 4.30. It is coherent with the zero desorption order deduced for Zn desorption from the Zn / Ti / Mo-S sample. This idea is supported by (i) the already high Zn vapour pressure at 300 °C (∼10^{-5} mbar compared to the vacuum level of 10^{-9} mbar) and (ii) the results of HAXPES after annealing at 250 °C that reveal the presence of Zn metal in the stack which does not desorb at that point (Section 4.5). The non-zero desorption order for the peak (i) of ZnO (300 °C, 26.6) / Ti / Mo and its shift to higher temperatures suggest that this peak is not any more limited only by diffusion through Ti. Indeed, it seems to appear in parallel with the redox reaction between ZnO and Ti observed by HAXPES (Section 4.5). Finally, the difference in intensity ratios of the two Zn desorption bands between ZnO (RT, 29.7) / Ti / Mo and ZnO (300 °C, 26.6) / Ti / Mo remains unclear.

4.10 Scenario of the reaction at Ti/ZnO interface

4.10.1 A summary

Like in Knut *at al.* [310], the reaction between ZnO and Ti films in the ZnO (RT, 29.7) / Ti / Mo sample started already during deposition (Section 4.5). Sample annealing at up to 550 °C resulted in gradual oxidation of the Ti film, as seen from Ti $2p$ core level evolution from metallic Ti (Ti^0) (94% in the Ti $2p$ spectrum of the as-deposited sample) to fully oxidized Ti^{4+} (97% in the spectrum after annealing at 550 °C). The change of the intensity of the O $1s$ spectra with annealings corresponded to oxygen diffusion from ZnO (being the only source of oxygen in the system) to Ti. Therefore, the oxidation states of Ti Ti^{2+}, Ti^{3+}, and Ti^{4+} can be formally associated with the formation of Ti (sub)oxides (TiO, $TiO_{1.5}$, and TiO_2) that

thickened the Ti film and damped the Ti $2p$ and Zn $2p_{3/2}$ core level intensities after subsequent annealings (Fig. 4.17).

In the meanwhile ZnO was reduced by Ti. Knut *et al.* observed signatures of metallic Zn after annealing at 200 °C that disappeared after annealing 350 °C [310]. Authors did not notice intensity variations of the Zn $2p$ core level and suggested that Zn formed during annealing at 200 °C represented a reduced ZnO which was re-oxidized by oxygen coming from the bulk of ZnO during annealing at 350 °C. In the present study, Zn metal was also observed during annealing at 250 °C. By decomposing the spectra, it was found that the Zn^0-related component was prevailing in the Zn $2p_{3/2}$ peak. In addition, the absolute intensity of the peak was much higher than that for the as-deposited sample. Therefore, it was suggested that metallic Zn corresponded not to Zn atoms in the ZnO layer, but to Zn which was set free and diffused to the upper part of the sample. Similarly, after annealing at 400 °C of a Ti film deposited on monocrystal ZnO(0 0 0 1), Rahman and Narusawa observed a significant amount of Zn metal that outdiffused onto the sample surface [309]. Analogous results were obtained by Ip *et al.* for the ZnO-W system annealed at 700 °C [342]. In our system, Zn metal disappeared from the spectrum after annealing at 350 °C, and the peak intensity dropped, suggesting that Zn probably left the stack. The comparison of the layer thicknesses evaluated by EPMA before and after thermal treatment (Table 4.8) revealed a loss of 8.7 nm of ZnO due to the reaction with Ti, which was never reported for the ZnO-Ti system. This happened in all samples, regardless ZnO deposition conditions. In addition, electron microscopy showed no evolution (in particular, no cracks) of the sample surface after annealing cycles (Fig. 4.19). Therefore, Zn metal had to diffuse through the Ti(O_x) and Mo overlayers to escape the sample.

A study of two samples with ZnO thicknesses reduced down to 10.5 and 8.5 nm allowed for the determination of a minimal ZnO thickness needed to completely oxidise 3.4 nm of Ti (Section 4.6). The found value in the range of ∼9 nm matches with the 9.4 nm theoretical thickness based on the ZnO-Ti redox reaction (Eq. 4.12). When the thickness of ZnO is less than this limit, Ti film remains under-oxidized after annealing at 550 °C (and even at 650 °C).

In all samples, after annealing at 550 °C the Zn $2p$ peak shifted to higher binding energies. Therefore, like in Knut *et al.* [310], formation of a $ZnTiO_x$ mixed compound was suggested. A likely hypothesis is the formation of zinc ortho-titanate Zn_2TiO_4, as it was already observed in the literature (see Section 4.2.2). HAXPES data allowed estimating the quantities of Zn produced during annealing at 250 °C and Zn_2TiO_4 produced during annealing at 550 °C: ∼6 nm (corresponding to an equivalent ZnO thickness of ∼11 nm) and 2.8 nm, respectively. Although this estimation did not take into account the exact location of Zn within the stack, the obtained values are comparable with those measured by EPMA.

Deposition of ZnO at higher temperatures led to noticeable changes in the ZnO-Ti reaction (Section 4.7). First, a shift of the threshold of Ti oxidation to temperatures higher than 350 °C was observed. Second, although the quantity of ZnO in the ZnO (300 °C, 26.6) / Ti / Mo sample was sufficient, the degree of oxidation of Ti in contact with a ZnO film deposited at 300 °C was significantly reduced (average oxidation state 3.37). In other words, the improved ZnO quality has limited its reactivity with Ti. Also, in contrast with the samples containing RT-deposited ZnO, metallic Zn was formed and moved upwards in the sample during annealing at 350 °C. After annealing at 550 °C Zn disappeared from the Zn $2p$ spectrum, and a mixed $ZnTiO_x$ compound was formed. *A posteriori* EPMA measurement again confirmed the departure of Zn.

Thermal desorption completed the temperature landscape given by high energy photoemission. ZnO layers themselves were stable upon annealing, but two Zn desorption peaks appear for ZnO / Ti / Mo samples containing ZnO deposited at room temperature or at 300 °C. The existence and positions of the peaks agreed with HAXPES findings after annealing at 350 and 550 °C (Section 4.17). The second desorption peak around 520 °C seems "intrinsic" to the Ti-ZnO reaction, as it is also observed for single crystals [224]. TDS studies of test samples containing metallic Zn showed that Zn diffusion through Mo starts after 200 °C, and through TiO_2 – after 450-550 °C. The higher temperature for diffusion activation through TiO_x goes in line with the HAXPES observation on the oxidation barrier role of TiO_x deposited between ZnO and Ti. Zn diffusion through Ti is activated at 350 °C, and when covered by Ti, Zn desorbs in multiple peaks.

Based on these findings, we suggest that in the case of the RT-deposited ZnO the first desorption peak is mainly limited by the diffusion through Ti. This is coherent with the zero desorption order of the peak. But when ZnO is deposited at higher temperature, the threshold temperature of its reaction with Ti increases beyond a value at which the desorption is no longer determined by Zn diffusion through Ti, but only by the ZnO-Ti reaction. This is in line with the change of the desorption order from zero to 1.5-2 and the variation of the apparent activation energy.

4.10.2 Reaction scenario based on HAXPES, TDS, EPMA, and thermodynamic simulations

As discussed in the introduction of this chapter, thermodynamics provide already a good basis to rationalize metal/oxide reactions and therefore the present findings. In order to better understand the HAXPES, TDS and EPMA results summarized above and in the absence of data concerning the Zn-Ti-O ternary phase diagram, especially at reduced pressure (see Section 4.2), thermodynamic simulations using the *FactSage* software [343] were performed. *FactSage* software combines numerous databases of pure substances and solutions with various modules which can perform different thermochemical calculations based on the minimization of the Gibbs energy, in order to find equilibria between the possible bulk phases.

These simulations are based on homogeneous mixtures and, thus, do take into account neither the stack thin film structure of the samples, nor, obviously, kinetics. However, such thermochemical calculations can indicate the formation of the most stable phases and, therefore, the most probable solid state reactions during thermal treatments. Furthermore, the presence of the Mo capping layer deposited on top of Ti and ZnO was not considered. But according to the Ti-Mo phase diagram, Mo is immiscible with titanium up to 695 °C [313]. On the one hand, Mo showed no special evolution of its oxidation state by HAXPES. On the other hand, even if MoO_x had stability similar to that of TiO_x (*FactSage* values at 25 °C, 1 atm: $\triangle H_f^{Ox}(MoO_3)$ = -745 kJ/mol, $\triangle H_f^{Ox}(MoO_2)$ = -587 kJ/mol, $\triangle H_f^{Ox}(TiO_2)$ = -945 kJ/mol, and $\triangle H_f^{Ox}(TiO)$ = -543 kJ/mol), the fact that the oxidation of the Ti layer starts at the interface with ZnO limits the possibility of reaction between Mo and TiO_x.

FactSage simulations were carried out for the ternary Zn-Ti-O system introduced as a homogeneous mixture of the pure elements: Zn, Ti and O. Thermochemical calculations were performed using available experimental and calculated data concerning the different possible compounds, namely:

- Crystalline phases: ZnO, rutile and anatase TiO_2, TiO, $Ti2O_3$, $(ZnO)_2(TiO_2)$=Zn_2TiO_4, Zn, Ti, $TiZn_x$, $(ZnO)_x(TiO_2)_y$,
- Liquids: Zn, TiZn, etc.
- Gases: Zn, O_2.

First, the Zn-Ti-O ternary diagram was established at atmospheric pressure. Fig. 4.32 presents an example determined at a fixed temperature of 650 °C.

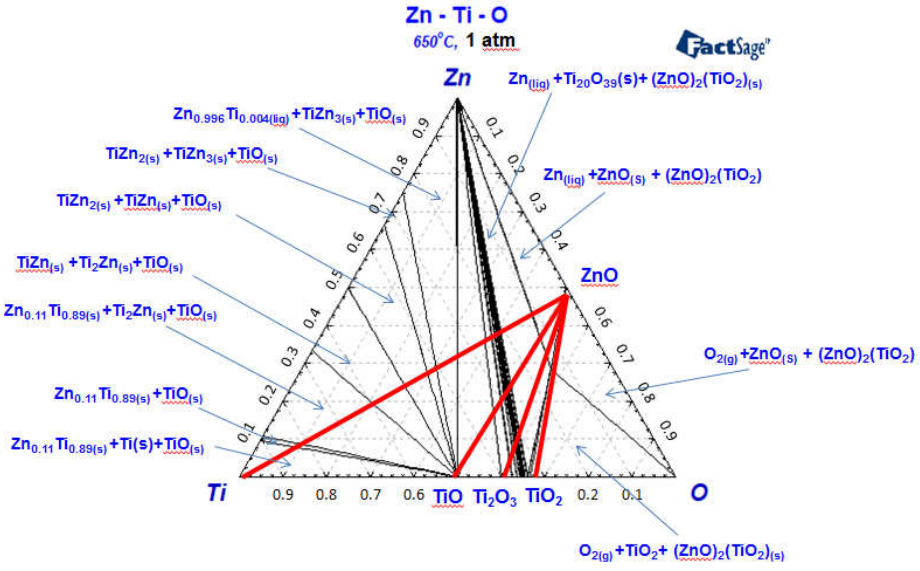

Figure 4.32: Zn-Ti-O ternary phase diagram at 650 °C, 1 atm. The indices stand for solid (s), liquid (liq), and gas (g) states.

Based on this diagram, some binary diagrams have been extracted, as shown in Fig. 4.33 for the Ti-Zn and ZnO-TiO_2 systems. In the case of pure metals, numerous alloys or defined Ti_xZn_y compounds appear,

in agreement with the experimental phase equilibrium diagram proposed by Vassilev *et al.* [344]. Concerning the ZnO-TiO_2 system, the computed phase diagram is close to the cumulative one proposed in Fig. 4.3, except for the eutectic temperatures and the lack of $ZnTiO_3$, $Zn_2Ti_3O_8$ phases. These two compounds are not proposed by *FactSage* due to the absence of experimental thermodynamic data. Nevertheless, these phases have been observed only at temperatures higher than those in our experiments, and therefore, it is likely that the formation of these compounds should not impact the following conclusions.

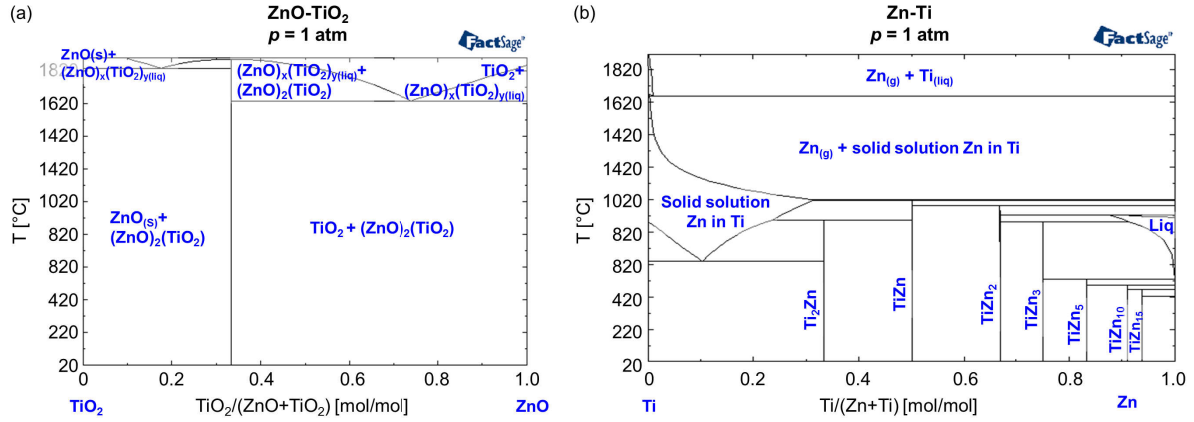

Figure 4.33: (a) TiO_2-ZnO and (b) Ti-Zn phase diagrams simulated in *FactSage* at atmospheric pressure.

Thanks to these first results obtained at ambient pressure which demonstrate that the approach and the data used for the calculations are reasonable compared to the data published in the literature (Section 4.2), a Zn-Ti-O ternary diagram was simulated at low pressure $p = 10^{-9}$ mbar which is close to that in TDS and HAXPES measurements. ZnO-Ti and Zn-Ti binary diagrams shown in Fig. 4.34 were extracted from the ternary one. These two systems were chosen, because they are related to two interfaces (ZnO/Ti and Zn/Ti) which, we suggest, are involved in solid state reactions between Ti and ZnO layers.

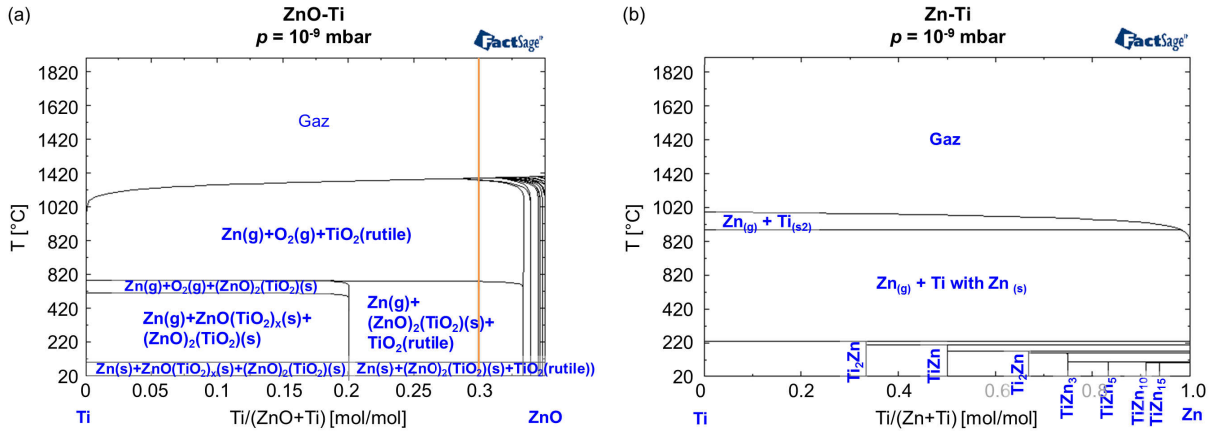

Figure 4.34: (a) ZnO-Ti and (b) Ti-Zn phase diagrams simulated in *FactSage* at $p = 10^{-9}$ mbar. Vertical orange line corresponds to the composition with 33% of Ti, *i.e.* ZnO (9.5 nm) / Ti (3.4 nm).

Since the ZnO-Ti system represents the interface between ZnO (thick layer) and Ti (thin layer), the phase diagram is limited to low titanium molecular fractions. The vertical line in Fig. 4.34a corresponds to a homogeneous mixture with 33% of Ti, equivalent to a 3.5 nm thick Ti layer reacting with a 9.4 nm thick ZnO layer. This line should represent the pathway of the thermochemical reactions which occur in our sample with increasing temperature at reduced pressure. The following compounds are formed: Zn(s), Zn(g), TiO_2 (rutile), $(ZnO)_2TiO_2$, as suggested by different experiments (mainly HAXPES). Zn(g) can be formed above 100 °C from Zn(s). A second Zn(g) formation is observed at 580 °C which corresponds to the decomposition of the $(ZnO)_2TiO_2$ compound. These temperatures poorly depend on the Ti fraction in a

large domain. However, the stratified structure of the sample and the propagation of the redox front might induce a shift of these reactions to lower Ti fractions as they are calculated in the frame of homogeneous mixtures. The main outcome of this simulation is the possibility to form a non-stoichiometric solid solution $ZnO(TiO_2)_x$ which can decompose into Zn(g) at a lower temperature, *e.g.* at 520 °C. This argument could explain the high temperature Zn desorption peak in TDS (Fig. 4.27). Regarding the low temperature one at 350 °C, it seems to be delayed, compared to thermodynamics predictions (100 °C), due to Zn diffusion through Ti and Mo layers and/or the formation of $TiZn_x$ (Fig. 4.34b).

Finally, based on the combination of HAXPES, TDS, and EPMA results, and thermodynamic calculations, the following reaction scheme of RT-deposited ZnO with Ti can be proposed (Fig. 4.35). A thin TiO_x film inevitably produced during deposition is initially present at the interface between ZnO and Ti films [310]. While heating up to 250 °C, Ti reduces ZnO, leading to the growth of a TiO_x layer and the release of Zn metal. Zn produced in this reaction becomes mobile and goes upwards in the stack. Limited by the diffusion through metallic Ti and/or by the formation of $TiZn_x$ compounds, Zn metal stays "blocked" inside the Ti film until approximately 350 °C, when its diffusion through Ti and desorption becomes possible. Metallic Zn which is further produced in the reaction is encapsulated under TiO_x until ~450-500 °C. During annealing at 550 °C, a $ZnTiO_x$ compound is formed. By the end of annealing the Ti film is fully oxidized – if there is enough ZnO in the as-deposited sample (~9.4 nm), and the excess of metallic Zn is desorbed from the sample.

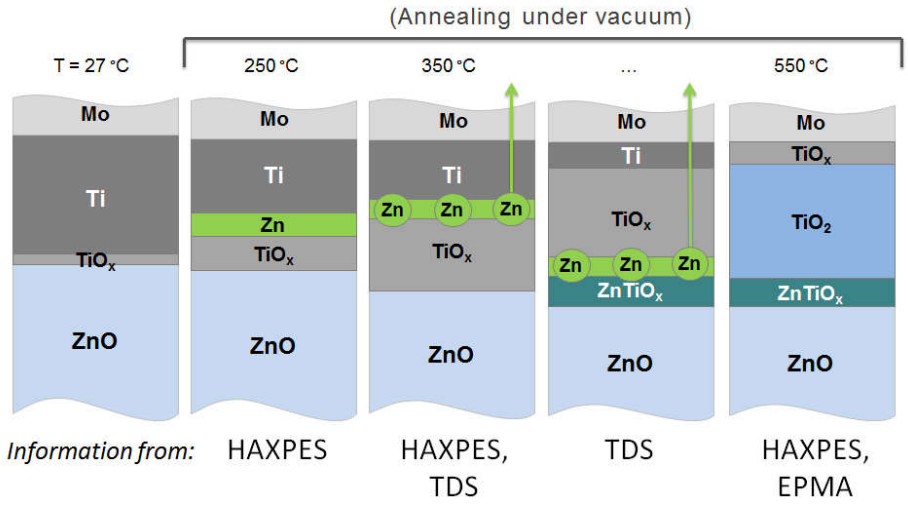

Figure 4.35: Schematic of the proposed reaction mechanism.

To conclude, this study aimed to understand the pathway of the chemical reaction at the Ti/ZnO interface which is involved in low-emissive coatings developed for the glass industry. Model thin film stacks were synthesized by sputtering deposition and analysed as function of annealing temperature, film thickness and ZnO crystalline quality. The main originality of this work was to intensively use the advantage of HAXPES to look *in situ* at buried interfaces in a non-destructive way. An unexpected strong diffusion of Zn due to the redox reaction was witnessed, which may impact crystallinity and optical properties of the other layers of the functional coating, and in particular, of silver overlayers. Further structural studies (X-ray diffraction or transmission electron microscopy) may confirm the final scenario.

Conclusions

This thesis tried to tackle several fundamental aspects of the physics and chemistry of silver thin films developed by the glass industry. It combined surface sciences approaches on single crystals and sputtered model thin films. On an experimental point of view, photoemission spectroscopy was central to determine (i) band alignment at Ag/ZnO interface with ultra-violet (UPS) and high energy photoemission (HAXPES), (ii) polarity orientation in polycrystalline films using laboratory X-ray source (XPS) and (iii) to follow the reaction at the buried Ti/ZnO interface with synchrotron excitation (HAXPES).

The first part of the thesis focused on the interplay between morphology, polarity and hydrogen adsorption on the band alignment at the interface between silver and the polar faces of ZnO. Whatever the terminations, polar ZnO surfaces present a strong upward band bending of around 1 eV. The preparation technique by sputtering-annealing, although leading to a hydroxyl free surface on the photoemission point of view, yields a degenerated semi-conductor with a Fermi level above the conduction band by a fraction of electron-volt. Exposure to atomic hydrogen (i) hydroxylates both terminations but etches the ZnO(0001)-Zn surface by breaking Zn-O back bonds and producing metallic zinc and (ii) bends downwards the bands. But no accumulation layer is observed probably because of the degenerated character of our substrates. The found hexagon-on-hexagon epitaxy of silver is driven probably by the growth along the step edges. The growth is quasi-2D up to a critical thickness of a fraction of monolayer before the appearance of the fcc stacking and the growth of 3D metallic particles. One the originality of this work was to combine HAXPES and UPS to determine the band alignment at Ag/ZnO interface. For thick film, a Schottky contact with a barrier height of 0.5-0.7 eV was found whatever the surface or its hydrogenation state. This is interpreted by the dominant role of the metal induced gap states that pins the Fermi level. However, for thinnest films, the concomitant evolutions of work function and band bending sign a different dipole orientation with a cationic adsorption on ZnO(000$\bar{1}$)-O and anionic on ZnO(0001)-Zn in the submonolayer regime followed afterwards by a neutral adsorption. This findings parallels the structural investigations and may be related to nucleation along step edges. However, the nature sites of both H and Ag remain unknown. The present study could be extended towards the wetting enhancement induced by migration of subsurface defects as observed in the case of Cu [189, 94]. Further experiments with higher hydrogen exposure would also be welcome to check if an ohmic contact could be actually reached by doping more the subsurface.

In a systematic way, the conditions of growth of ZnO films by magnetron-sputtering was explored with the objective to control the orientation by a applying a bias to the sample. As a function of temperature and bias, three distinct zones were discovered corresponding to films with {0001} out-of-plane texture with Zn-, O-terminations and re-sputtering. As expected, 28, 33, 17, 32better crystallinity was achieved at higher temperatures. Still the opportunity offered by the control of the orientation of the sputtered ZnO films on Ag film growth, adhesion, resistivity or Schottky contact remains to be explored.

The above developed ZnO films have been used as substrates to tackle the question of reactivity at Ti/ZnO. Synchrotron HAXPES provided the opportunity to follow the evolution of buried interfaces in specially designed samples through several nanometres of matter. A progressive reduction of ZnO by Ti was evidenced when ramping the temperature from 250 °C to 550 °C. Through a decomposition of the Ti $2p$ core level, the average oxidation state of Ti changed from 0.23 to nearly 4. For a given Ti thickness, the reaction is limited only by the thickness of the ZnO film and accompanied by the desorption of Zn. During annealing at 550 °C, some fingerprints of the formation of a mixed $ZnTi_yO_x$ are present in the Zn $2p$ core level. The temperature threshold of the reaction is impacted by the crystalline quality of the zinc oxide films; film grown at higher temperatures are more resilient than defective ones. The desorption of zinc was confirmed by Electron Probe MicroAnalysis and Thermal Desorption Spectroscopy. In agreement with

photoemission findings, two desorption peaks at $350-380$ °C and ~ 520 °C were evidenced. Desorption from reference samples containing metallic Zn layers demonstrated that the first peak is limited by diffusion of Zn through the Ti layer while the second is intrinsic to the ZnO/Ti system. Combined with thermodynamic simulations of the Ti-ZnO phase diagram, a scenario emerged regarding the reaction. This study pointed at a phenomenon which was not suspected by the industrialist, the diffusion of zinc. It also highlighted the potentialities of HAXPES to analyse interdiffusion and reactivity in a film stack in conditions closed to those faced by the glass coating industry. Beyond the obvious extension to other reactive metals, a future direction of research could be the exploration of the efficiency of different oxides or nitrides as diffusion barriers for reactive species present in the stack or in the glass itself.

Bibliography

[1] R. Hill, *Coated Glass Applications and Markets*, Fairfield, CA: BOC Coating Technology (1999)

[2] J. Carmody, et al., *Residential windows: a guide to new technologies and energy performance*, New York: Norton (1996)

[3] H. Lüth. *Surface and Interfaces of Solids*, Springer Verlag (1992)

[4] H. Ibach, *Physics of Surfaces and Interfaces*, Springer Verlag (2006)

[5] M. Henini, *Molecular beam epitaxy. From research to mass production*, Elsevier (2013)

[6] H. S. Nalwa, *Handbook of thin film materials*, Academic Press (2002)

[7] Retrieved from http://www.umms.sav.sk

[8] S. Hüfner, *Photoelectron spectroscopy: principles and applications*, Springer (1995)

[9] S. Hofmann, *Auger and X-ray photoelectron spectroscopy in material science*, Springer (2013)

[10] Retrieved from: https://desy.cfel.de/e100031/e162254/e162270/.

[11] D. Briggs, *Surface Analysis by Auger and X-ray Photoelectron Spectroscopy*, IM Publication and Surface Spectra Limited (2003)

[12] M. P. Seah, and W. A. Dench, *Surface and interface analysis* **1.1** (1979) 2

[13] Retrieved from http://www.helmholtz-berlin.de/, KMC-1, HIKE end station description

[14] Retrieved from: http://www.sciencesway.com/vb/showthread.php?t=15464#.Udu5zPkwd14.

[15] F. Schaefers, et al., *Rev. Sci. Instrum.* **78** (2007) 123102

[16] M. Gorgoi, et al., *Nuclear Instruments and Methods in Physics Research A* **601** (2009) 48

[17] Retrieved from: http://www.casaxps.com/help_manual/line_shapes.htm.

[18] J. J. Olivero and R. L. Longbothum, *Journal of Quantitative Spectroscopy and Radiative Transfer* **17(2)** (1977) 233

[19] S. Doniach and M. Sunjic, *Journal of Physics C: Solid State Physics* **3.2** (1970) 285

[20] P. Van der Straten, et al., *Z. Phys. D* **8** (1988) 35

[21] D. A. Shirley, *Physical Review B* **5.12** (1972) 4709

[22] E. Kukk, Spectrum Analysis by Curve Fitting (SPANCF) - macro package for Igor Pro. Available from: http://www.geocities.ws/ekukk/intro.htm

[23] C. J. Powell and A. Jablonski, *Journal of Electron Spectroscopy and Related Phenomena* **178** (2010) 331

[24] B. O. Kolbesen, et al., *Analytical and diagnostic techniques for semiconductor materials, devices, and processes*, The Electrochemical Society ECS PV 99-16, Leuven (1999)

[25] Y. Waseda, *The structure of non-crystalline materials*, Mc. Graw-Hill (1980)

[26] J. I. Langford and A. J. C. Wilson, *J. Appl. Cryst.* **11** (1978) 102

[27] W. H. Hall, *Acta Metall.* **1** (1953) 22

[28] D. K. Bowen and B. K. Tanner, *X-Ray Metrology in Semiconductor Manufacturing*, Taylor & Francis Group (2006)

[29] M. Björck and G. Andersson, *J. Appl. Cryst.* **40** (2007) 1174

[30] A. J. Tousimis and L. Marton, *Electron Probe Microanalysis*, Academic Press (1969)

[31] J. L. Pouchou and F. Pichoir, *J. de Physique* **45** (1984) C2

[32] P. A. Redhead, *Vacuum*, **12(4)** (1962) 203

[33] S. Fearn, *An Introduction to Time-of-Flight Secondary Ion Mass Spectrometry (ToF-SIMS) and its Application to Materials Science*, Morgan & Claypool Publishers, IOP Concise Physics (2015)

[34] S. Perkowitz, *Optical Characterization of Semiconductors: Infrared, Raman, and Photoluminescence Spectroscopy*, Academic Press (1993)

[35] H. Kuzmany, *Solid-state spectroscopy*, Springer (2009)

[36] R. Lazzari and J. Jupille, *Nanotechnology* **22** (2011) 445703

[37] C. F. Bohren and D. R. Huffman, *Absorption and Scattering of Light by Small Particles*, New York: Wiley (1983)

[38] U. Kreibig and M. Vollmer, *Optical Properties of Metal Clusters*, Springer Verlag (1995)

[39] C. Noguez, *J. Phys. Chem. C* **111** (2007) 3806

[40] C. G. Granqvist, et al., *Phys. Rev. B* **16** (1977) 3513

[41] U. Kreibig and L. Genzel, *Surf. Sci.* **156** (1985) 678

[42] D. Bedeaux and J. Vlieger, *Physica A* **67** (1973) 55

[43] R. Lazzari, et al., *Phys. Rev. B* **68** (2003) 045428

[44] D. Bedeaux and J. Vlieger, *Optical Properties of Surfaces*, Imperial College Press (2001)

[45] M. T. Haarmans and D. Bedeaux, *Thin Solid Films* **258** (1995) 213

[46] M. M. Wind and J. Vlieger, *Physica A* **141** (1987) 33

[47] I. Simonsen, et al., *Phys. Rev. B* **61.11** (2000) 7722

[48] R. Lazzari, et al., *Eur. Phys. J. B* **24** (2001) 267

[49] R. Lazzari, et al., *Phys. Rev. B* **65** (2002) 235424

[50] E. H. Sondheimer, *Adv. Phys.* **1:1** (1952) 42

[51] A. F. Mayadas and M. Shatzkes, *Phys. Rev. B* **1** (1970) 1382

[52] C. Wöll, *Progress in surface science* **82.2** (2007) 55

[53] P. W. Tasker, *Journal of Physics C: Solid State Physics* **12.22** (1979) 4977

[54] J. Goniakowski, et al., *Rep. Prog. Phys.* **71(1)** (2008) 016501

[55] C. Noguera and J. Goniakowski, *Chemical reviews* **113(6)** (2013) 4073

[56] C. Tuscheet, et al., *Phys. Rev. Lett.* **99** (2007) 026102

[57] J. Goniakowski et al., *Phys. Rev. Lett.* **98** (2007) 205701

[58] Wander, A., et al., *Physical review letters* **86.17** (2001) 3811

[59] B. Meyer and D. Marx, *Phys. Rev. B* **67(3)** (2003) 035403

[60] R. T. Girard, et al., *Surf. Sci.* **373** (1997) 409

[61] K. Ozawa and K. Mase, *Phys. Rev. B* **83** (2011) 125406

[62] M. Sambi, et al., *Surf. Sci.* **319** (1994) 149

[63] S. H. Overbury, et al., *Surf. Sci.* **410** (1998) 106

[64] H. Maki, et al., *Surf. Sci.* **457** (2000) 377

[65] N. Jedrecy, et al., *Applied surface science* **162** (2000) 69

[66] Y. Ding and Z. L. Wang, *Surf. Sci.* **601** (2007) 425

[67] O. Dulub, et al., *Surf. Sci.* **519** (2001) 201

[68] O. Dulub, et al., *Physical review letters* **90.1** (2003) 016102

[69] U. Diebold, et al., *Applied surface science* **237.1** (2004) 336

[70] O. Dulub, et al., *Surface Science* **519.3** (2002) 201

[71] T. M. Parker, et al., *Surface science* **415.3** (1998) L1046

[72] S. Torbrügge, et al., *J. Phys. Chem. C* **113** (2009) 4909

[73] C. Noguera, et al., *Phys. Rev. B* **81** (2010) 155409

[74] M. H. Du, et al., *Phys. Rev. B* **78** (2008) 155424

[75] G. Kresse, et al., *Physical Review B* **68.24** (2003) 245409

[76] M. Valtiner, et al., *Phys. Rev. Lett.* **103.6** (2009) 065502

[77] H. Meskine and P. A. Mulheran, *Phys. Rev. B* **84** (2011) 165430

[78] J. H. Lai, et al., *Phys Rev B* **82** (2010) 155406

[79] F. Ostendorf, et al., *Phys. Rev. B* **77** (2008) 041405R

[80] H. Zheng, et al., *Phys. Rev. Lett.* **111** (2013) 086101

[81] M. Kunat, et al., *Physical Review B* **66.8** (2002) 081402.

[82] T. Becker, et al., *Surface science* **486.3** (2001) L502

[83] M. Kunat, et al., *J. Phys. Chem. B* **107** (2002) 14350

[84] B. Meyer, *Physical Review B* **69.4** (2004) 045416

[85] B. Meyer and D. Marx, *Phys. Rev. B* **69** (2004) 235420

[86] V. Staemmler, et al., *Phys. Rev. Lett.* **90** (2013) 106102

[87] S. E. Chamberlin, et al., *Phys. Rev. B* **84** (2011) 075437

[88] R. Wahl, et al., *Phys. Rev. B* **87.8** (2013) 085313

[89] R. Lindsay, et al., *Surface science* **565.2** (2004) L283

[90] M. Valtiner, et al., *Phys. Chem. Chem. Phys.* **9** (2007) 2406

[91] M. Valtiner, et al., *Langmuir* **24** (2008) 5350

[92] S. T. King, et al., *Surf. Sci.* **602** (2008) L131

[93] J. V. Lauritsen, et al., *ACS nano* **5.7** (2011) 5987

[94] I. Beinik, et al., *Nat. Commun.* **6** (2015) 8845

[95] U. Özgür, et al., *Journal of applied physics* **98.4** (2005) 041301

[96] S. J. Pearton, et al., *Prog. Mat. Sci.* **50** (2005) 293

[97] M. D. McCluskey and S. J. Jokela, *J. Appl. Phys.* **106** (2009) 071101

[98] A. Janotti and C. G. Van de Walle, *Rep. Prog. Phys.* **72(12)** (2009) 126501

[99] C. F. Klingshirn, et al., *Zinc oxide*, Springer (2010)

[100] J. C. Fan, et al., *Progress in Materials Science* **58(6)** (2013) 874

[101] A. Janotti and C. G. Van de Walle, *Phys. Rev. B* **76** (2007) 165202

[102] L. J. Brillson and Y. Lu, *Journal of Applied Physics* **109(12)** (2011) 121301

[103] E. V. Monakhov, et al., *J. Phys. D: Appl. Phys.* **42(15)** (2009) 153001

[104] C. G. Van de Walle, *Phys. Rev; Lett.* **85** (2000) 1012

[105] C. G. Van der Walle and J. Neugebauer, *Nature* **423** (2003) 626

[106] D. G. Thomas and J. J. Lander, *J. Chem. Phys.* **25** (1956) 1136

[107] D. M. Hofmann, et al., *Phys. Rev. Lett.* **88** (2002) 045504

[108] C. H. Seager and S. M. Myers, *J. Appl. Phys.* **94** (2003) 2888

[109] H. Qiu, et al., *Phys. Rev. Lett.* **101** (2008) 236401

[110] E. V. Lavrov, et al., *Phys. Rev. B* **79** (2009) 165210

[111] C. Ton-That, et al., *New J. Phys.* **16** (2014) 083040

[112] M. D. McCluskey, et al., *Appl. Phys. Lett.* **81** (2002) 3807

[113] E. V. Lavrov, et al., *Phys Rev B* **66** (2002) 165205

[114] N. H. Nickel and K. Fleischer, *Phys Rev Lett* **90** (2003) 197402

[115] G. Alvin Shi, et al., *Phys. Rev. B* **72** (2005) 195211

[116] N. H. Nickel, *Phys. Rev. B* **73** (2006) 195204

[117] E. V. Lavrov, et al., *Phys. Rev. Lett.* **102** (2009) 185502

[118] S. F. J. Cox, et al., *Phys. Rev. Lett.* **86** (2001) 2601

[119] J. Cvizvek, et al., *J. Appl. Phys.* **103(5)** (2008) 053508

[120] S. J. Jokela and M. D. McCluskey, *Phys. Rev. B* **72** (2005) 113201

[121] G. Alvin Shi, et al., *Appl. Phys. Lett.* **85** (2004) 5601

[122] G. Brauer, et al., *Phys. Rev. B* **79** (2009) 115212

[123] N. H. Nickel and K. Brendel, Phys. Rev. B **68** (2003) 193303

[124] K. M. Johansen, et al., *Appl. Phys. Lett.* **97** (2010) 211907

[125] M.-H. Du and K. Biswas, *Phys. Rev. Lett.* **106** (2011) 115502

[126] F. Traeger, et al., *Phys. Rev. B* **84** (2011) 075462

[127] K. Ip, et al., *Appl. Phys. Lett.* **82** (2003) 385–387

[128] M. G. Wardle, et al., *Phys. Rev. Lett.* **96** (2006) 205504

[129] L. J. Brillson, et al., *J. Vac. Sci. Technol. B* **30** (2012) 050801

[130] W. H. Doh, et al., *Langmuir* **26** (2010) 16278–16281

[131] Ch. Wöll, *J. Phys.: Condens. Matter* **16** (2004) S2981

[132] M. Losurdo and M. M. Giangregorio, *Appl. Phys. Lett.* **86** (2005) 091901

[133] G. Bruno, et al., *Adv. Mater.* **21** (2009) 1700

[134] E. D. Batyrev and J. C. van den Heuvel, *Phys. Chem. Chem. Phys.* **13** (2011) 13127

[135] G. Heiland and P. Kunstmann, *Surf. Sci.* **13** (1969) 72

[136] M. D'Angelo, et al., *Phys. Rev. Lett.* **108** (2012) 116802

[137] H. Lüth, *Surf. Sci.* **37** (1973) 90

[138] O. Schmidt, et al., *Superlattices Microstruct.* **39** (2006) 8

[139] M. W. Allen, et al., *Phys. Rev. B* **81** (2010) 075211

[140] D. Kohl and G. Heiland., *Surf. Sci.* **63** (1977) 96

[141] D. Kohl, et al., *Surf. Sci.* **73** (1978) 160

[142] Y. Goldstein, et al., *Phys. Rev. B* **19** (1979) 2256

[143] Y. Goldstein, et al., *Surf. Sci.* **98** (1980) 599

[144] A. Many, et al., *Phys. Rev. Lett.* **46** (1981) 1648

[145] Y. Wang, et al., *Phys. Rev. Lett.* **95** (2005) 266104

[146] L. F. J. Piper, et al., *Phys. Rev. B* **81** (2010) 233305

[147] K. Ozawa and K. Mase, *Phys. Rev. B* **81** (2010) 205322

[148] Y.M. Strzhemechny, et al., *Appl. Phys. Lett.* **84** (2004) 2545

[149] Y. Margoninski and D. Eger, *Surf. Sci.* **80** (1979) 579

[150] G. Yaron, et al., *J. Appl. Phys.* **58** (1985) 3508

[151] D. Eger, et al., *Phys. Lett.*, **55A** (1975) 197

[152] D. Eger and Y. Goldstein, *Phys. Rev. B* **19** (1979) 1089

[153] R. Heinhold, et al, *Phys. Rev. B* **88** (2013) 235315

[154] J. I. Gersten, et al., *Phys. Rev. B* **29(5)** (1984) 2458

[155] M. Nitzan, et al., *Phys. Rev. B* **19** (1979) 4107

[156] E. Veuhoff and D. Kohl, *J Phys C: Solid State Phys* **14** (1981) 2395

[157] Y. Goldstein and Y. Grinshpan, *Phys. Rev. Lett.* **39** (1977) 953

[158] M. Wolovelsky, et al., *Phys. Rev. B* **57** (1998) 6274

[159] K. Ozawa and K. Mase, *Physica Status Solidi (a)* **207** (2010) 277

[160] K. Jacobi, et al., *Surf. Sci.* **141** (1984) 109

[161] W. Sun, et al., *J. Appl. Phys.* **117** (2015) 165304

[162] Moorman H., et al., *Surf. Sci.* **80** (1979) 261

[163] Moorman H., et al., *Surf. Sci.* **100** (1980) 302

[164] S. A. Chevtchenko, et al., *Appl. Phys. Lett.* **89** (2006) 182111

[165] F. L. Kuo, et al.,. *J. Phys. D: Appl. Phys.* **45** (2012) 065301

[166] M.W. Allen, et al., *Appl. Phys. Lett.* **98(10)** (2011) 101906

[167] R. Heinhold and M.W. Allen, *J. Mater. Res.* **27** (2012) 2214

[168] R. Heinhold, et al., *J. Phys. Chem. C* **118(42)** (2014) 24575

[169] P. Blumentrit, et al., *Appl. Surf. Sci.* **258(2)** (2011) 780

[170] K. Ozawa, et al., *Phys. Rev. B* **68(12)** (2003) 125417

[171] K. Ozawa and K. Edamoto, *Surf. Sci.* **524** (2003) 78

[172] K. Ozawa, et al., *J. Phys. Chem. B* **109** (2005) 14619

[173] O. T. Hofmann, et al., *J. Chem. Phys.* **139** (2013) 174701

[174] K. H. Ernst, et al., *Phys. Rev. B* **47(20)** (1993) 13782

[175] S. V. Didziulis, et al., *J. Am. Chem. Soc.* **111** (1989) 7110

[176] D. Schmeisser and K. Jacobi, *Surf. Sci.* **88** (1979) 138

[177] R. K Swank, *Phys. Rev.* **153** (1967) 844

[178] T. Kim, et al., *Surf. Interface Anal.* **42** (2010) 1528

[179] D. Kohl, et al., *Surf. Sci.* **41** (1974) 403

[180] M. Kobayashi, et al., *J. Appl. Phys.* **105(12)** (2009) 122403

[181] H. Mathieu, *Physique des semiconducteurs et des composants électroniques*, Masson (1990)

[182] W. Mönch, *Semiconductor surfaces and interfaces*, Springer (1995)

[183] L. J. Brillson, *Surf. Sci. Rep.* **2** (1982) 123

[184] W. Mönch, *Rep. Prog. Phys.* **53** (1990) 221

[185] R. T. Tung, *Mat. Sci. and Eng. R.* **35** (2001) 1

[186] Z. Zhang and J. T. Yates, *Chem. Rev.* **112(10)** (2012) 5520

[187] N. Cabrera and N. F. Mott, *Rep. Prog. Phys.* **12** (1949) 163

[188] U. Diebold, *Surf. Sci. Rep.* **48** (2003) 53

[189] A. Zychma, et al., *Physica Status Solidi B* **250** (2013) 1071

[190] E. F. Wassermann and K. A. Polacek, *Surf. Sci.* **28** (1971) 77

[191] C. T. Campbell, et al., *Surf. Sci.* **182** (1987) 458

[192] N. Jedrecy, et al., *Phys. Rev. B* **64** (2001) 085424

[193] N. Jedrecy, et al., *Phys. Rev. B* **72** (2005) 045430

[194] N. Jedrecy, et al., *Phys. Rev. B.* **72** (2005) 195404

[195] H. Jacobs, et al., *Surf. Sci.* **160** (1985) 217

[196] W. T. Petrie and J. M. Vohs, *J. Chem. Phys.* **101(9)** (1994) 8098

[197] P. V. Radulovic, et al., *J. Phys. Chem.* **104** (2000) 3028

[198] W. P. Vellinga and T. M. De Hosson, *Acta. Mat.* **45(3)** (1997) 933

[199] J. Yoshihara, et al., *Surf. Sci.* **406** (1998) 235

[200] J. Yoshihara, et al., *Surf. Sci.* **439** (1999) 153

[201] C. T. Campbell, *Surf. Sci. Rep.* **27(1-3)** (1997) 1

[202] M. Kroll and U. Köhler, *Surf. Sci.* **601** (2007) 2182

[203] L. G. Koplitz, et al., *J. Phys. Chem. B* **107** (2003) 10583

[204] O. Dulub, et al., *Top. Catal.* **36** (2005) 65

[205] U. Köhler, et al., *Physica Status Solidi b* **250** (2013) 1222

[206] E. Duriau, et al., *Appl. Surf. Sci.* **253** (2006) 549

[207] E. D. Batyrev, et al., *J. Phys. Chem. C* **116** (2012) 19335

[208] M. Kroll, et al., *Phys. Chem. Chem. Phys.* **14(5)** (2012) 1654

[209] P. Borghetti, Y. Mouchaal, Z. Dai, S. Chenot, R. Lazzari, and J. Jupille, *Orientationdependent band-bending and chemistry for Ti on polar ZnO surfaces*, submitted (2016)

[210] M. Galeotti, et al., *Surf. Sci.* **375** (1997) 63

[211] I. Spolveri, et al., *Surf. Sci.* **412-413** (1998) 631

[212] D. Wett, et al., Appl. *Surf. Sci.* **254** (2008) 2309

[213] M. P. Hyman, et al., *J. Phys. Chem. C* **114** (2010) 16892

[214] M. Yoshitake, et al., *J. Vac. Sci. Technol. A* **31** (2013) 020601

[215] H. Kim, et al., *Journal of Electronic Packaging* **135** (2013) 011010

[216] Y. Dong, et al., *J. Vac. Sci. Technol. B* **27** (2009) 1710

[217] B. J. Coppa, et al., *J. Appl. Phys.* **97** (2005) 103517

[218] H. L. Mosbacker, et al., *Appl. Phys. Lett.* **87** (2005) 012102

[219] J.-M. Lee, et al., *Appl. Phys. Lett.* **78** (2001) 3842

[220] M. W. Allen, et al., *Appl. Phys. Lett.* **94** (2009) 103508

[221] A. Y. Polyakov, et al., *Appl. Phys. Lett.* **88** (2003) 1575

[222] M. W. Allen, et al., *Appl. Phys. Lett.* **89** (2006) 103520

[223] K. Maeda, et al., *Sci. Technol.* **20** (2005) 549

[224] Y. Mouchaal, *Elaboration et étude de nouvelles électrodes transparentes substituts de l'ITO dans les dispositifs optoélectroniques*, PhD thesis, Université d'Oran 1 (2016)

[225] V. E. Henrich, et al., *Surf. Sci.* **74(3)** (1978) 682

[226] I. Valenti, *Coupling metals with zinc oxide: structure, morphology and optical properties*, PhD thesis, University of Modena, Italy (2015)

[227] R. Lazzari and J. Jupille, *Nanotechnology* **23** (2012) 35707

[228] R. Lazzari, *Vers la maîtrise de la croissance des couches minces: une étude par spectroscopie optique et d'électrons*, PhD thesis, Université Paris 11 (2000)

[229] R. Lazzari, et al., *J. Phys. Chem. C* **118** (2014) 7032

[230] R. Lazzari, et al., *Phys. Rev. B* **79** (2009) 125428

[231] Y. Borenstzein, et al., *Europhys. Lett.* **31(5-6)** (1995) 311

[232] H. Hövel, et al., *Phys. Rev. B* **48(24)** (1993) 18178

[233] R. Cavallotti, *Effets de la terminaison de l'a-alumine sur le comportement au mouillage du zinc*, PhD thesis, Université Pierre et Marie Curie Paris 6 (2014)

[234] R. Lazzari, et al., *Plasmonics* **9** (2014) 261

[235] S. Castilla, *Nanoplasmonics of supported particles*, MSc thesis, NanoMat, Université Pierre et Marie Curie Paris 6 (2016).

[236] P. Ruffieux, et al., *Rev. Sci. Instr.* **71** (2000) 3634

[237] R. A. Powell, et al., *Phys. Rev. B* **6** (1972) 3056

[238] W. Göpel, et al., *Phys. Rev. B* **26** (1982) 3144

[239] S. V. Didziulis, et al., *Inorg. Chem.* **27** (1998) 2238

[240] P. D. C. King, et al., *Phys. Rev. B* **79** (2009) 205205

[241] L. Y. Lim, et al., *Phys. Rev. B* **86** (2012) 235113

[242] C.D. Wagner, et al., NIST Standard Reference Database 20, Version 3.4 (web version, http://srdata.nist.gov/xps/) (2003)

[243] J. Lahiri, et al., *Phys. Rev. B* **78** (2008) 155414

[244] P. A. Thiel and T. A. Madey, *Surf. Sci. Rep.* **7(68)** (1987) 211

[245] R. L. Kurtz, et al., *Surf. Sci* **218** (1989) 178

[246] K. Ozawa, et al., *Phys. Rev. B* **79** (2009) 075314

[247] J. H. Fox, et al., *Surf. Sci.* **63** (1977) 390

[248] S. Tanuma, et al., *Surface and Interface Analysis* **21.3** (1994) 165

[249] C. J. Powell and A. Jablonski, *NIST Electron Inelastic-Mean-Free-Path Database, Version 1.2,* SRD 71, National Institute of Standards and Technology, Gaithersburg MD (2010).

[250] T. C. Chiang, *Surf. Sci. Rep.* **39** (2000) 181

[251] G. K. Wertheim, et al., *Phys. Rev. Lett.* **51** (1983) 2310

[252] G. K. Wertheim, et al., *Phys. Rev. B* **33** (1986) 5384

[253] H. Hövel, et al., *Phys. Rev. Lett.* **81** (1998) 4608

[254] A. Howard, et al., *Surf. Sci.* **518** (2002) 210

[255] M. G. Helander, et al., *Appl. Surf. Sci.* **256** (2010) 2602

[256] A. A. Chambers, et al., *J. Vac. Sci. Technol. B* **22** (2004) 2205

[257] A. W. Dweydari and C. H. B. Mee, *Phys. Stat. Sol.* **27** (1975) 233

[258] H. B. Michaelson, *J. Appl. Phys.* **48** (1977) 4729

[259] H. L. Skriver and N. M. Rosengaard, *Phys. Rev. B* **46** (1992) 7157

[260] M. Uda, et al., *J. Electron. Spectos. Rel. Phenom.* **643-648** (1998) 88

[261] http://www.webelements.com (2014)

[262] W. Hirschwald, *Zinc Oxide: properties and behaviour of the bulk, the solid/vacuum and solid/gas interfaces*, North Holland Publishing (1981)

[263] M. H. Hecht, *Phys. Rev. B* **41** (1990) 7918

[264] J. P. Long and V. M. Bermudez, *Phys. Rev. B* **66** (2002) 121308

[265] N. Ohashi, et al., *Appl. Phys. Lett.* **101** (2012) 251911

[266] C. E. ViolBarbosa, et al., *Phys. Rev. B* **88(19)** (2013) 195128

[267] A. Hirose, et al., *Appl. Phys. Lett.* **106** (2015) 191602

[268] M. W. Allen and S. M. Durbinm, et al., *Appl. Phys. Lett.* **92** (2008) 122110

[269] J. Li, *Origin, location and trasnport of excess charges in titanium dioxide*, PhD thesis, Université Pierre et Marie Curie (2016)

[270] J. Zúñiga-Pérez, et al., *Appl. Phys. Rev.* **3** (2016) 041303

[271] A. N. Mariano and R. E. Hanneman, *J. Appl. Phys.* **34** (1963) 384

[272] H. Maki, et al., *Thin Solid Films* **411** (2002) 91

[273] J. R. Williams, et al., *Surface Science* **605** (2011) 1336

[274] J. R. Williams, et al., *J. Appl. Phys.* **111** (2012) 033525

[275] N. Ohashi, et al., *Appl. Phys. Lett.* **94** (2009) 122102

[276] J. R. Williams, et al., *Applied Physics Letters* **100** (2012) 051902

[277] T. Ohsawa, et al., *Applied Physics Letters* **107** (2015) 171604

[278] T. D. Veal, et al., *Physical Review B* **76** (2007) 075313

[279] J. R. Williams, et al., *Applied Physics Letters* **103** (2013) 042107

[280] Y. Adachi, et al., *Thin Solid Films* **519** (2011) 5875

[281] C.B. Alcock, et al., *Can. Metall. Q.* **23** (1984) 309

[282] Ellingham diagram, *e.g.* http://web.mit.edu/2.813/www/readings/Ellingham_diagrams.pdf

[283] Y.-C. Lee, et al., *3rd International Nanoelectronics Conference (INEC)* (2010)

[284] S. Kuriakose, et al., *Physical Chemistry Chemical Physics* **16** (2014) 12741

[285] A. Pflug, et al., *Surf. and Coat. Technol.* **267** (2015) 81

[286] C. Li, et al., *Nanoscale Res. Lett.* **5** (2010) 773

[287] F. J. J. Van Loo and A. A. Kodentsov, *Pure & Appl. Chem.* **70(2)** (1998) 501

[288] Q. Fu and T. Wagner, *Surf. Sci. Rep.* **62** (2007) 431

[289] M. He and T. M. Lu, *Metal-Dielectric Interfaces in Gigascale Electronics*, Springer (2012)

[290] Q. Fu, et al., *J. Phys. Chem. B* **109** (2005) 944

[291] E. Bauer, *Zeitschrift für Kristallographie* **110** (1958) 372

[292] M. Ohring, Materials science of thin films, Academic (2002)

[293] C. T. Campbell, *Phys. Rev. Lett.* **96** (2006) 066106

[294] M. Mühlbacher, et al., *Journal of Applied Physics* **118** (2015) 085307

[295] R. G. C. Beerkens and H. Waal, *Journal of the American Ceramic Society* **73(7)** (1990) 1857

[296] H.-K. Kim, et al., *Jpn. J. Appl. Phys.* **1-43** (2004) 976

[297] H.-K. Kim, et al., *J. Electrochem. Soc.* **151** (2004) G223

[298] D. R. Lide, *CRC Handbook of Chemistry and Physics*, Chemical Rubber (1995)

[299] F. H. Dulin and D. E. Rase, *Journal of The American Ceramic Society* **43(3)** (1960) 125

[300] S. F. Bartram and R. A. Slepetys, *Journal of The American Ceramic Society* **44(10)** (1961) 493

[301] H. T. Kim, *J. Am. Ceram. Soc.* **84(5)** (2001) 1081

[302] X. Qian, et al., *J. Vac. Sci. Technol. A* **31** (2013) 01A133

[303] Y.-C. Lee, et al., *Thin Solid Films* **518** (2010) 7366

[304] U. Steinike and B. Wallis, *Cryst. Res. Technol.* **32** (1997) 1

[305] J. Yang and J. H. Swisher, *Materials Characterization* **37(2-3)** (1996) 153

[306] Y. Yang, et al., *ACS Nano* **3(3)** (2009) 555

[307] S. K. Manik, et al., *Materials Chemistry and Physics* **82** (2003) 837

[308] Activity report 2002-2005, UMR 125 Saint-Gobain Recherche/CNRS (2005)

[309] A. M. A. Rahman and T. Narusawa, *Nucl. Instr. and Meth. in Phys. Res. B* **266** (2008) 1378

[310] Knut et al., *J. Appl. Phys.* **115** (2014) 043714

[311] Kim, et al., *Appl. Phys. Lett.* **77(11)** (2000) 1647

[312] K. Ip, et al., *J. Vac. Sci. Technol. B* **21** (2003) 2378

[313] J. L. Murray, *Bulletin of Alloy Phase Diagrams* **5(1)** (1984) 52

[314] D. Briggs and M. P. Seah, *Practical Surface Analysis*, John Willey & Sons (1993)

[315] L. Cao and Y. Zhu, *Applied Surface Science* **133** (1998) 213

[316] J. Le Hericy and J. P. Langeron, *Analysis* **9(5)** (1981) 188

[317] C. D. Wagner, et al., *J. Vac. Sci. Technol.* **21(4)** (1982) 933

[318] C. D. Wagner, *J. Vac. Sci. Technol.* **15(2)** (1978) 518

[319] C. D. Wagner, et al., *Applications of Surface Science* **9** (1981) 203

[320] J. C. Lascovish, et al., *Applied Surface Science* **47** (1991) 17

[321] A. Pérez del Pino, et al., *Thin Solid Films* **415** (2002) 201

[322] T. Godfroid, et al., *Thin Solid Films* **437** (2003) 57

[323] M. C. Biesinger, et al., *Applied Surface Science* **257** (2010) 887

[324] D. Coster and R. De L. Kronig, *Physica* **2** (1935) 13

[325] C. D. Wagner, et al., *Handbook of X-Ray Photoelectron Spectroscopy*, Perkin-Elmer Corporation (1979)

[326] J. C. Klein and D. M. Hercules, *J. Catal.* **82** (1983) 424

[327] P. S. Wehner, et al., *J. Catal.* **84** (1983) 244

[328] G. Deroubaix and P. Marcus, *Surf. Interface Anal.* **18** (1992) 39

[329] S.W. Gaarenstroom and N. Winograd, *J. Chem. Phys.* **67** (1977) 3500

[330] B. R. Strohmeier, *Surf. Sci. Spectra* **3** (1994) 128

[331] L. S. Dake, et al., *Surf. Interface Anal.* **14** (1989) 71

[332] D. Borgmann, et al., *Journal of Electron Spectroscopy and Related Phenomena* **63** (1993) 91

[333] B. A. Staskiewicz, et al., *J. Am. Chem. Soc.* **77(11)** (1955) 2987

[334] C. R. Clayton and Y. C. Lu, *Journal Electrochem. Soc.* **133(12)** (1986) 2465

[335] S. Tougaard, QUASES-IMFP-TPP2M program, Quases-Tougaard Inc (2002)

[336] S. Tougaard, *Applied Surface Science* **100/101** (1996) 1

[337] L. Brewer and R.H. Lamoreaux, *Binary Alloy Phase Diagrams*, Materials Information Soc. (1990)

[338] King D.A., *Surface Sciences* **47** (1975) 384

[339] A. M. DeJong and J. W. Niemantsverdriet, *Surf. Sci.* **233** (1990) 355

[340] A. J. Franz, et al., *J. Phys. Chem. B* **103** (1999) 4457

[341] J. L. Falconer and K. Schwarz., *Catal. Rev. Sci. Eng.* **25** (1983) 141

[342] K. Ip, et al., *Appl. Phys. Lett.* **84(25)** (2004) 5133

[343] C.W. Bale, et al., *Calphad Journal*, **62** (2002) 189

[344] G. P. Vassilev, et al., *Journal of Alloys and Compounds* **375** (2004) 162

List of Figures

List of Tables